

University of St Andrews



Full metadata for this thesis is available in
St Andrews Research Repository
at:

<http://research-repository.st-andrews.ac.uk/>

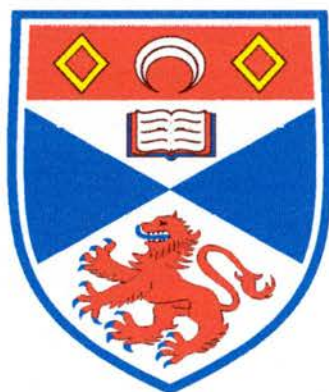
This thesis is protected by original copyright

Niobium based materials for use as current collectors in the anode of Solid Oxide Fuel Cells

A thesis presented for examination for the title of Ph.D

by

Anna Lashtabeg



University of St. Andrews

June 2004



I, Anna Lashtabeg, hereby certify that this thesis, which is approximately 40,000 words in length, has been written by me, that it is the record of work carried out by me and that it has not been submitted in any previous application for a higher degree.

Date 14/6/04 Signature of Candidate

I was admitted as a research student in June 2001 and as a candidate for the degree of Doctor of Philosophy in June 2002, the higher study for which this is a record was carried out in the University of St. Andrews between 2001 and 2004.

Date 14/6/04 Signature of Candidate

I hereby certify that the candidate has fulfilled the conditions of the Resolution and Regulations appropriate for the degree of Doctor of Philosophy in the University of St. Andrews and that the candidate is qualified to submit this thesis in application for that degree.

Date 14/6/04 Signature of Supervisor

In submitting this thesis to the University of St. Andrews I understand that I am giving permission for it to be made available for use in accordance with the regulations of the University Library for the time being in force, subject to any copyright vested in the work not being affected thereby. I also understand that the title and abstract will be published, and that a copy of the work may be made and supplied by any *bona fide* library or research worker.

Date 14/6/04 Signature of Candidate

Table of contents

Acknowledgements.....	iv
Abstract.....	v
Chapter 1 – Introduction.....	1
Chapter 2 – Experimental.....	40
Chapter 3 – Theory.....	53
Chapter 4 – Nb ₂ O ₅ –TiO ₂ System.....	93
Chapter 5 – Strontium Niobates.....	167
Chapter 6 – MNb ₂ O ₆ (M=Ba,Ca).....	217
Chapter 7 – Discussion and further work.....	240

Acknowledgements

I cannot imagine having a better supervisor than Prof. J.T.S. Irvine, whom I would like to thank for getting me through my three years of work and study, especially during the more trying times, with his infinite patience, unending support and excellent advice which I was never reserved in seeking.

I would also like to thank all the members of the JTSI research group for the part they played in my work and social life. Jesus Canales-Vazquez I would like to thank for the parties and tequila nights, and he made up for the killer hangovers by his invaluable help with TEM images presented in this thesis. Paul Connor for his friendship and advice in the lab and along with Nadja Zakowski they got me off the couch and into the fitness lifestyle of gymming and swimming.

Especial thanks to John Bradley for his undying support, help and amazing patience both at work and home. Many thanks is for his help in the lab and particularly with AC Impedance.

A big thanks goes to the technical staff at St. Andrews especially Sylvia Williamson whose help was invaluable in TGA and dilatometer measurements.

Finally but most importantly I would like to thank my mother, whose hard work, dedication and sacrifices through all my life made it possible for me to achieve this.

Abstract

In this work I present the results of my studies on a series of reduced niobium based rutile structures: Nb_2TiO_7 doped with Fe and Zr, $\text{Ti}_{1-2x}\text{Cr}_x\text{Nb}_x\text{O}_2$ solid solution series. Strontium niobates of the stoichiometry $\text{Sr}_4\text{Nb}_2\text{O}_9$, $\text{Sr}_2\text{Nb}_2\text{O}_7$, SrNb_2O_6 and their reduced phases were also investigated, along with CaNb_2O_6 and BaNb_2O_6 .

Thermal expansion and electronic conductivity of these materials were investigated under oxidising and reducing conditions. Nb_2TiO_7 goes to rutile structure $\text{Nb}_{1.33}\text{Ti}_{0.67}\text{O}_4$ under reducing conditions, and this has the highest conductivity of all materials investigated at 300 Scm^{-1} at 900°C with $p(\text{O}_2)=10^{-20}$ atm, but the lowest thermal expansion of $3.00\pm 0.05\times 10^{-6} \text{ K}^{-1}$ (100°C - 900°C), which is incompatible with the thermal expansion coefficient of the Ni/YSZ anode in the solid oxide fuel cell of $10.3\times 10^{-6} \text{ K}^{-1}$. Doping $\text{Nb}_{1.33}\text{Ti}_{0.67}\text{O}_4$ decreases its conductivity, but increases its thermal expansion to a maximum of $6.3\times 10^{-6} \text{ K}^{-1}$ for $\text{Nb}_{1.347}\text{Ti}_{0.639}\text{Fe}_{0.014}\text{O}_4$.

The $\text{Ti}_{1-2x}\text{Cr}_x\text{Nb}_x\text{O}_2$ solid solution series shows a maximum thermal expansion of $8.5\times 10^{-6} \text{ K}^{-1}$ for $x=0.1$ which then drops with increasing x to $5.6\times 10^{-6} \text{ K}^{-1}$ for $x=0.5$. The conductivity of these samples, however, reaches a maximum of $\sim 20 \text{ Scm}^{-1}$ at $p(\text{O}_2)=10^{-20}$ atm at 900°C for $x=0.1$ - 0.3 , then drops to $\sim 10 \text{ Scm}^{-1}$ for $x=0.4$ and $\sim 6 \text{ Scm}^{-1}$ for $x=0.5$.

$\text{Sr}_4\text{Nb}_2\text{O}_9$, $\text{Sr}_2\text{Nb}_2\text{O}_7$, SrNb_2O_6 , CaNb_2O_6 and BaNb_2O_6 all show fairly poor electronic conductivities in air and $5\%\text{H}_2/\text{Ar}$ ($p(\text{O}_2)=10^{-20}$ atm) at 900°C which make them unsuitable for use in the anode of the SOFC. Structurally they are very stable to reducing conditions up to 1200° - 1300°C in $5\%\text{H}_2/\text{Ar}$ compared to Nb_2TiO_7 whose structure changes to rutile upon reduction.

In the systems studied, there are two types of conductivity that dominate. BaNb_2O_6 or $\text{Sr}_2\text{Nb}_2\text{O}_7$ show a linear dependence over the $p(\text{O}_2)$ range with simple defect equilibrium and fair kinetics. The rutile $\text{Ti}_{1-2x}\text{Cr}_x\text{Nb}_x\text{O}_2$ series, on the other hand, shows complex phase transitions throughout the $p(\text{O}_2)$ range with kinetically limited reduction.

Chapter 1. Introduction

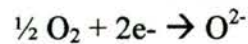
1.1 FUEL CELLS	3
<i>1.1.1 Historical background.....</i>	<i>4</i>
<i>1.1.2 Environmental impacts.....</i>	<i>5</i>
1.2 THERMODYNAMICS AND EFFICIENCY	7
<i>1.2.1 Thermodynamics.....</i>	<i>7</i>
<i>1.2.2 Thermodynamic Efficiency.....</i>	<i>8</i>
<i>1.2.3 Efficiency and Fuel Cell Voltage.....</i>	<i>11</i>
1.3 TYPES OF FUEL CELL.....	14
<i>1.3.1 Alkaline Fuel Cells.....</i>	<i>14</i>
<i>1.3.2 Proton Exchange Membrane.....</i>	<i>17</i>
<i>1.3.3 Phosphoric Acid Fuel Cells (PAFC).....</i>	<i>20</i>
<i>1.3.4 Molten Carbonate Fuel Cells (MCFC).....</i>	<i>21</i>
1.4 SOLID OXIDE FUEL CELLS (SOFC)	23
<i>1.4.1 Overview</i>	<i>23</i>
<i>1.4.2 Electrolyte</i>	<i>25</i>
<i>1.4.3 Anode</i>	<i>26</i>
<i>1.4.4 Cathode.....</i>	<i>28</i>
<i>1.4.5 Interconnect.....</i>	<i>29</i>
<i>1.4.6 Design and Stacking.....</i>	<i>30</i>

1.5 CURRENT COLLECTORS.....	34
<i>1.5.1 General overview.....</i>	<i>34</i>
<i>1.5.2 Ni/YSZ.....</i>	<i>35</i>
<i>1.5.3 Niobium based materials as current collectors.....</i>	<i>35</i>
<i>1.5.4 Aims of research.....</i>	<i>36</i>
1.6 REFERENCES:	37

1.1 Fuel Cells

A fuel cell is an energy conversion device which directly converts chemical energy into electricity and heat by electrochemical conversion of fuel gas. A typical fuel cell consists of two electrodes around an ion conducting electrolyte (e.g. O^{2-} , H^+ , CO_3^{2-})(Fig.1.1)

Solid oxide fuel cells work by electrochemical oxidation of hydrocarbon fuels, or H_2 , to water and carbon dioxide, releasing energy in the form of electricity and heat. Oxygen passes over the cathode, and a fuel such as H_2 , CO or alkanes, is passed over the anode. The catalyst in the anode splits the hydrogen, which then releases electrons to the external circuit, thus electrons travel to the cathode to combine with oxygen, creating a direct current which can be utilised. Depending on the type of electrolyte, either the proton is conducted to the cathode or the oxide ion is conducted to the anode, where it reacts with oxygen to form water as the product. For a solid oxide fuel cell the reactions at the electrodes are:



Overall reaction:

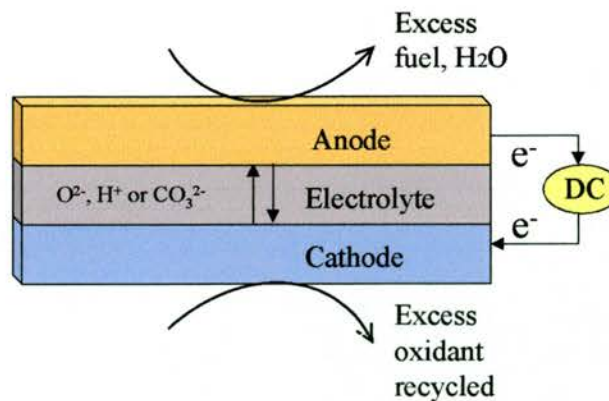
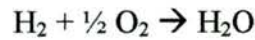


Fig.1.1 Fuel Cell setup

1.1.1 Historical background

Johann W. Ritter may have been the first person to observe voltage when hydrogen and oxygen were in galvanic contact with Pt electrodes [1]. Christian Friedrich Schoenbein was the first to report the “fuel cell effect” in 1839 [2], in which he combined hydrogen with oxygen and other gases in the presence of platinum. Sir William Grove, however, is widely credited with the invention of a fuel cell, not due to his first publication, which reported an observed voltage during the combination of hydrogen and oxygen using platinum electrodes [3], but with his application of this effect to produce a first working fuel cell.

Grove put the fuel cell effect to practical use in 1842, when he used dilute sulphuric acid as the electrolyte and combined hydrogen and oxygen by platinum at room temperature (Fig.1.2) [4]. This was a demonstration of the fuel cell then referred to as a “gas battery”. He demonstrated that his experiment on the electrolysis of water could be reversed, with electricity as the by-product, which could then be used to decompose water again.

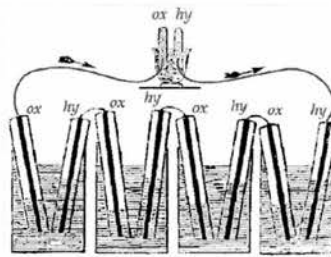


Fig.1.2 Figure from Grove's publication of 1842[4]

Nernst's discovery of a solid oxide electrolyte in 1899 [5] paved a way for the first operational SOFC in 1937, tested by Baur and Preis [6] at 1000°C.

A search for more environmentally friendly sources of energy has recently produced a widening interest in fuel cell technology, increasing research in this field. One of the first uses was on manned spacecraft, where it produced power and water for the astronauts. More recently fuel cell research is trying to develop and commercialise fuel cells for use in applications that range from portable electronics, mobile power sources, residential energy systems and vehicle propulsion to power plants.

1.1.2 Environmental impacts

Amongst the most important global problems is that of climate change, which over the last decade showed significant increase in pace, with continuous reporting of record rainfalls, droughts, winds etc. Glaciers and polar ice caps are decreasing yearly due to an increase in average global temperature.

This climate change is commonly attributed to the production of greenhouse gases from the increasing use of fossil fuels to meet our energy demands. Between 1990 and 1999 the world's total output of primary energy increased by an average annual rate of 0.9%, and correspondingly the world's production of energy increased to 380 quadrillion Btu (110×10^{15} Wh) in 1999 [7]. Currently about 80% of world energy demand is met by fossil fuels [8], with a release of 6.144 billion metric tons of carbon equivalent (1 ton carbon equivalent = 3.667 tons of CO₂ gas), an increase of 4.6 % from 1990 [7]. Petroleum and coal usages account for the majority of the CO₂ emissions (Fig. 1.3).

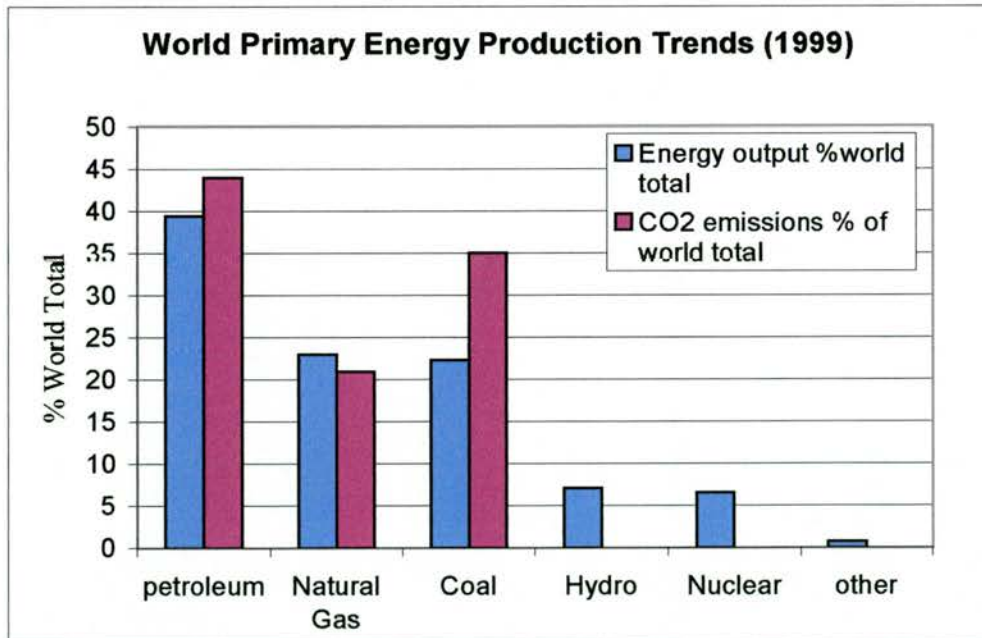


Fig.1.3 Showing world primary energy output sources and the corresponding CO₂ emissions (Data taken from Energy Information Administration (U.S. Department of Energy [7]))

This increase in energy demand and the corresponding detrimental effects on the environment have fuelled research into alternative, renewable and environmentally friendly energy sources, such as solar, wind and wave power.

The non-polluting nature of a fuel cell also makes it an ideal replacement for conventional power sources. In an ideal fuel cell the fuel source is hydrogen and the oxidant is oxygen from the air, producing water as the chemical product, which in turn can be recovered and used. If the source of hydrogen is methane or other lightweight hydrocarbon, CO₂ emissions are significantly smaller than those for a conventional combustion system, and pollutants such as NO_x and SO_x are undetectable [9]. The CO by-product, from reforming the fuel into hydrogen, can also be utilised as fuel by further oxidation to CO₂. In a high temperature fuel cell co-generation of electricity and heat allows by product heat to be recovered and utilised, which further increases efficiency, thereby decreasing waste CO₂ and other emissions produced when using natural gas.

Methane contributes least to CO₂ emissions because of the high H/C ratio of 4. Using methane or other lightweight hydrocarbons as fuel source has other advantages besides that of higher efficiency in the cogeneration cycles. The fuel gas is practically free of sulphur dioxide, heavy metal traces and halogen compounds after combustion or reformation.

The main advantage of the fuel cell, however, is its much higher efficiency over the combustion system. This will be discussed further in the next section. Typically a cell generates a voltage of around 0.7 – 0.8 volts per cell, and as the efficiency of a fuel cell is independent of size, modularity of fuel cells allows fuel cell size to be increased or decreased to a required power output for the task at hand.

1.2 Thermodynamics and efficiency

1.2.1 Thermodynamics

In order to determine the electrical power and energy output in the fuel cell, energy released by the chemical reaction of H_2 (or other fuel) with O_2 to form H_2O must be calculated. Gibbs free energy is used when dealing with chemical energy liberated, and can be defined as “maximum amount of non-expansion work that can be extracted from a system that is undergoing a change at constant temperature and pressure” [10]. Non-expansion work refers to any work that does not arise from the expansion of the system, and in the fuel cell this is electrical work. The total work of a system, w can be expressed as :

$$w = w' - p_{ex}\Delta V$$

where w' is non-expansion work, i.e. $w'(\text{maximum}) = \Delta G$. Thus when a system can do no additional work, $\Delta G = 0$. Gibbs free energy of a system is then expressed in terms of enthalpy and entropy as:

$$\Delta G = \Delta H - T\Delta S$$

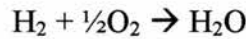
Thus at higher temperatures the contribution of entropy change to ΔG , becomes significantly more important than the contribution of enthalpy.

When dealing with the energy released in a fuel cell, the Gibbs free energy of formation is used, ΔG_f . This is because it is the change in energy that is important, thus the change between the Gibbs free energy of the products and the Gibbs free energy of the reactants is measured:

$$\Delta G_f = G_{f(\text{products})} - G_{f(\text{reactants})}$$

Where G_f is the molar specific Gibbs free energy of formation. In an ordinary hydrogen fuel cell operating at standard temperature and pressure (25°C, 0.1Mpa), the Gibbs free energy of formation of the input reactants is zero because both hydrogen and oxygen are elements in their standard states.

In the hydrogen/oxygen fuel cell, the reaction is:



$$\Delta G_f = (G_f)_{\text{H}_2\text{O}} - (G_f)_{\text{H}_2} - \frac{1}{2}(G_f)_{\text{O}_2}$$

In a reversible system, all Gibbs free energy is converted into electrical energy, thus the electrical work done will be equal to the Gibbs free energy released ΔG_f :

$$\text{Electrical work done} = \text{charge} \times \text{voltage} = -nFE \quad (\text{J})$$

$$\Delta G_f = -nFE$$

Where n is the number of electrons transferred for each molecule of fuel, and E is the voltage of the fuel cell, giving the EMF (also known as the reversible open circuit voltage) of the hydrogen fuel cell as:

$$E = -\frac{\Delta G_f}{2F}$$

1.2.2 Thermodynamic Efficiency

One of the main attractions of fuel cells is the high fuel-electricity conversion efficiency. A conventional system of converting fuel to thermal energy, then to mechanical energy and eventually to electrical energy is subject to the Carnot limitation in its efficiency, where the efficiency η of a system operated between high and low – temperatures (T_h and T_l respectively (in K)) is given by:

$$\eta = \frac{T_h - T_l}{T_h}$$

$$\text{i.e. } \eta = 1 - \frac{T_l}{T_h}$$

T_h is the maximum temperature of the high temperature heat reservoir and T_l is the temperature of the low temperature heat reservoir. High efficiency is obtained when T_h is very high and T_l is very low. In a combustion system the practical limit is determined by limits placed on T_h , in the form of material stability at high temperatures and limits placed on T_l , that of a room temperature. A fuel cell is not subject to Carnot limitation, as electrical energy is obtained directly from the chemical reaction.

When talking about the efficiency of fuel cells, a change in “enthalpy of formation”, ΔH_f , is important. This is the comparison of electrical energy produced with the heat that would be produced by burning the fuel. Thus the efficiency of a fuel cell is defined as:

Electrical energy produced per mole of fuel

$$-\Delta H_f$$

The negative value of ΔH_f indicates that energy is released. The maximum thermodynamic efficiency possible in the fuel cell is equal to the change in Gibbs free energy:

$$\varepsilon_T = \frac{\Delta G_f}{\Delta H_f} \times 100\%$$

The values of ΔG_f and ΔH_f change with temperature and state (liquid or gas), thus for the “burning” of hydrogen:



The difference of 44.01 kJmol^{-1} is the molar enthalpy of vaporisation of water (or latent heat of evaporation), and the higher value is referred to as the higher heating value (HHV), and the lower as the lower heating value (LHV).

(Fig.1.4) shows how the electrical efficiency values vary with temperature and how they compare with the Carnot limitation. From the graph it can be seen that fuel cells do not always have higher efficiencies than heat engines, and although the efficiency of the fuel cell is seen to drop with increasing temperature, it will be explained later that voltage losses are much less at higher temperatures, hence fuel cell voltages under load are higher at higher temperatures. In addition SOFC can increase the efficiency even further by fully utilising by-product heat. As shown in Fig. 1.4, the maximum theoretical efficiency of a fuel system, which directly oxidises hydrogen, is 83% at room temperature [11]. In practice however due to the high irreversibility characteristic of an oxygen electrode this is reduced to 68%.

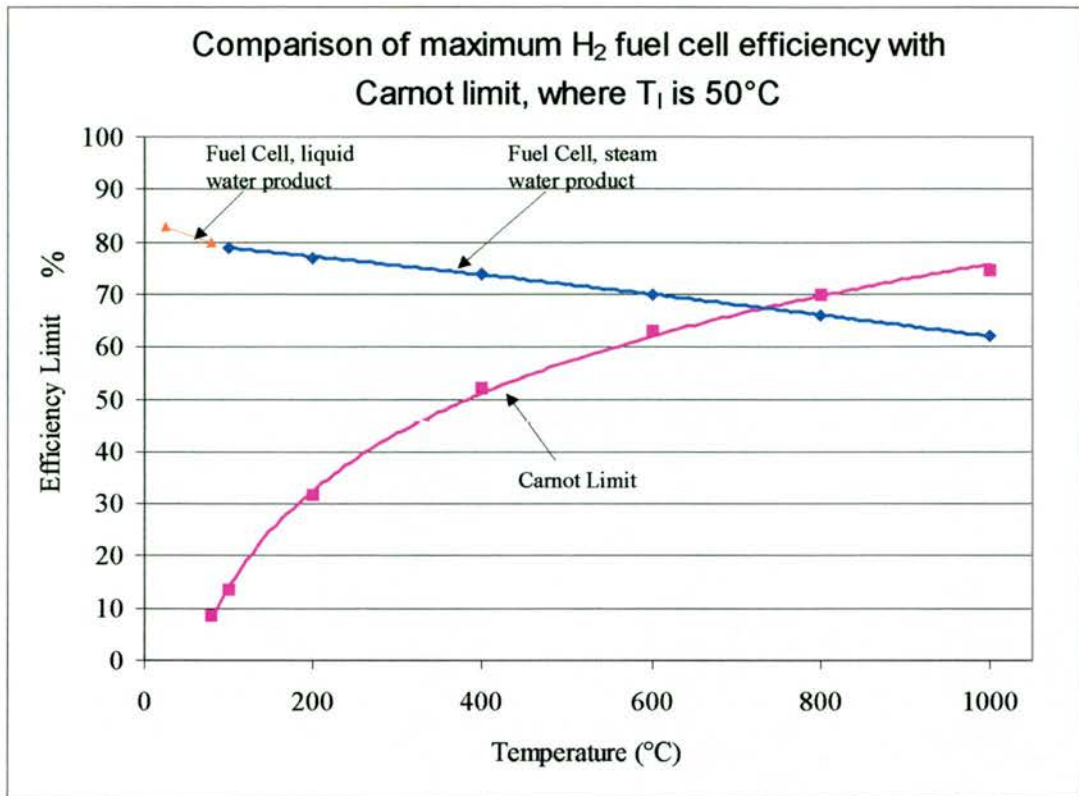
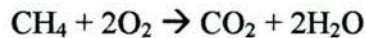


Fig.1.4 [12]. Comparison of maximum H_2 fuel cell efficiency, using HHV of ΔH_f , with Carnot limit, where exhaust temperature is 50°C .

The efficiency change with temperature does not follow the same path when using alternative fuels to H_2 . For example, when using CO as fuel:



ΔG_f changes more quickly with temperature, where the maximum efficiency of 82 % at 100°C falls to 52% at 1000°C . When using CH_4 :



ΔG_f is relatively constant with temperature, and the maximum possible efficiency shows little change due to the much larger enthalpy of combustion, ΔH , of -890.4kJmol^{-1} . Hence the $T\Delta S$ term, although larger in magnitude than for the formation of water, does not reduce the Gibbs free energy of formation significantly.

1.2.3 Efficiency and Fuel Cell Voltage

The operating voltage of the fuel cell is related to its efficiency, and if all the energy from the enthalpy of formation were transformed into electrical energy, the EMF of the cell would be given by:

$$E = -\frac{\Delta H_f}{nF}$$

Using the HHV for hydrogen, this would be 1.48 V, or 1.25 V when using the LHV value. These are voltages for a 100% efficient system, thus the actual efficiency of the cell is the actual voltage divided by these values:

$$\text{Cell efficiency} = \frac{V_c}{1.48} \cdot 100\% \text{ (ref. HHV)}$$

Fuel usage also has to be taken into account when talking about fuel cell efficiencies, as not all the fuel input into the system is used. A fuel utilisation coefficient is thus defined as:

$$\mu_f = \frac{\text{mass of fuel reacted}}{\text{mass of fuel input}}$$

Thus the fuel cell efficiency in terms of voltage output and fuel used is given as:

$$\eta = \mu_f \frac{V_c}{1.48} \cdot 100\%$$

However, the pressure and the concentration of reactants affect the Gibbs free energy and in turn the voltage. For a general reaction:



where a, b and c are the moles of A, B and C reactants and products respectively. Both the reactants and the products have “activity”, α , associated with them, which describes the deviation from ideal behaviour. For ideal gases, activity is given by:

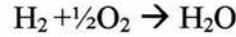
$$\alpha = P/P^0$$

where P is the pressure of the gas, and P^0 is the standard pressure, 0.1 Mpa. Thus activity is proportional to partial pressure, and in the case of solutions it is proportional to the molarity of the solution. The activity modifies the Gibbs free energy change of a reaction as:

$$\Delta G_f = \Delta G_f^0 - RT \ln \left(\alpha_A^a \cdot \frac{\alpha_B^b}{\alpha_C^c} \right)$$

Where ΔG_f^0 is the change in molar Gibbs free energy of formation at standard pressure.

Thus for a hydrogen fuel cell reaction:



the equation becomes:

$$\Delta G_f = \Delta G_f^0 - RT \ln \left(\alpha_{\text{H}_2} \cdot \frac{\alpha_{\text{O}_2}^{1/2}}{\alpha_{\text{H}_2\text{O}}} \right)$$

ΔG_f becomes more negative when the activity of the reactants is increased, and less negative when the activity of the products is increased, releasing less energy. Voltage is related to ΔG_f by the Nernst equation:

$$\begin{aligned} E &= -\frac{\Delta G_f^0}{2F} + \frac{RT}{2F} \ln \left(\alpha_{\text{H}_2} \cdot \frac{\alpha_{\text{O}_2}^{1/2}}{\alpha_{\text{H}_2\text{O}}} \right) \\ &= E^0 + \frac{RT}{2F} \ln \left(\alpha_{\text{H}_2} \cdot \frac{\alpha_{\text{O}_2}^{1/2}}{\alpha_{\text{H}_2\text{O}}} \right) \end{aligned}$$

Where E^0 is the EMF at standard pressure. Thus raising the activity of reactants increases the cell voltage. This equation is also useful in predicting EMF throughout the cell. As air and fuel pass through the fuel cell, they are used up in a reaction, and the proportion of reactants to products decreases. Thus from the above equation the EMF of the cell will also fall, and will be worst near the fuel outlet where the concentration of the reactants is lowest.

Although the theoretical value of the open circuit voltage of a hydrogen fuel cell is given by:

$$E = -\frac{\Delta G_f}{2F}$$

in practice the fuel cells have much lower voltages than the expected value. For example, for a cell operating below 100°C, the predicted value is 1.2V, but a typical fuel cell generates about 0.7 – 0.8 V per cell.

The difference between the voltage expected from a fuel cell operating ideally, i.e. reversibly, and the actual voltage is due to irreversibilities present in the fuel cell. There are four major irreversibilities:

1. Activation losses – caused by the speed of the reaction taking place on the surface of the electrodes, in which some voltage is always lost in driving the reaction that transfers the electrons to or from the electrode.
2. Fuel crossover and internal currents – energy loss caused by the waste of fuel passing through the electrolyte, and electron conduction through the electrolyte.
3. Ohmic losses – Voltage drop due to the resistance to the flow of the electrons through the material. The voltage drop is proportional to the current density.
4. Mass transport or concentration losses – caused by the change in concentration of the reactants at the surface of the electrodes as fuel is gradually used up.

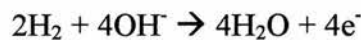
For higher temperature fuel cells the reversible voltage is lower, but operating voltage under load is generally higher due to smaller irreversibilities, i.e. smaller voltage drop at high temperature.

1.3 Types of Fuel cell

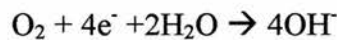
There are a number of different types of fuel cell, depending on the nature of the electrolyte used, which in turn dictates the operating temperatures of these fuel cells and the type of ion conduction that occurs. Operating temperature determines the potential uses of each type of fuel cell. Low operating temperature fuel cells have potential application in transport as they do not require high heat for operation and thus have a very short start up period of a few minutes. High operating temperature fuel cells are better for stationary applications, such as power generation. Also, at high temperatures methane can be used as fuel, rather than H₂, thus steam reforming to H₂ and CO is necessary before use. In the SOFC this can be done at the anode using the steam produced by the fuel cell.

1.3.1 Alkaline Fuel Cells

The alkaline electrolyte fuel cell has an overall reaction that is the same as the one described as the typical fuel cell reaction, but the reaction at each electrode differs, with the mobile ions being the hydroxyl (OH⁻). At the anode the reaction is:



Electrons then pass around the external circuit to the cathode:



There are a number of different types of alkaline electrolyte fuel cell design:

- Mobile Electrolyte – in which the KOH solution is pumped around the fuel cell, hydrogen is supplied to the anode, producing water. Air is used rather than oxygen, which causes problems to the fuel cell operation in that carbon dioxide from the air reacts with potassium hydroxide electrolyte:



This reaction changes KOH to K_2CO_3 thus reducing the concentration of OH^- ions, and increasing CO_3^{2-} ions, reducing the fuel cell performance. A way of dealing with this problem is to remove as much CO_2 from the air as possible using a CO_2 scrubber in the cathode air supply system.

The disadvantage of this system is that the mobile electrolyte is corrosive, and circulation of the electrolyte means that extra equipment is needed, such as a pump to move the fluid and extra external pipework, increasing the possibility for leaks. The advantages of this system, however, outweigh its problems. Amongst these, the circulating electrolyte acts as a cooling system for the fuel cell and it is easy to replace with a fresh electrolyte solution. Also the continuous stirring of the electrolyte avoids the problem of solidification of the electrolyte at the cathode due to double the rate of water production at the anode to its consumption at the cathode.

- Static Electrolyte – where each cell in the stack has its own electrolyte, which is held in the matrix material (usually asbestos), between the electrodes. Although asbestos has excellent porosity, strength and corrosion resistance there are associated safety problems with this material, and as such these fuel cells are not viable for domestic use.

The advantage of this system over the mobile electrolyte system, is that the electrolyte does not need to be pumped around, thus reducing the cost of additional equipment and maintenance. As the problem of electrolyte contamination with CO_2 is still there, the renewal of electrolyte is not as easy as for the mobile electrolyte system, in that the matrix of the entire cell has to be rebuilt.

Traditionally nickel electrodes were used in the AFC, made porous by sintering powdered nickel. The nickel electrodes were made in two layers by using two sizes of nickel powder in order to get a good three-phase contact between the liquid electrolyte, the gas and the solid electrode. These electrodes, however, were improved upon with the use of Raney metals. The procedure involves the mixing of two metals, the active metal such as

nickel for the anode and silver for the cathode, with an inactive one, such as aluminium. When the metals are mixed the distinct regions of aluminium and host metals are maintained, so that when the mixture is treated with strong alkali, aluminium is dissolved, leaving the porous material with very high surface area for use in the electrodes. This method gives an additional advantage over the sintering of nickel powder in that varying the degree of mixing of the two metals can control the pore size and density.

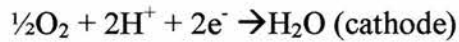
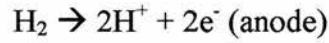
Modern electrodes, however, use carbon supported catalysts mixed with PTFE and rolled out onto a conducting material, such as nickel mesh. The role of PTFE has a two-fold function; firstly to act as a binder, and secondly being hydrophobic it stops the electrode from flooding, providing a controlled permeation of the electrode by the liquid electrolyte. Carbon fibre can also be added to increase strength, conductivity and roughness of the electrodes.

As was shown earlier, the open circuit voltage of the fuel cell increases with pressure, thus for a best efficiency AFC are operated at above standard temperature and pressure. Additionally an increase in pressure and/or temperature increases the exchange current density, which in turn reduces the activation overvoltage at the cathode.

Research activity in the AFC is low at the moment, due to limited terrestrial applications of alkali fuel cells. This is due to the reaction of CO_2 with the electrolyte, which degrades the performance of the fuel cell. The problem is worse if hydrocarbons and/or air (due to the presence of CO_2 in air) are used as fuel sources. Thus so far their main application has been in space missions, e.g. Apollo and Orbiter missions, where pure hydrogen and oxygen were used as fuel; this is Bacon's cell and was essential to Apollo's success.

1.3.2 Proton Exchange Membrane

In PEM fuel cells the electrolyte is an ion conducting sulphonated fluoropolymer, usually fluoroethylene. The mobile ion is H^+ , which means that water is produced at the cathode side rather than the anode as in AFC and SOFC:



There are a number of advantages of PEMFC, one of which is compact construction due to a very thin ($\sim 50\mu\text{m}$) one-item membrane electrode assemblies. As well as being gas-tight, polymer membranes reduce ohmic losses in the electrolyte, by being very thin. PEMFCs work at low temperature, which allows a fast start up period. There are also no corrosive liquids nor problems associated with them. These advantages mean that PEMFC are suitable for vehicles and portable applications, as well as CHP (Combined Heat and Power) systems.

The electrolyte is made by the substitution of hydrogen in the polymer, such as polyethylene by fluorine, in the process known as perfluorination, to give the final polymer as polytetrafluoroethylene (PTFE). Addition of fluorine serves two purposes:

1. Fluoropolymers are resistant to chemical attack, mechanically strong and durable due to strong carbon-fluorine bonds, thus thin films down to $50\mu\text{m}$ can be made.
2. They are strongly hydrophobic, driving the by-product water out of the electrode.

The PTFE is then sulphonated, to produce a sulphonic acid, HSO_3 , side chain. In the presence of water, this side chain dissociates into SO_3^- and H^+ ionomer. The strong attraction between the ions results in the clustering of these regions in the material. These hydrophilic regions absorb large quantities of water (Fig.1.5), thus increasing the weight of the material by up to 50%. The dissociation of SO_3H into SO_3^- and H^+ produces mobile H^+ ions, hence a dilute acid region. A large number of hydrated region in the material allow H^+ ions to move freely and quickly through this material, thus making it a good proton conductor.

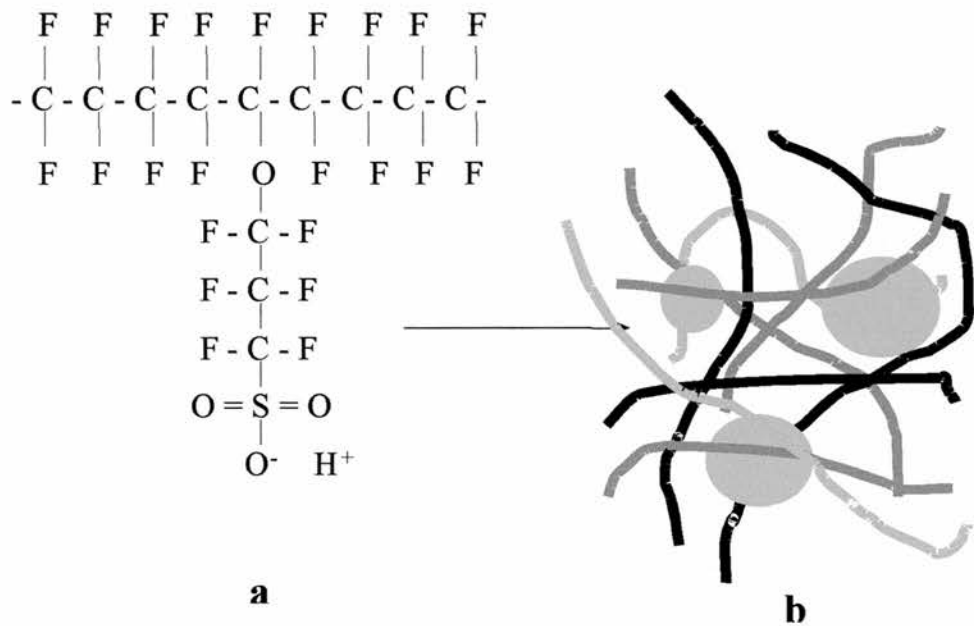


Fig.1.5 Showing the structure of a sulphonated fluoroethylene (a), and the resultant structure (b) containing hydrated regions (blue) around the sulphonated side chains.

The catalyst at both the anode and the cathode is platinum, fine particles of which are supported on the larger particles of carbon, giving a highly divided and large Pt surface area for contact with the reactants.

PEMFC has problems, however, associated with construction and maintenance. The main problem is that of water management. A correct balance of water content in the electrode is needed. There must be enough water for good proton conductivity, but not too much water, as the electrodes next to the electrolyte will flood and block the pores for gas diffusion. Relative dehydration of the membrane occurs over time, thus complicated cooling and transpiration systems have to be used. CO in this system is a catalyst poison and thus cannot be used as fuel or be present in reformed hydrocarbon fuels.

Electro-osmotic drag is the main feature that causes water balance problems. This is caused by the pull of water molecules by H^+ ions moving from the anode to the cathode. Between 1 and 2.5 water molecules are dragged by a proton [13], thus the anode side of the fuel cell can become dehydrated, a problem made more pronounced at high current densities.

Another problem is the drying of the electrodes by flowing gas, especially air at temperatures of over 60°C , faster than the water is produced by the reaction. Addition of water to gas solves the problem, and improves the performance of PEMFC.

When designing large cells and stacks for various applications there is also a problem of homogeneous distribution of water in the electrolyte throughout the cell, i.e. one part of the cell cannot become too dry or too flooded relative to another.

These problems can be dealt with, as water movements are predictable and hence controllable. For example, water production and electro-osmotic drag are directly proportional to the current:

$$\text{Water production} = \frac{P_e}{2 \cdot V_c \cdot F} \text{ mol/s}$$

Where P_e is the electrical output power:

$$P_e = V_c \cdot I \cdot n$$

V_c is the mean voltage of each cell in the stack, I is the current, n is the number of cells in the stack. Water evaporation can also be predicted from:

$$\text{Rate of Evaporation} \propto (P_{\text{sat}} - P_w)$$

Where P_w is the partial pressure of water, and P_{sat} is the saturated vapour pressure. When air is fully humidified, $P_w = P_{\text{sat}}$, and the air has no drying effect. Also the back diffusion of water from cathode to the anode depends on the thickness of the electrolyte, and relative humidity of each side:

$$\text{Relative humidity, } \phi = \frac{P_w}{P_{\text{sat}}}$$

1.3.3 Phosphoric Acid Fuel Cells (PAFC)

PAFCs operate at temperatures up to 220°C, thus they require noble metal catalysts at the electrodes, of which Pt is used. As such they suffer from a similar problem to AFC, that of CO poisoning. However, they can tolerate up to 2% of CO in the air stream [8], which is much higher than AFC. Even so, PAFC require complex fuel processing systems, which adds to the cost of construction and maintenance.

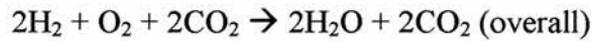
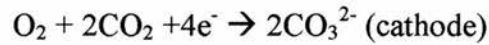
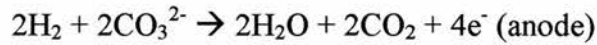
Overall the reaction in the PAFC is the same as that in the PEM. The electrolyte is proton conducting, concentrated phosphoric acid, and the electrodes are dispersed Pt electrocatalyst particles supported on carbon black. The electrolyte is contained within the silicon carbide matrix.

There are a number of advantages of using phosphoric acid as an electrolyte, such as good thermal, chemical, electrochemical stability, and low volatility at 200°C. It also has high tolerance to CO₂ in the fuel gases.

Disadvantages include the loss of acid electrolyte with time, thus the need for constant replenishment of the electrolyte during operation, and the decay of electrolyte performance with time, due to sintering of Pt particles and the obstruction of gases through the porous structure caused by electrolyte flooding. The Pt catalyst at the anode side is subject to CO and sulphur poisoning, in the form of H₂S. These are present in the fuel gas, and in turn reduce the performance and lifetime of the fuel cell.

1.3.4 Molten Carbonate Fuel Cells (MCFC)

The molten carbonate fuel cell is a high temperature fuel cell, operating at about 600°-700°C. The electrolyte is typically a molten mixture of 62Li₂CO₃ - 38K₂CO₃ or 52Li₂CO₃ - 48Na₂CO₃ held in a ceramic matrix of LiAlO₂. The conducting ion is CO₃²⁻ giving the following reactions at the anode and the cathode:



In contrast to other fuel cells such as the AFC and PEMFC, CO₂ needs to be supplied to the cathode along with oxygen. CO₂ is then recycled externally from the anode to the cathode, requiring additional fuel cell components.

The advantage of MCFC is the cost reduction in that noble metals are not required for the electrodes, where Ni and NiO are used in the anode and the cathode respectively. Additionally the high operating temperature means that CO and hydrocarbon fuels can be reformed internally cutting down on the cost of expensive external reformers. Higher operating temperature also means that higher overall system efficiencies are achieved. It was found that when using the traditional methods of constructing components, by hot pressing process into tiles, the electrolyte accounted for 70% of the ohmic losses [14], and the losses were dependent on the thickness of the electrolyte, t (in cm):

$$\Delta V = 0.533t$$

Thus by reducing electrolyte thickness using tape casting methods, ohmic losses are reduced and the efficiency of the MCFC is increased. However there is a trade off between low resistance and long term stability obtained in thicker materials, especially at high temperatures.

There are also disadvantages associated with using high operating temperature fuel cells in the form of high demands being placed on the life time of cell components and corrosion stability, especially with the use of very corrosive molten carbonate electrolyte. The major problem occurs at the NiO cathode. NiO has a small solubility in molten carbonates:



Ni ions are formed in the electrolyte through dissolution, which then diffuse towards the anode. The presence of hydrogen reduces Ni²⁺ and Ni metal precipitates out. Ni metal can then go on to cause an internal short circuit with a resultant loss of power. Nickel dissolution becomes worse with increasing CO₂ partial pressures. To reduce this problem several methods are employed:

1. More basic carbonates are used rather than the more acidic ones, where acidity increases going from Li₂CO₃ < Na₂CO₃ < K₂CO₃. The lowest dissolution rates were found for the currently used mixtures of 62Li₂CO₃ - 38K₂CO₃ and 52Li₂CO₃ - 48Na₂CO₃.
2. Keeping CO₂ partial pressure at the cathode low, and operating at atmospheric pressures
3. Using a relatively thick electrolyte matrix to increase the Ni²⁺ diffusion path.

At the moment MCFCs are being earnestly developed in USA, Europe and Asia by many companies, some of which are Fuel Cell Energy (U.S), MTU Friedrichshafen (Germany), and Hitachi and Mitsubishi Electric Corporation (Japan).

The uses will be mainly CHP cogeneration systems for commercial and domestic power production. These will have negligible SO_x and NO_x emissions, and better efficiencies of 50-55% (LHV), than conventional power sources. With low noise levels of 65dbA, MCFC is also seen as a better alternative to competing technologies such as engine and turbine-based power generation systems.

1.4 Solid Oxide Fuel Cells (SOFC)

1.4.1 Overview

SOFCs are different from other fuel cells in that they are completely solid-state devices, with a ceramic oxide ion or proton conducting electrolyte. As only two phases are present, gas and solid, they are much simpler in design than other fuel cell systems. The reactions at the cathode and the anode, of an oxide ion conducting electrolyte, are similar to other fuel cells:



CO and other light hydrocarbons can also be used as fuel, with the same reactions at the anode and the cathode in addition to the elimination of CO_2 at the anode. A basic SOFC design and operating principle is shown in (Fig.1.6) below. H_2 , however, can be circulated on the outside with the consequent possibility of using Ni metal as interconnect; a design preferred by companies such as Siemens Westinghouse Power Corporation.

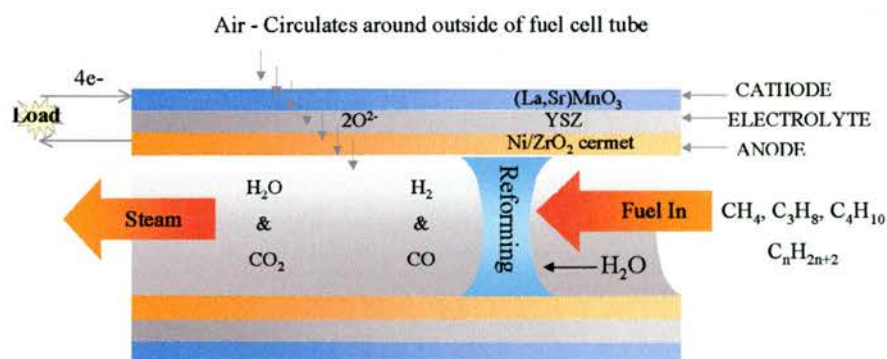
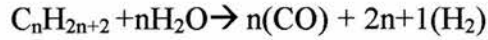


Fig.1.6 A schematic diagram of a basic SOFC design and operating principle.

SOFCs have an advantage over other types of fuel cells in stationary applications, such as large-scale power generation in power plants, because they do not require the use of precious metals or corrosive liquids, hence low maintenance cost, a longer lifetime and simpler design with no electrolyte management issues that are present in other fuel cell types.

With a solid ceramic electrolyte it can operate at high temperatures, 850-1000°C, which has two main advantages. One is the high operation temperature allowing internal fuel reforming:



Second is that the heat generated can be recovered and utilised in a combined heat and power mode (CHP), hence providing efficiencies of over 70%; 10% higher than present day technology [15].

There is no CO₂ recycling like in MCFC, and no need to remove CO₂ from the gas stream like in the AFC, thus gas management is much simpler and cheaper.

Additionally, there are no moving parts in a SOFC which means low maintenance cost and a long running lifetime with low noise levels. Solid components allow compact lightweight structures, and modularity means that fuels cell can be easily scaled up or down with stacking and interconnecting to task at hand.

The state of the art SOFC electrolyte is Ytria-stabilised Zirconia (YSZ), with (La,Sr)MnO₃ cathodes and Ni/YSZ cermets as the anode. At high temperatures, which are needed for adequate ionic conduction of the YSZ electrolyte, a number of problems arise:

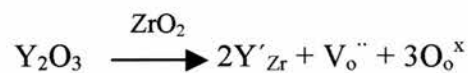
- Stability of metals diminishes.
- Ni sinters on prolonged operation, reducing the efficiency of the fuel cell.
- Large temperature gradients are created over the anode because the reforming reaction of methane in the presence of steam into H₂ and CO is endothermic, whereas the cell reaction is exothermic; this causes cracks that damage the cell.
- Carbon deposition at the anode causes further problems with the life expectancy of the fuel cell reduced by coking of the nickel metal, blocking the reaction sites.

New anode materials are being searched for in order to address these problems, and attention is focused mainly on transition metal oxides. The advantage of metal oxides over metals is that they are less likely to promote coking and to suffer from sulphur poisoning. Ceramic materials can also be individually designed to improve on a particular task at hand, such as matching thermal expansion coefficients of all cell components, improving ionic and electronic conductivity of materials, and designing materials with greater stability at high operation temperatures.

1.4.2 Electrolyte

The most important type of ion conducting electrolyte is the oxide ion conductor in SOFCs, in which water is eliminated at the anode. In the solid proton fuel cells (SPFC) the electrolyte is the proton conductor and water is eliminated at the cathode.

The electrolyte must be a fully dense material in order to prevent gas cross leakage. Currently, the preferred electrolyte is zirconia doped with 8-10 mole % yttria (YSZ). ZrO_2 is chemically very stable both to the reducing and the oxidising environments encountered at high operating temperatures. Although pure ZrO_2 has low ionic conductivity, YSZ has high oxide ion conductivity at the operating temperatures. This is due to the replacement of Zr^{4+} by Y^{3+} in the fluorite crystal structure and the creation of oxygen vacancies at the tetrahedral sites in the lattice:



The oxide ion then moves through vacancies, giving a high ionic conductivity of 0.02Scm^{-1} at 800°C .

There are other oxide ion conducting electrolytes being researched. One of the most promising is gadolinium doped ceria, $Ce(Gd)O_{2-x}$ [16,17,18,19], for example, $Ce_{0.9}Gd_{0.1}O_{1.95}$. This material achieves good power densities in excess of 100mW/cm^2 at lower temperatures of 650°C [19], and is thus suited for the intermediate temperature SOFC.

Other promising materials have shown higher oxide ion conductivity at temperatures lower than those required by zirconia. The most promising of which is the perovskite series $\text{La}(\text{Sr})\text{Ga}(\text{Mg})\text{O}_{3.8}$ originally researched by Ishihara et al. [20], but recently by other groups[21,22]. This material showed an OCV of $>1\text{V}$, and ionic conductivity in the range of 0.1Scm^{-1} at 800°C [22].

The most widely studied proton conducting electrolytes are perovskite solid solutions based on BaCeO_3 and SrCeO_3 [23,24], such as $\text{BaCe}_{0.9}\text{Gd}_{0.1}\text{O}_{2.95}$ which shows protonic conductivity of $2 \times 10^{-3}\text{Scm}^{-1}$ at 900°C [25].

1.4.3 Anode

The anode provides the site for the electrochemical oxidation of the fuel. As such the materials for the anode must satisfy certain requirements, such as high electronic conductivity, adequate porosity (20-40%) to allow gas transport to and from the reaction sites, and sufficient catalytic activity for the oxidation of fuel.

The preferred choice of anode at this time is still a cermet made of metallic Ni dispersed on a YSZ support. Nickel is preferred mainly due to its low cost and the purpose of YSZ is to inhibit the sintering of Ni particles, and to give the thermal expansion coefficient similar to that of the electrolyte, of $12.5 \times 10^{-6}\text{K}^{-1}$. YSZ provides an extension of the three phase boundary through ionic conduction. The electronic conductivity and catalytic activity are provided by nickel. The problem with this system, however, is that at high operating temperatures and in long-term operation nickel particles sinter, as it is thermodynamically driven to decrease free energy present in high surface area solids, and thus reduces the catalytic activity of the anode. The rate of sintering is driven by several factors, such as nickel particle size distribution and nickel content in the anode

The disadvantage of using a Ni/YSZ anode is that Ni/YSZ has a higher thermal expansion coefficient than YSZ and other cell components. This can result in large stresses, causing cracking or delamination during fabrication and operation. Thermal expansion increases with Ni content, and at 20% volume NiO the thermal expansion of the anode is $>11 \times 10^{-6} \text{ K}^{-1}$ [26]. Some methods are employed to minimise the thermal expansion mismatch, such as improving the fracture toughness of the electrolyte by means of additives, and varying the thickness and thickness ratio of cell components to increase tolerance to thermal expansion mismatch.

There is a lot of research at the moment into mixed conducting anodes, which are materials that show both ionic and electronic conductivities. The advantage of mixed conductors is the active region between reactant-anode-electrolyte is extended from the three-phase boundary (Fig.1.7) to a two-phase boundary, and thus significantly reduces polarisation losses by increasing the active electrode area.

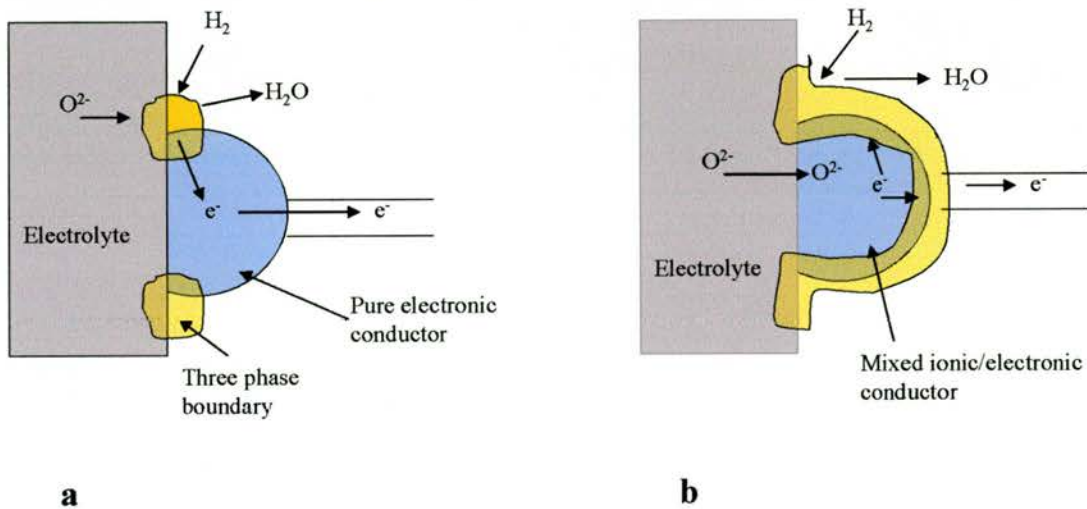


Fig.1.7 Three and two phase boundary regions of different SOFC anode materials. (a) Pure electronically conducting cermet and (b) mixed ionic/electronic conducting cermet.

Examples of materials under investigation are $ZrO_2 - Y_2O_3 - TiO_2$ systems, due to the compatibility with the YSZ electrolyte [27], and CeO_2 based materials [28], which exhibit mixed conduction in the reducing environment. Doped CeO_2 can be used as anode support material, replacing ZrO_2 , as it has shown an improved catalytic activity at reduced temperatures [29].

1.4.4 Cathode

The cathode is the site of the electrochemical reduction of the oxidant, and as such some of the material properties need to be similar to those of the anode, i.e. good electronic and ionic conductivity, good porosity to allow the gas transport and sufficient catalytic activity for the reduction of the fuel gases.

The preferred cathode at the moment is doped (mainly with Sr) $LaMnO_3$, which is a *p*-type semiconductor. It is still widely researched due to several factors, such as high electrical conductivity of 0.1 Scm^{-1} at 700°C , good compatibility with YSZ electrolyte and a matching thermal expansion, of $11.2 \times 10^{-6} \text{ K}^{-1}$, with other cell components. Doping with materials such as Ba, Ca and Sr on the A site has been used to modify its properties for different SOFC applications. Ti, Cu, Pb, Mg, Ni, Co, Cr, K, Na and Y have also been tried as dopants. SrO and CaO dopants enhance the electronic conductivity, to above 200 Scm^{-1} at 1000°C [30]. SrO doping also increases the thermal expansion coefficient and the increase is proportional to the Sr content [31]. Substituting La with smaller cations, e.g. Ca or Y, lowers the thermal expansion coefficient of $LaMnO_3$ [32].

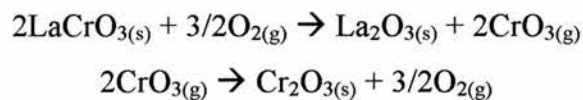
Another material being widely researched is $LaCoO_3$, which is similar in structure and properties to $LaMnO_3$. Doped with Ca and Sr it shows high *p*-type conductivity, of up to 1200 Scm^{-1} for $La_{0.8}Ca_{0.2}CoO_{3-\delta}$ at 1000°C [33]. Thermal expansion of $LaCoO_3$ is $22\text{-}24 \times 10^{-6} \text{ K}^{-1}$ [34], which like $LaMnO_3$ can be modified by Sr, Ca and other cations. The problem with this material, however, is that even with doping the TEC is significantly higher than that of the YSZ electrolyte, and it has high reactivity with other fuel cell components.

1.4.5 Interconnect

The interconnect is used to connect the anode of one fuel cell to the cathode of the neighbouring fuel cell. As such it has several requirements that must be satisfied to fulfil its task. It must exhibit high electronic conductivity in order to conduct electrons between adjacent cells and it must be a fully dense material in order to prevent gas cross leakage between the electrodes. There must also be low ionic conductivity or catalytic properties so that no internal currents are observed between the electrodes.

The preferred material for use as interconnect has been doped LaCrO_3 . LaCrO_3 has suitable electronic *p*-type conductivity of 1 Scm^{-1} at 1000°C and good compatibility with other cell components. Conductivity can be increased by doping with Ca, Sr and other cations. Doping with 10% CaO has increased the conductivity of LaCrO_3 to 20 Scm^{-1} [35].

The problems with lanthanum chromites is the difficulty in sintering to high densities, requiring firing temperatures of $>1600^\circ\text{C}$ and low oxygen partial pressures, and expansion on reducing side creating thermal expansion gradients. This is because chromium oxide has a high vapour pressure and under oxidising atmosphere a layer of Cr_2O_3 is formed from CrO_3 gases during the first stage of sintering:



Thus several approaches have been used to enhance the sinterability, such as the use of highly reactive powders, nonstoichiometric materials, dopants and sintering aids such as the addition of a second phase with significantly lower melting point.

1.4.6 Design and Stacking

One of the advantages of fuel cells mentioned earlier is the modularity, which allows fuel cells to be stacked according to the requirements of the task in hand. Thus individual fuel cell units are connected via the interconnect, to form larger stacks. The power generated by a single stack is related to the number and area of individual cells, and the current produced is directly proportional to cell area. Thus the design of the fuel cell and the resultant stack is an important part of the fuel cell system and currently there are 5 possible fuel cell designs: sealless tubular, monolithic, segmented-cell-in-series, planar and more recently the SOFCoRoll design [36] (Fig.1.8), in which the tape cast fuel cell components are rolled into shape with the gas diffusion layers between the sheets, and cofired together.

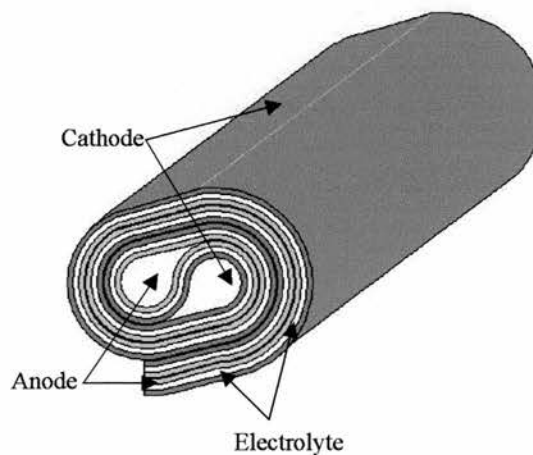


Fig.1.8 SOFCoRoll design[36].

Currently, the sealless tubular design is the most advanced of all due to the many advantages with this design (Fig.1.9(a)). The main advantage is that this design has no need for gas seals, thus the problem with designing gas tight seals at high temperature is eliminated (Fig.1.9(b)). As each cell is formed on a thick support this design provides a robust ceramic structure for the fuel cell. Also, as the connections are possible in both the series and parallel, additional protection is added to the whole stack if a single cell fails.

The disadvantage of this cell design, however, is the long current path in the electrodes, which results in higher cell resistance and hence larger resistive losses. The support tube restricts the gas diffusion to the cathode/electrolyte interface, and may become the rate-limiting step in the reaction, thus providing a limiting current for the cell and causing a reduction in the cell performance.

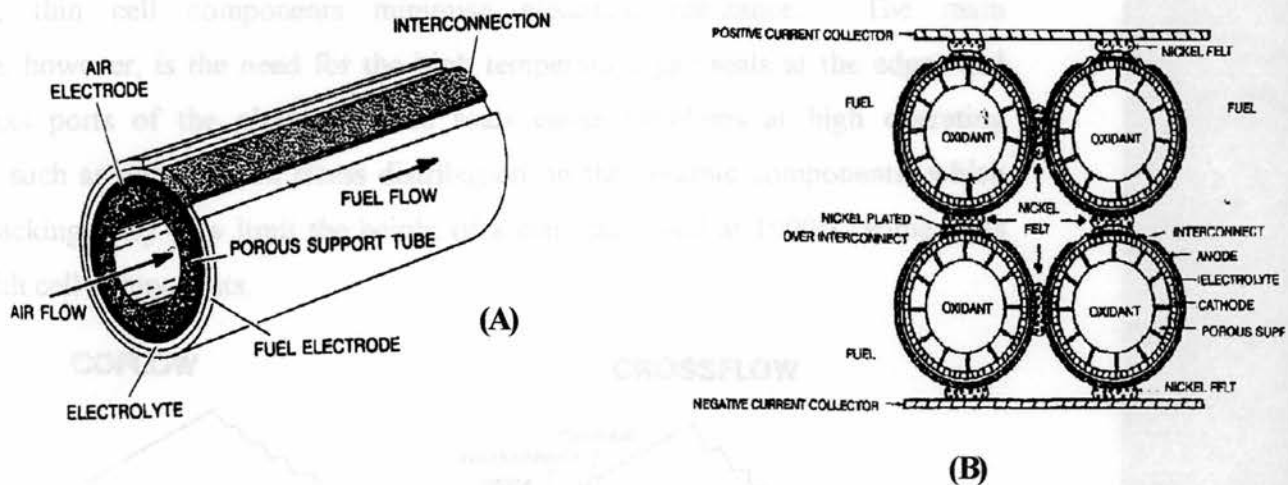


Fig.1.9 (a) Sealless tubular design. (b) Stacking arrangement in sealless tubular design fuel cell[37].

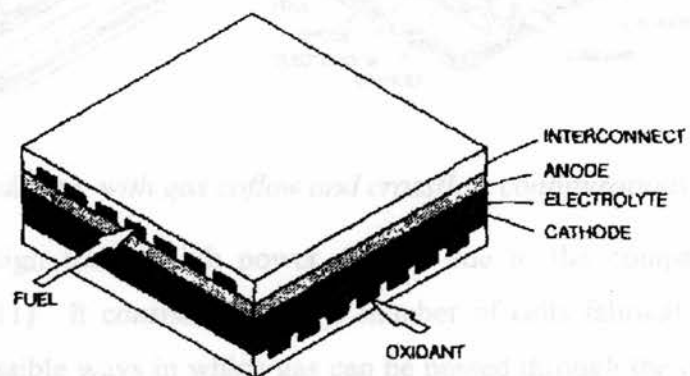


Fig.1.10 Flat-plate SOFC design [37].

1.5 Current collectors

1.5.1 General overview

Current collectors carry the current generated by the cell reaction. After the oxidation of fuel takes place at the anode the current generated must be carried out of the electrode by a current collector. In the cathode the current collector carries the electrons to the electrode/electrolyte interface, in order to allow the reduction of the fuel. Thus a material in question must fulfil a number of requirements to establish its suitability as the current collector. The main requirements are high electronic conductivity of $10\text{-}1000\text{ Scm}^{-1}$ ($30\%\text{Ni/YSZ}=500\text{Scm}^{-1}$), in the reducing (anode) and oxidising (cathode) environments at operating temperature, and thermomechanical and chemical compatibility with other fuel cell components. There must also be sufficient porosity to allow gas transport to and from the reaction sites.

There are many different current collectors, ranging from carbon black paper which supports carbon black particles with Pt electrodes in the PAFC and PEMFC, to Raney metals which also serve as electrodes in AFC. In MCFC the bipolar plates are made from thin sheets of stainless steel, and the anode side is coated by nickel, due to its stability in the reducing environment.

The interconnect in many SOFC designs currently serves as a current collector as well as the gas separator between the anode of one cell and the cathode of the another. The material used is doped LaCrO_3 which has adequate electronic conductivity as mentioned in section 1.4.5. The advantage of using ceramic current collecting materials is that they allow greater chemical and thermomechanical compatibility between the fuel cell components. Steel and other chromium alloys have also been used as current collectors in the flat-plate design. The advantage of metallic interconnects is the improved mechanical properties and lower costs, however, they do suffer from long term instability and under fuel cell operating conditions are prone to oxidation and corrosion.

There are other types of current collectors, which fall in to two main types, the paste and the mesh. Paste has the advantage that it can easily be coated onto the electrode and the contact area between the electrode and the electrolyte can be determined with a high degree of accuracy. However, current collectors in mesh form mimic the interconnect material in planar SOFC designs. Metals, such as Ni, Pt and Au have been studied as current collectors [38].

1.5.2 Ni/YSZ

As already mentioned, the state of the art anode/current collector is the 30%Ni/8YSZ. It has, however, problems associated with it:

- sintering over prolonged operation at high temperatures
- poor redox stability
- suffers from carbon deposition
- Ni is toxic

Thus when designing current collectors a number of factors have to be kept in mind. On the anode side, the current collector must operate in the reducing conditions at 700 - 900°C, thus stability at manufacturing and operating conditions, as well as compatibility with other fuel cell parts are essential when looking for suitable materials.

1.5.3 Niobium based materials as current collectors

Niobium based materials tend to show good electronic conductivity in reducing conditions. This conductivity is due to the reduction of the insulating Nb(V) to a semiconducting Nb (IV), with good electronic conductivity. The polymorph designated H-Nb₂O₅ itself has a very low conductivity of $\sigma = 3 \times 10^{-6} \text{Scm}^{-1}$. When it is reduced to NbO₂, its electronic conductivity increases to $\sigma = 100 - 200 \text{Scm}^{-1}$ at 1000°C. Variation in literature-reported conductivity may be due to the variability of the grain boundary contribution to electronic conductivity.

Due to their high electronic conductivity, niobia based rutile materials make promising candidates for full or partial replacement of Ni in Ni/YSZ anode of SOFC.

1.5.4 Aims of research

The aims of my research are to investigate a range of Niobium based materials and their suitability for use in the SOFC anode as a full or partial replacement for nickel.

Several structures will be examined, starting with Nb_2TiO_7 , which is known to reduce to a highly conducting rutile phase, $\text{Nb}_{1.33}\text{Ti}_{0.67}\text{O}_4$ [39]. The aim is to dope this material in order to enhance its thermomechanical and electrochemical compatibility with other fuel cell components. Stability with other anode materials will be examined by making composites with a known good ionic conductor, $\text{Ce}(\text{Gd})\text{O}_{2-x}$, and in this way evaluate this material's potential as a current collector in the SOFC anode.

Other rutile materials of the composition $\text{Ti}_{1-x}\text{Cr}_x\text{Nb}_x\text{O}_2$ will be investigated and their electronic conductivity and thermal expansion will be compared to $\text{Nb}_{1.33}\text{Ti}_{0.67}\text{O}_4$.

Other materials to be investigated are strontium niobates: $\text{Sr}_4\text{Nb}_2\text{O}_9$ and $\text{Sr}_2\text{Nb}_2\text{O}_7$, and MNb_2O_6 where $\text{M}=\text{Sr}, \text{Cr}, \text{Ba}$.

1.6 References:

- 1 U.Bossel, "The Birth of the Fuel Cell 1835-1845"(2000), European Fuel Cell Forum, Switzerland, p.16
- 2 C.F.Schoenbein, *Phil.Mag.(III)*, (1839), **14**, 43
- 3 W.R.Grove, *Philos.Mag.(III)*, (1839), **14**, 127
- 4 W.R.Grove, *Philos.Mag.(III)*, (1842), **21**, 417
- 5 W.Nernst, *Z. Elektrochem.*, (1899), **6**, 41-43
- 6 E.Baur and H.Preis, *Z. Electrochem.*, (1937), **43**, 727-732
- 7 Energy Information Administration, *International Energy Annual 1999: World Energy Overview*, (1999), U.S. Department of Energy,
<http://www.eia.doe.gov/emeu/iea/overview.html>
- 8 K.V.Kordesch and G.R.Simader, *Chem. Rev.*, (1995), **95** (1), 191
- 9 W.T.Langan, in *Proceedings of the Fourth Annual Fuel Cell Contractors Review Meeting, July, 14-15, 1992, Morganton, WV*, W.J. Huber (ed.), U.S. Department of Energy, Washington, DC, 1992, p3
- 10 P.W.Atkins, *The Elements of Physical Chemistry 2nd edition*, Oxford University Press (1996), 90
- 11 E.N. Balko and W.Avery, *Int. J. Hydrogen Energy*, (1981), **6** (3), 255
- 12 J.Larminie and A.Dicks, *Fuel Cell Systems Explained*, John Wiley & Sons ltd (2001), 26
- 13 T.A.Zawodzinsky, C.Derouin, S.Radzinski, R.J.Sherman, V.T.Smith, T.E.Springer, S. Gottesfield, *J.Electrochem.Soc.*, (1993), **140** (4), 1041

-
- 14 C.Yuh, Farooque, R.Johnsen, *Proceedings of the fourth Annual Fuel Cells Contractors Review Meeting*, (1992), U.S.DOE/METC, p53
- 15 A.J.Feighery, *Zirconia-based Electroceramic Materials for SOFC Applications*, Thesis (1998), p3
- 16 K.Zheng, B.C.H.Steele, M.Sahibzada, I.S.Metcalf, *Solid State Ionics*, (1996), **86-88(2)**, 1241
- 17 E.Ramirez-Cabrera, A. Atkinson, D.Chadwick, *Applied Catalysis B:Environmental*, (2002), **36**, 193
- 18 M.Sahibzada, B.C.H.Steele, D.Barth, R.A.Rudkin, I.S.Metcalf, *Fuel*, (1999), **78**, 639
- 19 M.Sahibzada, B.C.H.Steele, K.Zheng, R.A.Rudkin, I.S.Metcalf, *Catalysis Today*, (1997), **38**, 459
- 20 T.Ishihara, H.Matsuda, Y.Takita, *Journal of the American Chemical Society*, (1994), **116 (9)**, 3801
- 21 M.Feng, J.Goodenough, K.Huang, C.Milliken, *Journal of Power Sources*, (1996), **64**, 47
- 22 P.R.Slater, J.T.S.Irvine, T.Ishihara, Y.Takita, *J.Solid State Chemistry*, (1998), **139**, 135
- 23 N.Bonanos, in *Proceedings of the 14th Riso International Symposium on Materials Science, High Temperature Electrochemical Behaviour of Fast Ion and Mixed Conductors, Sep.6-10, 1993, Roskilde, Denmark*, National Laboratory, Roskilde, Denmark, (1993), p19
- 24 H.Iwahara, T.Esaka, H.Uchida, N.Maeda, *Solid State Ionics*, (1981), **3/4**, 359

-
- 25** R.C.T.Slade, S.D.Flint, N.Singh, in *Proceedings of the 14th Risø International Symposium on Materials Science, High Temperature Electrochemical Behaviour of Fast Ion and Mixed Conductors, Sep.6-10, 1993, Roskilde, Denmark*, National Laboratory, Roskilde, Denmark, (1993), p417
- 26** S.Majumdar, T.Claar, B.Flandermeyer, *J.Am.Ceram.Soc.*,(1986), **69**, 628
- 27** S.S.Liou, W.L.Worrell, in *Proceedings of the First International Symposium on Solid Oxide Fuel Cells, October 16-18, 1989, Hollywood, FL*, S.C.Singhal(ed.), Electrochemical Society, Pennington, NJ, 1989, p.81
- 28** I.S.Metcalf, P.H.Middleton, P.Petrolekas, B.C.H.Steele, *Solid State Ionics*, (1992), **57**, 259
- 29** M.Watanabe, H.Uchida, M.Shibata, N.Mochizuki, K.Amikura, *J.Electrochem.Soc*, (1994), **141**, 342
- 30** A.Mackor, T.P.M.Koster, J.G.Kraaijkamp, J.Gerretsen and J.P.G.M.vanEijk, in *Proceedings of the Second International Symposium on Solid Oxide Fuel cells, July2-5, 1991, Athens, Greece*, F.Gross, P.Zegers, S.C.Singhal and O.Yamamoto (eds.), Commission of the European Communities, Luxembourg, 1991, 463
- 31** S.Srilomsak, D.P.Schilling and H.U.Anderson, *Proceedings of the First International Symposium on Solid Oxide Fuel cells, October 16-18, 1989, Hollywood, FL*, S.C.Singhal (ed.), Electrochemical Society, Pennington, NJ, 1989, 129
- 32** C.Scotti, B.Gharbage, H.Lauret, M.Levy and A.Hammou, *Mater.Res.Bull.* (1993), **28**, 1215
- 33** J.Mizusaki, J.Tabuchi, T.Matsuura, S.Yamaguchi and K.Fueki, *J.Electrochem.Soc*. (1989), **136**, 2082.

- 34** Y.Ohno, S.Nagata, H.Sato, *Solid State Ionics*, (1983), **9/10**, 1001
- 35** I.Yasuda, T.Hikita, *J.Electrochem.Soc*, (1993), **140**, 1699
- 36** J.T.S.Irvine, F.G.E.Jones, P.A.Connor, Univerity Court of the University of St Andrews. "Fuel Cell". British Patent Applied for 0125276.6, 20October **2001**.
- 37** N.Q.Minh, *J.Am.Ceram.Soc*, (1993), **73 (3)**, 563
- 38** M.Guillodo, P.Vernoux, J.Fouletier, *Solid State Ionics*, (2000), **127**, 99
- 39** C.M.Reich, A.Kaiser and J.T.S.Irvine, *Fuel Cells-From Fundamentals to Systems*, (2001), **1**, 249

Chapter 2 - Experimental

2.1 SOLID STATE SYNTHESIS	42
2.1.1 Powder preparation.....	42
2.1.2 Ball milling.....	43
2.1.3 Pelletising.....	43
2.1.4 Reaction	44
2.1.5 Reduction.....	45
2.2 X-RAY DIFFRACTION	46
2.2.1 Sample mounting	46
2.2.2 Pattern collection.....	46
2.2.3 Bragg's Law	47
2.3 CONDUCTIVITY MEASUREMENTS	49
2.3.1 Sample preparation.....	49
2.3.2 Four terminal DC conductivity	49
2.4 DILATOMETRY	51
2.5 THERMOGRAVIMETRIC ANALYSIS (TGA)	52

2.1 Solid state synthesis

Properties of ceramic materials, such as conductivity, thermal expansion coefficient and colour, depend to some degree on their microstructure. Microstructure in turn is determined by the synthesis technique variables, such as starting particle size, heating/cooling rates, impurities, and synthesis temperature. There are a number of possible solid state techniques for sample preparation and each is adopted depending on the type of product desired, which can be any one of the following:

- Single crystal – “free” from defects
- Single crystal – with controlled type/number of defects
- Powder – large number of small crystals
- Polycrystalline solid – a sintered powder, e.g. pellet/piece of ceramic with large number of crystals in different orientations
- Thin film
- Amorphous solid – e.g. glass

In this work, samples were prepared using a “shake-n-bake” synthesis procedure, in which metal oxide powders are mixed together in stoichiometric amounts and fired at the high temperatures required for the reaction to occur. The resultant product is in the form of a polycrystalline solid, usually a pellet, whose properties were tested once phase purity was achieved.

2.1.1 Powder preparation

Reagent standard starting powders were dried under appropriate conditions in order to remove water and carbon dioxide. Higher temperatures of 700°-1200°C were used to decompose nitrates and carbonates into oxides. No powder was of lower purity than 99.5%; those that were of greater significance to the study were not less than 99.9%, e.g. Nb₂O₅, TiO₂, SrCO₃, all obtained from Aldrich. The powders were weighed using a “College B154” balance correct up to ±0.0001g. Powder mixtures were prepared by mixing dry metal oxides in the appropriate ratios using mortar and pestle and acetone as a lubricant.

2.1.2 Ball milling

Ball milling increases the homogeneity of the powder mixture and reduces the particle size of starting materials, which in turn reduces the sintering time and the sintering temperature by increasing the surface area of the reactants, thus higher densities are more readily obtained.

Powder mixtures were ball milled for up to an hour, in a Fritsch planetary micromill pulverisette 7 at speed 4, using a zirconia container and 5 zirconia balls of 12mm diameter, with acetone as a lubricant. Alternatively, in order to reduce or eliminate the cross contamination problem, single use plastic bottles with Zr balls and acetone as lubricant were used. The disadvantage of using plastic bottles over the zirconia container is that the ball milling times are up to 10 times longer due to slower rotary speed of 100rpm.

2.1.3 Pelletising

Pelletising the powder prior to high temperature reaction is required to obtain a faster reaction and phase purity, as the contact area between grains of the reacting solids is maximised, hence allowing for faster nucleation of solids and diffusion of ions through the reacting solid, especially if the mixture is not perfectly homogeneous.

The powder mixture was pressed into 13 mm wide pellets using a stainless steel die at pressures between 1000-1500 kgcm⁻². Higher pressures were avoided due to “capping” of some samples, which can break the pellets during sintering or produce badly sintered samples with a large grain boundary contribution to their conductivity. The capping is caused by non uniform pressure on the top of the pellet at the edges due to friction between the die wall and powder. This can be avoided by isostatic pressing of the pellets.

The pellets were synthesised to be 1-3 mm thick for conductivity studies, and 9-15 mm thick for thermal expansion studies.

2.1.4 Reaction

As solids usually react together at room temperature over geological time scales and conditions it is necessary to heat them to high temperatures. The reaction temperature varied widely from sample to sample and was changed within the sample series in order to control the density/porosity.

In this reaction step both the thermodynamic and the kinetic factors have to be taken into account in order to produce the correct, phase pure and well sintered material. Phase diagrams are often a very good guide when deciding the starting firing temperature, which can vary by many hundreds of degrees if dopants are used, although other factors have to be considered in order to control the phase, density and porosity of the product. The main factors to control during the reaction step are:

- Heating and cooling ramp rate – quenching is a good way of obtaining single phases or a certain crystallographic system observed at high temperature, e.g. cubic rather than monoclinic.
- Correct temperature has to be chosen – at lower temperatures the reaction will be very slow and possibly incomplete with low crystallinity. At too high temperatures the phases may segregate, or in extreme cases melt the solid altogether.
- Regrinding and re-firing – usually to achieve phase purity faster it is necessary to regrind and re-fire the sample. The first step of the reaction is nucleation, which may be difficult due to the difference in structure between reactants and product. Once this nucleation occurs, and the product layer forms, the reaction must proceed through the cation migration to the reaction site through the new reactant-product interface. As the product layer gets larger the ions have longer distances to migrate through, slowing down the reaction rate. By regrinding the pellet after initial firing, the interface between the reacting powders can be re-established, speeding up the total reaction to produce a product. Smaller particle sizes increase the reaction rate by increasing the number of interfaces.

A combination of these factors will determine the microstructure of the material. Many studies are solely focused on finding the optimum conditions for firing certain industrially important materials, such as YSZ. The use of sintering aids in order to bring down the reaction temperatures or time, and increase the density of the product, is another important field of study.

2.1.5 Reduction

When looking at materials designed to be used in a fuel cell anode it is necessary to study their properties under reducing conditions similar to those encountered in a fuel cell.

To this end the samples were reduced in a tube furnace at temperatures between 900°C and 1400°C, depending on the sample, and under flowing 5% H₂/Ar or pure Ar. The heating ramp rate was kept low at 2°C/min for some materials, in order to avoid the cracking of the pellets caused by rapid reduction. Rapid reduction can cause thermal stress on some structures, due to rapid oxygen loss and rapid density change, if the sample changes phase upon reduction. The cooling rate was 2°-10°Cmin⁻¹ depending on the sample and its stability on cooling once reduced.

2.2 X-ray Diffraction

2.2.1 Sample mounting

Phase purity was checked on the Philips X'pert PW 3020 diffractometer with a Cu radiation source and the unit cell parameters were determined using a STOE Stadi-P diffractometer. Although Philips diffractometer is more sensitive to low levels of impurities than the STOE diffractometer, it does not remove the $K\alpha_2$ beam from the incident radiation, which the STOE diffractometer does. This may make it difficult to distinguish between two closely overlapping peaks and the $K\alpha_2$ peaks.

The samples were ground to a fine powder using a pestle and a mortar. For the Philips diffractometer the powder was placed on an aluminium plate before being placed into the diffractometer. A typical run was done over a period of 1 hour. When using the STOE diffractometer a small amount (~ 0.5 mg) of powder was placed on a thin plastic sheet with a thin layer of Vaseline to hold the powder in place. Another plastic sheet was placed over the first, and the powder was placed on a rotating disk. A typical run on a STOE diffractometer was done over 1 hour 30 min-2 hours.

2.2.2 Pattern collection

X-ray crystallography is the tool used for characterising crystal structures by providing information on unit cell size and type, position of atoms in the cell, phases present, symmetry and space group of the crystal system. As each crystalline material has its own unique X-ray pattern, the technique is used for fingerprint identification of crystal structures. With a wavelength of $\sim 1\text{\AA}$ (10^{-10} m) X-rays are used to measure inter-atomic distances of that magnitude in crystals.

Monochromatic x-rays are produced when a beam of electrons, provided by a heated tungsten filament, is accelerated through a potential difference of 30 – 50 kV to strike a metal target. Although Cu is usually used in most powder x-ray diffractometers other metal targets are also available, such as Fe, Mo etc. When fluorescence is a problem it is often appropriate to use another source.

The incident beam ionises Cu 1s (K shell) electrons, and an electron from an outer orbital (2p or 2s) drops down to occupy the vacant 1s electron hole. In the process a quantum of energy is released in the form of x-rays. The transition energies between orbitals have fixed values, hence a $2p \rightarrow 1s$ $K\alpha$ transition has a wavelength of 1.5418 Å. The $3p \rightarrow 1s$ $K\beta$ transition, has a wavelength of 1.3922Å, and is usually filtered out using a sheet of Ni foil.

The Cu- $K\alpha$ transition also has two slightly different energies relative to the spin of the vacant 1s orbital due to two possible spin states of the 2p electrons. Hence the $K\alpha$ transition is a doublet corresponding to $K\alpha_1 = 1.54051\text{Å}$ and $K\alpha_2 = 1.54433\text{Å}$. A weaker $K\alpha_2$ beam may also be removed from the incident radiation using a single crystal monochromator, in which a single crystal of, for example, quartz, Si or Ge is oriented in such a way that one set of planes which diffracts strongly, (e.g. [111]), is at the Bragg angle for $\lambda_{K\alpha_1}$ to the incident beam, producing a monochromatic $K\alpha_1$ beam.

Moseley's Law relates atomic number, Z , of the metal to the wavelength of the $K\alpha$ transition:

$$f^{1/2} = (c/\lambda)^{1/2} \propto Z$$

Where f is the frequency of the $K\alpha$ line. Thus the wavelength decreases with increasing atomic number.

2.2.3 Bragg's Law

Bragg's Law requires that for two x-ray beams, diffracted by parallel planes A and B, to be in phase (i.e. constructive interference) (Fig.2.1), distance xyz must equal an integral number of wavelengths. The distance, d-spacing (d), between the planes and the Bragg angle θ are related to the xy distance by:

$$xy = yz = d \sin \theta$$

$$xyz = 2d \sin \theta$$

$$xyz = n\lambda$$

Thus Bragg's Law is given by: $2d \sin \theta = n\lambda$

When Bragg's Law is satisfied, the beams are in phase and interfere constructively, producing a diffraction beam.

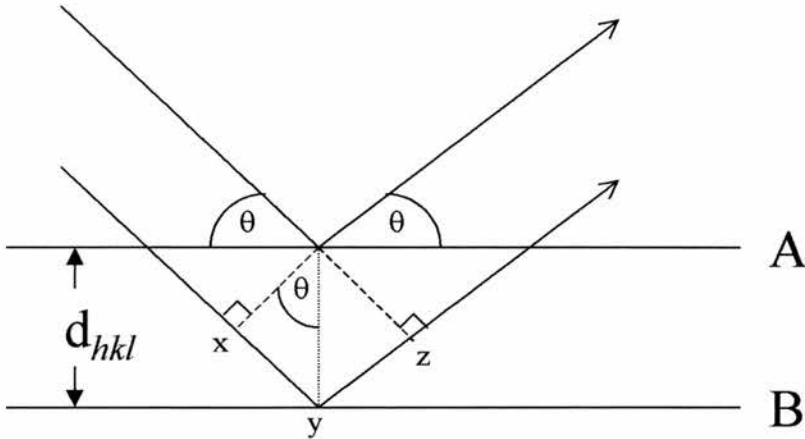


Fig.2.1 Explanation of Bragg's Law in X-ray diffraction.

Bragg's Law allows the determination of the unit cell parameters, e.g. for an orthorhombic lattice:

$$1/d_{hkl}^2 = h^2/a^2 + k^2/b^2 + l^2/c^2$$

The Laue equations give a more accurate way of describing diffraction by crystals. The Laue equations treat crystals as a three-dimensional arrangement of atoms, and relate the separation, a , of atoms in a row, the beam wavelength, λ , and the diffraction angle, ϕ :

$$a_1 \sin \phi = n\lambda, \quad a_2 \sin \phi = n\lambda, \quad a_3 \sin \phi = n\lambda$$

Each equation corresponds to a single direction of atomic arrangement in a three-dimensional crystal. All three equations must be satisfied for a diffracted beam to occur.

2.3 Conductivity Measurements

2.3.1 Sample preparation

Pellet densities for conductivity studies were between 70% and 90% of theoretical density. DC electrical conductivity measurements were carried out as a function of temperature under constant atmosphere of dry or wet 5% H₂/Ar, using the four terminal DC technique. Four equidistant strips of platinum paste were pasted on one face of the pellet. The pellet was then fired at 900°C for 2 hours to sinter the platinum. Resistance was then checked across each strip using a voltmeter, and if below 0.1μΩ, the pellets were mounted in a four terminal jig (Fig.2.2). If the resistance across each strip was too high, another coating of Pt paste was applied and sintered at 900°C.

For impedance measurements, platinum paste was painted on each pellet face, fired at 900°C for 2 hours and, once the resistance was low enough, the pellet was mounted in an impedance jig.

2.3.2 Four terminal DC conductivity

DC current, **I**, which when applied across a material with resistance, **R**, results in a potential difference between any two points, **V**. There is a direct relationship between these values, expressed in the form of Ohm's law:

$$V = IR$$

Electronic conductivity (σ_e) is determined from equation:

$$\sigma_e = \frac{L}{A} \left(\frac{\partial I}{\partial V} \right)$$

Where A is the electrode area and L is the thickness of sample pellets. The dependence of conductivity upon oxygen partial pressure provides considerable information on the mechanism of conduction. For n-type conduction, conductivity typically decreases with increasing p(O₂). For p-type conduction, conductivity typically increases with increasing p(O₂), and for ionic conduction there is no change in conductivity with p(O₂).

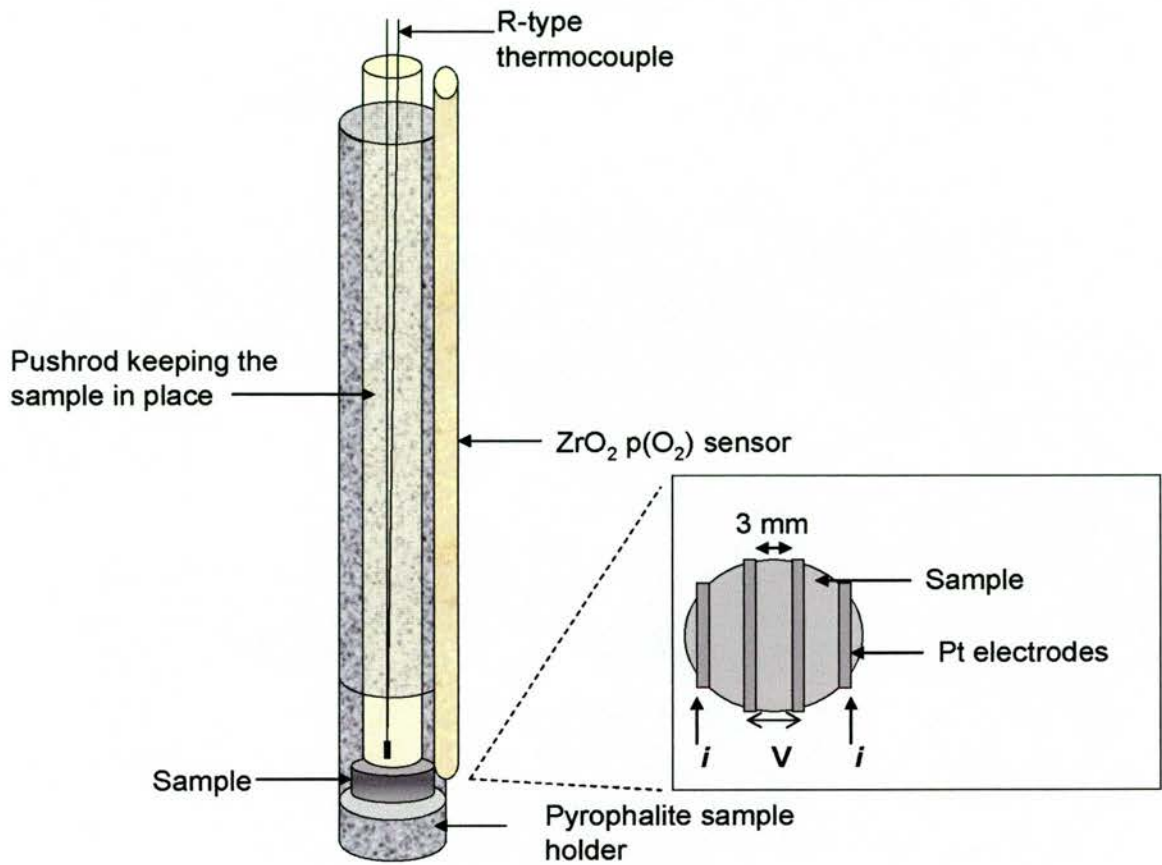


Fig.2.2 $p(O_2)$ conductivity jig setup

The correction for the 4-terminal DC geometry was taken from 2-terminal AC impedance measurements on the same pellet in air.

2.4 Dilatometry

Dilatometry is a technique that monitors dimensional changes of the sample as a function of temperature and/or time, while the sample is under negligible mechanical load. From this thermal expansion coefficients of samples are determined.

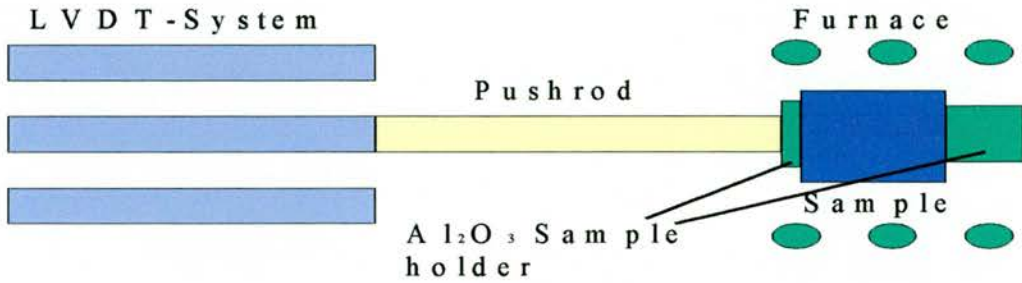


Fig.2.3 Schematic diagram of Netzsch dilatometer Dil 420C.

A Netzsch dilatometer Dil 420C is used in these experiments. The furnace heats the sample and the change in the sample length is measured via the pushrod by the Linear Variable Displacement Transducer, LVDT-System, which in turn is positioned in the cold part of the system. The expansion of the alumina sample holder and other alumina components is corrected for by calibration correction, taken using an alumina standard (Multilab 99.7% purity) of length that matches the sample to within 10%. Any larger discrepancy in the length between the calibration standard and the sample results in a significant decrease in accuracy of the results. Pellets were between 8 and 15 mm length and 70-90% dense.

The coefficient of linear expansion α can be defined as:

$$\alpha(T) = \frac{dL(T)}{L_0 dT}$$

$L(T)$ = Sample length at temperature T

L_0 = Sample length at 20°C

The physical expansion coefficient is the slope of the thermal expansion curve, corresponding to the first derivative of the dL/L_0 curve according to the temperature. The physical expansion coefficient is defined by the following equation:

$$\alpha_{phys}(T) = \frac{1}{L_0} \cdot \frac{dL(T)}{dT} = \frac{1}{L_0} \cdot \frac{(L(T + \delta T) - L(T - \delta T))}{((T + \delta T) - (T - \delta T))}$$

δT = infinitesimal small temperature difference

$L(T)$ = Sample length at temperature T

The technical expansion coefficient, α_{tech} , at a temperature T allows the determination of expansion at that temperature, and can also be referred to as the average expansion coefficient for the temperature interval $T_{upper} - T_{lower}$. It is defined by the following equation:

$$\alpha_{tech}(T) = \frac{1}{L_0} \cdot \frac{\Delta L}{\Delta T} = \frac{1}{L_0} \cdot \frac{(L(T) - L_0)}{(T - T_0)}$$

2.5 Thermogravimetric Analysis (TGA)

TGA measures a change in the mass of a sample as the temperature or pO_2 is varied. The TGA instrument used was a RheoTherm TGA 1000M+, consisting of a sensitive balance with the sample pan in a furnace. There are a number of uses for TGA, such as kinetic studies where weight change can be attributed to a particular reaction, the study of volatisation, adsorption and desorption of samples. By controlling the atmosphere at the sample it is possible to encourage or suppress reduction/oxidation reactions. Under the reducing atmosphere of 5% H_2/Ar a previously oxidised sample will lose weight. From the amount of weight loss it is possible to determine the extent of oxidation, hence providing additional information of the nature of the material, e.g. number of oxygen vacancies and a new stoichiometry of the material.

Chapter 3. Theory

3.1 STRUCTURE TYPES	54
3.1.1 <i>Perovskite</i>	55
3.1.2 <i>Tungsten bronzes</i>	56
3.1.3 <i>Rutile (TiO₂)</i>	58
3.2 ELECTRONIC CONDUCTIVITY IN SOLIDS.....	60
3.2.1 <i>The free-electron theory</i>	60
3.2.2 <i>Ohm's Law</i>	62
3.2.3 <i>Band Model</i>	65
3.2.4 <i>Simple Metals</i>	67
3.2.5 <i>Semiconductors/Insulators</i>	68
(i) <i>Intrinsic semiconductors</i>	69
(ii) <i>Extrinsic semiconductors</i>	70
3.2.6 <i>Defects and non-stoichiometry in crystals</i>	73
(i) <i>Energetics and concentration of defects</i>	74
(ii) <i>Effects of oxygen partial pressure</i>	77
3.3 THERMAL EXPANSION THEORY	82
3.3.1 <i>Heat transport in solids</i>	82
3.3.2 <i>Lattice Vibrations</i>	86
3.3.3 <i>Negative thermal expansion</i>	90
3.4 REFERENCES:	92

3.1 Structure types

The unit cell is the smallest repeating unit in a crystal system, which is determined from the x-ray diffraction pattern. It is characterised by six parameters: the lengths of three sides a , b , c , and the angles between these sides α , β , γ (Fig.3.1). Crystal system of the unit cell describes its shape and symmetry. There are 7 crystal systems: triclinic monoclinic, orthorhombic, tetragonal, trigonal, hexagonal and cubic. Cubic system has the highest symmetry: $a=b=c$, $\alpha=\beta=\gamma=90^\circ$, and triclinic has lowest symmetry $a\neq b\neq c$ and $\alpha\neq\beta\neq\gamma\neq 90^\circ$.

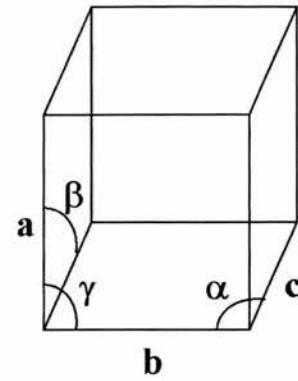


Fig.3.1 Unit cell parameters

Along with the different crystal systems a unit cell can adopt, structures can also have additional lattice points in the lattice, i.e. centring, located at the centre of faces in the unit cell, or the body centre of the unit cell. Thus there are 14 Bravais lattices, giving the information on the overall symmetry in the crystal and consisting of the combination of crystal systems with centring conditions. If point symmetry and translational symmetry are taken into account along with 14 Bravais lattices this gives 230 space groups, and any one crystal structure belongs to one of these space groups.

3.1.1 Perovskite

The perovskite structure has a general formula ABO_3 and is based on the ReO_3 structure, which can be considered as cubic close packed with $\frac{1}{4}$ of the oxygens missing in the **abc** stacking sequence, and the A site cation occupies these vacant sites. The ideal perovskite structure is cubic, an example of which is $SrTiO_3$, $A^{(II)}B^{(IV)}O_3$ structure, in which the Ti occupies $\frac{1}{4}$ of the octahedral sites and TiO_6 octahedra share corners to give a 3D framework (Fig.3.2). Sr and O atoms in $SrTiO_3$ form the cubic close packing structure, and Sr^{2+} is co-ordinated by 12 oxygens.

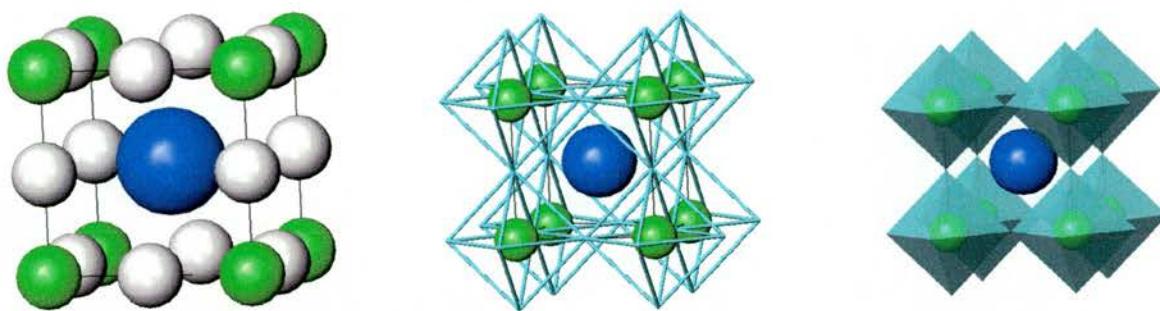


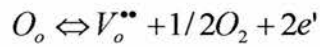
Fig.3.2 Ideal perovskite structure in different representations

The ideal perovskite structure is very rare, as they all tend to show a certain degree of distortion from cubic symmetry. This distortion is responsible for interesting magnetic and electric properties and is important in the electronic and ionic conductivity of these classes of materials.

Tetragonal to cubic transformation is the most important distortion for the electronic properties occurring in $BaTiO_3$, below $120^\circ C$. In the close packed Ba-O planes the large size of Ba^{2+} of 1.60\AA in a 12 fold co-ordination, causes the oxygen octahedron co-ordinating Ti^{4+} to expand relative to $SrTiO_3$. This in turn causes the titanium, which is now in a slightly larger site, to be displaced by 0.1\AA off its centre to a position of lower energy, in the direction of one of the apical oxygens, giving rise to spontaneous polarization. The irregular TiO_6 octahedra result in the change of crystal symmetry and the tetragonal distortion of the perovskite.

Hence the distortion of BaTiO₃, for example, causes it to be ferroelectric with the Curie temperature $T_c = 120^\circ\text{C}$ and very high dielectric constant, and this has great industrial importance in the capacitor industry, e.g. multilayer capacitor, thermistor, underwater sonar etc. Substitution of Ba by Sr ions reduces the tetragonal distortion and hence the magnitude of the ferroelectric response, with a lower $T_c = -55^\circ\text{C}$.

Perovskites are intensively studied due to the oxide ion conduction through the introduction of oxygen vacancies. These are done either by substitution of A^{3+} by A^{2+} or from a partial reduction of B^{3+} or B^{4+} to B^{2+} or B^{3+} , respectively. The following equilibrium then applies:



The oxygen mobility through these vacancies is the basis of oxide ion conductivity.

3.1.2 Tungsten bronzes

Tungsten bronzes, based on WO₃ are a distorted form of ReO₃, and can be considered to be an A-site deficient perovskite. Their relationship to ReO₃ and the perovskite structure is seen in (Fig.3.3). In the WO₃ structure the W atoms are shifted from the octahedron centres thus producing varying W-O bond lengths. The structure contains channels which, as in the perovskite structure, can be occupied by other metal ions, giving the composition of M_xWO₃.

There are different types of tungsten bronze structures: cubic, hexagonal and tetragonal. The cubic tungsten bronzes have a ReO₃ structure, with only a partial occupation of the channels with small cations, such as Li⁺ or Na⁺, and can be considered to be a halfway house between ReO₃ and perovskite structures. Hexagonal tungsten bronzes as can be seen from (Fig.3.3), to contain large channels, which can contain much larger cations such as Cs or Rb. Tetragonal tungsten bronzes have five, four or three sided channels (Fig.3.3). Three sided channels are unoccupied, and the four and five sided channels have slightly different diameters. As such the cations may preferentially occupy either one or

the other of these channels, with the smaller cations preferentially occupying the four sided channels.

Tungsten bronzes are often metallic conductors, with a metallic luster. Due to their chemical resistance and their colour, they are being used in industry as catalysts and pigments.

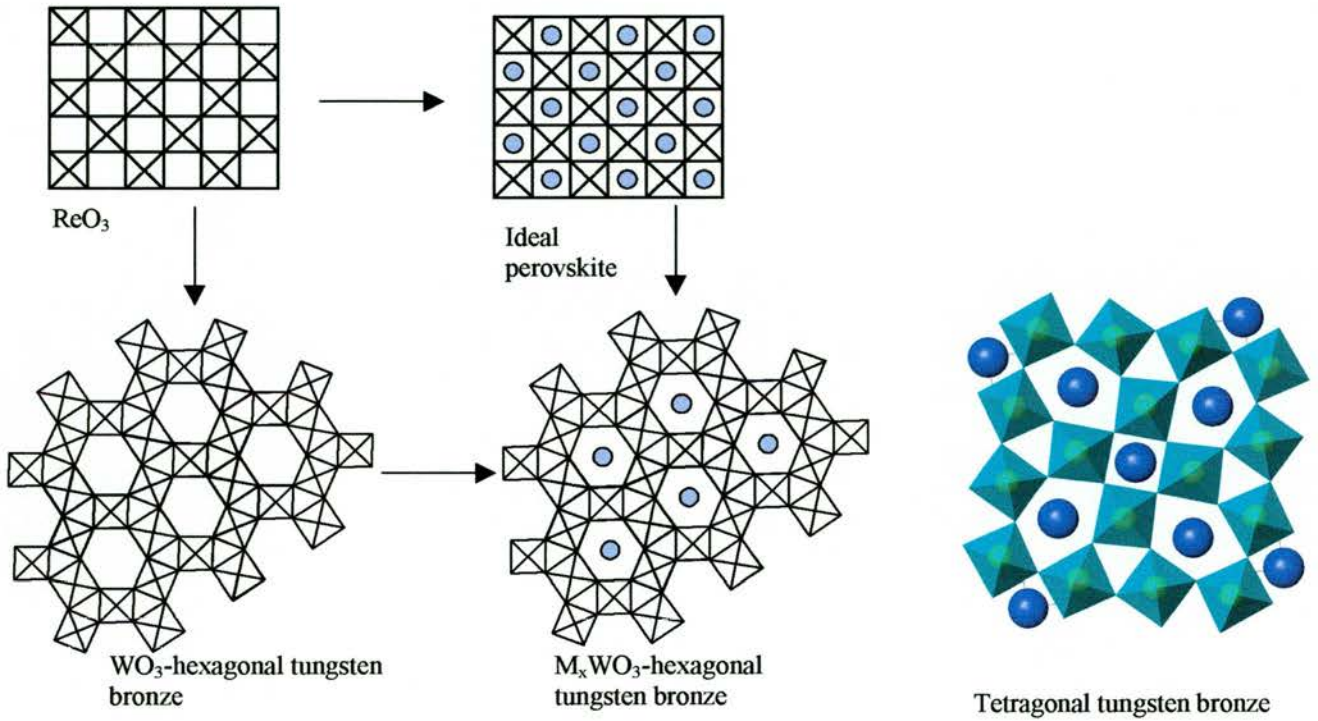


Fig.3.3 Relationship between the structures of ReO_3 , perovskite and hexagonal or tetragonal tungsten bronze, WO_3 .

3.1.3 Rutile (TiO_2)

TiO_2 has a rutile structure, which is characterised by a distorted hexagonal close packing of anions (oxygen) with half the octahedral sites occupied by cations (Fig.3.4(a)). This, therefore, produces corner sharing octahedra in the [110] plane (Fig.3.4(d)), and edge sharing along the c -axis (Fig.3.4(c)). The chains of edge sharing TiO_6 octahedra share corners hence giving square tunnels which run parallel to the c -axis (Fig.3.4(d)). Every O atom is shared by three octahedra, $\text{TiO}_{6/3}$.

The rutile structure, along with fluorite constitute the main structure types for AX_2 materials, e.g. NbO_2 , CrO_2 , NiF_2 etc. Usually in the rutile structure metal atoms are equidistant in the edge sharing chains. However, if the metal atoms still contain d -electrons, metal-metal bonding will occur, and atoms become shifted from the octahedron centres. This produces alternating short and long M-M distance in these chains. This is seen in low temperature forms of VO_2 , NbO_2 , MoO_2 and WO_2 , with high temperature forms having the regular rutile structure. In TiO_2 the Ti co-ordination is slightly distorted, producing two Ti-O bond lengths of 1.95 and 1.98Å.

Other cations can be inserted in to the square tunnels, resulting in different electronic and magnetic properties.

There are also double and triple rutile phases which occur when there are two or three metal sites and ordering of the metal sites doubles or trebles the unit cell.

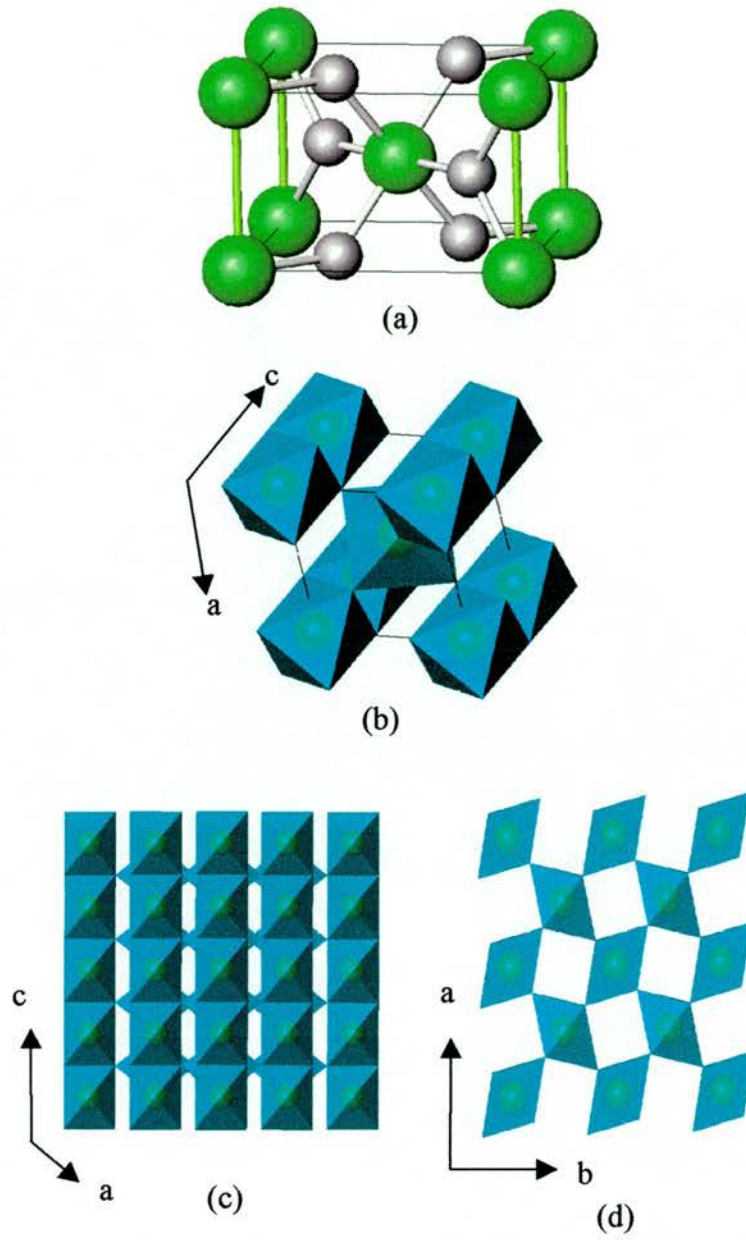


Fig.3.4 (a) TiO₂ Rutile structure. Green atoms at corners are Ti atoms, and grey are O atoms (b) Rutile structure represented with TiO₆ octahedra (c) Edge sharing TiO₆ octahedra in the c-direction (d) Tunnels running parallel to the c-axis

3.2 Electronic Conductivity in Solids

3.2.1 The free-electron theory

The electron arrangement around the nucleus consists of a number of closed shells, outside of which are the remaining few electrons, which are not as strongly bound to the nucleus as a result of shielding by the electrons closer to the nucleus. These outer electrons are responsible for the electrical properties of materials. Sommerfield's free-electron model considers valence electrons in metals as noninteracting gas particles, not bound to their individual atoms but free to move through the lattice. That is to say the electrons can be considered to sit in the potential well of the crystal lattice, rather than the potential well of the atom. The energy levels in this potential well are quantized, where the highest filled level at $T=0\text{K}$ is the Fermi level, with the corresponding energy E_F .

The concentration of electrons at any particular energy level can be expressed in a form:

$$n(E) = N(E) \cdot F(E)$$

where $N(E)$ is the density of states, i.e. the volume density of electron levels of energy E , and $F(E)$ is the probability that they are occupied, also known as the Fermi-Dirac function. The electron density of states, $N(E)$, is a function which varies with energy level and represents the maximum allowed density of electrons of energy, E , per unit volume of a crystal, as dictated by the Pauli exclusion principle. As can be seen from (Fig.3.5), at the edges of the conduction and valence bands $N(E)$ varies parabolically with energy away from the edges of the bands. From integration near the edges of the conduction band, the effective conduction band density of states, N_c , becomes:

$$N_c = 2 \left[\frac{2\pi m_e kT}{h^2} \right]^{3/2} \approx 10^{19} \text{ cm}^{-3} \text{ (at } T = 300\text{K)}$$

Where m_e , is the effective mass of electrons in the conduction band, and h is Planck's constant. The equation for the effective valence band density of states for electron holes is the same, substituting the effective mass of electrons by that of holes in the valence band.

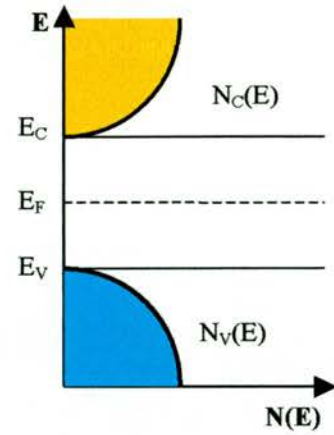


Fig.3.5 Density of states function

The Fermi-Dirac function $F(E)$, is given by:

$$F(E) = \frac{1}{1 + \exp\left[\frac{E - E_f}{kT}\right]}$$

When this equation is plotted against energy the graph in (Fig.3.6) shows that all the electron levels are occupied up to a maximum energy, E_f , the Fermi energy at 0K.

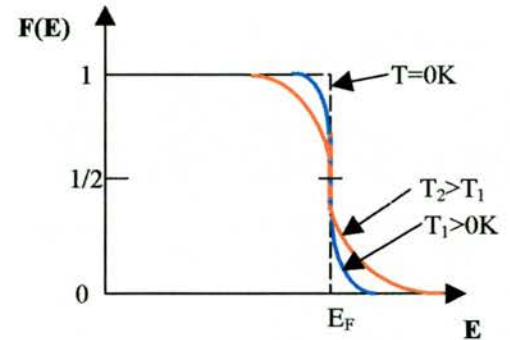


Fig.3.6 Fermi probability function,

$F(E)$ as a function of electron energy E

The probability function has a value of unity below E_f and 0 above. When the temperature is above 0K, $T_1 > 0\text{K}$, some electrons are excited above E_f , resulting in a more diffuse probability function. At the Fermi energy, however, the probability function is $F(E) = 1/2$ [1]. Thus for a semiconductor or insulator, the product of $N(E)$ and $F(E)$ gives a concentration of electrons in the conduction band. At higher temperatures still, $T_2 > T_1$, even more electrons are excited above E_f , producing a more diffuse spread of energies.

3.2.2 Ohm's Law

In a conductor in zero electric field the free electrons are distributed through all the energy states up to E_F , hence there will be as many states occupied which have a positive wave vector as a negative wave vector, hence the electrons are travelling in all directions with no preference for any direction, with the average net velocity being zero. The free electrons are constantly exchanging energy with the lattice ions by inelastic collisions and exchanging momentum by elastic collisions.

When an electric field, \mathbf{E} , is applied the electrons are accelerated with a definite velocity, in the direction opposite to the applied field and are scattered by phonons, thus losing their kinetic energy. The distance travelled by the electron between each scattering is its mean free path, l .

The drift velocity, \mathbf{v}_d , is directly proportional to the applied electric field, \mathbf{E} :

$$\mathbf{v}_d = \mu\mathbf{E}$$

where μ is the electron mobility ($\text{m}^2/(\text{V}\cdot\text{s})$). The drift velocity of the electrons is thus directly related to the current density, \mathbf{J} :

$$\mathbf{J} = ne\mathbf{v}_d$$

where n is the number of electrons per unit volume, and e is the electronic charge (-1.60×10^{-19} C)

The velocity v_F at the Fermi surface is $\sim 10^6 \text{ ms}^{-1}$ [2], and is very high compared to any change in velocity produced by the applied field, so the time between collisions is mostly constant with $\parallel v_F$. Increasing the field increases the drift velocity and a larger change of velocity is produced in the same time $\parallel v_F$. The resultant higher current is thus a basis for Ohm's Law.

Ohm's law relates the current flow, I (in amps), to the applied voltage V (in volts) and the resistance of the material, R (in ohms): $I=V/R$. The resistance of an electrical conductor is directly proportional to its length, l , and inversely proportional to its cross-sectional area, A : $R=\rho l/A$, in which ρ is the electrical resistivity given in terms of Ωm .

The current density in an applied electric field is also expressed in terms of resistance as:

$$\mathbf{J} = \frac{\mathbf{E}}{\rho} \text{ or } \mathbf{J} = \sigma\mathbf{E}$$

where \mathbf{J} =current density, A/m^2 , \mathbf{E} =electric field, V/m , ρ =electrical resistivity Ωm
 σ =electrical conductivity Sm^{-1} .

There are two main types of contribution to electrical resistivity:

- The thermal component is the result of phonon interaction with conduction electrons, decreasing their mean free paths and relaxation times between collisions.
- The residual component is usually small in pure metals and is the result of structural imperfections such as grain boundaries, impurity atoms and dislocations, all of which scatter electrons.

The total electrical resistivity of a metal, ρ_{total} , is approximated as the sum of the thermal component, ρ_T , and the residual component, ρ_r :

$$\rho_{\text{total}} = \rho_T + \rho_r$$

The residual component is usually temperature independent, and is only significant at low temperatures.

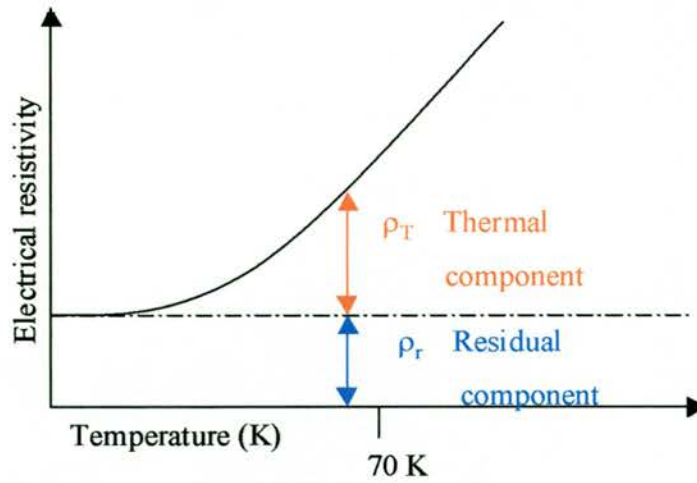


Fig.3.7 Variation of electrical resistivity with temperature, showing the contribution of different components

For most metals, above about 70K, the resistivity varies almost linearly with temperature, as the thermal component is the main cause of resistivity. At temperatures below 70K, the residual component becomes much more dominant, and there is no longer a linear relationship between electrical resistivity and temperature (Fig.3.7). The ratio of $\rho_{\text{total}}/\rho_r$ can be used as a measure of the purity of the samples.

Electronic conductivity is directly related to:

1. Number of charge carriers – increasing the number of charge carriers increases the conductivity
2. Their charge magnitude – for the same number and mobility of charge carriers, the larger is the charge carried the larger is the perceived conductivity
3. Mobility of charge carriers – faster charge carriers with the least amount of resistance from the material itself produces larger conductivity

Thus the electronic conductivity is given by:

$$\sigma = nZe\mu$$

where n is the number of charge carriers, Ze is their charge and μ is a measure of velocity/mobility of charge carriers in an electric field.

The conductivity dependence on temperature is present in the n term and the μ term, as the charge of the charge carriers is independent of T . The mobility of charge carriers, μ , decreases to a varying degree in all materials with temperature, due to increasing number of collisions between charge carriers and phonons as the temperature increases. Thus the main difference between metals, semiconductors and insulators must lie in the number of charge carriers, n . In metals, n is large and does not change significantly with temperature, thus the other variable, μ , which decreases with temperature, must be responsible for the resultant decrease of σ with temperature for metals. For semiconductors/insulators, n is smaller than in metals but increases rapidly with temperature. The rapid increase in n outweighs the small decrease of μ , thus σ increases rapidly with temperature.

3.2.3 Band Model

According to the linear combination of atomic orbitals (LCAO) model, when two atoms bond the orbitals on each atom overlap in phase, to give a low energy bonding orbital, and out of phase, to give a higher energy anti-bonding orbital. This is shown in (Fig.3.8) for Li 2s atomic orbitals.

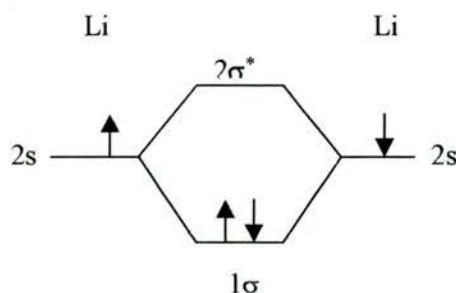


Fig.3.8 LCAO diagram of two Li atoms showing bonding and anti-bonding orbitals

In crystal systems with many atoms bonded, there are N molecular orbitals formed for N bonded atoms. The lowest energy orbital is the in phase combination of atomic orbitals, and the highest is the out of phase combination of atomic orbitals. In between these there are $N-2$ molecular orbitals, in which some have in phase and some have out of phase combination. As the number of atoms increases the number of levels increases, but the spread of energies is over a very small range.

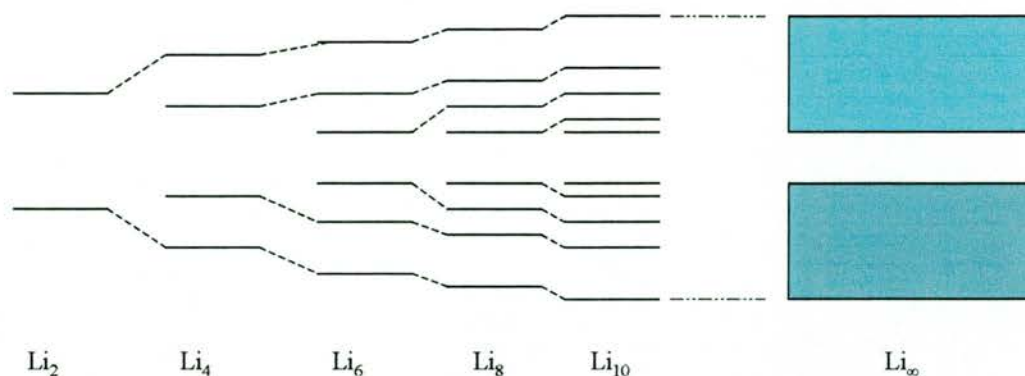


Fig.3.9 Band formation from individual bonding and anti-bonding orbitals.

In crystals with infinite number of atoms two energy bands are formed, consisting of an infinite number of molecular orbitals at infinitesimally small separations between them, producing a continuous range of energies within each band (Fig.3.9). The width of the band depends on the degree of overlap between atomic orbitals. In small molecules, the greater the overlap, the greater the difference between bonding and anti-bonding orbitals; in solids this translates to a greater spread of energies in the band.

Thus in metals, semiconductors and insulators the differences in their conductivities depend on the band structure of each, whether the valence bands are full or partly full, and the magnitude of the energy gap between full and empty bands. In semiconductors the band gap is usually in the range of 0.5-3.0eV, and in insulators the band gap can be as large as 6-7eV, thus energy has to be applied to promote the electrons across this band gap for conduction to occur. In insulators the band gap is much larger than in semiconductors, hence much more energy is required before conductivity can occur.

3.2.4 Simple Metals

The free electron theory separates the core and valence electron states, in which the valence electrons are delocalised over the entire crystal forming a valence band. In metals the valence band is partly filled and is hence also the conduction band. Hence in pure metals, the charge carriers are the valence electrons. The width of a valence band is related to the interatomic separation and therefore the degree of overlap between orbitals of adjacent atoms (Fig.3.10)

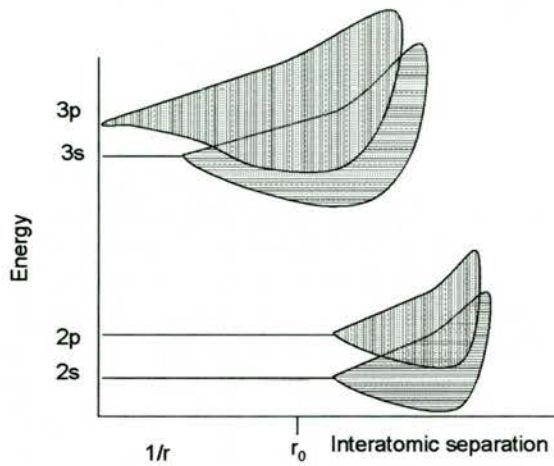


Fig.3.10 Energy levels and band of sodium as a function of interatomic spacing

In a sodium metal where the interatomic separation is at r_0 , i.e. the crystal spacing between adjacent atoms, the $3s$ and $3p$ orbitals overlap significantly to form a broad conduction band. The $2s$ and $2p$ orbitals do not overlap at this separation, but with additional compression under pressure would overlap to form another energy level band.

Semimetals are similar to semiconductors, however the conduction band minimum lies slightly below the valence band maximum, hence in the ground state at 0K a small number of conduction band states are occupied, and an equal number of valence band states are empty. Due to the partial filling of bands the electronic properties are those of a metal, but because of the smallness of the overlap there are a very small number of carriers which contribute to the conductivity.

3.2.5 Semiconductors/Insulators

Semiconductors, however, have a full valence band which is separated by a large energy gap, E_g , from the next energy band, the conduction band, which is empty (Fig.3.11).

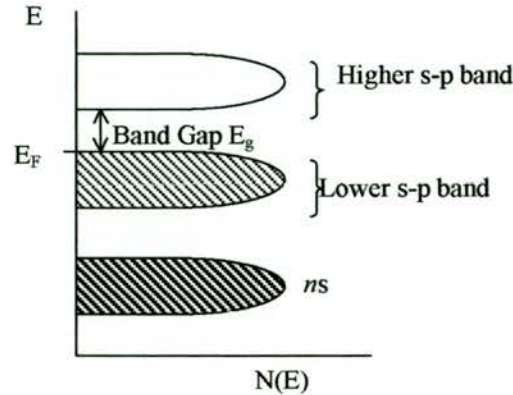


Fig.3.11 Energy level diagram for a semiconductor, showing conduction bands, E_F and the band gap.

There are two types of semiconductor, intrinsic and extrinsic. Intrinsic semiconductors are pure materials, whose conduction is governed by the size of the band gap and temperature. Extrinsic semiconductors are materials in which conductivity is controlled by the addition of dopants (Fig.3.12).

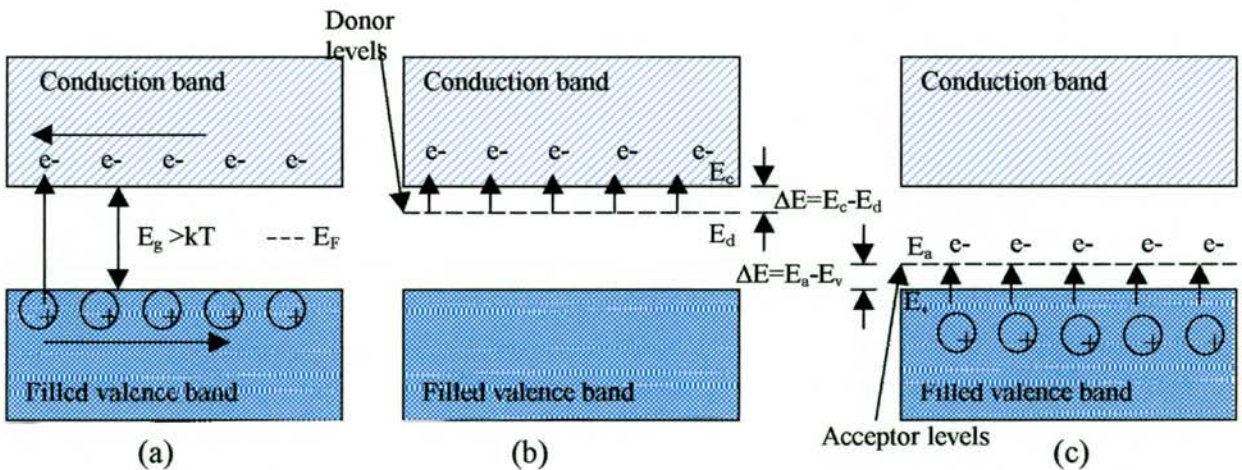


Fig.3.12 (a) Intrinsic semiconductor, (b) n-type extrinsic semiconductor (c) p-type extrinsic semiconductor

(i) Intrinsic semiconductors

As electrons are excited into a conduction band a positively charged “hole” is left in a crystal lattice (Fig.3.12(a)). In a pure intrinsic semiconductor, such as silicon or germanium, the electrons and the holes are charge carriers, and both move in an applied electric field. The current density is the sum of the conduction by electrons and holes:

$$\mathbf{J} = n|e|\mathbf{v}_n + p|e|\mathbf{v}_p \quad (\text{c.f. } \mathbf{J}=nev_d \text{ for metals})$$

n = number of conduction electrons per unit volume,

p = number of conduction holes per unit volume,

e = value of electron or hole charge (1.60×10^{-19} C)

v_n and v_p = drift velocities of electrons and holes

The relationship between current density and conductivity: $\mathbf{J}=\sigma\mathbf{E}$, allows the measurement of electron and hole mobilities from:

$$\sigma = \frac{\mathbf{J}}{\mathbf{E}} = \frac{n|e|\mathbf{v}_n}{\mathbf{E}} + \frac{p|e|\mathbf{v}_p}{\mathbf{E}}$$

where v_n/\mathbf{E} and v_p/\mathbf{E} are electron and hole mobilities, and is their drift speed in an applied electric field \mathbf{E} . μ_n and μ_p are mobilities of electron and holes respectively thus:

$$\sigma = n|e|\mu_n + p|e|\mu_p$$

As in an intrinsic semiconductor the number of holes and electrons are equal as they are created in pairs: $n=p=n_i$ where n_i is the intrinsic carrier concentration per unit volume; thus the electrical conductivity of the semiconductor is expressed as:

$$\sigma = n_i|e|(\mu_n + \mu_p)$$

The increase in temperature promotes more electrons from the valence band into the conduction band and the number of electrons promoted varies with temperature in an exponential manner:

$$n_i \propto e^{-(E_g - E_F)/kT}$$

where E_g = band energy gap, E_F = the Fermi level, k = Boltzmann's constant, T = temperature (K).

In semiconductors, E_F is halfway across the band gap, i.e. $E_g/2$, and the concentration of charge carriers can be expressed as:

$$n_i \propto e^{-E_g/2kT}$$

As the electronic conductivity, σ , of an intrinsic semiconductor is proportional to the concentration of charge carriers, n_i , thus:

$$\sigma = \sigma_0 e^{-E_g/2kT}$$

$$\ln \sigma = \ln \sigma_0 - \frac{E_g}{2kT}$$

(where σ_0 is an overall constant incorporating the mobilities of electrons and holes and has a slight temperature dependence: $\sigma_0 = |e|(\mu_n + \mu_p)$). This equation is the Arrhenius equation, where a plot of $\ln \sigma$ vs $1/T$ (K^{-1}) gives a straight line of $E_g/2kT$, where E_g can be determined from the slope of the plot.

(ii) Extrinsic semiconductors

In extrinsic semiconductors conductivity is controlled by the addition of dopants. Depending on which charge carriers are created, the negative charge carriers in the conduction band and positive holes in the valence band, extrinsic semiconductors can be classed into *p-type* or *n-type*. *p-type* conductivity occurs when the current is carried by the positive holes created by doping (Fig.3.12(c)), and *n-type* conduction occurs when the extra electrons carry the current (Fig.3.12(b)).

When an electronically neutral lattice is doped with an atom with a lower valence than the average atom in the lattice, the extra electron will have a much higher energy than the valence band creating a donor level slightly below the conduction band (Fig.3.12(b)). The energy gap an electron will then be required to jump across is much lower than the electrons from the valence band, i.e. $\Delta E = E_c - E_d$.

If an electronically neutral lattice is doped with an atom with a higher valence than the average atom in the lattice, an acceptor level just above the valence band is created

(Fig.3.12(c)). The application of an electric field will cause one of the neighbouring electrons from the valence band to move to the acceptor level, leaving behind a hole in the valence band which then acts as a positive charge carrier. The energy band the electron will be required to jump to the acceptor level is much smaller than the band gap to the conduction band, i.e. $\Delta E = E_a - E_v$.

As the mobile electrons and holes are constantly being generated and recombined, at constant temperature once the equilibrium has been reached, the relationship between the concentration of holes and electrons is:

$$[n][p] = n_i^2$$

n_i is the intrinsic concentration of charge carriers in a semiconductor and is a constant at any given temperature. $[n]$ and $[p]$ is the concentration of free electrons and holes respectively. In an extrinsic semiconductor the increase in one type of carrier reduces the concentration of another through recombination, hence the product of the two is a constant.

In order to maintain electro-neutrality in a crystal the total negative charge density must equal the total positive charge density, thus:

$$N_a + n = N_d + p$$

that is the sum of the number of positive donor dopant ions N_d and holes p , is equal to the sum of the number of negative acceptor dopant ions N_a and electrons, n .

In an n -type semiconductor $N_a=0$, thus the number of electrons is much greater than the number of holes, i.e. $n \gg p$, thus the above equation can be reduced to:

$$[n] \approx N_d$$

i.e. the free electron concentration is equal to the number of donor atoms, and the concentration of holes is obtained from:

$$[p] = \frac{n_i^2}{[n]} \approx \frac{n_i^2}{N_d}$$

Similarly in a p -type semiconductor $N_d=0$ and $p \gg n$ thus:

$$[p] \approx N_a$$

and:

$$[n] = \frac{n_i^2}{[p]} \approx \frac{n_i^2}{N_a}$$

Usually, the mobilities of electrons and holes at room temperature are at a maximum at low concentrations of dopants. As the concentration of dopants rises, the mobility of electrons and holes decreases and the conductivity drops. This is because neutralising one type of charge carrier by another leads to a lower mobility of the majority carriers

Increasing the temperature provides more energy for the dopant atoms to lose/gain electrons. However, in comparison to the intrinsic semiconductor, only a small amount of energy is required to ionise the impurity atoms.

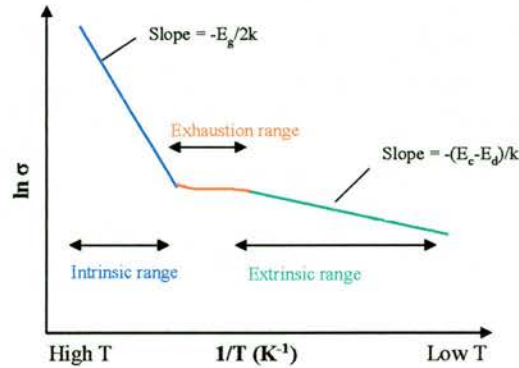


Fig.3.13 Schematic diagram of $\ln \sigma$ vs $1/T$ for an n -type extrinsic semiconductor

The amount of energy required to excite an electron into a conduction band is $E_c - E_d$. Thus the slope of the Arrhenius plot (Fig.3.13) is $-(E_c - E_d)/k$. For a p -type semiconductor the slope then becomes $-(E_a - E_v)/k$. The *exhaustion range* occurs in an n -type semiconductor over a temperature range where all the dopant atoms are completely ionised, and not enough energy is supplied to the valence electrons to jump the E_g barrier into a conduction band. In a p -type semiconductor this temperature range is known as the *saturation range*. Further increases in temperature provide sufficient energy for the valence electrons to jump the semiconductor gap. In this range intrinsic semiconduction becomes dominant, and the slope becomes much steeper being equal to $-E_g/2k$.

3.2.6 Defects and non-stoichiometry in crystals

Many properties of crystals, such as electrical conductivity, optical properties, mass transport etc., are determined by the number and type of defects. There are a large number of possible defects in a crystal and the relationship between them is shown in (Fig.3.14).

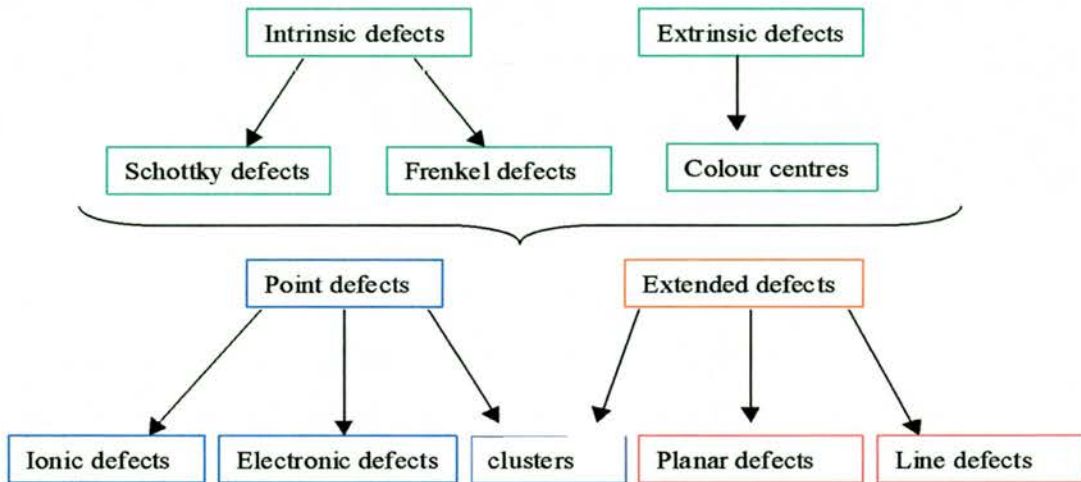


Fig.3.14 Different types of defects in crystals

Point defects are short order deviations from the perfect atomic arrangement, such as missing ions, interstitial ions etc. Electronic defects are responsible for the electronic conduction and are deviations from the ground state of orbital electronic configuration, such as electrons in a conduction band or holes in a valence band. Ionic defects include Schottky and Frenkel defects. Point defects may be created with thermal excitation (intrinsic defects), by addition of solutes and impurities (extrinsic defects) or by the oxidation/reduction processes causing the variation in metal/anion stoichiometry.

Extended defects are long range deviations from the perfect crystal and include clusters of point defects, line defects such as dislocations, and planar defects which include grain boundaries, external surfaces, stacking faults and shear planes.

Intrinsic and extrinsic defects characterise the two main types of defects. Intrinsic defects are those that do not alter the composition of the crystal and fall into two main categories; Schottky defects [3], in which there is the same number of cationic and anionic vacancies in the crystal; and Frenkel defects [4], in which some of the ions in the ionic crystal move from their normal lattice points forming interstitial ions.

Extrinsic defects are those that alter the composition of the crystal, usually achieved by doping. Then concentration of extrinsic defects, unlike intrinsic defects and non-stoichiometry, is usually constant with changes in temperature.

(i) Energetics and concentration of defects

The formation of defects is a thermally activated process, requiring energy to overcome the activation energy barrier, thus the process is endothermic. This would mean that the formation of defects is not thermodynamically favourable, but for the commensurate gain in entropy balancing the decrease in enthalpy upon the formation of defects. The additional entropy is due to the distribution of a small number of defects over a large number of lattice sites. Thus at equilibrium the change in free energy of the crystal upon defect formation is zero, and the free energy of a system is given by:

$$\Delta G = \Delta H - T\Delta S$$

In a crystal at any temperature above 0K there will always be defects.

If we take a perfect crystal with initial free energy G_0 , and form n Frenkel defect pairs at an energy expense of Δg_f per pair, the free energy of a crystal becomes:

$$G = G_0 + n\Delta g_f - T\Delta S_c$$

ΔS_c is the increase in entropy of the crystal. The change in free energy, ΔG is thus given by:

$$\Delta G = (G - G_0) = n\Delta g_f - T\Delta S$$

both parts of the equation on the right hand side are dependent on the number of defects, n . At equilibrium, the configurational entropy ΔS_c is given by:

$$\Delta S_c = k \ln \Omega$$

where Ω is the number of ways in which a defect can be arranged; and for n Frenkel defects there are n_i interstitials and n_v vacancies, arranged on a total of N lattice sites. The total number of ways, Ω_v , the vacancies can be arranged is:

$$\Omega_v = \frac{N!}{(N-n_v)n_v!}$$

The total number of ways, Ω_i , the interstitials can be arranged is:

$$\Omega_i = \frac{N!}{(N-n_i)n_i!}$$

The total number of configurations is $\Omega = \Omega_v \Omega_i$, and as the defects were formed in pairs, $n_i = n_v = n$. Substituting this into the equation for the configurational entropy ΔS_c , we get:

$$\Delta S_c = 2k \ln \left(\frac{N!}{(N-n)n!} \right)$$

If the numbers of N and n is very large, for example when dealing with a mole of atoms, Stirling's approximation is used: $N! = N \ln N - N$, ΔS_c then becomes:

$$\Delta S_c = 2k \left[N \ln \left(\frac{N}{N-n} \right) + n \ln \left(\frac{N-n}{n} \right) \right]$$

and the total free energy change is:

$$\Delta G = n\Delta g - 2kT \left[N \ln \left(\frac{N}{N-n} \right) + n \ln \left(\frac{N-n}{n} \right) \right]$$

At equilibrium, where $(\partial \Delta G / \partial n)_{T,P} = 0$ and $(N-n) \sim N$, the concentration of defects given as a fraction of the total number of atoms, N , becomes:

$$\frac{n}{N} = \exp \left(-\frac{\Delta g}{2kT} \right) = \exp \left(\frac{\Delta s_v}{2k} \right) \exp \left(-\frac{\Delta h}{2kT} \right)$$

From the above equation it can be seen that the defect concentration is exponentially dependent on the free energy of formation, Δg , and on the temperature, T . Δs_v is entropy associated with lattice strains and changes in vibrational frequencies upon defect formation. Vibrational entropy arises due to the change in vibrational modes of the atoms next to a vacancy [7].

The appearance and disappearance of Schottky defects mainly occur at the crystal surface or a dislocation face, and their concentration is given by:

$$n_s = N \exp(-\Delta H_s / 2kT)$$

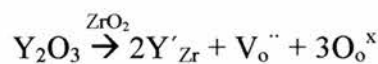
where n_s is the number of Schottky defects (ionic pairs per unit volume), at temperature $T(K)$, in a crystal with N cation and N anion sites per unit volume; k is the Boltzmann constant, ΔH_s is the enthalpy required to form one defect. The Schottky defect most commonly occurs when there is a small difference between the cation and anion radii, and their polarisabilities are small, then the van der Waals energy and the dielectric constants are also relatively small. Due to the simultaneous formation of anion and cation sites, the total number of lattice sites is increased by one formula unit upon the formation of the Schottky defect.

Frenkel defects occur due to thermal fluctuation in the crystal and are calculated from a similar expression:

$$n_F = (NN_i)^{1/2} \exp(-\Delta H / 2kT)$$

where N is the number of lattice sites and N_i is the number of interstitial sites available. Interstitial ions move to other sites by thermal fluctuations, chemical diffusion or an applied electric field. Vacancies can also move in a crystal when vacant lattice points are occupied by other lattice points. Frenkel defects most commonly occur when there is a large difference between the anion and cation radii, and the van der Waal energy and dielectric constant are also large. Frenkel defects conserve the number of lattice sites upon formation.

The third type of defect is Koch-Wagner defect [5], in which the defect is a result of the introduction of impurities or dopants into the crystal lattice; e.g. the formation of oxygen vacancies by introduction of Y_2O_3 into ZrO_2 to form yttria stabilised zirconia used as an electrolyte in solid oxide fuel cells and oxygen sensors. The replacement of Zr^{4+} by Y^{3+} in the fluorite crystal structure and the creation of anion vacancies at the tetrahedral sites in the lattice:

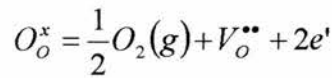


These vacancies enhance ionic conductivity, as the oxide ion moves through these oxygen vacancies.

In order to alter the properties of materials, such as changing ionic and electronic conductivity, thermal expansion etc., defects have to be introduced in to the crystal. There are a number of ways of doing this, one of which is simply an increase in temperature. Because the formation of defects is endothermic, Le Chatelier's principle tells us that increasing the temperature of an endothermic reaction will favour the products, i.e. the defects. Additionally, ΔH of the formation of defects is smaller at higher temperature, this increases the number of defects present.

(ii) Effects of oxygen partial pressure

The concentration of defects also varies with oxygen partial pressure, thus if a metal oxide is reduced and oxygen is removed into the gas phase leaving behind oxygen vacancies, the reaction can be expressed as:

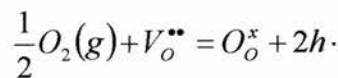


the two electrons associated with O^{2-} ion are liberated in to the solid. The equilibrium constant for this reaction, where n is the concentration of electrons, is given by:

$$K_R = n^2 [V_o^{\bullet\bullet}] P_{O_2}^{1/2} = K_R^0 \exp\left(-\frac{\Delta g_R}{kT}\right)$$

oxygen partial pressure, P_{O_2} , is the oxygen activity, K_R^0 is a constant, and Δg_R is the free energy of reduction. The concentration of oxygen ions on their sites is left out of the equation, as $[O_o^x] \approx 1$; i.e. the concentration of vacancies is assumed to be very dilute.

The reverse of this reduction reaction is the oxidation reaction, involving the consumption of oxygen vacancies:



and the equilibrium constant, where p is the concentration of holes, is:

$$K_o = \frac{P^2}{[V_o^{**}]P_{O_2}^{1/2}} = K_o^\circ \exp\left(-\frac{\Delta g_o}{kT}\right)$$

Highly stoichiometric cations, such as MgO and Al₂O₃ have fixed valence and hence large free energy for reduction/oxidation. Thus changes in the P_{O₂} cause little change in defect concentration. Multivalent cations, such as Ti⁴⁺, Nb⁴⁺, etc form nonstoichiometric oxides, TiO_{2-x}, Nb₂O_{5-x}, ZrO_{2-x}, CeO_{2-x} etc, which can be easily reduced, with oxygen deficiencies of up to 1% for Ti³⁺, before decomposition or transition to a different phase occurs. Other cations, such as Fe_{1-x}O or Ni_{1-x}O are easily oxidised, resulting in cation deficiencies. Some cations, such as strontium in Sr_{1-x}NbO₃ can never be stoichiometric, having a minimum cation deficiency of about 0.02[6].

The concentration of the electrons and the neutral, singly and doubly charged oxygen vacancies are related in the following three equations:

$$[V_o^x]p_{O_2}^{1/2} = K_1[O_o]$$

$$[V_o^\bullet][e'] = K_a[V_o^x]$$

$$[V_o^{**}][e'] = K_b[V_o^\bullet]$$

Assuming that the oxygen vacancies and the complementary electrons are the main defects in the oxygen deficient oxide then in order to maintain electroneutrality the following equation must be true:

$$[e'] = [V_o^\bullet] + 2[V_o^{**}]$$

By combining these equation the electron concentration is given by:

$$[e']^3 = K_1K_a p_{O_2}^{-1/2} (2K_b + [e'])$$

the above equation has two main limiting conditions:

- If $[e'] \gg 2K_b$ $[e'] = (K_1K_a)^{1/2} p_{O_2}^{-1/4}$
- If $[e'] \ll 2K_b$ $[e'] = (2K_1K_aK_b)^{1/3} p_{O_2}^{-1/6}$

Thus the concentration of electrons, and thus conductivity, is a function of the ambient oxygen partial pressure. The electron concentration will increase with decreasing oxygen partial pressure and the p(O₂) dependence ranges from pO₂^{-1/4} to pO₂^{-1/6}.

To maintain electroneutrality, the following limiting conditions apply to the concentration of oxygen vacancies:

- If $[V_O^x] \gg [V_O^{\cdot}] + [V_O^{\cdot\cdot}]$ $[V_O]_{total} = K_1 pO_2^{-1/2}$
- If $[V_O^{\cdot}] \gg [V_O^x] + [V_O^{\cdot\cdot}]$ $[V_O]_{total} = (K_1 K_a)^{1/2} pO_2^{-1/4}$
- If $[V_O^{\cdot\cdot}] \gg [V_O^x] + [V_O^{\cdot}]$ $[V_O]_{total} = (1/4 K_1 K_a K_b)^{1/3} pO_2^{-1/6}$

From these equations it can be seen that the concentration of oxygen vacancies has a $p(O_2)$ dependence that ranges from $pO_2^{-1/2}$ to $pO_2^{-1/6}$.

At high temperatures, however, the doubly charged vacancies vastly outnumber the neutral or the singly charged oxygen vacancies [7], hence the equation can be simplified to involve only the doubly charged vacancies.

Metal oxides which have a defect structure involving oxygen and metal vacancies, will have a dependency on $p(O_2)$, so that at:

- low $p(O_2)$ $[V_O^{\cdot\cdot}] \gg [V_M^{\cdot\cdot}]$
- high $p(O_2)$ $[V_O^{\cdot\cdot}] \ll [V_M^{\cdot\cdot}]$

Thus in order to maintain the Schottky constant, $K_s = [V_O^{\cdot\cdot}][V_M^{\cdot\cdot}]$, as the $p(O_2)$ decreases and the concentration of oxygen vacancy increases, the metal vacancies decrease correspondingly. In order to satisfy the bulk electrical neutrality:

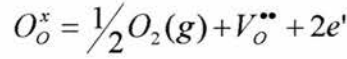
$$2[V_M^{\cdot\cdot}] + [e] = 2[V_O^{\cdot\cdot}] + [h]$$

This can be reduced to a *Brouwer approximation* in which there is only one positive and negative defect, hence:

1. $[e] = 2[V_O^{\cdot\cdot}]$
2. $[h] = 2[V_M^{\cdot\cdot}]$
3. $[V_M^{\cdot\cdot}] = [V_O^{\cdot\cdot}]$
4. $[h] = [e]$

In non-stoichiometric oxides, such as MgO, at high temperature the intrinsic Schottky concentration (3) is greater than the electronic carrier concentration (4), and equation (3) can thus be considered to be dominant.

Thus for an n -type electronic conductor the defect equation describing the incorporation of oxygen into the lattice at low $p(\text{O}_2)$ becomes:



and the mass action relation for this equation is given by:

$$K_1 = p_{\text{O}_2}^{1/2} [V_o^{\bullet\bullet}] [e']^2$$

If $[V_o^{\bullet\bullet}] \cong \text{constant}$ and is large, at either very low $p(\text{O}_2)$ or upon creation of oxygen ion vacancies by doping (e.g. $\text{Y}_2\text{O}_3 + \text{ZrO}_2 \rightarrow 2\text{Y}'_{\text{Zr}} + V_o^{\bullet\bullet} + 3\text{O}_o^x$), the equation reduces to:

$$[e'] \propto p_{\text{O}_2}^{-1/4}$$

Hence the conductivity of the electrons, σ_e , is proportional to the inverse fourth root of $p(\text{O}_2)$:

$$\sigma_e \propto p_{\text{O}_2}^{-1/4}$$

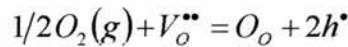
Lowering the $p(\text{O}_2)$ further, the vacancy concentration is no longer constant as sufficient reduction occurs so that the concentration of electrons is twice that of the oxygen vacancies ($[e'] = 2[V_o^{\bullet\bullet}]$), the equation for the law of mass action is then:

$$[e'] = (2K_1)^{1/3} p_{\text{O}_2}^{-1/6}$$

$$\sigma_e \propto p_{\text{O}_2}^{-1/6}$$

Thus when the number of oxygen vacancies are in excess compared to the number of charge carriers created by reduction, then the conductivity dependence for an n -type oxide on $p(\text{O}_2)$ is $-1/4$. When the majority of vacancies are associated with creation of charge carriers, the conductivity has a $p(\text{O}_2)$ dependence of $-1/6$ [8].

At high $p(\text{O}_2)$, the predominant defects are metal vacancies and electron holes. Thus for a p -type conductivity, the equation for oxygen incorporation into a lattice and the concentration of holes, $[h]$, can be described as follows:



the mass action relation is given by:

$$K_2 = [h']^2 / p_{\text{O}_2}^{1/2} [V_o^{\bullet\bullet}]$$

thus if $[V_o^{\bullet\bullet}] \cong \text{constant}$ and is large, then $[h]$ increases to preserve electroneutrality ($[e][h] = K_i$), thus this equation can be approximated to:

$$[h] \propto p_{O_2}^{1/4}$$

thus the p -type conductivity of the holes, σ_h , is proportional to the inverse fourth root of $p(O_2)$:

$$\sigma_h \propto p_{O_2}^{1/4}$$

At higher $p(O_2)$, there is a consumption of oxygen vacancies and an increase in the creation of charge carriers, i.e. the metal vacancies and/or holes. In these conditions the $[h]$ is approximated to: $[h] \propto p_{O_2}^{1/6}$ and correspondingly $\sigma_h \propto p_{O_2}^{1/6}$.

In an “intermediate” $p(O_2)$ region, $[V_M^{\bullet\bullet}] = [V_O^{\bullet\bullet}] = K_s^{1/2}$ ($K_s = [V_M^{\bullet\bullet}][V_O^{\bullet\bullet}]$), and the concentration of both types of vacancies is constant. The schematic representation of defect concentration as a function of oxygen partial pressure for a metal oxide forming predominantly Schottky defects is shown in (Fig.3.15(a)).

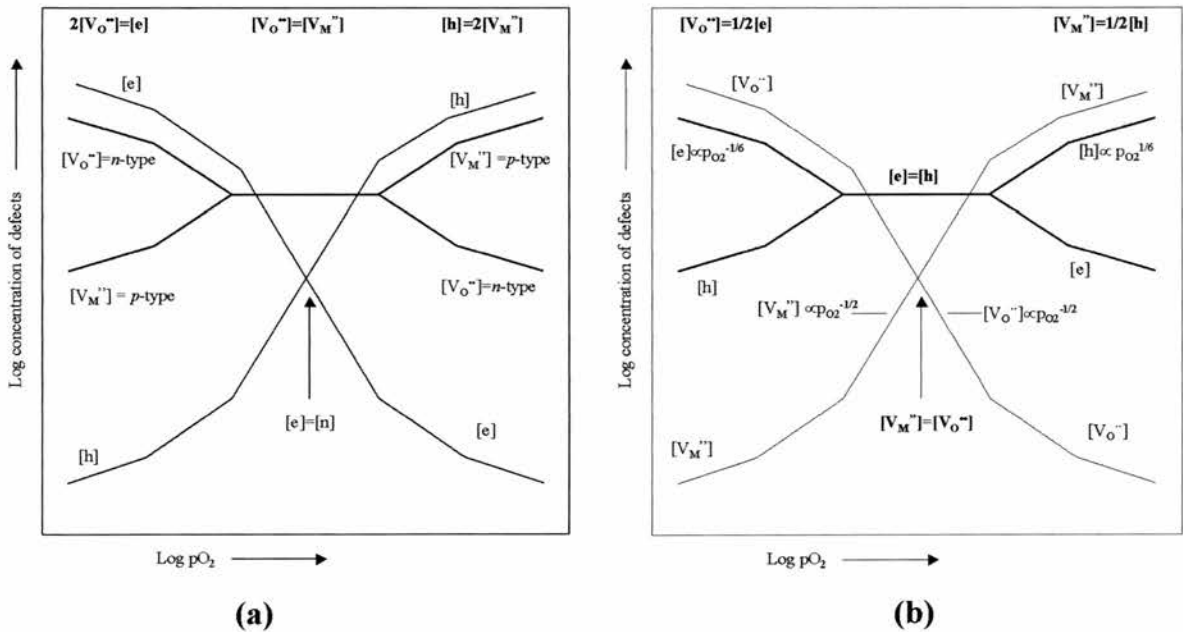


Fig.3.15(a) Brouwer diagram showing a schematic representation of defect concentration as a function of $p(O_2)$ for a metal oxide that forms predominantly Schottky defects (b) Kröger-Vink diagram for a metal oxide in which electronic defects dominate

If a band gap in a semiconductor is small enough, then electronic defects will dominate (Fig.3.15(b)); here the oxide is a pure electronic conductor at all oxygen pressures, and exhibits no appreciable ionic conduction.

A measurement scanning the conductivity of a metal oxide at constant temperature and over a large range of $p(\text{O}_2)$ gives an indication of the electronic and ionic conductivity regimes, showing p -type or n -type conductivities and vacancy concentration dependencies for the conduction processes.

3.3 Thermal Expansion Theory

3.3.1 Heat transport in solids

When a solid is heated, heat is transported as an elastic lattice wave, thus heat is related to the kinetic energy of the molecules, atoms and electrons in metals. The vibrations of adjacent atoms are coupled due to atomic bonding, and these vibrations are quantized. A phonon is thus a single quantum of lattice vibrational energy (Fig.3.16).

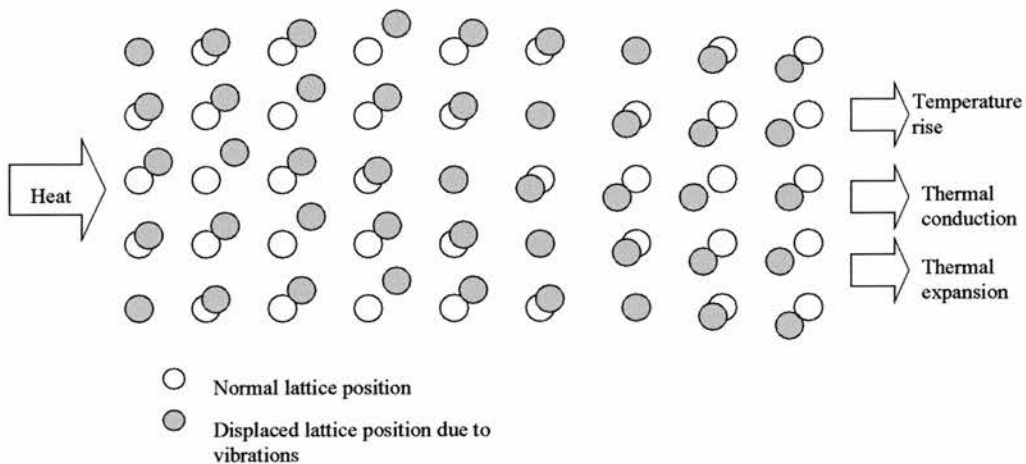


Fig.3.16 An elastic lattice wave

Directly related to the heat transfer is the heat capacity of the solid, which is the derivative of rate of transfer of heat with temperature:

$$C = \frac{dQ}{dT} = \text{Jmol}^{-1}\text{K}^{-1}$$

This is usually expressed as the specific heat capacity of the material, where m is mass of material.

$$C = \frac{1}{m} \frac{dQ}{dT} = Jkg^{-1}K^{-1}$$

Specific heat can be expressed in terms of internal energy of the system:

$$C_v = dU/dT$$

Where C_v is molar specific heat at constant volume. The internal energy of the system, U , corresponds to the average energy of all oscillators:

$$U = N_A \langle E \rangle$$

N_A is Avogadro's number. The energy of the single, uncoupled harmonic oscillator is expressed as:

$$E = E_x + E_y + E_z$$

In classical treatment of specific heat U is expressed as:

$$U = 3N_A k_B T$$

The corresponding specific heat is known as Dulong and Petit's law:

$$C_v = 3N_A k_B = 3R$$

Thus it can be seen from the classical expression that specific heat is independent of temperature. This agrees with experimental observation only at infinite temperature, but fails at low temperature because it does not take into account quantisation of atomic vibrations. Einstein proposed that the temperature dependence of specific heat results from the quantum nature of the phonons, thus the quantum behaviour of a harmonic oscillator has to be included in the expression for specific heat:

$$U = 3N_A \hbar \Omega \left(\langle n \rangle + \frac{1}{2} \right)$$

Where $\langle n \rangle$ is the average phonon number. This expression rearranges to:

$$C_v = 3R \left(\frac{T_E}{T} \right)^2 F_E(x)$$

where T_E is the Einstein temperature. This equation shows increasing specific heat with increasing temperature and reproduces the Dulong-Petit rule at infinite temperature (where a constant behaviour, $3R$, is observed at high temperature). As this equation only

takes a single phonon frequency into account the equation does not reproduce the T^3 law observed experimentally.

Debye extended Einstein's treatment by including the phonon spectrum given by the classical density of states expression, giving specific heat from:

$$C_v = 9R \left(\frac{T}{\theta_D} \right)^3 F_D(x)$$

Specific heat is now seen to increase with T^3 . As will be shown later, specific heat capacity has two contributions: vibration of atoms around the equilibrium position and translation of electrons to higher energy states.

At $T=0\text{K}$: $C_v = 0$

At low T : $C_v = AT^3$, i.e. specific heat increases with T^3 .

Above θ_D (Debye temperature at which the mean thermal energy of an oscillator is equal to a single quantum step $\hbar\omega_{\max}$, where ω_{\max} is the frequency of the oscillator): $C_v \approx 3R \approx 25\text{Jmol}^{-1}\text{K}^{-1}$ ($R=8.31\text{Jmol}^{-1}\text{K}^{-1}$); i.e. a constant value of $3R$ is reached (Fig.3.17).

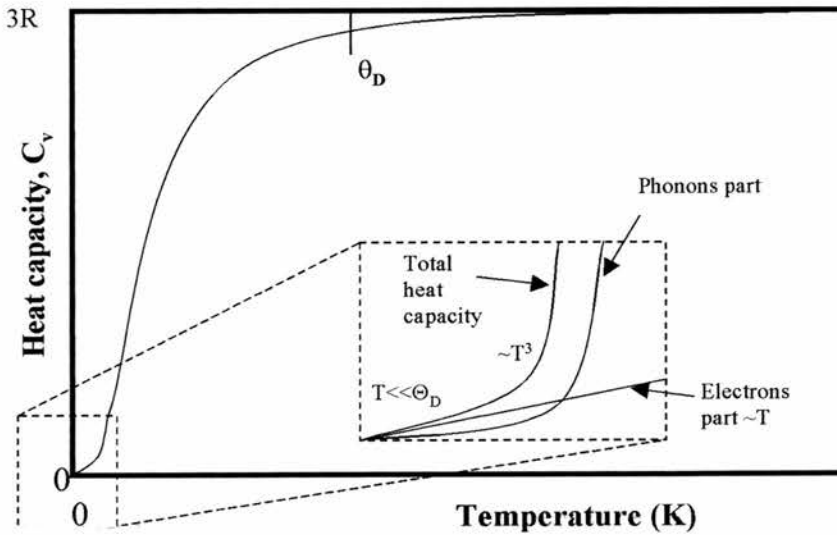


Fig.3.17 Heat capacity as a function of temperature

Thermal conductivity is related to heat capacity, and is a means of quantifying heat transfer, i.e. the rate at which heat flows through a certain area of a body. It is given by Fourier's equation:

$$\frac{dq}{dt} = -kA \frac{dT}{dx}$$

Where q is heat flux (flow) per unit area per unit time: $[q] = \text{Wm}^{-2}$, in the x direction through the area A , during time t , where dT/dx is the temperature gradient and k is the thermal conductivity: $[k] = \text{Wm}^{-1}\text{K}^{-1}$ (minus sign symbolises heat flow from hot to cold) (Fig.3.18).

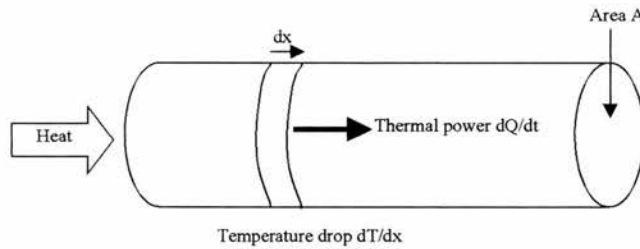


Fig.3.18 Schematic heat flow diagram.

As was said earlier the heat is transported in solids by lattice vibration waves (phonons) and free electrons. Thus the total thermal conduction is the sum of these pathways:

$$k = k_l + k_e$$

Where k_l is lattice vibration thermal conductivity and k_e is electron thermal conductivity. In metals/alloys there is a strong correlation between thermal conductivity k_e and electrical conductivity σ expressed in the Weidemann-Franz-Lorentz law:

$$\frac{k}{\sigma T} = \text{constant}$$

where T is the temperature. The constant has the same value for all metallic conductors. Although a good approximation at room temperature, once again this equation becomes inaccurate at low temperatures as T approaches absolute zero. But the equation shows that heat conduction like electrical conduction in metals is mostly entirely by free electrons. In semiconductors and insulators there is no correlation between k and σ , as heat conduction is essentially due to phonons. Although conduction by phonons occurs in all materials, in metals, where the predominant conductivity is due to the flow of electrons, it is greatly reduced due to scattering of the free electrons by phonons. There

are some materials in which the thermal conductivity is due to the combination of electronic and phonon contributions.

Thermal expansion is defined either as linear coefficient of thermal expansion $[\alpha_l] = \text{K}^{-1}$:

$$\frac{\Delta l}{l_0} = \alpha_l \cdot \Delta T$$

or as volume coefficient of thermal expansion:

$$\frac{\Delta V}{V_0} = \alpha_v \cdot \Delta T$$

As a general rule, with a number of exceptions, thermal expansion is inversely proportional to the melting point of the material as this is related to the interatomic forces and separation:

$$\alpha_l \propto 1/T_{mp}$$

The greater the atomic bonding energy, the smaller the value of α_l . α_l for different materials is found typically to be in the ranges:

- Metals $5 \times 10^{-6} - 25 \times 10^{-6} \text{ K}^{-1}$
- Ceramics $< 0.5 \times 10^{-6} - 15 \times 10^{-6} \text{ K}^{-1}$
- Polymers $50 \times 10^{-6} - 400 \times 10^{-6} \text{ K}^{-1}$

3.3.2 Lattice Vibrations

In a crystal, each atom cannot behave as an independent oscillator, due to strong interatomic forces. Thus the movement of each atom affects and is in turn affected by the movement of neighbouring atoms. When atoms move they move in a phase-related way, producing wave motions. Elastic vibrational waves in solids are produced by internal thermal motion of atoms and molecules. When an elastic vibrational wave moves along the direction, for example, of the cube edge [100], face diagonal [110] or body diagonal [111], planes of atoms move in phase with corresponding displacements. Two main types of displacements are longitudinal (Fig.3.19), induced by the longitudinal acoustic wave and transverse (Fig.3.20), induced by the transverse acoustic wave. A third type of displacement is caused by the optical wave (Fig.3.21).

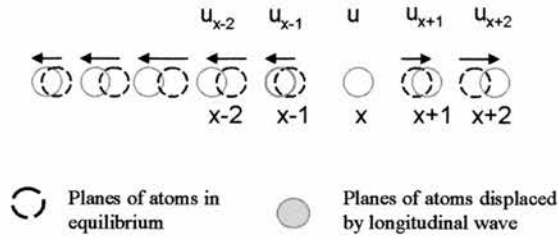


Fig.3.19 Longitudinal acoustic wave

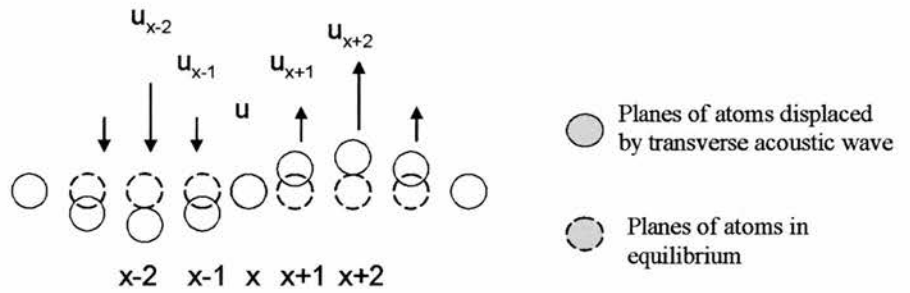


Fig.3.20 Transverse acoustic wave

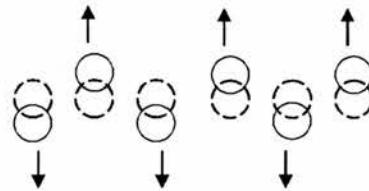


Fig.3.21 Optical wave

In the acoustic branch neighbouring atoms vibrate in phase, and for the optical branch different atoms vibrate in opposite directions.

Atoms in a crystal are always undergoing thermal vibrations around their mean position. The amplitude of these oscillations always increases with increasing temperature. The amplitudes also differ for different atoms in the same structure, and for the same atom in different directions. A diatomic molecule vibrates with a potential energy which depends on the square of the displacement from equilibrium. The energy levels are quantised at equally spaced values (Fig.3.22). This simple harmonic oscillator has energy levels given by:

$$E_n = \left(n + \frac{1}{2} \right) h\omega$$

$n=0,1,2,3\dots$ ω =frequency/ 2π and h =Planks constant/ 2π

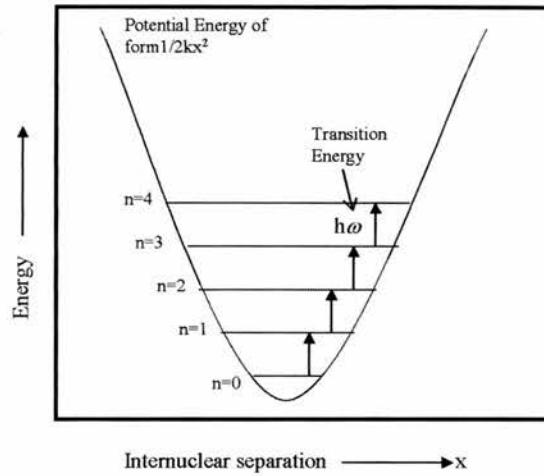


Fig.3.22 Simple harmonic potential energy curve as a function of internuclear separation producing harmonic oscillations

In the many planes of atoms in crystals, the collection of oscillators in thermodynamic equilibrium have an energy distribution that follows Boltzmann's law. From this it can be seen that at any temperature, the r.m.s. amplitudes will be large for low frequency oscillations, and small for high frequency oscillations: i.e. the r.m.s. is inversely proportional to the frequency of the oscillation. Low frequencies mean low force constants and thus weak forces.

Simple harmonic oscillators are an unrealistic picture of lattice movements and do not give rise to thermal expansion. Thermal expansion is a consequence of anharmonic thermal oscillation (Fig.3.23). Atoms with an anharmonic potential well expand on heating, because the additional kinetic energy allows atoms to move more to stretch the bond than to compress it.

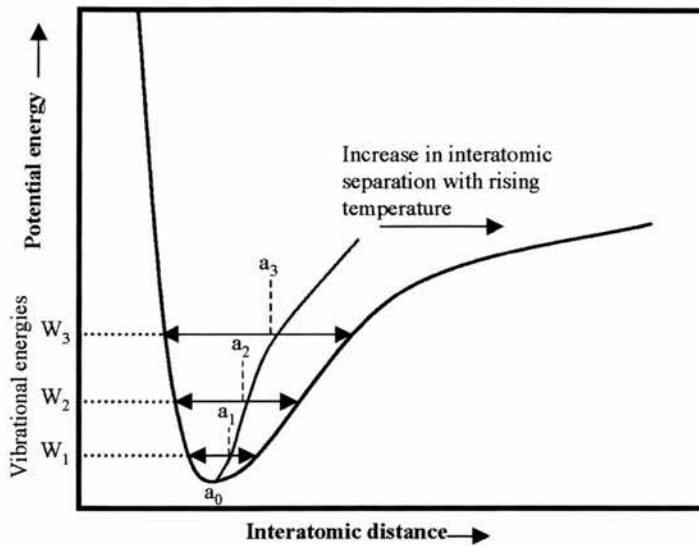


Fig.3.23 Anharmonic potential energy as a function of interatomic distance producing anharmonic thermal oscillations.

Large anharmonicity produces large thermal displacements and thus weak forces. Thus weak cohesive forces are associated with large thermal expansion coefficients.

The Gruneisen theory of thermal expansion relates the linear thermal expansion coefficient α to the specific heat as:

$$\alpha = \frac{1}{3B} \sum_i \gamma_i c_i$$

The summation is over normal vibrational modes, where $B = -dP/d\ln V$ is the bulk modulus (the inverse of compressibility), c_i is the specific heat contribution of a single mode and $\gamma_i = -(\delta \ln \omega_i / \delta \ln V)$ is the Gruneisen parameter which measures the contribution of each vibrational mode to thermal expansion. The Gruneisen parameter is defined as a measure of anharmonicity and is related to specific heat C_v as:

$$\gamma(T) = 3B\alpha / C_v$$

Where C_v is the molar specific heat at constant volume.

At fixed volume the expansion coefficient is nearly constant for temperatures above the Debye temperature [9, 10], while at zero pressure the expansion coefficient continues to increase with temperature.

3.3.3 Negative thermal expansion

There are two main sources of expansion, which may simultaneously contribute to the overall expansion:

- bond-length expansion - simple structures such as cubic systems, which prevent angular distortion, have a rough empirical rule: “the mean linear expansion coefficient is inversely proportional to the square of the electrostatic valence”[9]. As was described earlier, the atomic vibrations about their positions will be increased with increasing temperature and the increase is proportional to interatomic forces
- bond-angle changes - In 3D network structures with strong bonds, changes in angle may be brought about by either the distortion of polyhedra, without change of orientation, or tilts of polyhedra relative to one another without shape change. If the arrangement of polyhedra goes from a cubic system to a distorted system negative thermal expansion is observed

One of the reasons for the negative thermal expansion is the tilting of the octahedra. In the ideal cubic perovskite structure, where the cation, B , is in the centre of the octahedra, the $B-O$ bondlength is d , the lattice parameter $a=2d$. In a system with rigid octahedra, rotating one octahedra causes its immediate neighbour to rotate in the opposite direction, reducing the separation between neighbouring B sites (Fig.3.24).

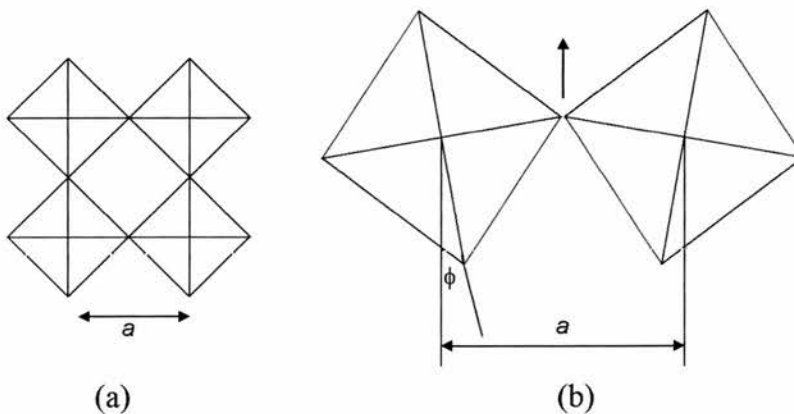


Fig.3.24 Tilting of the octahedra in the ideal perovskite thus reducing the unit cell parameter

The new separation between neighbouring B cations is:

$$a = 2d \cos \phi \approx 2d \left(1 - \frac{\phi^2}{2} \right)$$

The rotation of the octahedra arises from the lattice vibrations, and the rotation angle defines the amplitude of the vibration from:

$$\langle \phi^2 \rangle \propto \frac{k_B T}{\omega^2}$$

From this equation the change in the lattice parameter becomes:

$$a \approx 2d \left(1 - \frac{k_B T}{2\omega^2} \right)$$

The thermal expansion is related to unit cell parameter a as:

$$a = 2d(1 + \alpha T)$$

$$\alpha \propto -k_B d / \omega^2$$

The value from this equation is negative indicating a negative thermal expansion. This, however, is an over-simplification of negative thermal expansion causes, as other factors such as lattice vibrations, including the stretching of bonds, can lead to positive thermal expansion.

The thermal expansion is dependent on the electrostatic forces within the lattice, and these are a function of the concentration of positive and negative charges and their distances within the lattice, thus thermal expansion will increase if the attraction forces decrease. In reducing conditions there is an oxygen loss from the lattice; this would have an effect of decreasing the electrostatic attraction, and a resultant increase in the thermal expansion coefficient [11]. In this way the thermal expansion is influenced by the oxygen vacancies and reduction. The degree of influence depends on the type of structure, the number of oxygen vacancies and whether any structural changes are observed upon reduction.

3.4 References:

- 1 Y.M.Chiang, D.P.Birnie and W.D. Kingery, "Physical Ceramics: Principles for Ceramic Science and Engineering", (1997), John Wiley and Sons Inc., New York
- 2 H.M.Rosenberg, "The Solid State (2nd Ed.)", (1978), Oxford University Press, Oxford, 125
- 3 W.Schottky, *Z.Phys.Chem.*(1935), **29B**, 335
- 4 J.Frenkel, *Z.Phys.Chem.*,(1926), **35**, 652
- 5 E.Koch and C.Wagner, *Z.Phys.Chem.*, (1937), **38B**, 295
- 6 S.Ya.Istomin, G.Svensson, O.G.D'yachenko, W.Holm and E.V.Antipov, *J.Solid State Chem.*, (1998), **141**, 514
- 7 P.Kofstad, "Nonstoichiometry, diffusion and electrical conductivity in binary metal oxide", (1972), Wiley-Interscience, New York, 182
- 8 P.R.Slater and J.T.S.Irvine, *Solid State Ionics*, (1999), **124**, 61
- 9 D.C.Wallace, *Phys.Rev.* (1965), **139 (3A)**, A877
- 10 D.C.Wallace, *Phys.Rev.* (1968), **176 (3)**, 827
- 11 H.Ullmann, N.Trofimenko, F.Tietz, D.Stover and A.Ahmad-Khanlou, *Solid State Ionics*, (2000), **138**, 79

Chapter 4. Nb₂O₅-TiO₂ system

4.1 Nb₂O₅-TiO₂ SYSTEM	95
4.1.1 Phase diagram.....	95
4.1.2 Structure.....	96
4.1.3 DC Conductivity studies.....	100
4.1.4 Thermal expansion data.....	102
4.1.5 Single Cell Testing.....	105
4.1.6 Doping of Nb ₂ O ₅ -TiO ₂	106
4.2 Nb₂O₅-TiO₂-ZrO₂ SYSTEM	108
4.2.1 Structure.....	108
4.2.2 Conductivity.....	116
4.2.3 Thermal Expansion Coefficient.....	117
4.3 Nb₂O₅-TiO₂-Fe₂O₃ SYSTEM	120
4.3.1. Structure.....	120
4.3.2 Conductivity.....	122
4.3.3 Thermal Expansion Coefficient.....	124
4.4 Nb₂O₅-TiO₂-CeO₂ SYSTEM.....	126
4.4.1 Doping Nb ₂ TiO ₇ with CeO ₂	126
4.4.2 Nb ₂ TiO ₇ -Ce _{0.8} Gd _{0.2} O _{1.9} composites	127
4.4.3 SEM Study of density and homogeneity of CGO-NbTiO composite.....	129
4.5 Nb_{2-x}Ti₁V_xO₇ SYSTEM.....	130

4.6 Nb_xCr_xTi_{1-2x}O₂	130
4.6.1 <i>Structure</i>	130
4.6.2 <i>Thermal expansion</i>	140
4.6.3 <i>Electronic conductivity at constant atmosphere</i>	141
4.6.4 <i>Electronic conductivity as a function of p(O₂)</i>	144
4.6.5 <i>AC Impedance study</i>	151
4.7 CONCLUSION	163
4.8 REFERENCES:	166

4.1 Nb₂O₅-TiO₂ system

4.1.1 Phase diagram

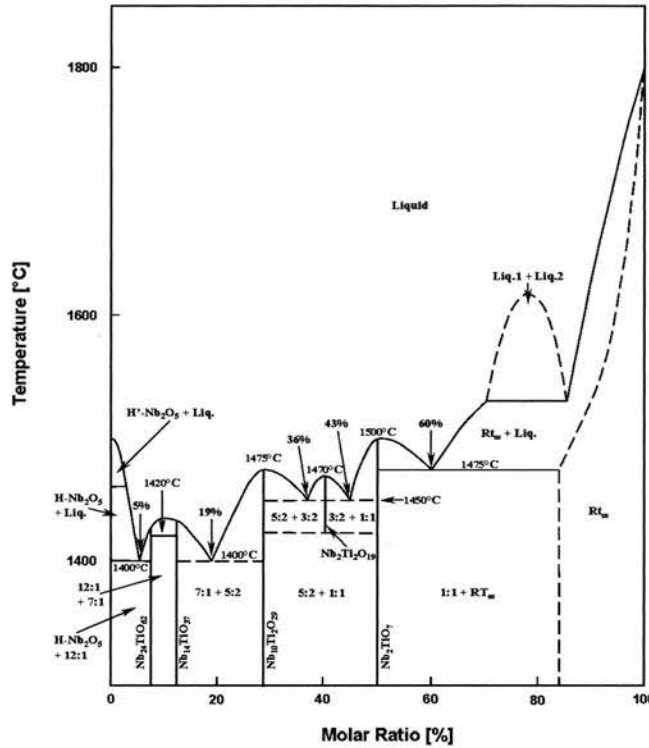


Fig. 4.1 Phase diagram for Nb₂O₅-TiO₂ [1]

Due to their high electronic conductivity niobia based rutile materials make good candidates for use as fuel cell electrode component materials in SOFCs. The addition of TiO₂ increases the thermal expansion of Nb₂O₅ and prevents its negative thermal expansion between 200°C and 600°C. It also facilitates the reduction of Nb₂O₅ to the NbO₂ rutile type structure and improves its sinterability. Niobium titanates have a number of possible phases as shown in (Fig.4.1). A 1:1 mixture of Nb₂O₅ – TiO₂ produces Nb₂TiO₇, which is then reduced to Nb_{1.33}Ti_{0.67}O₄, a double rutile-type structure like NbO₂.

The addition of TiO₂ increases both the unit cell and the thermal expansion coefficient of H-Nb₂O₅, from $1.76 \times 10^{-6} \text{ K}^{-1}$ to $2.31 \times 10^{-6} \text{ K}^{-1}$ [2]. The theoretical density is also lowered by addition of TiO₂, from 4.55 g cm^{-3} to 4.33 g cm^{-3} . Reducing Nb₂TiO₇ increases the theoretical density of 4.55 g cm^{-3} to 5.38 g cm^{-3} for Nb_{1.33}Ti_{0.67}O₄.

4.1.2 Structure

A least squares refinement was performed on the Nb₂TiO₇ sample (Table 4.1). Using literature starting values [3,4] two unit cells can be determined, both of which are interchangeable by a 45° rotation about the b axis (Fig.4.2).

Table 4.1 Refined unit cell parameters for Nb₂TiO₇ using literature unit cell parameters for starting values

Starting values	Using ref.[3]	Using ref.[4]
Symmetry	Monoclinic I	Monoclinic C
Cell a	17.6755 (9)	20.3610 (11)
Cell b	3.79876 (20)	3.79877 (20)
Cell c	11.8861 (5)	11.8861 (5)
β°	95.344 (3)	120.194 (3)
Cell Volume	794.62 (9)	794.63 (9)
Space group	I2/m	C2/m
Z	6	6

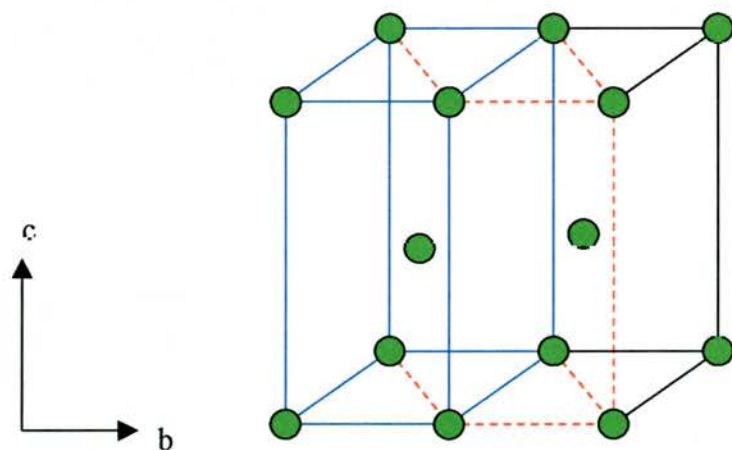


Fig.4.2 Schematic diagram of the two types of unit cell in a monoclinic system going from side centred C (red) to body centred I (blue) lattice.

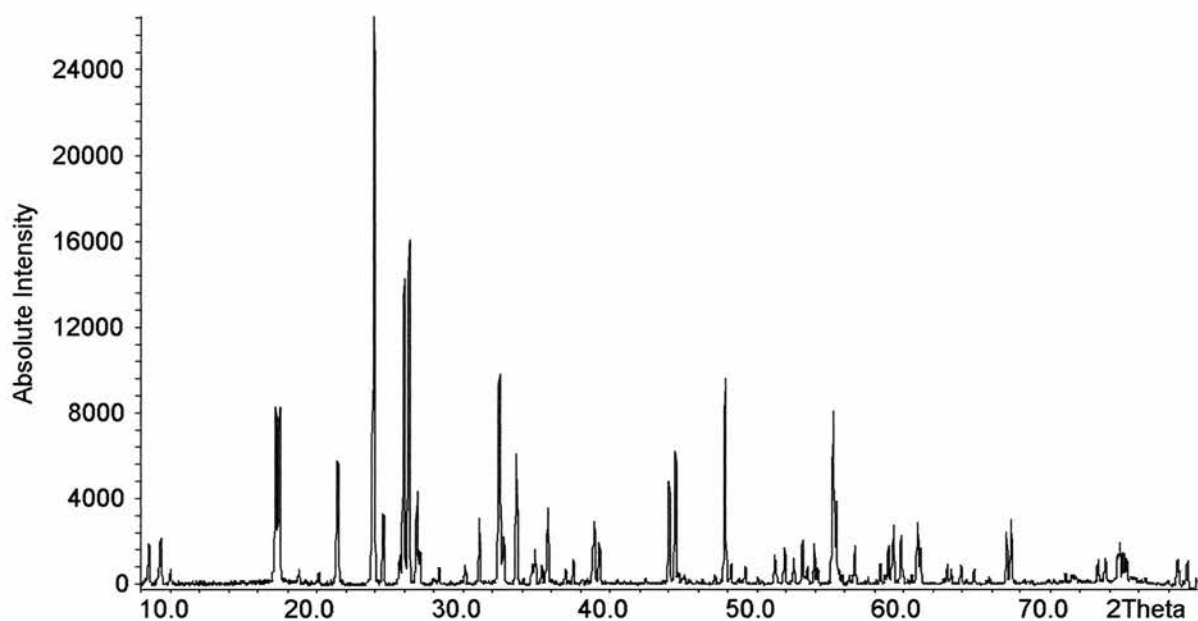


Fig.4.3 X-ray powder diffraction pattern for Nb₂TiO₇

The structure of both the oxidised, Nb₂TiO₇, and the reduced, Nb_{1.33}Ti_{0.67}O₄, forms have been reported previously by several authors [3, 4, 5, 6, 7]. When oxidised the structure of Nb₂TiO₇ has a complicated structure with a monoclinic unit cell, (C2/m) with $a=20.36\text{\AA}$, $b=3.80\text{\AA}$, $c=11.89\text{\AA}$ and $\beta=120.19^\circ$ (Fig.4.4).

In this structure Ti⁴⁺ and Nb⁵⁺ both occupy the same crystallographic site. This is mainly due to their similar ionic radii (0.60\AA and 0.64\AA respectively) and both coordinate oxygen predominantly in octahedra [7]. The two kinds of metal atoms are thus disordered, and the average population of any one site is 1/3Ti and 2/3 Nb. Each metal atom is co-ordinated to six oxygens forming an octahedron. These octahedra can either share corners to form linear strings, or edges to form a zig-zag string. This structure has a monoclinic shear, in which zig-zag strings of octahedra sharing corners are shifted with respect to each other to produce additional edge sharing to corner sharing octahedra (Fig.4.4)

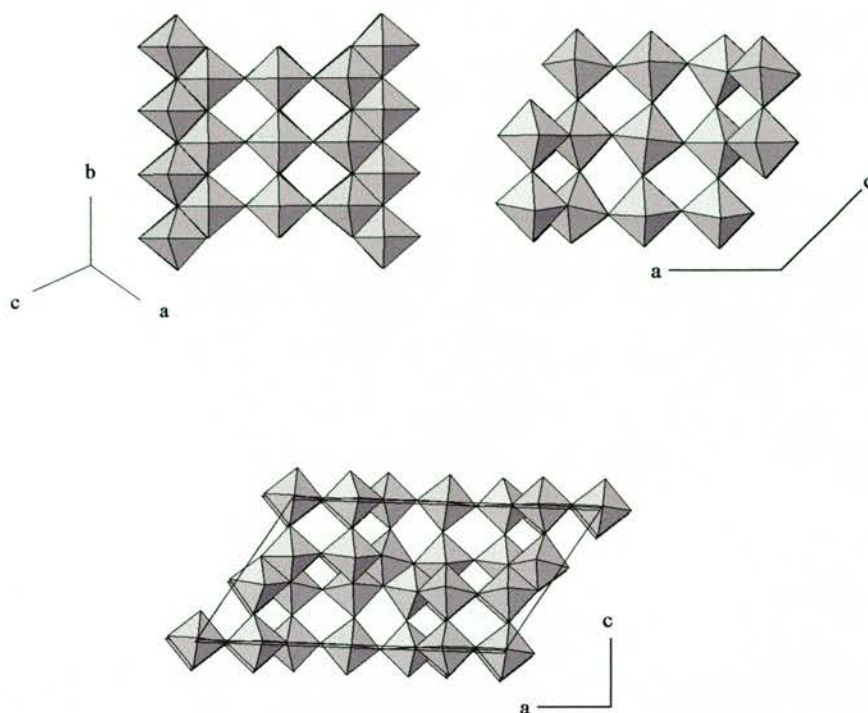


Fig.4.4 Nb₂TiO₇ unit cell drawn using atomic coordinates from ICSD [7].

Reducing Nb₂TiO₇ produces a double rutile-type structure of stoichiometry Nb_{1.33}Ti_{0.67}O₄. The structure is tetragonal (P4₂/mnm) space group, with a unit cell of a = 4.76Å and c = 3.00Å (Fig.4.5), consisting of chains of octahedra sharing corners (Fig.4.6). Upon reduction the theoretical unit cell density increases from 4.33 gcm⁻³ to 5.38 gcm⁻³, overall a 20% increase.

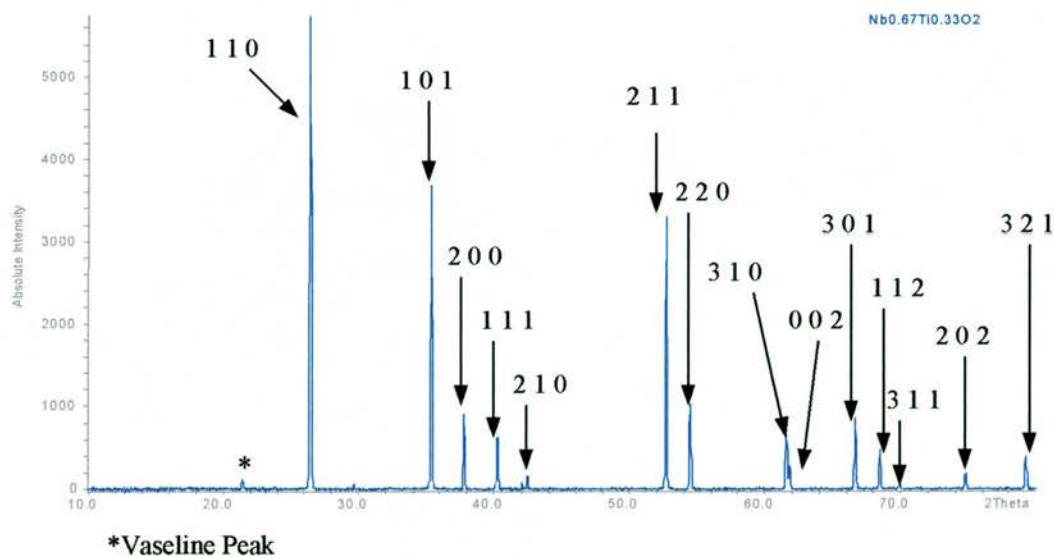


Fig.4.5 Stoe x-ray pattern for Nb_{1.33}Ti_{0.67}O₄

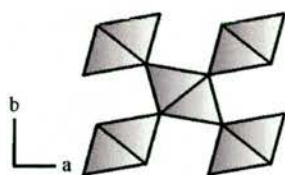


Fig.4.6 Nb_{1.33}Ti_{0.67}O₄ octahedra sharing corners

Complete oxidation of Nb_{1.33}Ti_{0.67}O₄ was achieved in 4 hours with a final mass change of 4.63%. The theoretical weight change expected for the fully reduced sample is 4.63%, indicating that one oxygen per formula unit is lost in the reduction of Nb(V) to Nb(IV) (Fig.4.7). There is no clear indication that Ti(IV) is reduced, as was also suggested by Wadsley [7]. In contrast to oxidation, reduction is a much slower process, taking a minimum of 36 hours and up to 72 hours to complete, depending on sample density, and is thus not easily monitored by TGA.

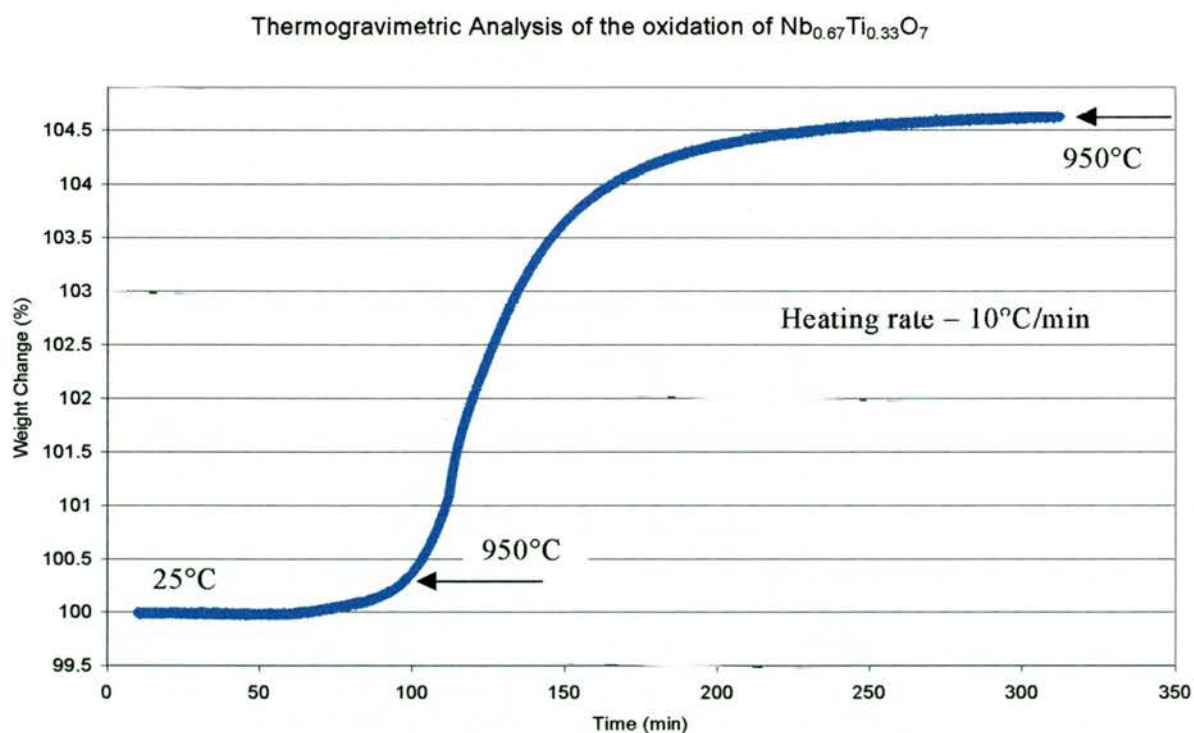


Fig.4.7 TGA oxidation run with increasing temperature in air.

Although the oxidation run in the TGA took <4 hours, the reduction run done on the Nb₂TiO₇ powder showed little reduction after 10 hours at 900°C. This shows that the kinetics of reduction are much slower than those on oxidation.

4.1.3 DC Conductivity studies

Conductivity was measured as a function of temperature in dry 5% H₂/Ar, and wet (3%H₂O) 5%H₂/Ar. Nb₂TiO₇ has a low conductivity of $4.1 \pm 0.5 \times 10^{-3} \text{ Scm}^{-1}$ in air at 900°C. When reduced in dry 5% H₂/Ar, Nb_{1.33}Ti_{0.67}O₄ is a semiconductor with a high electronic conductivity of $300 \pm 20 \text{ Scm}^{-1}$ at 900°C, in agreement with that reported by Reich et al [8].

In wet 5% H₂/Ar (10^{-16} atm), the conductivity is 40-41 Scm⁻¹ at 900°C (Fig.4.8). X-ray studies have shown that in wet hydrogen a similar phase to Nb₂TiO₇ is present with a larger unit cell of $a=20.387\text{\AA}$, $b=3.8030\text{\AA}$, $c=11.9038\text{\AA}$, $\beta=120.215^\circ$. TGA data indicated a phase with a stoichiometry of Nb₂TiO_{7- δ} , where $\delta=0.04-0.09$.

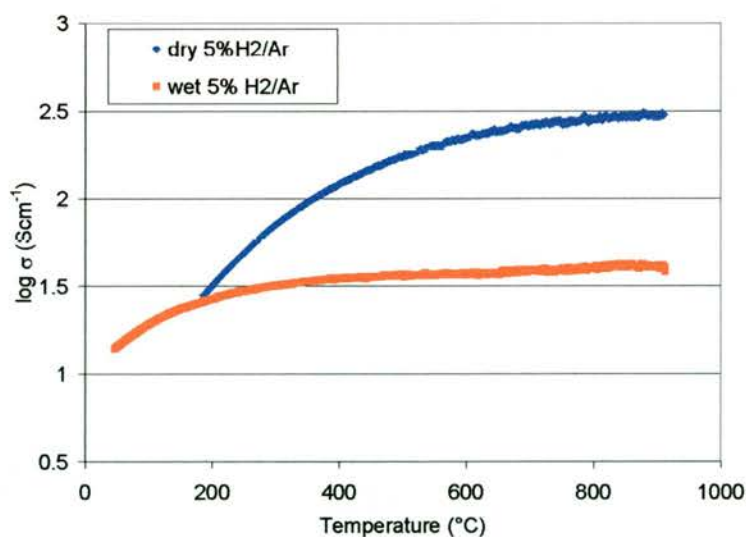


Fig.4.8 Geometry corrected conductivity plot vs temperature of Nb_{1.33}Ti_{0.67}O₄ in dry and wet hydrogen atmospheres.

Although the fully reduced sample showed a strong dependence on temperature, with a conductivity drop from 300 Scm⁻¹ at 900°C to 30-32 Scm⁻¹ at 200°C, the partially oxidised sample in 3%H₂O/5% H₂/Ar showed less dependence on temperature, with conductivity dropping from 40-41 Scm⁻¹ at 900°C to 25-27 Scm⁻¹ at 200°C. Thus the Arrhenius plot of Nb_{1.33}Ti_{0.67}O₄ (Fig.4.9) shows higher activation energy for the electronic conduction of 0.22±0.02 eV in dry hydrogen than in wet hydrogen, where activation energy is 0.09±0.01eV. The activation energies of the electronic conduction are typical of a good polaronic semiconductor.

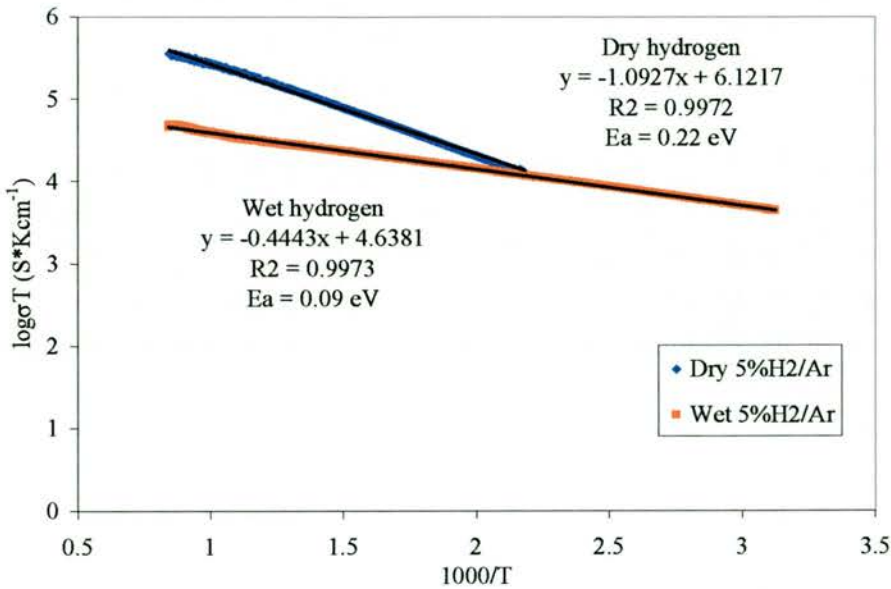


Fig. 4.9 Arrhenius plot of Nb_{1.33}Ti_{0.67}O₄ in dry and wet hydrogen atmospheres

Earlier studies [8], have shown that the conductivity dependence upon $p(\text{O}_2)$ of Nb_{1.33}Ti_{0.67}O₄, shows n-type behaviour, where on re-oxidation conductivity shows a $p(\text{O}_2)^{-1/6}$ dependence at $p(\text{O}_2) < 10^{-17}$ atm. A sharp step was observed in the conductivity at $p(\text{O}_2) = 10^{-17}$ atm, which may be indicative of the phase change due to the step in the stoichiometry of Nb_{0.67}Ti_{0.33}O₂, i.e. NbO₂ to NbO_{2.5}. The two equilibrium points measured in dry 5%H₂/Ar, at 10⁻²⁰ atm at 900°C, and wet 5%H₂/Ar, at 10⁻¹⁶ atm at 900°C, show the slope to be $p(\text{O}_2)=0.22\pm 0.01$, i.e. $p(\text{O}_2)^{-1/4}$.

In my study the $p(\text{O}_2)$ conductivity of $\text{Nb}_{0.67}\text{Ti}_{0.33}\text{O}_2$, also showed n-type conductivity. The maximum conductivity observed was 300 Scm^{-1} at 900°C and $p(\text{O}_2) = 10^{-20} \text{ atm}$. $\text{Nb}_{0.67}\text{Ti}_{0.33}\text{O}_2$ has very slow oxidation kinetics thus (Fig.4.10) shows that the oxidation run is too fast for the sample to achieve “equilibrium” at any one partial pressure.

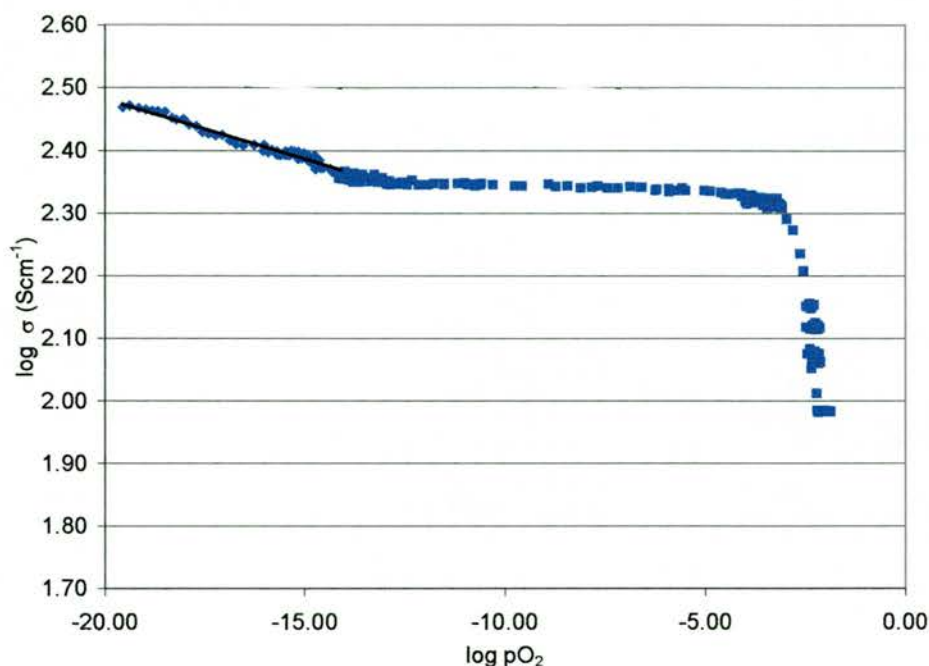


Fig.4.10 Conductivity plot of $\text{Nb}_{1.33}\text{Ti}_{0.67}\text{O}_4$ as a function of $p(\text{O}_2)$

4.1.4 Thermal expansion data

Nb_2TiO_7 exhibits a low thermal expansion coefficient (TEC) of $2.38 \pm 0.05 \times 10^{-6} \text{ K}^{-1}$ (100°C - 900°C) when sintered at 1400°C . When reduced to $\text{Nb}_{1.33}\text{Ti}_{0.67}\text{O}_4$ the TEC is increased to $3.00 \pm 0.05 \times 10^{-6} \text{ K}^{-1}$ (100°C - 900°C) (Fig.4.11 and Fig.4.12). Density studies have indicated a slight dependence of TEC on density of the sample, in which the increase in density causes a decrease in TEC of Nb_2TiO_7 . The average thermal expansion coefficient (100°C - 900°C) of Nb_2TiO_7 increases to $2.73 \pm 0.05 \times 10^{-6} \text{ K}^{-1}$ when sintered at 1200°C rather than 1400°C , and $3.74 \pm 0.05 \times 10^{-6} \text{ K}^{-1}$ when sintered at 1000°C .

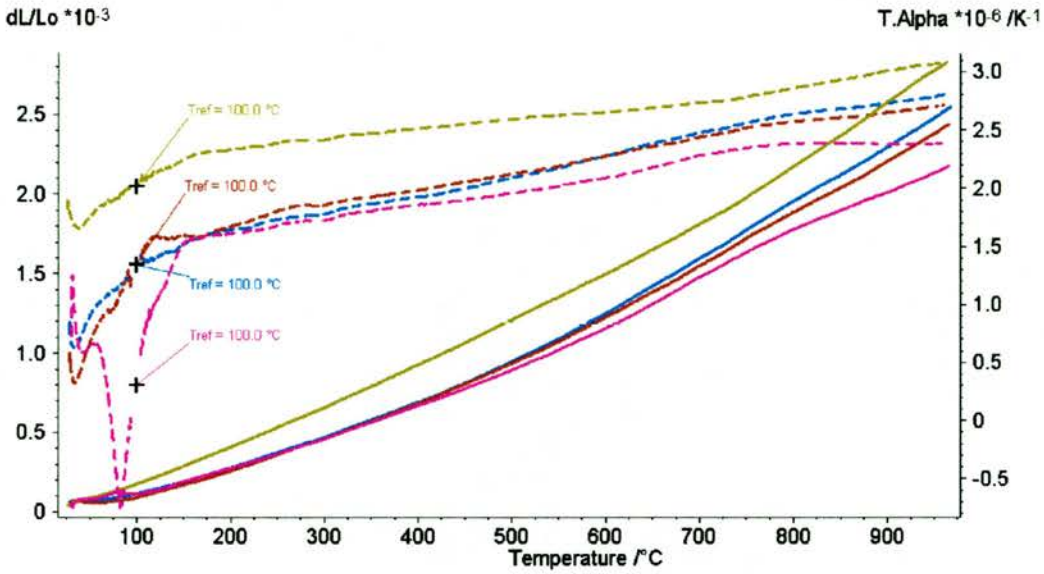


Fig.4.11 The technical α curve for Nb_2TiO_7 with different densities and $Nb_{1.33}Ti_{0.67}O_4$ rutile phase. The technical α reference temperature is $100^\circ C$.

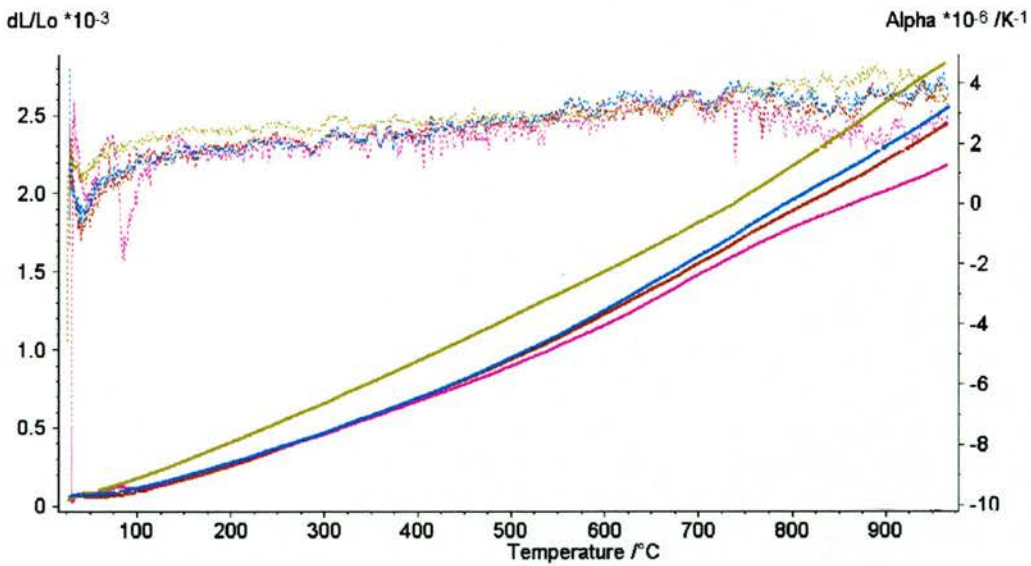


Fig.4.12 Physical α curve for Nb_2TiO_7 with different densities and $Nb_{1.33}Ti_{0.67}O_4$ rutile phase.

- Key:**
- Nb_2TiO_7 58.40% dense
 - Nb_2TiO_7 63.25% dense
 - Nb_2TiO_7 82.91% dense
 - $Nb_{1.33}Ti_{0.67}O_4$

At low densities, especially in materials with low thermal expansion coefficient, the expansion of the pellet on heating can be an important factor in the thermal expansion measurement, rather than the expansion of the unit cell. The difference in the thermal expansion coefficient can be as high as 15% between samples with high and low density. Denser samples should give a more accurate thermal expansion coefficient.

Increasing the titanium content in the structure increases the thermal expansion coefficient. Thus for Ti_{0.5}Nb_{0.5}O_{2.25} the thermal expansion $3.36 \pm 0.05 \times 10^{-6} \text{K}^{-1}$ and on reduction to a rutile structure, Ti_{0.5}Nb_{0.5}O₂, this increases to $4.48 \pm 0.05 \times 10^{-6} \text{K}^{-1}$.

The variation of α_{phys} with temperature for each sample is shown in (Fig.4.12). As was explained in Chapter 2, the physical expansion coefficient is the slope of the relative length-change curve when $T_2 - T_1 \approx 0$, i.e. $\delta T =$ infinitesimally small temperature difference:

$$\alpha_{\text{phys}}(T) = \frac{1}{L_0} \cdot \frac{\partial L(T)}{\partial T}$$

$L(T)$ = Sample length at temperature T and L_0 is the sample length at room temperature. Hence the variation of the thermal expansion coefficient with temperature as seen in (Fig.4.12) shows an overall increase in the thermal expansion coefficient (α_{phys}) until about 700°-750°C. Between 750° and 950°C the thermal expansion of the material reaches a constant steady value. This was seen to be true for samples with different density.

Fig.4.11 shows the technical alpha curve, defined as:

$$\alpha_{\text{tech}}(T) = \frac{1}{L_0} \cdot \frac{\Delta L}{\Delta T} = \frac{1}{L_0} \cdot \frac{(L(T) - L_0)}{(T - T_0)}$$

and is the average expansion coefficient for the temperature interval $T_{\text{upper}} - T_{\text{lower}}$, where T_{lower} is set to 100°C. As can be seen, the average thermal expansion increases with temperature.

4.1.5 Single Cell Testing

Tests were performed to evaluate Nb_{1.33}Ti_{0.67}O₄ as an electrolyte-supported cell anode current collector, to compare its performance with the standard Ni/8YSZ. Cells with tubular geometry were used in the form of 2mm diameter tubes. Nb₂TiO₇ cells were heated in air then reduced with 20ml/min dry H₂. Cells were then loaded at 0.7V and current versus time was measured every 30 seconds for 110 hours (Fig.4.13). At 850°C Ni/YSZ power outputs of 150-200mWcm⁻² were reached. In comparison, Nb_{1.33}Ti_{0.67}O₄ showed power output of 5.5-7.2 mWcm⁻² at 850°C, and the power output was seen to increase with time. However the electrochemical activity is not sufficient to use as a single phase anode but as a partial replacement for Ni in the Ni/YSZ cermet.

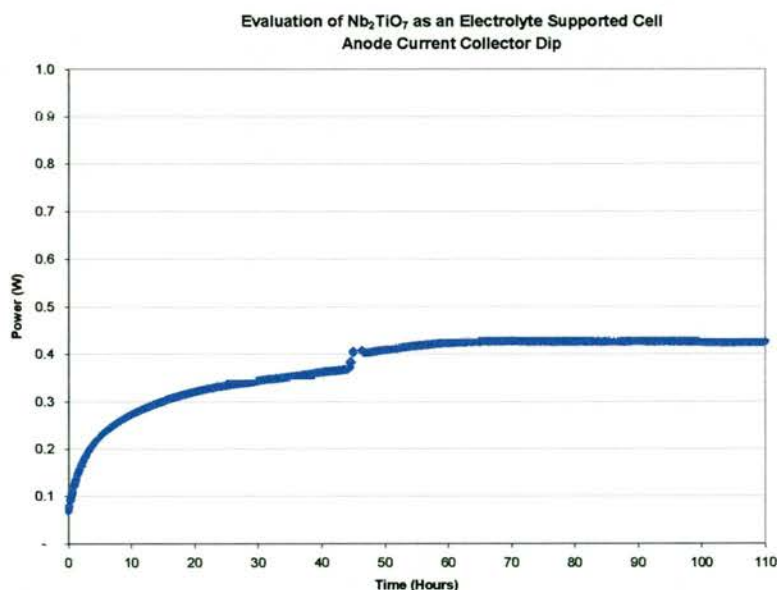


Fig.4.13 Power as a function of time in the Nb₂TiO₇ slurry dip

Although Nb_{1.33}Ti_{0.67}O₄ has much lower power output than Ni it has shown better stability at operating temperature.

Voltage-Current data were measured by fixing the voltage and recording the current between OCV and 0.2V, at 850°C, 800°C and 750°C, with gas flow rates of 20ml/min and 10 ml/min (Fig.4.14).

Although the power output shows a dependence on temperature, there seems to be little dependence on hydrogen gas flow rate, other than at a higher temperature of 850°C. As the fuel consumption does not increase significantly with an increase in gas flow rate the electrochemical processes must be rate limiting rather than the availability of fuel at the electrode.

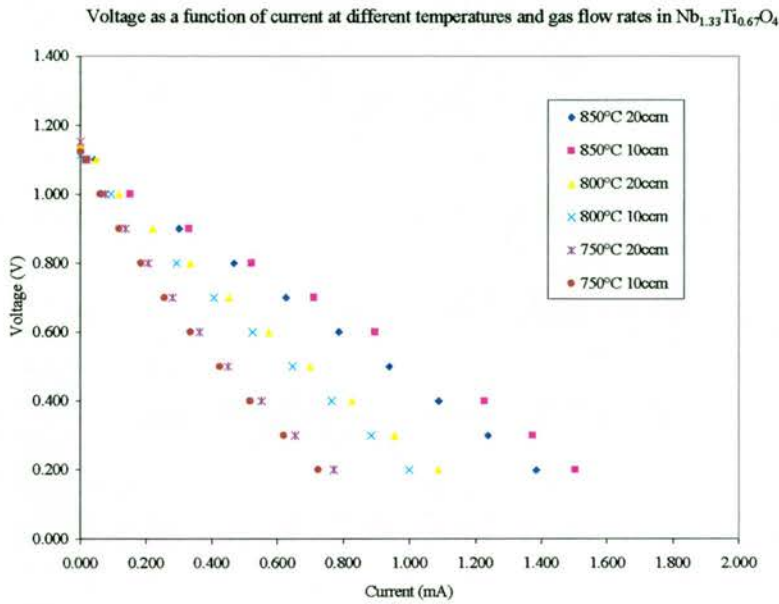


Fig. 4.14 Current as a function of voltage at different temperatures and hydrogen flow rates

4.1.6 Doping of Nb₂O₅-TiO₂

As already mentioned, although the electronic conductivity of Nb_{1.33}Ti_{0.67}O₄ is favourable for use as a fuel cell current collector the thermal expansion is rather low, with $3.00 \pm 0.05 \times 10^{-6} \text{ K}^{-1}$ (100-900°C). To compare that with other fuel cell components:

$$\text{YSZ} \text{ -----} 10.3 \times 10^{-6} \text{ K}^{-1}$$

$$\text{NiO} \text{ -----} 14.1 \times 10^{-6} \text{ K}^{-1}$$

$$\text{Ni metal} \text{ -----} 16.9 \times 10^{-6} \text{ K}^{-1}$$

$$30\% \text{ Ni/YSZ} \text{ --} 12.5 \times 10^{-6} \text{ K}^{-1}$$

A match in TEC between the fuel cell components is required in order to avoid cracking and separation between components at high operating temperatures of 700-900°C.

Doping is a common way of modifying the properties of materials, from conductivity to sinterability and thermal expansion, thus attempts have been made to dope Nb_{1.33}Ti_{0.67}O₄ with Zr, Fe, Ce and V.

4.2 Nb₂O₅-TiO₂-ZrO₂ system

4.2.1 Structure

Although the structure of doped Nb₂TiO₇ does not change, doping Nb₂TiO₇ with Zr increases the unit cell of oxidised and reduced materials almost linearly with dopant concentration (Fig.4.15). The least squares refinement performed on Nb₂Ti_{1-x}Zr_xO₇, using previously refined Nb₂TiO₇ values as starting values, showed an increase in the size of the unit cell with increasing Zr content; this is as would be expected from the ionic radius of Zr⁴⁺ (0.72Å, CN=6), which is larger than the ionic radius of Ti⁴⁺ (0.60Å, CN=6), that is being replaced (Table 4.1). No additional phases were observed for any samples up to 25% Zr dopant level.

Table 4.1 Refined unit cell parameters and thermal expansion coefficient of Zr doped Nb₂TiO₇

sample	a	b	c	β	V	TEC 300-900°C 10 ⁻⁶ K ⁻¹ (±0.05)
Nb ₂ TiO ₇	20.3610(11)	3.7988(2)	11.8861(5)	120.194(3)	794.63(9)	2.59
Nb ₂ Ti _{0.95} Zr _{0.05} O ₇	20.4104(10)	3.8061(2)	11.9160(5)	120.201(2)	800.03(8)	2.74
Nb ₂ Ti _{0.90} Zr _{0.10} O ₇	20.4328(10)	3.8079(2)	11.9308(6)	120.205(3)	802.25(9)	3.53
Nb ₂ Ti _{0.85} Zr _{0.15} O ₇	20.4878(15)	3.8144(3)	11.9646(8)	120.208(3)	808.05(14)	2.85
Nb ₂ Ti _{0.80} Zr _{0.20} O ₇	20.5055(14)	3.8168(2)	11.9718(8)	120.215(4)	810.34(11)	1.72
Nb ₂ Ti _{0.75} Zr _{0.25} O ₇	20.5381(10)	3.8213(2)	11.9940(6)	120.219(2)	813.39(9)	3.33
Nb ₂ Ti _{0.50} Zr _{0.50} O ₇	}	Multiphase with Nb ₂ O ₅ -TiO ₂ -ZrO ₂ phases				3.53
Nb ₂ Ti _{0.25} Zr _{0.75} O ₇						3.12
Nb ₂ ZrO ₇						3.81

The saturation point for substitution of ZrO₂ into Nb₂TiO₇ is ~25% after which other phases including ZrO₂ are seen in the samples.

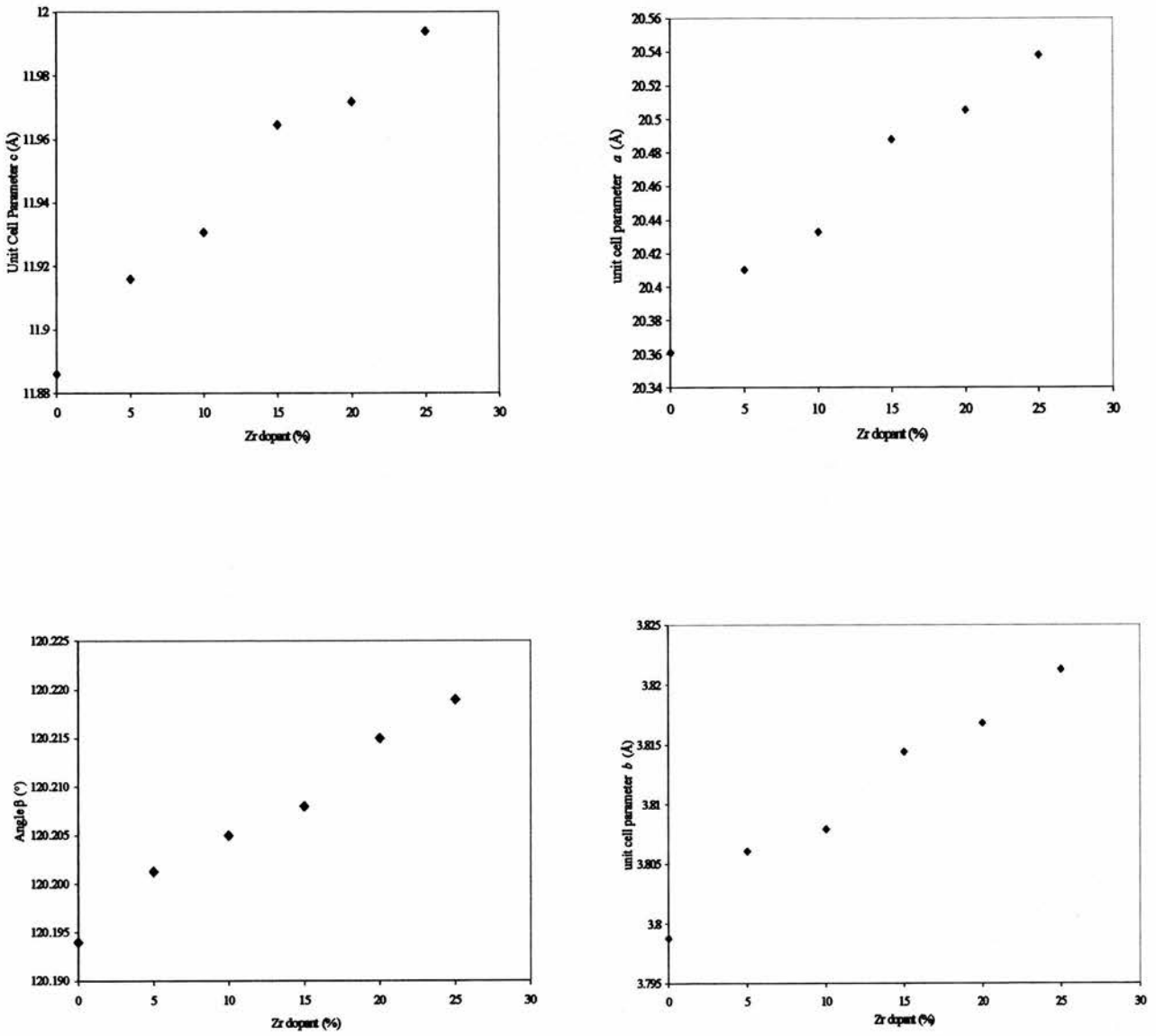


Fig.4.15 Change in the unit cell parameters β , a , b and c with increasing Zr doping

There is no clear and simple relationship between the unit cell size and the thermal expansion coefficient. Doping with Zr shows little change in the thermal expansion coefficient, and this seems to be independent of the unit cell size (Table 4.1).

Although substituting Ti by Zr produced single phase samples, substituting Nb by Zr, i.e. Nb_{2-x}TiZr_xO_{7-y} introduces oxygen vacancies into the structure. This deviation from the oxygen stoichiometry produced additional TiO₂ rutile phase (Fig.4.16), as indicated by the peak at 27.2° 2θ. Table 4.2 shows the unit cell parameters of Nb_{2-x}TiZr_xO_{7-y} and Nb₂Ti_{1-x}Zr_xO₇ to be increasing with dopant concentration.

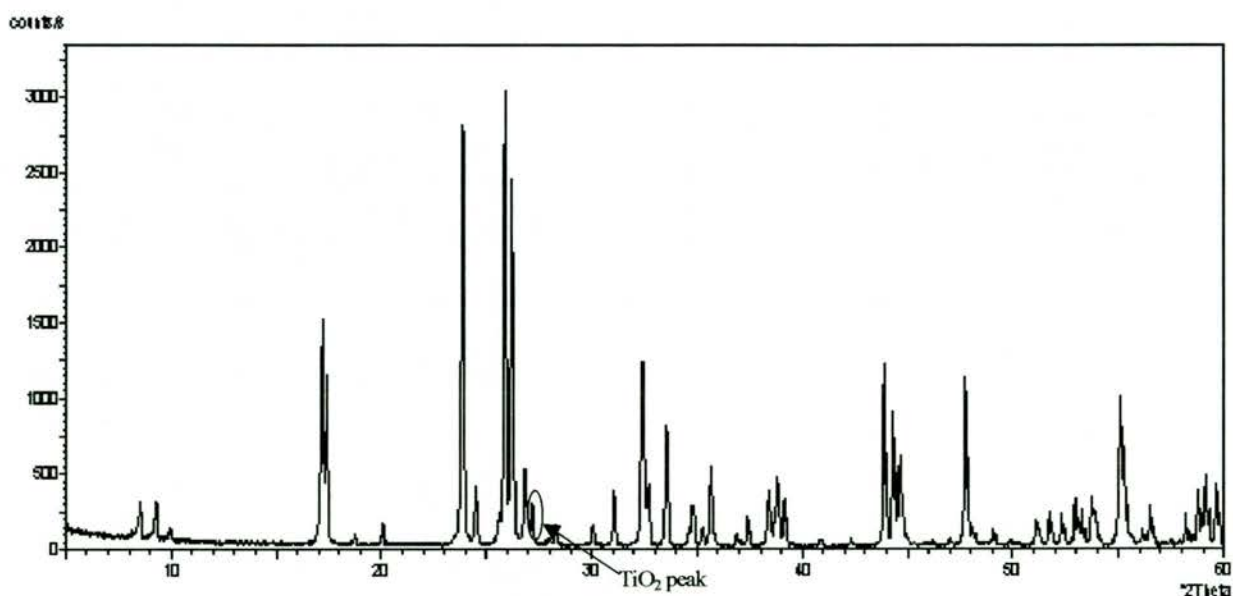


Fig. 3.20

Fig. 4.16 Philips X-ray pattern for Nb_{1.90}TiZr_{0.1}O_{6.95}

Table 4.2 Refined unit cell parameters of Zr doped Nb₂TiO₇ showing the unit cell of Zr substituted for Ti (black) and Zr substituted for Nb (blue)

	a	b	c	β	V
Nb ₂ TiO ₇	20.3610(11)	3.7988(2)	11.8861(5)	120.194(3)	794.63(9)
Nb ₂ Ti _{0.95} Zr _{0.05} O ₇	20.4104(10)	3.8061(2)	11.9160(5)	120.201(2)	800.03(8)
Nb _{1.90} TiZr _{0.10} O _{6.95}	20.4166(12)	3.8063(2)	11.9190(7)	120.185(3)	800.64(10)
Nb ₂ Ti _{0.80} Zr _{0.20} O ₇	20.4855(14)	3.8128(2)	11.9618(8)	120.219(4)	807.34(11)
Nb _{1.80} TiZr _{0.20} O _{6.90}	20.4598(22)	3.8111(5)	11.9464(14)	120.168(6)	805.35(20)

On reduction of Nb_{1.90}TiZr_{0.1}O_{6.95} no TiO₂ rutile phase was observed (Fig.4.17), indicating that Zr is incorporated into the structure with no significant increase in the unit cell (Table 4.3), and may be replacing Ti in the structure. This is due to similar ionic radii of Nb(IV) and Zr (IV) of 0.69Å and 0.72Å respectively.

Table 4.3 Refined unit cell parameters of Zr doped Nb₂TiO₇ and reduced at 900°C

	Nb _{1.33} Ti _{0.67} O ₄	Nb _{1.27} Ti _{0.67} Zr _{0.06} O ₄
Symmetry	<i>Tetragonal P</i>	<i>Tetragonal P</i>
Cell a	4.7563 (3)	4.7597 (5)
Cell c	2.9983 (2)	3.0088 (3)
Cell Volume	67.830 (11)	68.165 (15)
Space group	P4 ₂ /mm	P4 ₂ /mm

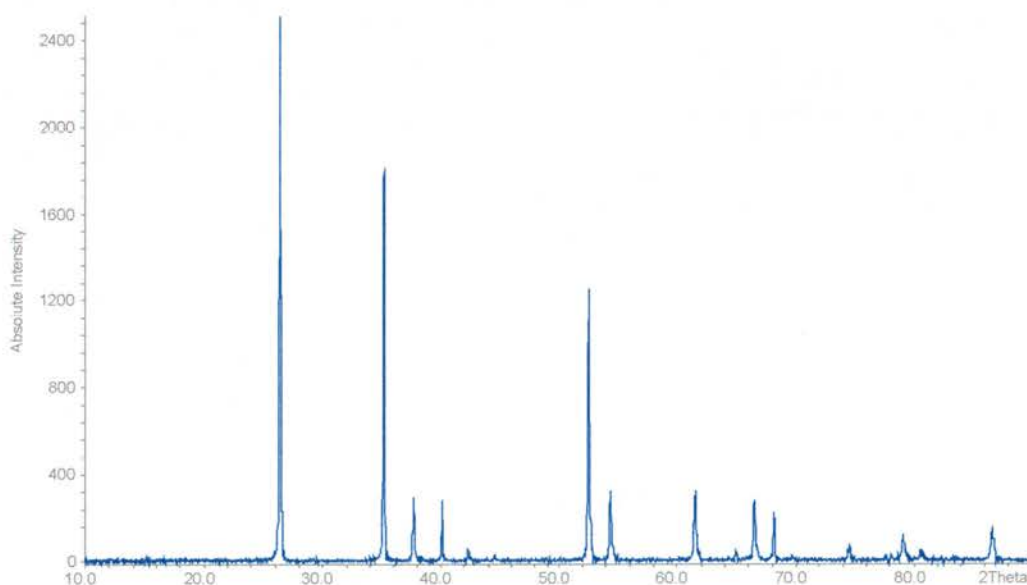


Fig.4.17 Philips X-ray pattern for Nb_{1.27}Ti_{0.67}Zr_{0.06}O₄

Reduction of Nb₂Ti_{1-x}Zr_xO₇, as in the parent Nb₂TiO₇ structure, produces a superstructure based on a rutile-type subcell, with a space group of P4₂/mm and the general formula of Nb_{1.33}Ti_{0.67-x}Zr_xO₄ (Table 4.4). As is observed with the oxidised samples there is an increase in the size of the unit cell with increasing Zr content. No additional phases were observed with powder diffraction x-ray technique (Fig.4.17).

Table 4.4 Refined unit cell parameters and thermal expansion coefficient of Zr doped
 $Nb_{1.33}Ti_{0.67}O_4$

	%Zr	a	c	V	c/a	TEC 300-900°C 10 ⁻⁶ K ⁻¹ (±0.05)
$Nb_{1.333}Ti_{0.667}O_4$	0	4.7563(3)	2.9983(2)	67.830(11)	0.6303	3.21
$Nb_{1.333}Ti_{0.634}Zr_{0.033}O_4$	5	4.7623(4)	3.0033(3)	68.112(13)	0.6306	3.20
$Nb_{1.333}Ti_{0.600}Zr_{0.067}O_4$	10	4.7639(7)	3.0111(5)	68.233(24)	0.6320	6.27
$Nb_{1.333}Ti_{0.567}Zr_{0.100}O_4$	15	4.7726(3)	3.0186(2)	68.755(11)	0.6324	6.09
$Nb_{1.333}Ti_{0.534}Zr_{0.133}O_4$	20	4.7739(10)	3.0147(6)	68.71(3)	0.6314	5.21

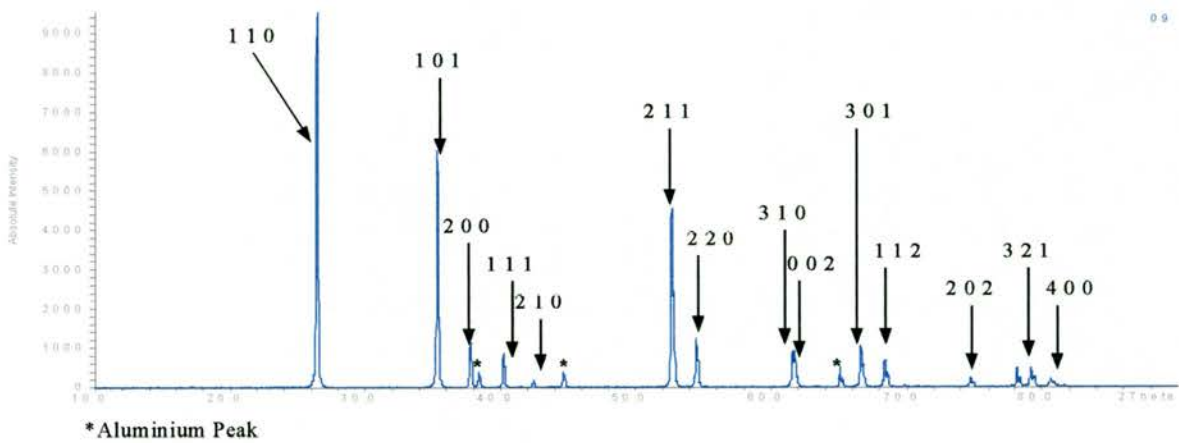


Fig. 4.18 Powder diffraction x-ray pattern for $Nb_{1.33}Ti_{0.634}Zr_{0.033}O_4$

The unit cell parameters of the rutile phases show a linear increase with the dopant concentration. This is as would be expected from Vegard's law which expects the larger size of the doping cation, in this case Zr, to increase the interatomic distance in the unit cell. The unit cell parameter a increases with Zr dopant and shows a slight deviation when Zr =10%, and starts to level off at 20% (Fig.4.19).

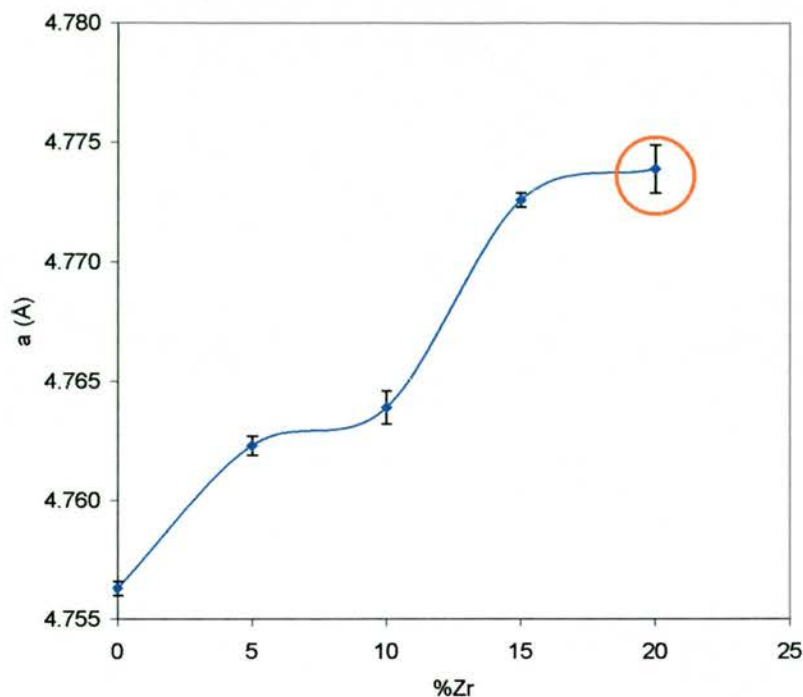


Fig.4.19 Unit cell parameter a as a function of %Zr doping. Red circle shows a 2 phase region

The unit cell parameter c , however, shows a linear increase with dopant concentration up to 15% ZrO₂, but then drops at 20%ZrO₂ (Fig.4.20). The x-ray diffraction showed a presence of ZrO₂ peaks. Thus where as the saturation point for the ZrO₂ doping for the oxidised sample was ~25%, for the reduced rutile structure, the saturation point seems to be ~15%. The edge-sharing c axis in the rutile structure seems to be affected more than the a/b plane with excess ZrO₂, however more thorough x-ray and possibly neutron data is required. No further work was done on structures with higher Zr doping.

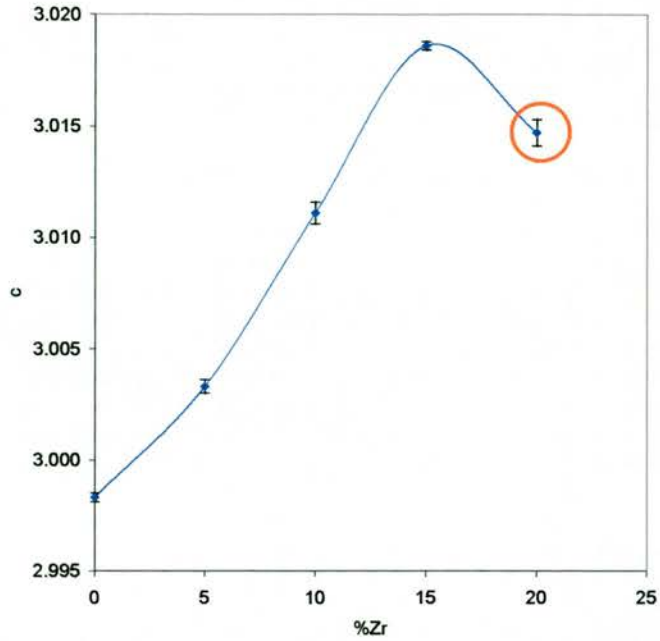


Fig.4.20 Unit cell parameter c as a function of %Zr. Red circle shows a 2 phase region

Unit cell volume is also seen to expand in line with the increase in unit cell parameters a and c (Fig.4.21). There is again a drop in the unit cell volume at 20% Zr, and the volume is similar to the 15% Zr, again indicating the saturation point at 15% dopant concentration. The ratio of unit cell parameter c/a increases as a function of dopant concentration, indicating that the expansion is not isotropic and is larger in the c direction. Up to 20% doping, in which there is a decrease in the c/a ratio (Fig.4.22), again indicating that ZrO₂ may not be accepted into the structure due to edge-sharing in the rutile system.

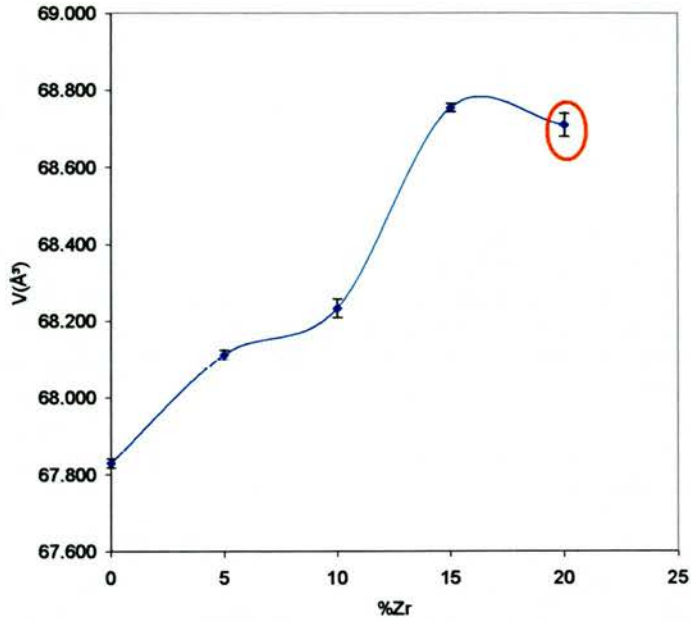


Fig.4.21 Unit cell volume as a function of %Zr. Red circle shows a 2 phase region

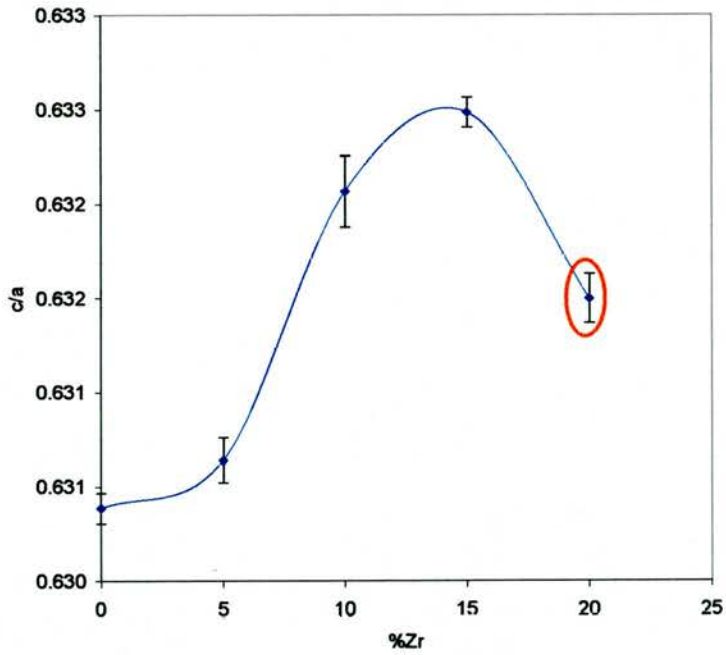


Fig.4.22 The ratio of unit cell parameter c/a as a function of %Zr. Red circle shows a 2 phase region

4.2.2 Conductivity

The conductivity for all doped samples is predominantly electronic, just as for Nb_{1.33}Ti_{0.67}O₄. In 5%H₂/Ar there is at first a gradual, then a rapid drop in the conductivity. After 10% doping, there is a gradual increase in the conductivity.

The decrease in conductivity may be due to one or more of several factors, such as density effects, defect ordering, or possibly due to the increase in the unit cell causing an increase in the distance between Nb atoms. As the conductivity is probably due to Nb electrons in the t_{2g} orbital hopping from one Nb to another, an increase in the unit cell will tend to have negative effects on the conductivity. There is also a break in the conducting M-M *d* orbitals overlap along the *c* axis due to the presence of Zr atoms.

In wet 5% H₂/Ar, p(O₂)=10⁻¹⁶, there is an initial increase in the conductivity at 5% doping, followed by a rapid decrease. The initial increase in the conductivity may be due to the importance of other factors such as density effects and the contribution of grain boundaries to the electronic conductivity at low dopant concentrations. Electronic conductivity shows a maximum at *x* = 0, with 300 Scm⁻¹ at 900°C in dry 5%H₂/Ar (Fig.4.23).

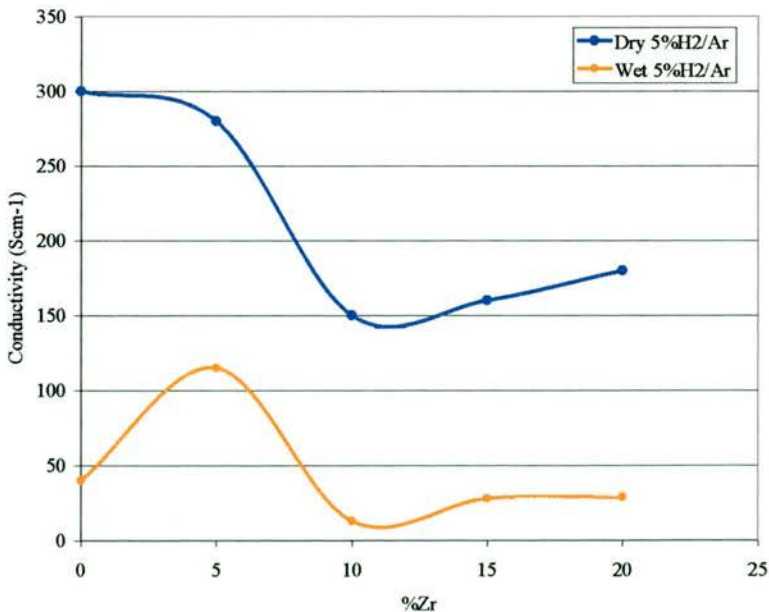


Fig.4.23 Conductivity of Nb_{1.33}Ti_{0.67-x}Zr_xO₄ as a function of dopant concentration

The slopes for the conductivity versus $p(\text{O}_2)$ of each sample, in the region of $p(\text{O}_2)=10^{-20}$ - 10^{-16} atm., are shown in Table 4.5. There is a general trend for all samples to have a slope of $-1/4$ or $-1/5$, except for the 5% doped sample, which shows a very low dependence on the $p(\text{O}_2)$ up to $p(\text{O}_2)=10^{-16}$ atm.

Table 4.5 Slopes for doped $\text{Nb}_{1.33}\text{Ti}_{0.67}\text{O}_4$ between 10^{-20} - 10^{-16} atmospheres

	%Zr	$\sigma \text{ Scm}^{-1} 10^{-20} \text{ atm}$	$\sigma \text{ Scm}^{-1} 10^{-16} \text{ atm}$	$P(\text{O}_2)$ dependence $10^{-20} - 10^{-16} \text{ atm} (\pm 0.02)$
$\text{Nb}_{1.333}\text{Ti}_{0.667}\text{O}_4$	0	300	40	-0.22
$\text{Nb}_{1.333}\text{Ti}_{0.634}\text{Zr}_{0.033}\text{O}_4$	5	280	115	-0.10
$\text{Nb}_{1.333}\text{Ti}_{0.600}\text{Zr}_{0.067}\text{O}_4$	10	150	13	-0.26
$\text{Nb}_{1.333}\text{Ti}_{0.567}\text{Zr}_{0.100}\text{O}_4$	15	160	28	-0.19
$\text{Nb}_{1.333}\text{Ti}_{0.534}\text{Zr}_{0.133}\text{O}_4$	20	180	29	-0.20

4.2.3 Thermal Expansion Coefficient

The thermal expansion of these samples was seen to increase up to 3 times from the oxidised to the reduced samples (Fig.4.24). Of the oxidised samples $\text{Nb}_2\text{Ti}_{0.90}\text{Zr}_{0.10}\text{O}_7$ shows the best thermal expansion of $3.53 \pm 0.05 \times 10^{-6} \text{ K}^{-1}$ between 300°C and 900°C in air, however, when fully reduced the 15% doped sample shows the highest expansion of $6.09 \pm 0.05 \times 10^{-6} \text{ K}^{-1}$ from 300°C in 5% H_2/Ar ($p\text{O}_2=10^{-20}$ atm) (Table 4.6).

Table 4.6 Thermal expansion coefficients of $\text{Nb}_2\text{Ti}_{1-x}\text{Zr}_x\text{O}_7$ when oxidised and fully reduced

	TEC 300-900°C $10^{-6}\text{K}^{-1} (\pm 0.05)$	%Zr	Reduced Sample	TEC 300-900°C $10^{-6}\text{K}^{-1} (\pm 0.05)$
Nb_2TiO_7	2.59	0	$\text{Nb}_{1.33}\text{Ti}_{0.667}\text{O}_4$	3.21
$\text{Nb}_2\text{Ti}_{0.95}\text{Zr}_{0.05}\text{O}_7$	2.74	5	$\text{Nb}_{1.33}\text{Ti}_{0.634}\text{Zr}_{0.033}\text{O}_4$	3.20
$\text{Nb}_2\text{Ti}_{0.90}\text{Zr}_{0.10}\text{O}_7$	3.53	10	$\text{Nb}_{1.33}\text{Ti}_{0.600}\text{Zr}_{0.067}\text{O}_4$	5.48
$\text{Nb}_2\text{Ti}_{0.85}\text{Zr}_{0.15}\text{O}_7$	2.85	15	$\text{Nb}_{1.33}\text{Ti}_{0.567}\text{Zr}_{0.100}\text{O}_4$	6.09
$\text{Nb}_2\text{Ti}_{0.80}\text{Zr}_{0.20}\text{O}_7$	1.72	20	$\text{Nb}_{1.33}\text{Ti}_{0.534}\text{Zr}_{0.133}\text{O}_4$	5.21

The thermal expansion of Nb₂Ti_{1-x}Zr_xO₇ initially increases with increasing dopant concentration, but then drops rapidly (Fig.4.24). Upon reduction all samples showed an increase in thermal expansion, with the greatest increase shown by the reduced 15% Zr doped Nb₂TiO₇, i.e. Nb_{1.33}Ti_{0.57}Zr_{0.10}O₄, with the maximum thermal expansion coefficient of $6.09 \pm 0.05 \times 10^{-6} \text{K}^{-1}$ at 300°-900°C and $5.99 \pm 0.05 \times 10^{-6} \text{K}^{-1}$ at 900°C. Thermal expansion is then seen to drop at 20%Zr, which could be related to the decrease in unit cell volume, i.e. less open structure.

The physical α curve (Fig.4.25) shows that the thermal expansion increases with temperature for all samples except for the 15% Zr doped, which shows a gradual decrease in the thermal expansion coefficient with temperature.

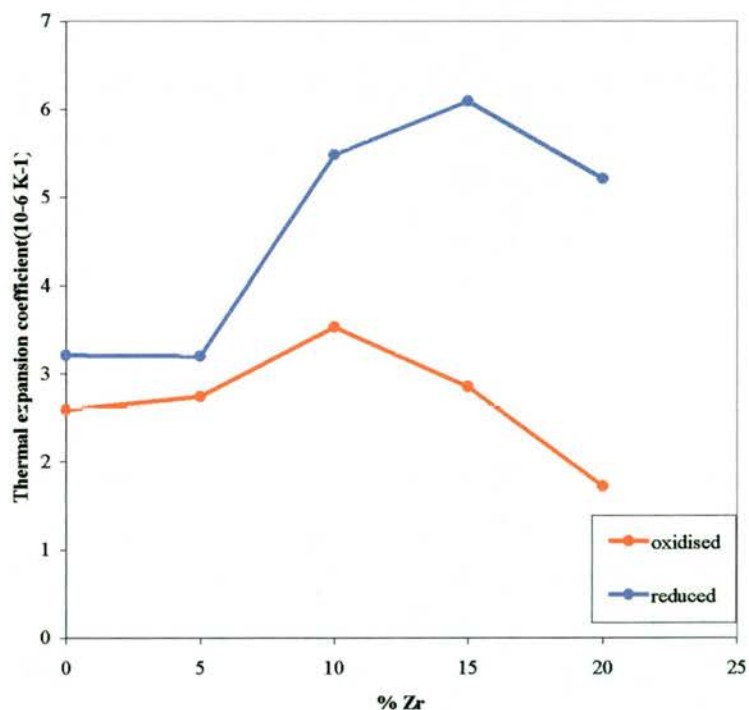


Fig.4.24 Thermal expansion coefficient from 300°-900°C, of Zr doped Nb₂TiO₇ when oxidised (red) and when reduced to a rutile structure Nb_{1.33}Ti_{0.67}O₄ (blue)

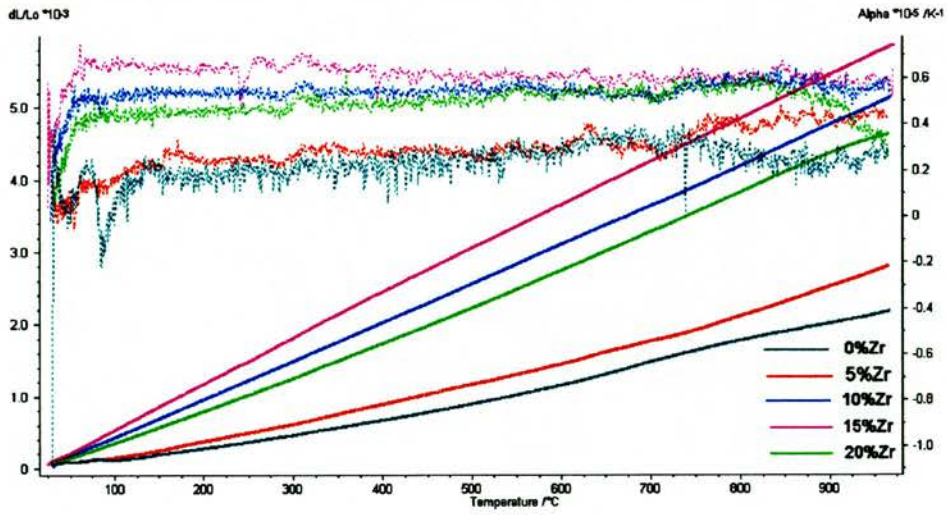


Fig.4.25 Physical α heating curve for Zr doped $\text{Nb}_{1.33}\text{Ti}_{0.67}\text{O}_2$

4.3 Nb₂O₅-TiO₂-Fe₂O₃ system

4.3.1. Structure

Compounds with the general formula of Nb_{2+x}Ti_{1-2x}Fe_xO₇ were synthesised and their structure, conductivity and thermal expansion studied in their oxidised and reduced forms. In order to maintain oxygen stoichiometry, 1 Fe and 1Nb were substituted for 2 Ti. Iron is readily incorporated into the structure with no additional phases being present. Doping with Fe(III) increases the unit cell of both the oxidised and the reduced material linearly with dopant concentration (Table 4.7). The increase, however is small compared to Zr doped materials, because the ionic radius of Fe(III) is 0.64Å, similar to that of Nb and Ti, and is significantly smaller than that of Zr. As such the thermal expansion of these oxidised samples changes little with addition of Fe, being around 2.0x10⁻⁶K⁻¹ from 300°-900°C. The saturation point seems to be lower than for Zr doped samples at 10% for the oxidised system.

Table 4.7 Refined unit cell parameters and thermal expansion coefficient of doped



	a	b	c	β	V	TEC 300-900°C 10 ⁻⁶ K ⁻¹ (± 0.05)
Nb ₂ TiO ₇	20.3610(11)	3.7988(2)	11.8861(5)	120.194(3)	794.63(9)	2.38
Nb _{2.025} Ti _{0.95} Fe _{0.025} O ₇	20.3823(11)	3.8026(2)	11.8984(6)	120.202(3)	797.01(9)	2.24
Nb _{2.05} Ti _{0.90} Fe _{0.05} O ₇	20.3960(11)	3.8055(2)	11.9057(5)	120.202(2)	798.65(9)	2.00
Nb _{2.10} Ti _{0.80} Fe _{0.10} O ₇	20.4067(14)	3.8082(3)	11.9143(8)	120.212(4)	800.13(12)	2.20
Nb _{2.20} Ti _{0.60} Fe _{0.20} O ₇	Complex, multiphase system					1.73

Reduction of these samples produces rutile-type structure with a space group of P4₂/mmn, with the general formula of Nb_{1.33+y}Ti_{0.67-2y}Fe_yO₄. Again there is an increase in the unit cell size with increasing Fe content (Table 4.8). However, this time it is comparable to the unit cell shown by the Zr doping, although a little higher, which is probably due to an increase in the size of the Fe ionic radius with partial reduction.

The increase in the unit cell size is not isotropic (Table 4.8), with a larger increase occurring in the a axis (Fig.4.26). The increase in the a axis is linear with y in the Nb_{1.33+y}Ti_{0.67-2y}Fe_yO₄ system.

Table 4.8 Unit cell parameters and thermal expansion coefficient for Nb_{1.33+y}Ti_{0.67-2y}Fe_yO₄

	a	c	V	TEC 100-900°C 10 ⁻⁶ K ⁻¹ (+0.05)
Nb _{1.333} Ti _{0.667} O ₄	4.7563(3)	2.9983(2)	67.830(11)	3.01
Nb _{1.347} Ti _{0.639} Fe _{0.014} O ₄	4.7575(6)	3.0016(3)	67.963(17)	6.28
Nb _{1.362} Ti _{0.609} Fe _{0.029} O ₄	4.7607(3)	2.9975(2)	68.022(10)	4.93
Nb _{1.390} Ti _{0.553} Fe _{0.057} O ₄	4.7649(5)	3.0037(3)	68.197(15)	5.00
Nb _{1.447} Ti _{0.439} Fe _{0.114} O ₄	4.7753(8)	3.0076(4)	68.581(13)	4.23

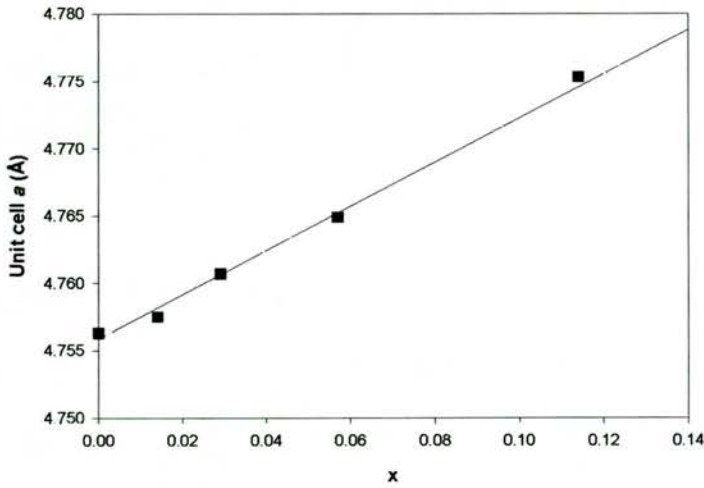


Fig.4.26 Unit cell parameter a as a function of dopant concentration y for Nb_{1.33+y}Ti_{0.67-2y}Fe_yO₄.

4.3.2 Conductivity

DC conductivity studies were also carried out as a function of temperature and dopant concentration. The conductivity of the reduced forms seems predominantly electronic, just as for Nb_{1.33}Ti_{0.67}O₄. It initially decreases with doping followed by an increase to a maximum at $y = 0.057$ for Fe doped samples, with 280 Scm⁻¹ at 900°C (Fig.4.27), but then decreases with increasing dopant concentration; dropping to 200 Scm⁻¹.

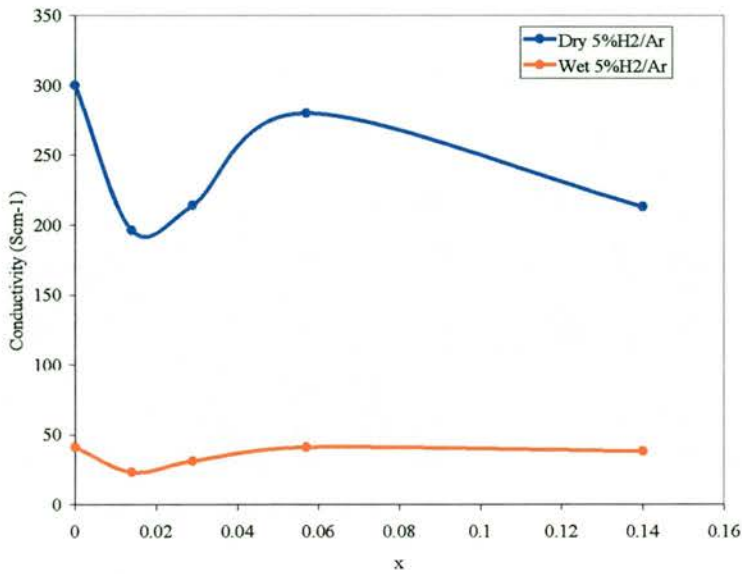


Fig.4.27 Conductivity plot for Nb_{1.33+y}Ti_{0.67-2y}Fe_yO₄ in dry and wet 5% H₂/Ar at 900°C

The change in the activation energies with doping is very small. The smallest activation energy, 0.18±0.01eV, is observed in the 2.5% Fe doped sample (Table 4.9), while the highest activation energy was shown by 20% Fe doped sample with 0.24±0.01eV. There was no significant difference in the activation energies in samples run in wet hydrogen; the activation energies being between 0.07-0.09eV. As with Nb_{1.33}Ti_{0.67}O₄ all the doped samples show very low activation energies.

Table 4.9 Showing the activation energies for Nb_{1.33+y}Ti_{0.67-2y}Fe_yO₄ in wet and dry hydrogen

Fe dopant level(%)	E _a (eV) in dry 5%H ₂ /Ar (±0.01)	Wet E _a (eV) in wet 5%H ₂ /Ar (±0.01)
0	0.22	0.09
2.5	0.18	0.07
5	0.22	0.08
10	0.21	0.08
20	0.24	0.08

Fig. 4.28 Slopes for Fe doped Nb_{1.33}Ti_{0.67}O₄ between 10⁻²⁰-10⁻¹⁶ atmospheres

	σ Scm ⁻¹ 10 ⁻²⁰ atm at 900°C	σ Scm ⁻¹ 10 ⁻¹⁶ atm at 900°C	Log p(O ₂) dependence 10 ⁻²⁰ - 10 ⁻¹⁶ atm (±0.02)
Nb _{1.333} Ti _{0.667} O ₄	300	40	-0.22
Nb _{1.347} Ti _{0.639} Fe _{0.014} O ₄	196	23	-0.23
Nb _{1.362} Ti _{0.609} Fe _{0.029} O ₄	214	31	-0.21
Nb _{1.390} Ti _{0.553} Fe _{0.057} O ₄	280	41	-0.21
Nb _{1.447} Ti _{0.439} Fe _{0.114} O ₄	213	38	-0.19

There is very little difference in the electronic conductivity of the samples in 5% wet H₂/Ar, and the slopes are around -1/5 as a function of p(O₂) (Fig.4.28), between 10⁻²⁰ and 10⁻¹⁶ atm.

4.3.3 Thermal Expansion Coefficient

There seems to be no simple relation between the composition and thermal expansion coefficient in this system. Thermal expansion of oxidised samples decreases with dopant concentration. The small change in the thermal expansion of the oxidised sample with doping is reflected by the previously mentioned small change in the unit cell size. As such we can conclude that there is no significant change in the thermal expansion coefficient with doping for the oxidised sample.

Once reduced, however, the samples exhibit a large increase in TEC. Initially thermal expansion increases with doping but, like conductivity, decreases at higher dopant concentrations. Thermal expansion of $6.28 \pm 0.05 \times 10^{-6} \text{ K}^{-1}$ was achieved for 2.5% Fe doped sample measured in 5%H₂/Ar (Fig.4.31), but once oxidised the thermal expansion is reduced to $2.24 \pm 0.05 \times 10^{-6} \text{ K}^{-1}$ in air. This three-fold reduction would be very problematic under the operation conditions of the fuel cell. As can be seen from (Fig.4.29), there is a large change in the unit cell volume with reduction, but due to the difference in the thermal expansion, this change decreases with temperature (Fig.4.30). As the anode current collector, it will be made in air and then reduced in situ, thus a large increase in thermal expansion would cause large thermal stresses and cracking in the fuel cell.

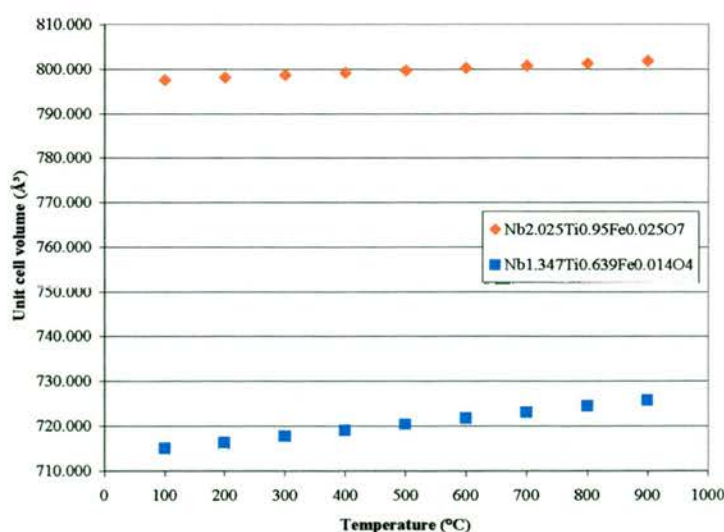


Fig.4.29 Unit cell volume change with temperature for $\text{Nb}_{2.025}\text{Ti}_{0.95}\text{Fe}_{0.025}\text{O}_7$ and $\text{Nb}_{1.347}\text{Ti}_{0.639}\text{Fe}_{0.014}\text{O}_4$

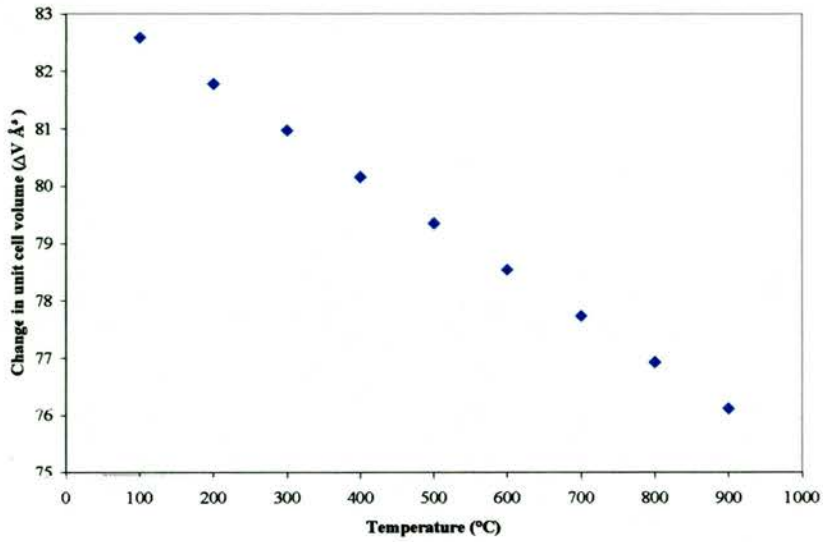


Fig. 4.30 Change in unit cell volume with reduction as a function of temperature
(V of $Nb_{2.025}Ti_{0.95}Fe_{0.025}O_7$ - V of $Nb_{1.347}Ti_{0.639}Fe_{0.014}O_4$)

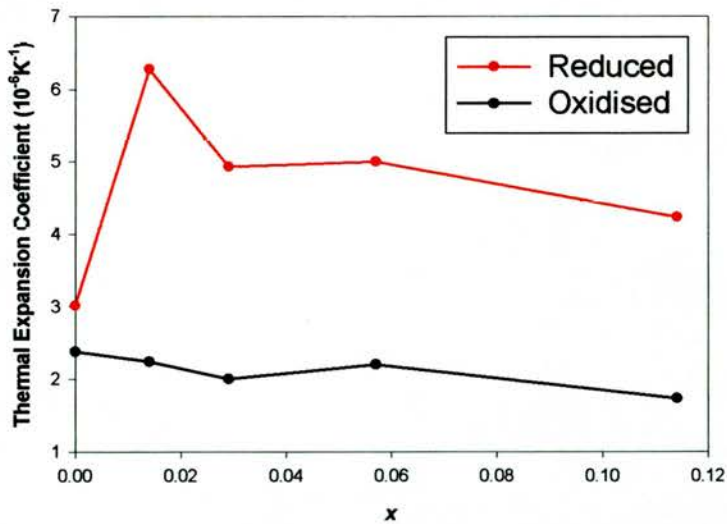


Fig. 4.31 Thermal expansion coefficient (100°C-900°C) of Fe doped Nb₂TiO₇ when fully oxidised and reduced

4.4 Nb₂O₅-TiO₂-CeO₂ system

4.4.1 Doping Nb₂TiO₇ with CeO₂

CGO as a mixed conductor offers a possible replacement for YSZ in the anode. As such, a possible doping of Nb₂TiO₇ with Ce may be of promise. Compounds with the composition Nb₂Ti_{1-x}Ce_xO_{7+y} were thus synthesised under a range of different sintering conditions. No single phase, however was achieved (Fig.4.32). This is probably due to a number of reasons. The much larger size of Ce (0.80Å) compared to Ti (0.61Å) and Nb (0.64Å), means that any substitution by Ce on a Ti or Nb site is very difficult. In these patterns TiO₂ rutile phase was observed, along with Ce₂O₃ (*) and CeNbO₄ (+).

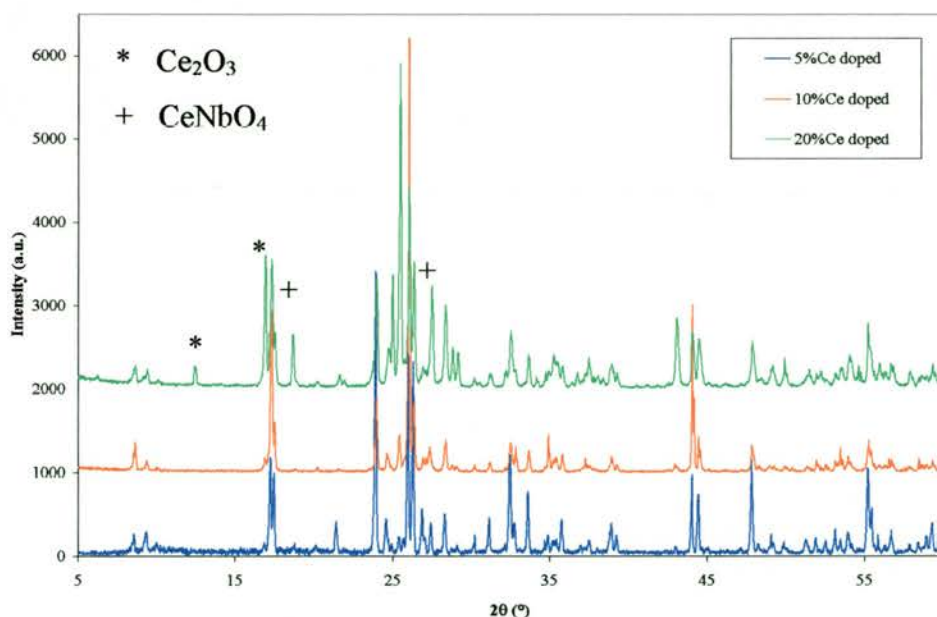


Fig.4.32 X-ray data of 5%, 10% and 20% Ce doped Nb₂TiO₇

Table 4.10 Refined unit cell parameters of doped Nb₂TiO₇

	a	b	c	β	V
Nb ₂ TiO ₇	20.3610(11)	3.7988(2)	11.8861(5)	120.194(3)	794.63(9)
Nb ₂ Ti _{0.95} Ce _{0.05} O ₇	20.360(4)	3.7973(7)	11.8811(20)	120.202(11)	793.9(3)
Nb ₂ Ti _{0.90} Ce _{0.10} O ₇	20.350(19)	3.893(9)	11.869(12)	120.22(6)	812.5(21)
Nb ₂ Ti _{0.80} Ce _{0.20} O ₇	20.375(7)	3.8027(13)	11.895(5)	120.18(2)	796.7(6)

The refinement of the x-ray data for these samples was very difficult due to high levels of impurities. In all these samples the unit cell shows very little change from Nb₂TiO₇, indicating that almost no CeO₂ is incorporated into the structure, most likely due to the large size of Ce(IV) of 0.80Å.

4.4.2 Nb₂TiO₇-Ce_{0.8}Gd_{0.2}O_{1.9} composites

Composites were made by firing pre-sintered powders of Nb₂TiO₇ with CGO at 700°C-1100°C for 4 hours, which were ball milled together under acetone. 2/3 Nb₂TiO₇-1/3CGO was prepared and X-ray data along with SEM, and density studies were performed on the material.

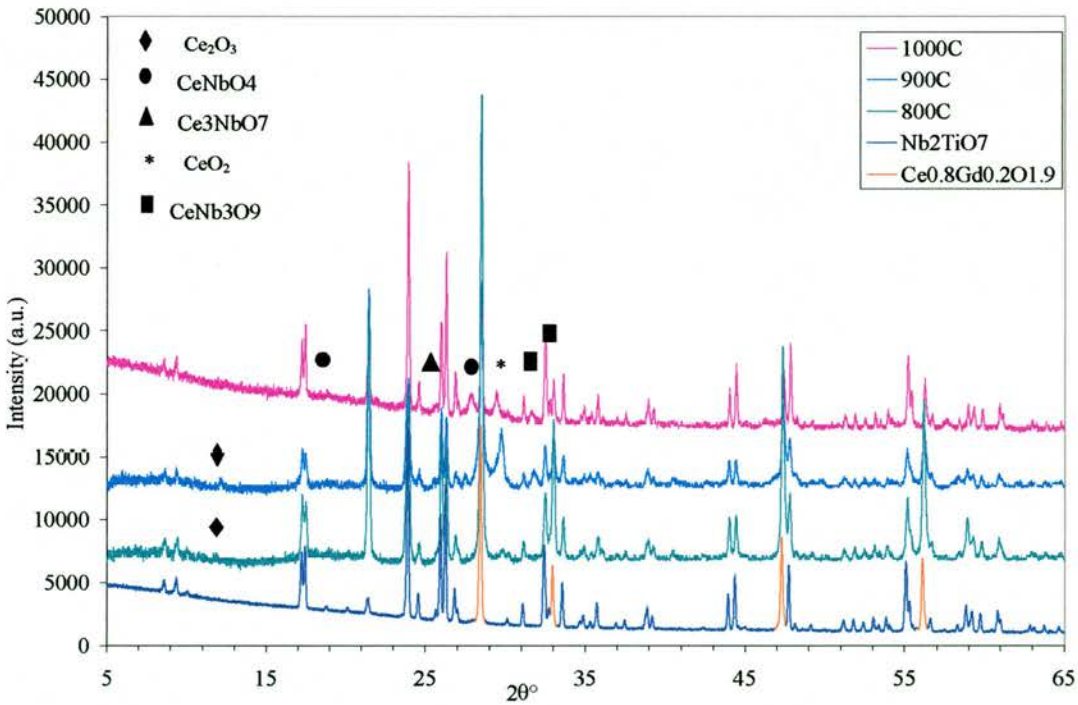


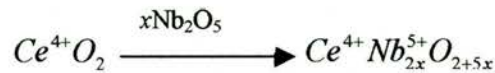
Fig.4.33 X-ray data for 2/3 Nb₂TiO₇-1/3CGO composite sintered at different temperatures between 700°C and 1100°C

X-ray data showed that the reaction of CeO₂ with Nb₂O₅ starts at ~900°C (Fig.4.33) with the formation of a pale green/lime coloured composite at this temperature, which becomes red/brown at 1000°C and the brown colour intensifies with increasing temperature. Similar colour change was observed by J.Sfeir [9] with increasing Nb content in low Gd concentration solutions (~12%Gd). He found the colour went from yellow at 4% Nb, to green-yellow for 6% Nb to olive green for 8%Nb.

Previous study by J.Sfeir [9] used Nb₂O₅ for the densification of Ce_{1-x}Gd_xO_{2-δ}, in which he found that the orthoniobate phase, CeNbO₄, formed when Nb₂O₅ exceeded its solubility limit of 0.6-0.8% in ceria. Other possible phases such as CeNb₃O₉, CeNb₅O₁₄ GdNbO₄ or Ce₂O₃ were also suggested by J.Sfeir in 6-8% Nb doped Ce_{0.88}Gd_{0.12}O_{1.94}.

It has been reported previously that the colour transition indicates the presence of Ce(III) [10]. The olive-green colour is observed in Ce₂O₃. Reports by N.A.Godina et al [11] and G.G.Kasimov et al [12] suggested that when Ce is in excess in ceria-niobia solutions, Ce reduces to the Ce(III) state without affecting the Nb(V) oxidation state. The reduction of Ce by Nb dissolution can be explained by the substitutional mechanism.

Doping with elements of valence higher than 4+ will lead to the incorporation of the excess oxygen as interstitials for low dopant concentration:



or to an electronic compensation, leading to cerium reduction with higher dopant concentration:

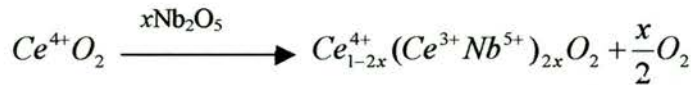


Table 4.11 shows the change in density of the pellet with firing at different temperatures. There is an almost linear increase up to 1000°C, however, due to the formation of impurities at 900°C, high sintering temperatures are not possible for the study of this composite.

Table 4.11 Densification of Nb₂TiO₇-CGO composite with temperature

Sintering Temp (°C)	Pellet density gcm ⁻³ (±0.02)
700	2.31
800	2.46
900	2.56
1000	2.63

4.4.3 SEM Study of density and homogeneity of CGO-NbTiO composite

SEM studies of the Nb₂TiO₇-CGO composite showed poor sinterability up to 1000°C (Fig.4.34). Higher temperatures produced an increasingly larger amount of second phases and no improved sinterability was observed up to 1200°C. Porosity is very important when considering anode uses and has to be high enough to allow gas transport to the reaction site, whilst low enough to allow good mass transport. The porosity of the Ni/YSZ is ~30%, optimised for mass transport and strength of the anode. From Fig.4.34, it can be seen that the porosity of the composite is very high even when sintered at 1000°C

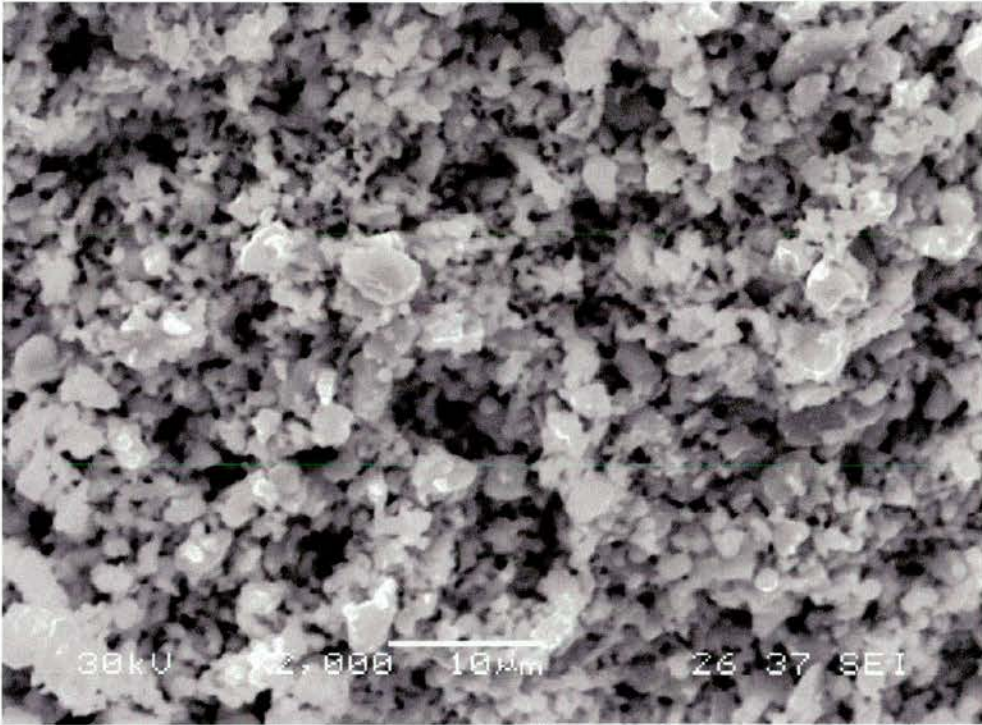


Fig.4.34 SEM image of Nb₂TiO₇ – CGO composite sintered at 1000°C

4.5 Nb_{2-x}Ti₁V_xO₇ system

Doping with 5% vanadium decreased the size of both the unit cell and the thermal expansion (Table 4.12). Additionally, vanadium is very volatile in the structure and at temperatures of 600°-1000°C readily leaves the structure onto the surrounding material, e.g. alumina. This material is therefore not suitable for use in a fuel cell where vanadium can leak onto surrounding components, thus affecting properties and performance of these materials. As such, no further samples with vanadium were made in these experiments.

Table 4.12 Unit cell and TEC of 5% Vanadium doped Nb₂TiO₇

	a	b	c	β	V	TEC 300-900°C 10 ⁻⁶ K ⁻¹
Nb ₂ TiO ₇	20.3610(11)	3.7988(2)	11.8861(5)	120.194(3)	794.63(9)	2.59±0.05
Nb _{1.95} TiV _{0.05} O ₇	20.3583(25)	3.7982(4)	11.8840(16)	120.192(7)	794.26(10)	2.02±0.05

4.6 Nb_xCr_xTi_{1-2x}O₂

4.6.1 Structure

Nb_xM_x^{III}Ti_{1-2x}O₂ (M=Al, Cr or Fe) solid solution materials were first synthesised and characterised by M.A.Tena et al [13], who found that these materials crystallised with a rutile structure with a space group P42/mnm, i.e. similar to that of Nb_{1.333}Ti_{0.667}O₄. They did not, however, report the conductivity of these samples in air or under reducing conditions. Nb_{1.333}Ti_{0.667}O₄ has a conductivity of ~300Scm⁻¹ which is mainly due to its rutile structure and the free electrons created when niobium is in oxidation state 4+. It was thus of interest to see if samples containing Cr would show a similar conductivity to Nb_{1.333}Ti_{0.667}O₄, and to compare their thermal expansion coefficient.

The samples are easily prepared by firing stoichiometric amounts of metal oxides in air at 1200-1400°C for 72 hours with intermediate regrinding, giving a rutile structure with increasing unit cell (Table 4.13) related to the increasing amount of Cr. The samples were seen to go from the green colour of Cr₂O₃ to dark red or purple on a single 24 hour firing at 1200°C. Phase purity was checked by refining the unit cell

parameters, and these were found to be in good agreement with those reported by M.A.Tena [13].

Table 4.13 Unit cell and thermal expansion coefficients of oxidised Ti_{1-2x}Cr_xNb_xO₂ (black) and of Ti_{1-2x}Cr_xNb_xO_{2-δ} reduced at 1000°C (in blue)

sample	a (Å)	c (Å)	V (Å ³)	TEC 300-900°C (x10 ⁻⁶ K ⁻¹)
TiO ₂	4.593(2)	2.961(1)	62.46	7.14-9.19
Ti _{0.8} Cr _{0.1} Nb _{0.1} O ₂	4.6089(7)	2.9732(4)	63.158(22)	8.57±0.05
Ti _{0.8} Cr _{0.1} Nb _{0.1} O _{1.90}	4.6367(6)	2.9821(3)	64.111(19)	8.34±0.05
Ti _{0.6} Cr _{0.2} Nb _{0.2} O ₂	4.6198(1)	2.9838(1)	63.682(4)	7.35±0.05
Ti _{0.6} Cr _{0.2} Nb _{0.2} O _{1.95}	4.6405(3)	2.9876(3)	64.334(11)	7.19±0.05
Ti _{0.4} Cr _{0.3} Nb _{0.3} O ₂	4.6306(1)	2.9947(1)	64.215(5)	6.65±0.05
Ti _{0.4} Cr _{0.3} Nb _{0.3} O _{1.97}	4.6694(2)	2.9980(1)	65.367(7)	6.82±0.05
Ti _{0.2} Cr _{0.4} Nb _{0.4} O ₂	4.6410(2)	3.0055(1)	64.736(7)	6.27±0.05
Ti _{0.2} Cr _{0.4} Nb _{0.4} O _{1.98}	4.6798(3)	3.0051(3)	65.814(12)	5.71±0.05
Cr _{0.5} Nb _{0.5} O ₂	4.6475(3)	3.0134(2)	65.098(10)	6.04±0.05
Cr _{0.5} Nb _{0.5} O _{1.98}	4.6830(5)	3.0104(4)	66.019(18)	5.57±0.05

In the Ti_{1-2x}Cr_xNb_xO₂ structure as in Nb_{1.333}Ti_{0.667}O₄, Ti, Nb and Cr all occupy the same crystallographic site, and as was mentioned earlier, this may be due to the similar sizes of ionic radii of the cations: the ionic radius of Cr³⁺ is 0.61 Å (c.f. 0.60 for Ti⁴⁺ and 0.64 for Nb⁵⁺). Chromium is most stable in the oxidation state +3 due to the symmetrical t_{2g}³ configuration [14], and in the oxidation state +2 it is strongly reducing (Cr³⁺/Cr²⁺ E°-0.41V)[14]. Thus upon reduction it is expected that in preference to Cr, Nb⁵⁺ or Ti⁴⁺ will reduce to Nb⁴⁺ or Ti³⁺ respectively, and hence will increase the conductivity of this material. No change in structure is expected upon reduction at 1000°C in 5%H₂/Ar.

The TGAs, done in flowing air up to 900°C on pre-reduced samples (Fig.4.35), show that the degree of reduction decreases with decreasing titanium content (Fig.4.36). This indicates that Ti is also being reduced, and the high conductivity shows that Nb is sufficiently reduced. There is no evidence that Cr is reduced to any degree, however, more work is needed to investigate the degree of reduction of each cation.

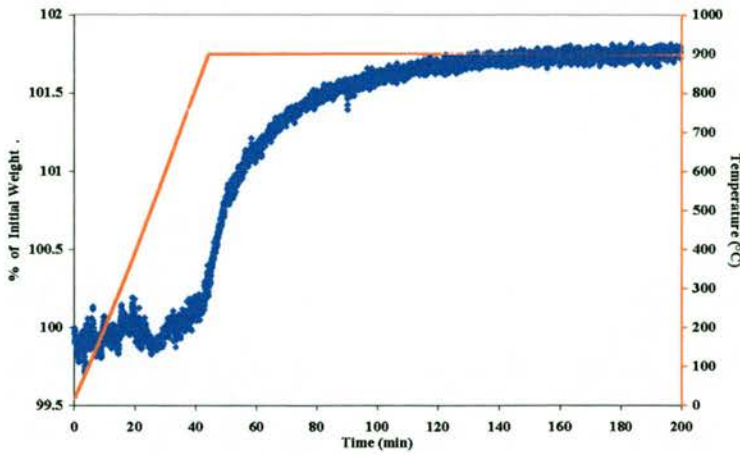


Fig.4.35 TGA oxidation run in flowing air

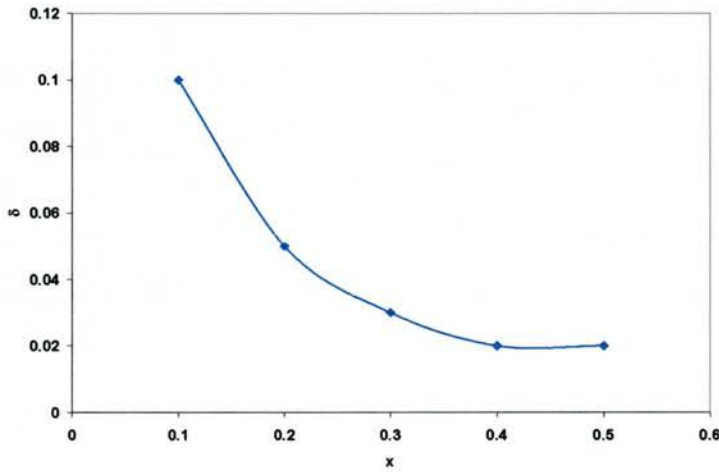


Fig.4.36 Change in δ as a function of x in $Ti_{1-2x}Cr_xNb_xO_{2-\delta}$

The unit cell parameters a and c vaguely follow Vegard's law (Fig.4.37), which states that the unit cell parameters should change linearly with composition. This law applies to solid solutions formed by random substitution or distribution of ions. Although Vegard's law is a good guide to certain solid solutions, it is not always obeyed and departures are seen from linearity, as is also observed in (Fig.4.37) for the $Ti_{1-2x}Cr_xNb_xO_2$ series. This is because Vegard's law assumes that the changes in unit cell parameters with composition are governed solely by the relative size of the atoms or ions that replace each other in a simple substitutional mechanism. Thus the unit cell expands if a small ion is substituted by a larger one, and vice versa. In a non-cubic system, however, the expansion or contraction with composition may not be the same for all axes, and sometimes one axis may expand and another contract.

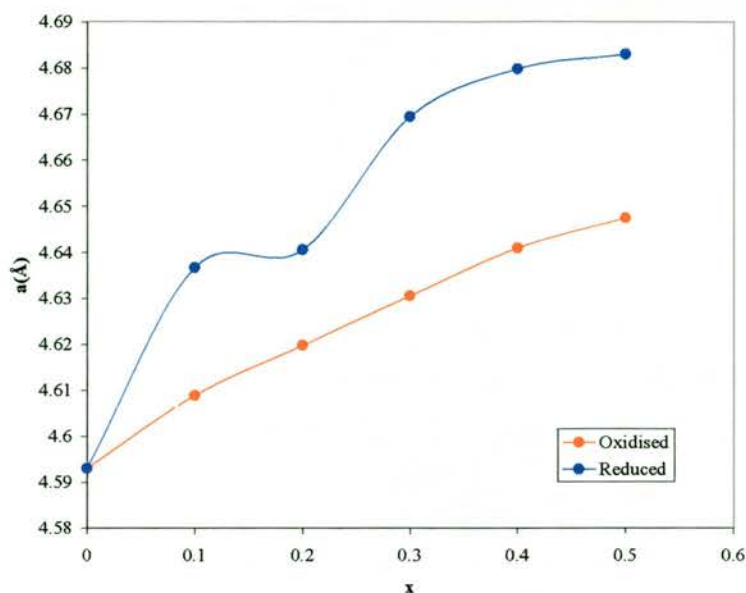


Fig. 4.37 Unit cell parameter a as a function of x in $Ti_{1-2x}Cr_xNb_xO_2$ made in air or reduced at 1000°C

The departure from Vegard's law may be positive or negative. Positive deviation may be an indicator of immiscibility domains in the structure, in which the atoms are not randomly distributed in the structure, but form "like with like" clusters, hence causing a small increase in the unit cell parameters compared to the random arrangement of atoms. Negative deviation from Vegard's law may be evidence for a net attractive interaction between unlike ions. For example, in an A-B system, A-B interaction may be stronger than A-A or B-B interaction, and in the case where A-B interaction is strong enough, cation ordering may occur to give a periodic superstructure. Less strong A-B interaction produces short range cation ordering, over a few atomic diameters, which crystallographically may appear to be disordered and homogeneous, and may or may not be linked to deviation from Vegard's law.

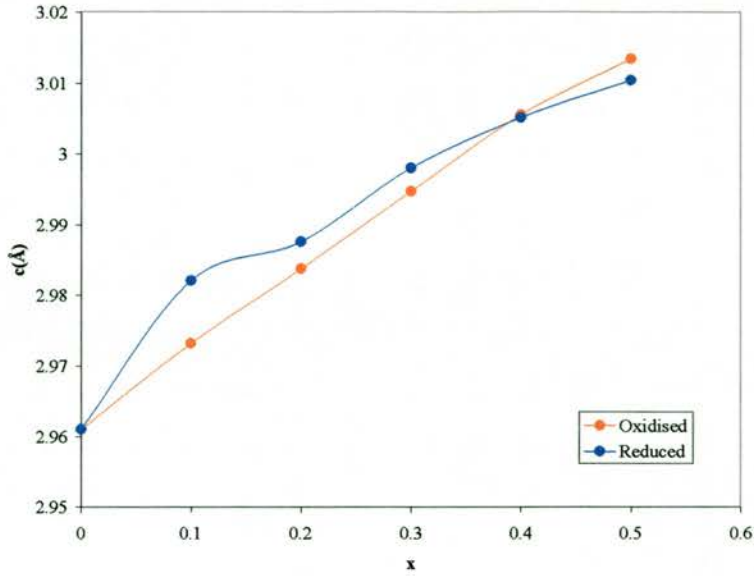


Fig.4.38 Unit cell parameter c of as a function of x in $Ti_{1-2x}Cr_xNb_xO_2$ made in air or reduced at $1000^\circ C$

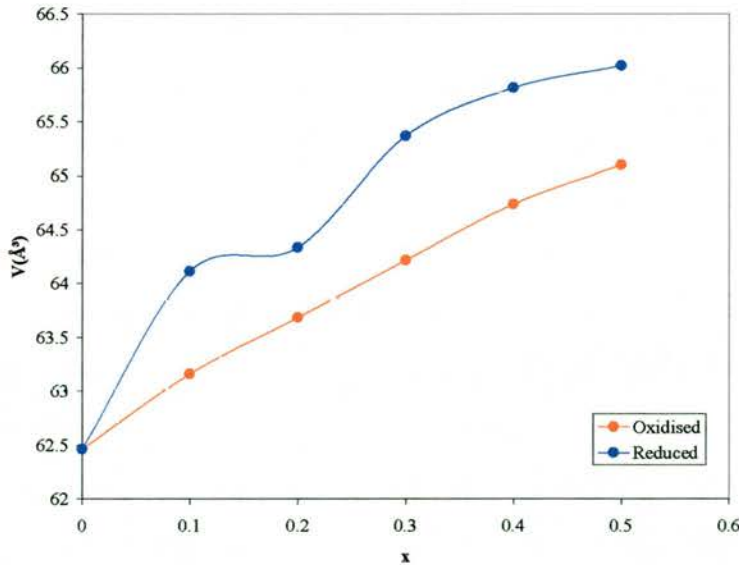


Fig.4.39 Unit cell volume of as a function of x in $Ti_{1-2x}Cr_xNb_xO_2$ made in air or reduced at $1000^\circ C$

The expansion of the unit cell is not isotropic. As can be seen from Fig.4.37 there is a large increase in the size of unit cell parameter a upon reduction. The change in the unit cell parameter c , however, is much smaller going from oxidised to reduced state (Fig.4.38) than that for a . The negative deviation from Vegard's law shifts it to the unit cell size of the oxidised sample. There is also a significant increase in the volume of the unit cell mostly due to the expansion of unit cell parameter a , and the increase is

greatest for the reduced sample. The difference in the expansion of the a axis and the c axis can be related back to the rutile structure seen in Chapter 3 –Theory (Fig.4.40). The ratio of c/a (Fig.4.41, Table 4.14), increases with x for the oxidised sample, indicating that the expansion is greater along the c direction rather than in the a direction. From Fig.4.40 it can be seen that M-M bonds overlap runs in this direction. By substituting the smaller cation, Ti by the larger Nb and Cr, would increase the average interatomic distance especially where there is a d orbital overlap in the M-M bond, in the c axis.

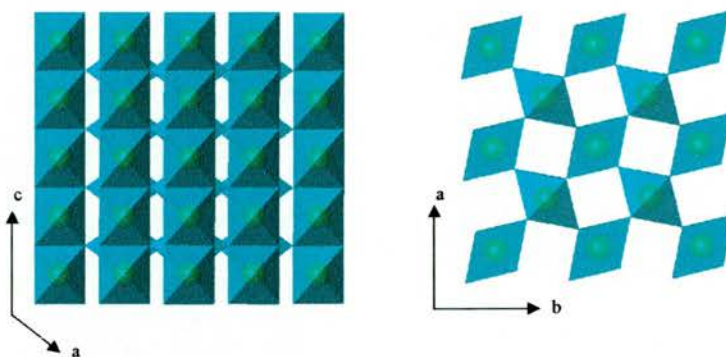


Fig.4.40 Rutile structure along the a/b and c axis

Table 4.14 c/a ratio in the oxidised and reduced $Ti_{1-2x}Cr_xNb_xO_2$

Oxidised	c/a	Reduced	c/a
TiO ₂	0.6447	TiO ₂	0.6447
Ti _{0.8} Cr _{0.1} Nb _{0.1} O ₂	0.6451	Ti _{0.8} Cr _{0.1} Nb _{0.1} O _{1.90}	0.6432
Ti _{0.6} Cr _{0.2} Nb _{0.2} O ₂	0.6459	Ti _{0.6} Cr _{0.2} Nb _{0.2} O _{1.95}	0.6438
Ti _{0.4} Cr _{0.3} Nb _{0.3} O ₂	0.6467	Ti _{0.4} Cr _{0.3} Nb _{0.3} O _{1.97}	0.6421
Ti _{0.2} Cr _{0.4} Nb _{0.4} O ₂	0.6476	Ti _{0.2} Cr _{0.4} Nb _{0.4} O _{1.98}	0.6421
Cr _{0.5} Nb _{0.5} O ₂	0.6484	Cr _{0.5} Nb _{0.5} O _{1.98}	0.6428

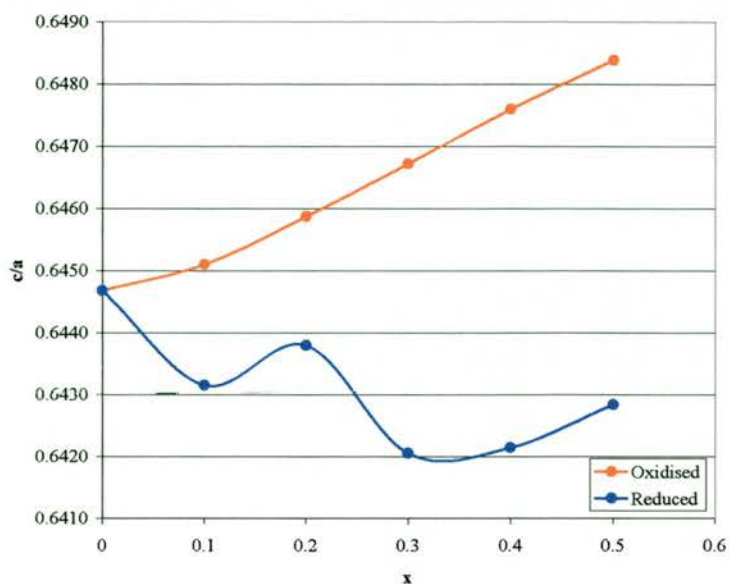


Fig.4.41 Graph of c/a ratio as a function of x in the $Ti_{1-2x}Cr_xNb_xO_2$

The reduced sample, however, does not follow the same trend, and is seen to decrease initially, indicating that the increase in the a axis is now greater than in the c axis. From Fig.4.40 it can be seen that the likely reason for this is the increase in the M-O distances. When $x=0.4-0.5$ the expansion is again larger in the c axis. This can be related to the degree of reduction. As can be seen from Fig.4.42 the average oxidation state increases as a function of x , showing that the degree of reduction drops with the decreasing TiO₂ content. When x is 0.1-0.2 the average oxidation state is 3.8 and 3.9 respectively. This would indicate a sufficient oxygen deficiency to increase the average M-O distance along the a/b axis. When $x = 0.4-0.5$ the average oxidation state is only 3.98, hence the slight reduction in Nb₂O₅ and TiO₂ broadens the d bands, increasing their overlap, thus increasing the M-M distance in the c direction. The cross over point for the two effects seems to be around $x=0.3$, with an average oxidation state of 3.94.

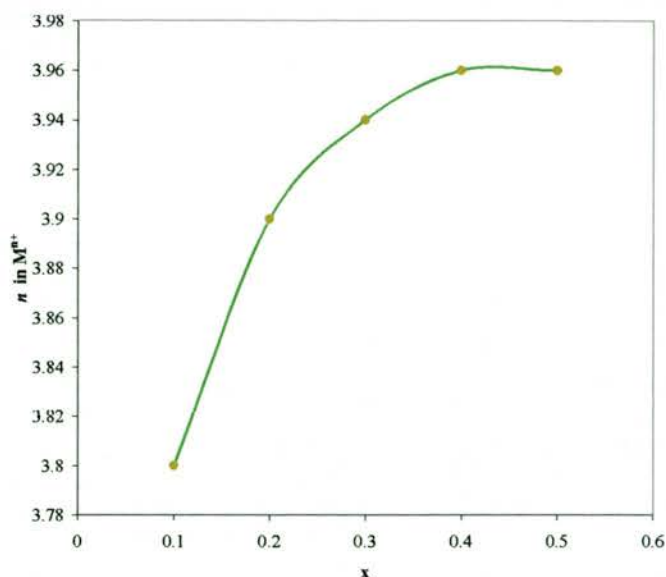


Fig.4.42 Average oxidation state, n in $M^{n+}O_{2-\delta}$ as a function of x in the reduced samples $Ti_{1-2x}Cr_xNb_xO_{2-\delta}$

From this trend it can also be assumed that TiO₂ is being reduced preferentially to Cr₂O₃. The degree of reduction of Nb is unclear, but can be assumed to be the reduced cation in Cr_{0.5}Nb_{0.5}O₂.

To understand the change in structure on reduction TEM was performed on the sample reduced at 1000°C. Preliminary TEM studies were performed on a Jeol JEM 2011 microscope operating at 200 kV and equipped with a double tilt ($\pm 20^\circ$) sample holder.

Magneli recognised that in certain non-stoichiometric metal oxide systems, such as TiO_{2-x}, instead of continuous solid solution formation, a series of closely related phases with similar formulae and structures exist in an oxide. In oxygen deficient rutile such as Ti_nO_{2n-1} ($n=4, \dots, 10$) or the Ti_{1-2x}Cr_xNb_xO₂ series, regions of normal rutile structure occur (Fig.4.43), separated from each other by crystallographic shear (CS) planes (Fig.4.44). CS planes are thin lamellae of different structure and composition, and all of the oxygen deficiency is concentrated within these CS planes. With increasing reduction, the variation in stoichiometry increases the number of CS planes and decreases the block of rutile structure between adjacent planes.

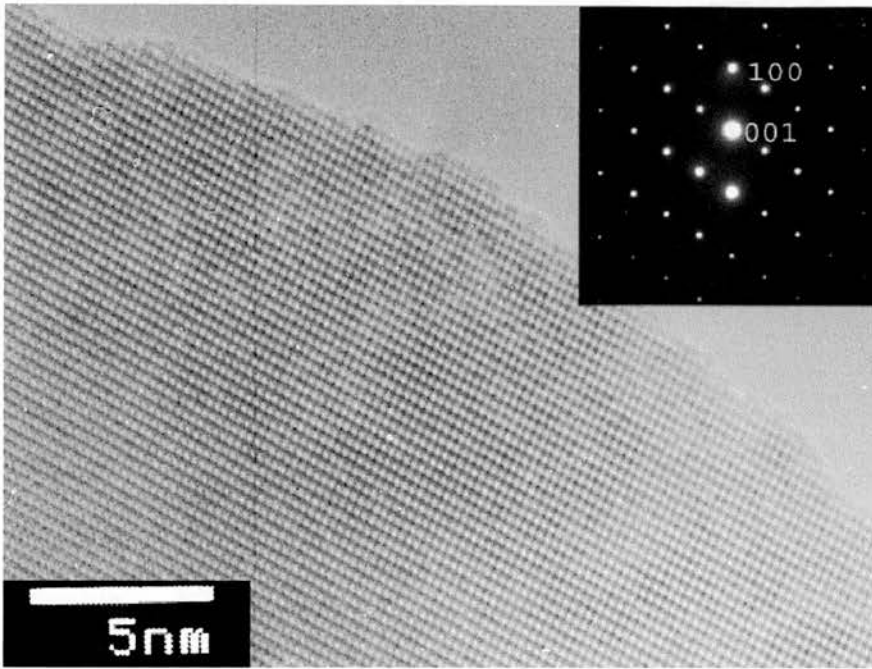


Fig.4.43 HRTEM image corresponding to a view down the $[010]_t$ of a tetragonal rutile domain and its corresponding SAED pattern (inset) of $Ti_{0.2}Cr_{0.4}Nb_{0.4}O_2$

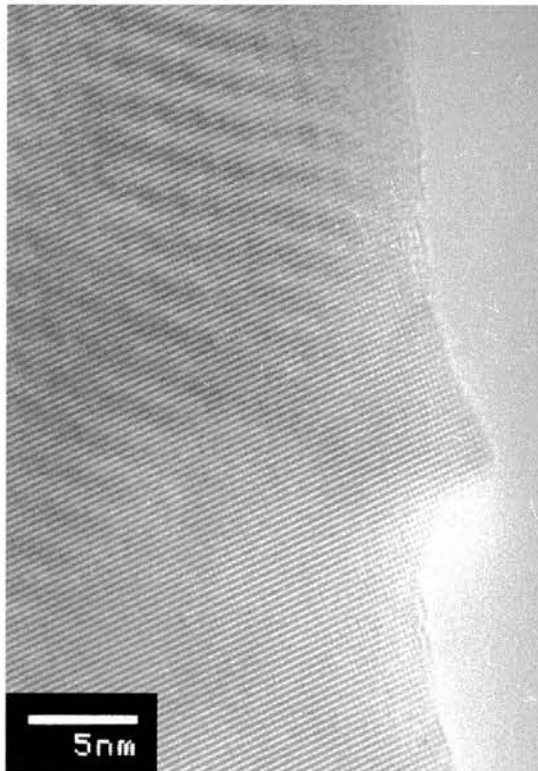


Fig.4.44 HRTEM image of an oxygen deficient domain, recorded on a different area of the same crystal, of fig.4.41, and in the same direction, showing crystallographic shear planes of $Ti_{0.2}Cr_{0.4}Nb_{0.4}O_2$

In TiO₂, reduction of Ti⁴⁺ to Ti³⁺ or Ti²⁺ results in the formation of vacant oxygen sites, which are not randomly distributed but are located on certain planes within the crystal. In order to minimise the layers of vacant sites, condensation of the structure occurs, eliminating the vacancies and forming CS planes, where the octahedra share faces rather than edges as in the corresponding unreduced rutile regions.

The Ti_{1-2x}Cr_xNb_xO₂ series, as seen in (Fig.4.43) and (Fig.4.44) produces these CS planes upon reduction with the spacing between the planes is 8 layers corresponding to ~24Å. The shear planes produce additional peaks seen in the X-ray diffraction pattern (Fig.4.45) of the reduced Ti_{1-2x}Cr_xNb_xO₂ series.

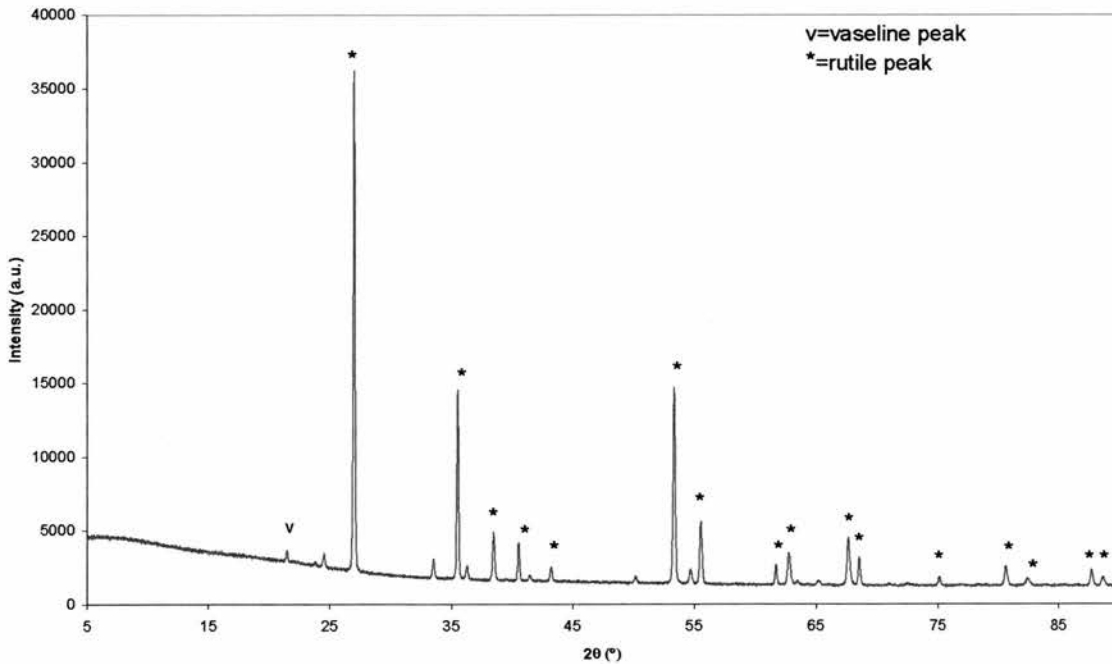


Fig. 4.45 X-ray powder diffraction pattern of reduced Ti_{0.2}Cr_{0.4}Nb_{0.4}O₂

4.6.2 Thermal expansion

Thermal expansion coefficient shows a general increase with reduction, and is related to the size of unit cell volume. The reduction in the unit cell parameters a or c seems to correlate to the increase in the thermal expansion coefficient (Fig.4.46), with the smallest unit cell and the largest thermal expansion corresponding to Ti_{0.8}Cr_{0.1}Nb_{0.1}O₂, i.e. $x=0.1$.

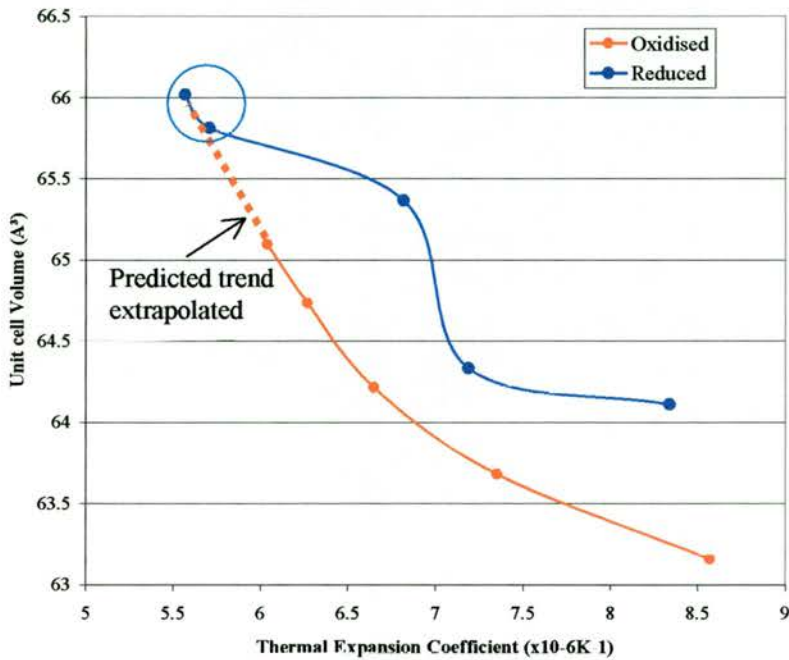


Fig.4.46 Thermal expansion coefficient as a function of unit cell volume for reduced and oxidised samples

The thermal expansion decreases linearly with increasing x in the Ti_{1-2x}Cr_xNb_xO₂ series (Fig.4.47), and is smaller for the reduced samples, which may be related to the increase in the unit cell size and the corresponding decrease in TEC. As can be seen in (Fig.4.46), the least reduced samples ($x=0.4-0.5$ highlighted by blue circle), follow the predicted trend line. Increasing the degree of reduction, however, seems to cause a deviation from the expected thermal expansion, if it was directly related to the unit cell volume as suggested by red line in (Fig.4.46). One would expect that the thermal expansion is also not isotropic and is probably closer related to the expansion of the c axis.

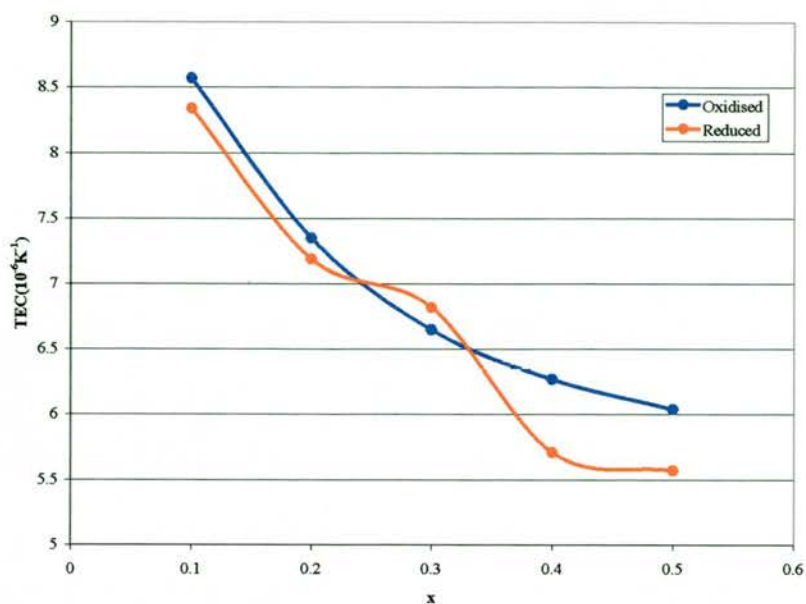


Fig. 4.47 Change in thermal expansion coefficient with x in the $Ti_{1-2x}Cr_xNb_xO_2$

From (Fig. 4.47) it can be seen that the change in the thermal expansion upon reduction is small for all samples, due to reduced and oxidised samples having the same rutile structure.

4.6.3 Electronic conductivity at constant atmosphere

The members of the $Ti_{1-2x}Cr_xNb_xO_2$ series shows similar conductivities in air at 900°C (Table 4.15), however the Arrhenius plot (Fig. 4.48) shows the difference in the activation energies for conduction. The activation energies are between 1.54 ± 0.01 eV and 0.38 ± 0.01 eV for oxidised samples. There is a general trend showing two activation energies, one at high temperature (900°-650°C) which is >1 eV, and one below $\sim 650^\circ$ -700°C, which is <1 eV. $Ti_{0.2}Cr_{0.4}Nb_{0.4}O_2$ seems to be an exception to the rule, showing a straight line from 900°C to 250°C, with an activation energy of 0.62 ± 0.01 eV for heating and cooling curves.

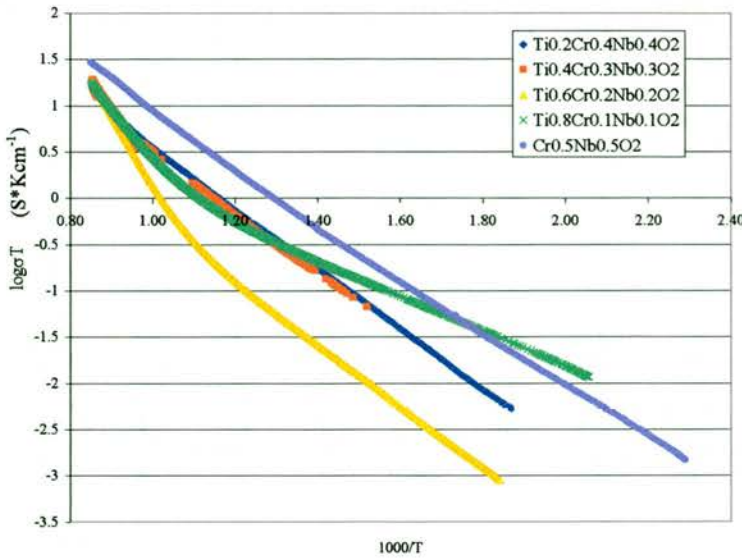


Fig. 4.48 Arrhenius plot of $Ti_{1-2x}Cr_xNb_xO_2$ for the conductivity run in air

The reduction of these materials increases the conductivity 1000 fold to $\sim 20\text{Scm}^{-1}$ for samples rich in titanium and 10Scm^{-1} for $Ti_{0.2}Cr_{0.4}Nb_{0.4}O_2$. The activation energies are very low, $<0.4\text{eV}$ (Table 4.15), and are only slightly larger at higher temperatures. The lowest activation energy was seen for $Ti_{0.8}Cr_{0.1}Nb_{0.1}O_2$ with 0.11-0.16eV for the run in 5% H_2 /Ar. The general trend is the increase in activation energy with decreasing amount of Ti and increasing the Cr and Nb content (Table 4.15).

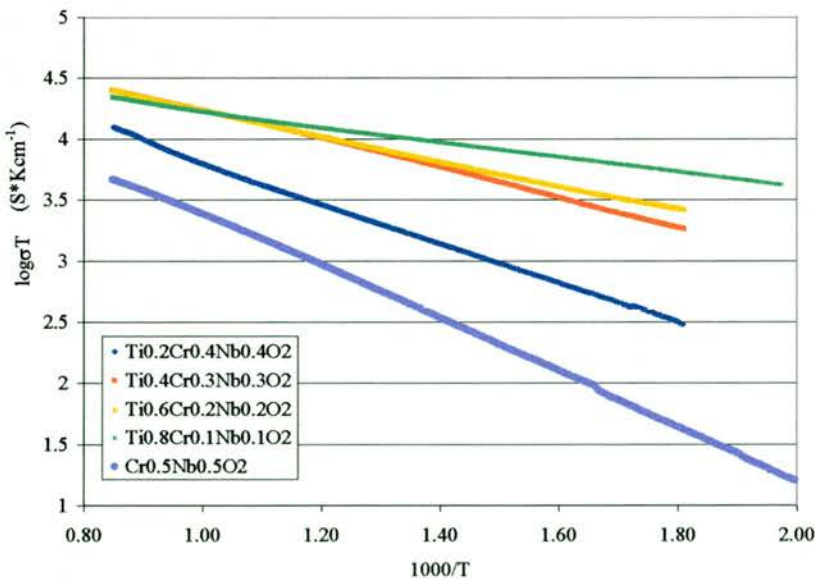


Fig. 4.49 Arrhenius plot of $Ti_{1-2x}Cr_xNb_xO_2$ for the conductivity run in 5% H_2 /Ar

Table 4.15 Electronic conductivities and activation energies of $Ti_{1-2x}Cr_xNb_xO_2$ in air and 5% H_2/Ar

	σ (Scm ⁻¹) in air at 900°C	Ea (eV) Heating (T °C range)	Ea (eV) Cooling (T °C range)	σ (Scm ⁻¹) 5% H_2/Ar at 900°C	Ea (eV) Heating (T °C range)	Ea (eV) Cooling (T °C range)
$Ti_{0.8}Cr_{0.1}Nb_{0.1}O_2$	1.53×10^{-2}	1.07(900-680) 0.38(560-230) Curve 680-560	1.05(900-680) 0.37(560-230) Curve 680-560	20.6	0.11(530-180) 0.16 (900-530)	0.12(530-180) 0.14(900-530)
$Ti_{0.6}Cr_{0.2}Nb_{0.2}O_2$	1.53×10^{-2}	1.54(900-640) 0.77(640-250)	1.37(900-640) 0.71(640-900)	22.3	0.17(280-580) 0.26(580-900)	0.19(400 -280) 0.21(400 -900)
$Ti_{0.4}Cr_{0.3}Nb_{0.3}O_2$	1.65×10^{-2}	1.30(900-750) 0.75(300-750)	1.29(900-750) 0.64(750-300)	21.2	0.23(900-250)	0.24(900-250)
$Ti_{0.2}Cr_{0.4}Nb_{0.4}O_2$	1.53×10^{-2}	0.62(900-250)	0.63(900-250)	10.9	0.39(900-635) 0.32(635-280)	0.30 (900-635) 0.33(635-280)
$Cr_{0.5}Nb_{0.5}O_2$	2.49×10^{-2}	0.66(700-900) 0.55(700-160)	0.60(900-370)	6.3	0.41 (200-900)	0.43 (900-200)

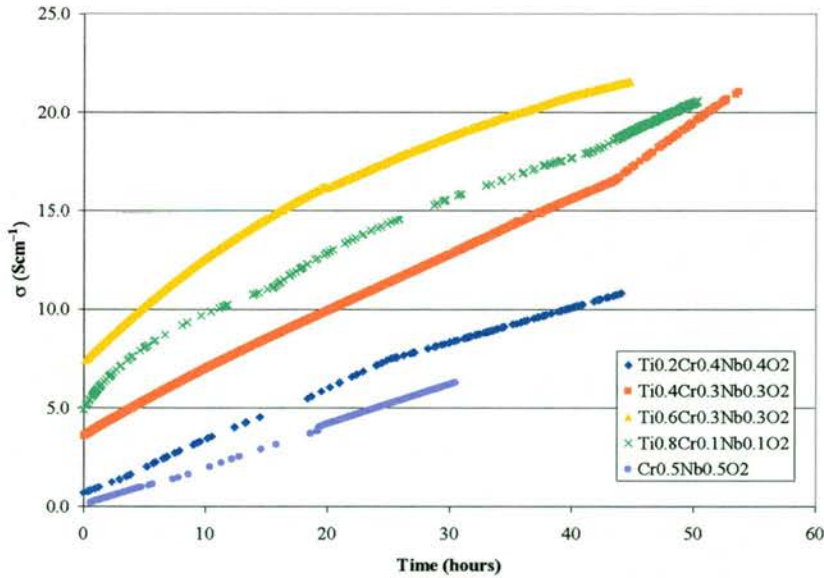


Fig.4.50 Change in conductivity with time at $\log p(O_2) < -18.5$

The reduction of these materials takes a long time, even with densities of 70-85%, and the final equilibrium in conductivity at $p(\text{O}_2)=10^{-20}$ is not achieved (Fig.4.50). The curves in (Fig.4.50) show the time taken from the reduction run region, $p(\text{O}_2)=10^{-19}$ - 10^{-20} atm, and the equilibration at 10^{-20} atm prior to oxidation seen in (Fig.4.51) as the last set of data after 10^{-19} atm. The actual conductivities of these samples when fully reduced are therefore necessarily higher than those reported in this thesis. Slow reduction kinetics are typical of the niobium based materials and indicate poor surface exchange rates or a low diffusion coefficient. This shows that investigating the dependence of conductivity on $p(\text{O}_2)$ in these materials is very difficult, requiring geological times to reach equilibrium. Hence the data obtained from $p(\text{O}_2)$ measurements indicates more of the general trend than actual defect equilibrium.

4.6.4 Electronic conductivity as a function of $p(\text{O}_2)$

Although the reduction run in the $p(\text{O}_2)$ experiment is mainly uncontrolled, the region of $p(\text{O}_2)$ of 10^{-15} to 10^{-20} atm takes up to 15 hours to traverse. The oxidation run is a much slower process, taking some 24-48 hours to complete, equilibrium, however, cannot be guaranteed and most likely has not been achieved.

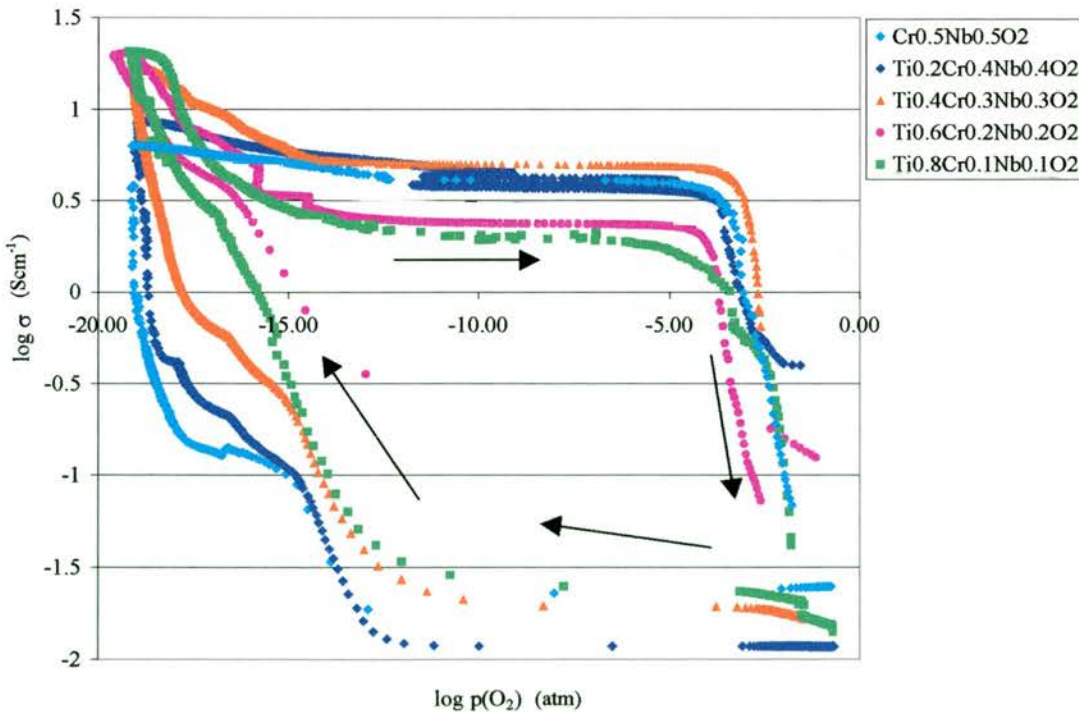


Fig.4.51 $\log \sigma$ as a function of $\log p(\text{O}_2)$ for $\text{Ti}_{1-2x}\text{Cr}_x\text{Nb}_x\text{O}_2$

Looking at electronic conductivity alone the Ti_{1-2x}Cr_xNb_xO₂ series can be separated into 2 similarly behaving group of materials (Fig.4.51). Ti_{0.2}Cr_{0.4}Nb_{0.4}O₂ and Cr_{0.5}Nb_{0.5}O₂ are very similar materials. In fact, Ti_{0.2}Cr_{0.4}Nb_{0.4}O₂ can be considered to be TiO₂ doped Cr_{0.5}Nb_{0.5}O₂. As was seen in the previous sections, there is a clear similarity in the unit cell parameters, the thermal expansion coefficient, electronic conductivity and the oxidation state when reduced at 900°-1000°C. This would also indicate a similar electronic conductivity and p(O₂) dependence (Fig.4.52).

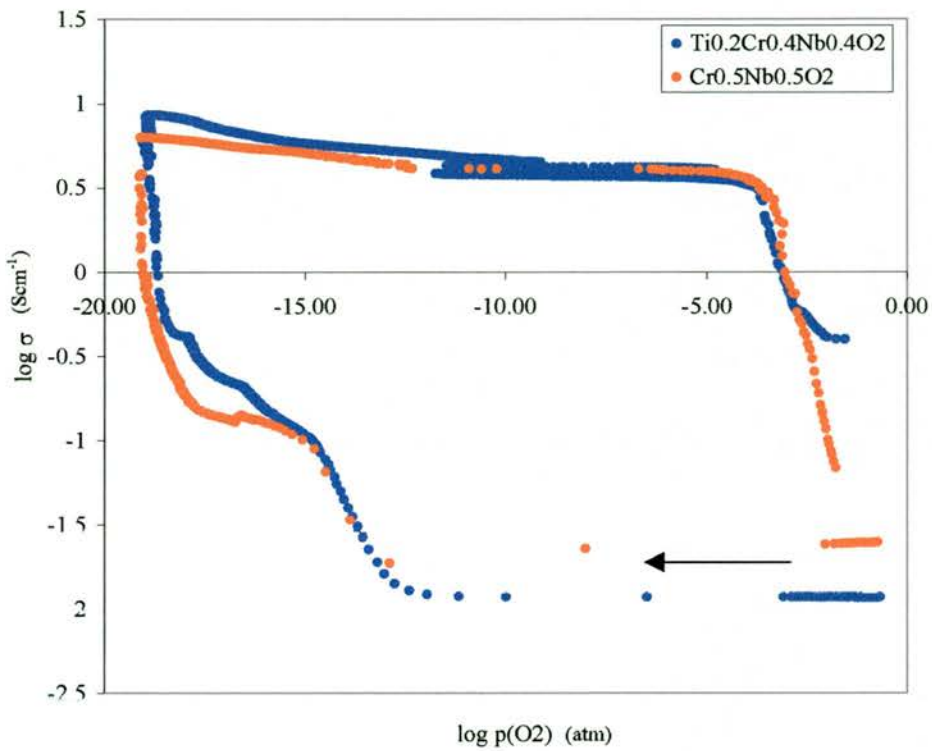


Fig.4.52 $\log \sigma$ as a function of $\log p(O_2)$ for $Ti_{0.2}Cr_{0.4}Nb_{0.4}O_2$ and $Cr_{0.5}Nb_{0.5}O_2$

A very large hysteresis is observed between the oxidation and the reduction run (Fig.4.52) for both Ti_{0.2}Cr_{0.4}Nb_{0.4}O₂ and Cr_{0.5}Nb_{0.5}O₂, indicating that the “titration” point for the oxidation and the reduction reactions are shifted. When oxidised the samples appear to be stable to reduction up to p(O₂) ~10⁻⁴ – 10⁻⁵ atm. The following p(O₂) region, 10⁻⁵-10⁻¹⁵ atm., was traversed too fast and no conclusion about the samples’ response can be drawn from it.

No reliable slopes can be derived from the reduction runs, due to such slow reduction kinetics, however a number of possible phase transitions or shear defect formation in both Ti_{0.2}Cr_{0.4}Nb_{0.4}O₂ and Cr_{0.5}Nb_{0.5}O₂, can be seen occurring at $\sim 10^{-15}$ atm, 10^{-16} atm, and 10^{-18} atm.

The reduced samples show high degree of stability to change in $p(\text{O}_2)$, and the conductivity changes little with $p(\text{O}_2)$, up to $p(\text{O}_2)=10^{-4}$ atm, followed by a rapid drop in conductivity indicative of rapid oxidation. Neither of these samples returned to their original σ value in air indicating that any structural changes occurring on reduction, such as shear defects, are “semi-permanent”.

For Ti_{0.2}Cr_{0.4}Nb_{0.4}O₂, the increase in the $p(\text{O}_2)$ range from 10^{-19} to 10^{-14} atm took 60 hours, and showed a slope with a very small gradient; the conductivity does not start to drop significantly until $p(\text{O}_2)=10^{-4}$ atm, the “titration” point, and the value stabilised an order of magnitude higher than the pre-reduction value.

(Fig.4.53) shows the time scale of the Ti_{0.2}Cr_{0.4}Nb_{0.4}O₂ experiment, showing the change of $\log p(\text{O}_2)$ and $\log \sigma$ with time. In the case of Ti_{0.2}Cr_{0.4}Nb_{0.4}O₂, self buffering can be seen across the “dead” zone of $p(\text{O}_2)=10^{-12}$ - 10^{-5} atm. The leak rate of oxygen was controlled with a needle valve and at two points the leakage rate was increased in order for the sample to reach $p(\text{O}_2)$ of 10^{-1} atm.

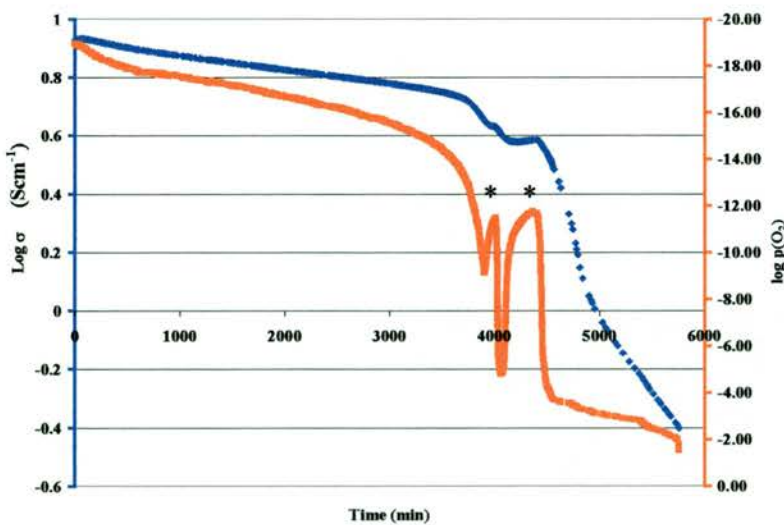


Fig.4.53 $\log p(\text{O}_2)$ (red) and $\log \sigma$ (blue) as a function of time for Ti_{0.2}Cr_{0.4}Nb_{0.4}O₂.

* shows the stage at which the needle valve was opened further

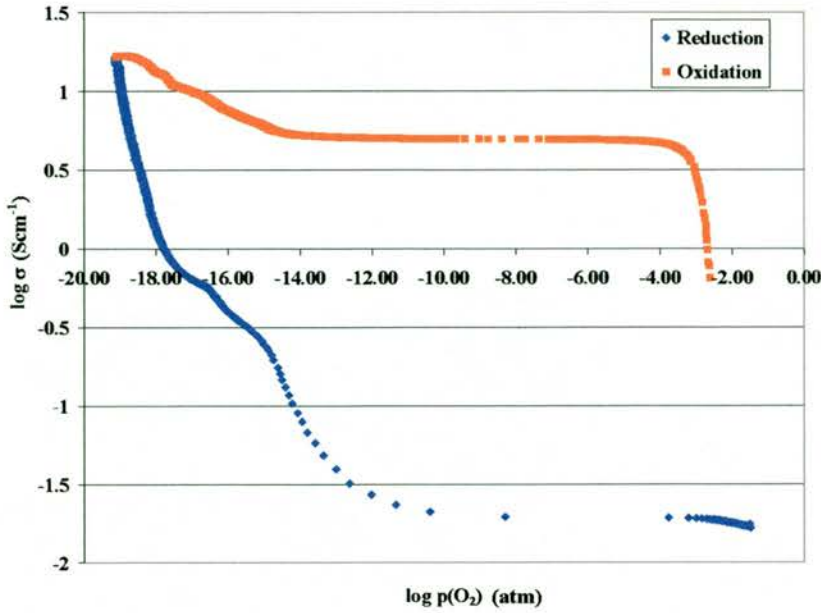


Fig.4.54 $\log \sigma$ as a function of $\log p(\text{O}_2)$ for $\text{Ti}_{0.4}\text{Cr}_{0.3}\text{Nb}_{0.3}\text{O}_2$

$\text{Ti}_{0.4}\text{Cr}_{0.3}\text{Nb}_{0.3}\text{O}_2$ shows a slope of -0.12 ± 0.02 ($-1/8$) between $p(\text{O}_2)$ 10^{-20} and 10^{-15} atm on oxidation (Fig.4.54). As seen for $\text{Ti}_{0.2}\text{Cr}_{0.4}\text{Nb}_{0.4}\text{O}_2$ and $\text{Cr}_{0.5}\text{Nb}_{0.5}\text{O}_2$, phase transitions occur at $\sim 10^{-15}$ atm, 10^{-16} atm, and 10^{-18} atm, seen in both the oxidation and the reduction runs. The sample did not return to its initial conductivity, again showing “semi-permanent” structural changes.

The second group is $\text{Ti}_{0.8}\text{Cr}_{0.1}\text{Nb}_{0.1}\text{O}_2$ and $\text{Ti}_{0.6}\text{Cr}_{0.2}\text{Nb}_{0.2}\text{O}_2$, which show similar $p(\text{O}_2)$ dependence (Fig.4.55). $\text{Ti}_{0.8}\text{Cr}_{0.1}\text{Nb}_{0.1}\text{O}_2$ also shows 2 slopes, one is at $p(\text{O}_2)$ 10^{-20} - 10^{-17} atm. with -0.49 ± 0.02 , and -0.11 ± 0.02 between 10^{-16} - 10^{-14} atm. These values, however, are again only to show a difference within this series of materials. The equilibrium value has not been achieved, which may be indicated by a curve seen in the oxidation run between 10^{-18} and 10^{-13} atm and the hysteresis seen between the reduction and the oxidation runs. During the reduction and the oxidation run there is a phase transition at 10^{-17} atm.

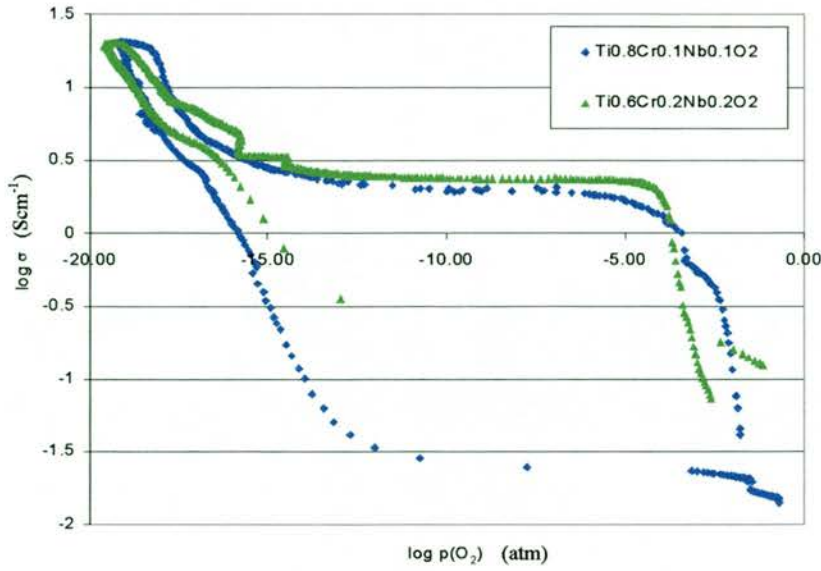
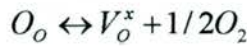


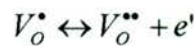
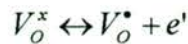
Fig.4.55 $\log \sigma$ as a function of $\log p(\text{O}_2)$ for $\text{Ti}_{0.8}\text{Cr}_{0.1}\text{Nb}_{0.1}\text{O}_2$ and $\text{Ti}_{0.6}\text{Cr}_{0.2}\text{Nb}_{0.2}\text{O}_2$

$\text{Ti}_{0.6}\text{Cr}_{0.2}\text{Nb}_{0.2}\text{O}_2$ shows two slopes of -0.32 ± 0.02 at $p(\text{O}_2) = 10^{-20} - 10^{-18}$ atm and -0.11 ± 0.02 when $p(\text{O}_2) = 10^{-18} - 10^{-16}$ atm, and a hysteresis is seen between the reduction and the oxidation runs. After reduction and re-oxidation the conductivity in air is lower than that of the original, pre-reduced material. A step-like phase transitions are seen at $10^{-14.5}$ atm, 10^{-16} atm, and 10^{-18} atm. As before, very little can be said about the defect equilibrium, but it is clear that in these materials the reduction and the oxidation reactions seem to be more reversible than those of $\text{Ti}_{0.4}\text{Cr}_{0.3}\text{Nb}_{0.3}\text{O}_2$, $\text{Ti}_{0.2}\text{Cr}_{0.4}\text{Nb}_{0.4}\text{O}_2$ and $\text{Cr}_{0.5}\text{Nb}_{0.5}\text{O}_2$. In fact the hysteresis between the reduction and the oxidation runs seems to increase with decreasing Ti.

The reduction of $\text{Ti}_{0.8}\text{Cr}_{0.1}\text{Nb}_{0.1}\text{O}_2$, produces oxygen vacancies, where a defect reaction can be written as:



In this equation the oxygen vacancy is neutral and the vacancy can lose the two trapped electrons and become either singly or doubly charged:



Thus the effective equilibrium can be written as:

$$[V_o^x] pO_2^{1/2} = K_1 [O_o]$$

$$[V_o^\bullet] n = K_a [V_o^x]$$

$$[V_o^{\bullet\bullet}] n = K_b [V_o^\bullet]$$

where $n=[e^-]$

As long as oxygen vacancies and their associated electrons are the main defect in the oxygen deficient oxide, electroneutrality dictates that: $n = [V_o^\bullet] + 2[V_o^{\bullet\bullet}]$

For the concentration of oxygen vacancies there are three limiting conditions:

$$\text{If } [V_o^x] \gg [V_o^\bullet] + [V_o^{\bullet\bullet}], \text{ then the } [V_o]_{total} = K_1 pO_2^{-1/2}$$

$$\text{If } [V_o^\bullet] \gg [V_o^x] + [V_o^{\bullet\bullet}], \text{ then the } [V_o]_{total} = (K_1 K_a)^{1/2} pO_2^{-1/4}$$

$$\text{If } [V_o^{\bullet\bullet}] \gg [V_o^x] + [V_o^\bullet], \text{ then the } [V_o]_{total} = (1/4 K_1 K_a K_b)^{1/3} pO_2^{-1/6}$$

Previous studies [15], however, on the oxygen partial pressure dependency of TiO₂ rutile structure suggested that a simple defect model in which either the oxygen vacancies or interstitial titanium defects predominate is inadequate to account for non linearity, with either temperature or $p(O_2)$, of defect concentration. Kofstad [15], thus proposed that the defect structure must simultaneously comprise of both the doubly charged oxygen vacancies and interstitial titanium atoms, with three or four effective charges, and he proposed the following defect equilibria:

$$[V_o^{\bullet\bullet}] n^2 = K_{V_o^{\bullet\bullet}} pO_2^{-1/2} \text{ (oxygen vacancy equilibrium)}$$

$$\text{therefore: } n \propto p(O_2)^{-1/4}$$

$$[Ti_i^{\bullet\bullet\bullet}] n^3 = K_{Ti_i^{\bullet\bullet\bullet}} pO_2^{-1}, \text{ equilibrium for the formation of triply charged Ti-interstitials}$$

$$\text{therefore: } n \propto p(O_2)^{-1/3}$$

$$[Ti_i^{\bullet\bullet\bullet\bullet}] n = K_a [Ti_i^{\bullet\bullet\bullet}], \text{ (equilibrium for the ionisation of } [Ti_i^{\bullet\bullet\bullet}])$$

here the following electroneutrality condition applies:

$$3[Ti_i^{\bullet\bullet\bullet}] + 4[Ti_i^{\bullet\bullet\bullet\bullet}] + 2[V_o^{\bullet\bullet}] = n$$

Thus the dependence of n on the partial pressure of oxygen can be seen to be complex.

There is no simple equilibrium equation to describe the defect equilibrium, however, for the doped TiO₂ rutile systems, but from the pO₂ dependencies observed there is a clear decrease in the slopes with decreasing x in the Ti_{1-2x}Cr_xNb_xO₂ series. The slope of -1, i.e. $\sigma \propto pO_2^{-1}$, is observed upon reduction, possibly indicating the formation of charged interstitial cations. The slope of the oxidation curve is also seen to decrease from -1/2 for Ti_{0.8}Cr_{0.1}Nb_{0.1}O₂ to an almost independent p(O₂) dependence of Cr_{0.5}Nb_{0.5}O₂ and Ti_{0.2}Cr_{0.4}Nb_{0.4}O₂, with the structures in-between displaying a large range of pO₂ dependencies indicative of the phase changes throughout the p(O₂) range. Although there is a general trend for the slopes to decrease it is questionable whether these systems really reached equilibrium, even though the oxidation between 10⁻²⁰ and 10⁻¹⁵ atm took 24-48 hours. As Fig.4.50 shows, the samples take a long time to reach equilibrium on reduction, which may also be an indication of their behaviour at low p(O₂). Thus at this stage it is not possible to comfortably analyse their defect equilibrium behaviour at these partial pressures, and longer studies are required for each sample.

The phase change is clearly observed as a step like process for Ti_{0.6}Cr_{0.2}Nb_{0.2}O₂ (Fig.4.55) at 10⁻¹⁶ and 10^{-14.5} atm., however, it is not clear if the equilibrium has been reached.

4.6.5 AC Impedance study

Two-terminal AC impedance was performed using a Solartron 1260 impedance analyser. The measurements were carried out in air on pre-sintered pellets, of densities 75-90% of theoretical, with sintered Pt paste on each face.

For all samples, AC impedance showed a visible distinction between bulk and grain boundary (Fig.4.56), showing good sinterability of these materials, indicated by large capacitance values associated with grain boundaries. It is interesting to note, however, that the large observed resistance of the Ti_{0.8}Cr_{0.1}Nb_{0.1}O₂ is entirely due to the grain boundary contribution, and the resistance of the bulk cannot be seen. The high grain boundary resistance is due to the relatively low density of the sample, 65% of theoretical, due to additional regrinding and refiring. As can be seen from the DC conductivity measurement versus temperature (Fig.4.48), the resistance of Ti_{0.8}Cr_{0.1}Nb_{0.1}O₂ should be the lowest of all these samples at temperatures below 500°C.

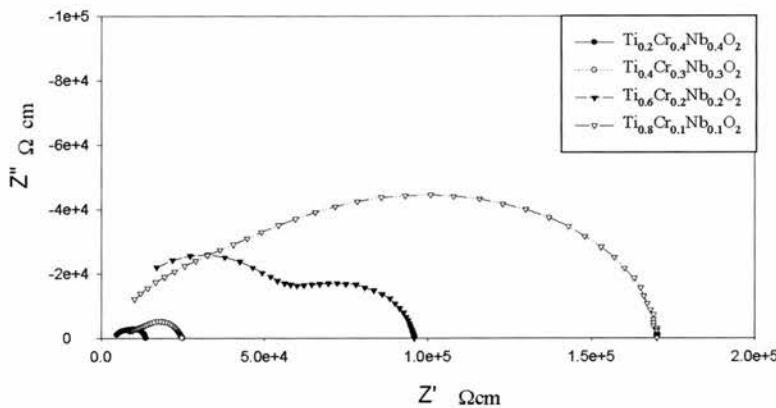


Fig.4.56 Geometry and density corrected Nyquist Impedance plot for $Ti_{1-2x}Cr_xNb_xO_2$ at 378°C

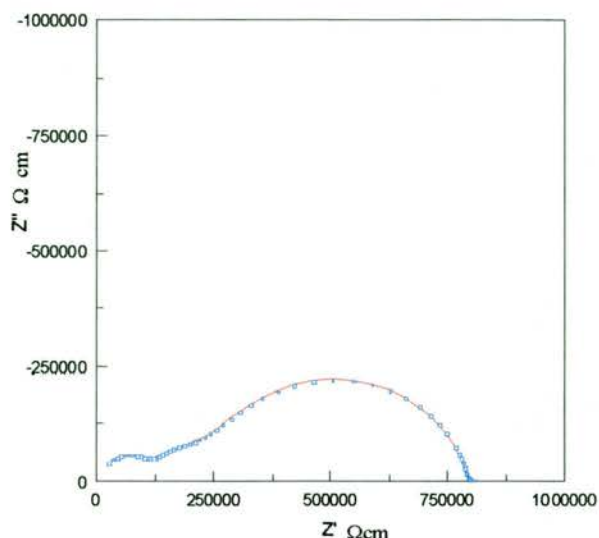
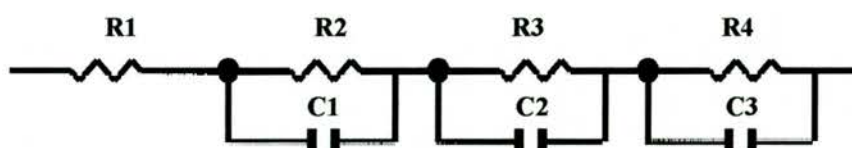
Cr_{0.5}Nb_{0.5}O₂

Fig.4.57 Geometry and density corrected Nyquist Impedance plot for Cr_{0.5}Nb_{0.5}O₂ at 174°C

The resistance of Cr_{0.5}Nb_{0.5}O₂ is too low to be visible in (Fig.4.56), but (Fig.4.57) shows that the resistance at low temperature is mostly due to the grain boundary contribution. The bulk resistivity at 174°C is 120 kΩcm and the two grain boundaries are clearly visible. gb1 has the resistivity has of 120 kΩcm and the second grain boundary, gb2, is 560 kΩcm (Table 4.16).

Refinement of the data using a simple 3 sub-circuits model:



it was possible to fit low temperature impedance data to get the activation energies for the bulk and the grain boundaries. By 300°C the bulk component has moved to high frequency and only the two grain boundaries can be seen. The grain boundary is no longer visible by 500°C. At 100°C the bulk accounts for 25% of the total resistivity, and this drops to ~5% by 200°C. In the modulus plot (Fig.4.58) the bulk capacitance is seen to increase with increasing temperature which may either indicate the change in the polarisability of the bulk or may be an artefact of the Solartron instrument itself.

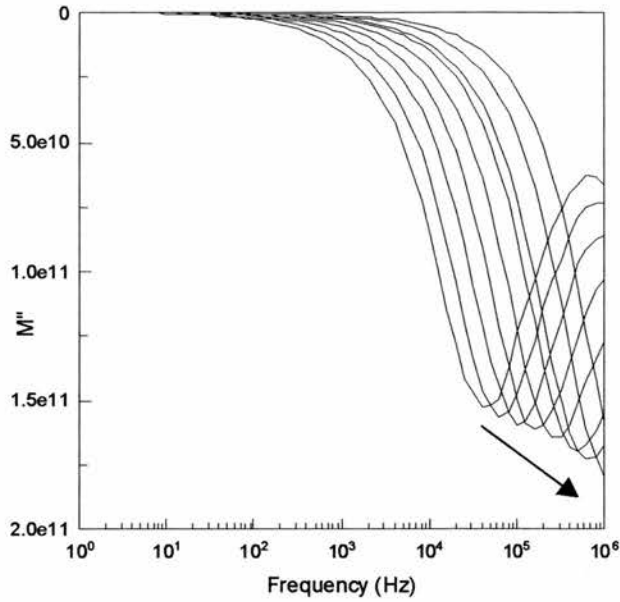


Fig.4.58 Modulus plot for $Cr_{0.5}Nb_{0.5}O_2$ from $86^\circ C$ to $200^\circ C$. The arrow shows increasing temperature

The activation energy of the grain boundaries is low; gb1 $E_a=0.46\pm 0.02$ eV and gb2 $E_a=0.37\pm 0.02$ eV (Fig.4.59). The total conductivities were plotted in a separate Arrhenius plot (Fig.4.60), and were found to have $E_a=0.68\pm 0.01$ eV on heating and $E_a=0.62\pm 0.01$ eV on cooling.

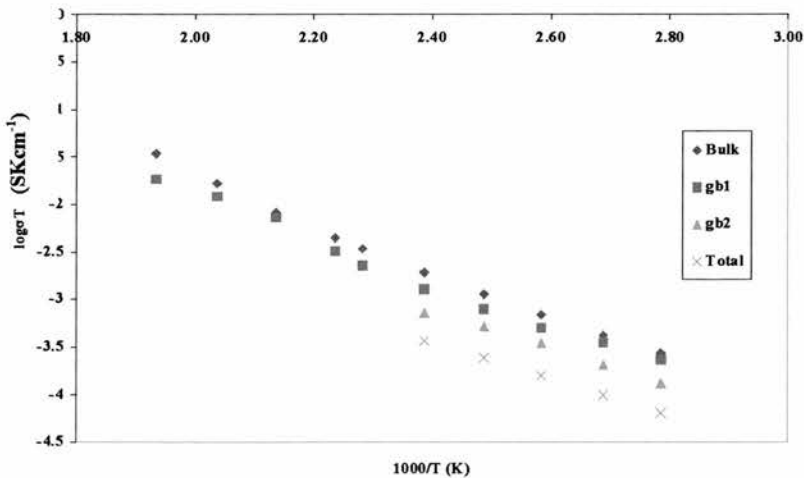


Fig.4.59 Arrhenius plot for $Cr_{0.5}Nb_{0.5}O_2$ for the bulk, the total and the gb conductivities at low temperatures

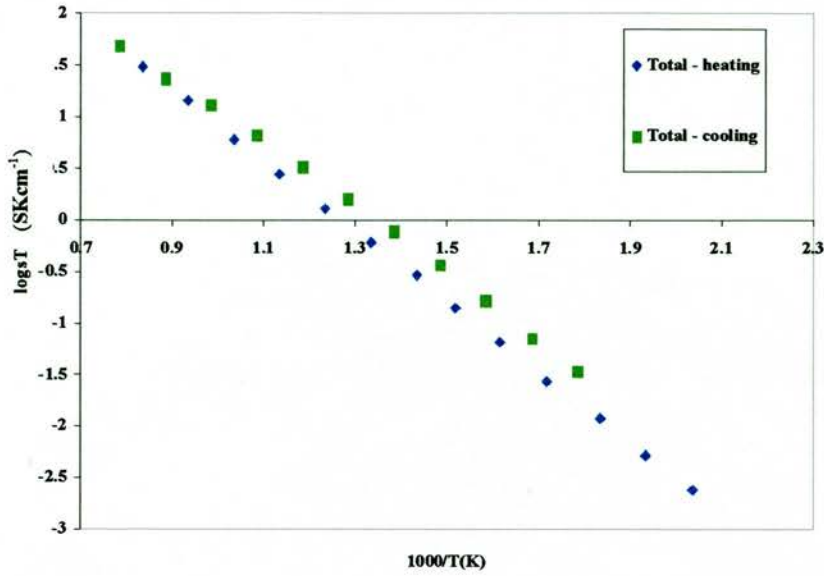
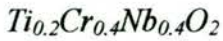


Fig.4.60 Arrhenius plot for $Cr_{0.5}Nb_{0.5}O_2$ for the the total conductivity across the temperature range

Table 4.16 Impedance data for $Cr_{0.5}Nb_{0.5}O_2$

Temperature	174°C
Ea total (eV) Heating:	0.68±0.02
Cooling:	0.62±0.02
R bulk (kΩcm)	120
Fa bulk (eV)	0.49±0.02
C bulk (Fcm ⁻¹)	1.3±0.1x10 ⁻¹¹
R gb1(kΩcm)	170
Ea gb1 (eV)	0.37±0.02
Cgb1 (Fcm ⁻¹)	9.5±0.1x10 ⁻¹⁰
R gb2(kΩcm)	560
Ea gb2	0.46±0.02
Cgb2	3.5±0.1x10 ⁻⁹



Similar to Cr_{0.5}Nb_{0.5}O₂, three components in the impedance response are clearly visible; the bulk, which disappears by 300°C, and the two grain boundaries. Although the grain boundaries are quite distinct at 300°C, they start to overlap significantly by 400°C (Fig.4.61), becoming increasingly difficult to separate.

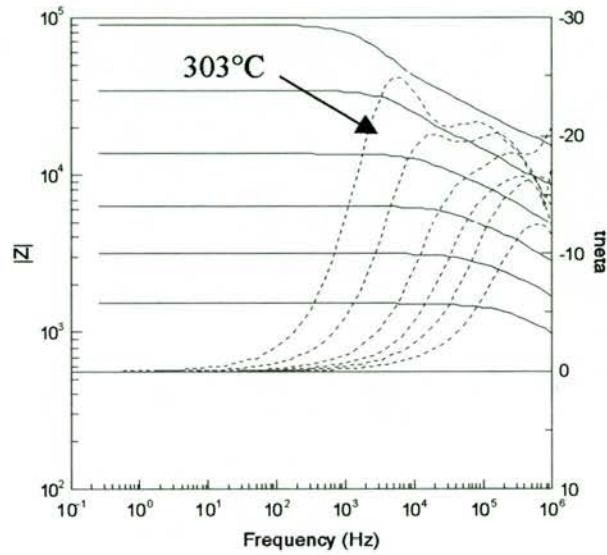


Fig.4.61 Geometry and density corrected bode plot for $Ti_{0.2}Cr_{0.4}Nb_{0.4}O_2$ at 303°, 339°, 378°, 424°, 476°, and 537°C

Table 4.17 Impedance data for $Ti_{0.2}Cr_{0.4}Nb_{0.4}O_2$

Temperature	303°C
Ea total (eV) Heating:	0.75±0.01
Cooling:	0.63±0.01
R gb1(kΩcm)	60
Ea gb1 (eV)	0.93±0.02 heating 0.77±0.02 cooling
Cgb1 (Fcm ⁻¹)	9.5±0.5x10 ⁻¹⁰
R gb2(kΩcm)	20
Cgb2	1±1x10 ⁻⁹

Although it was not possible to separate the bulk response at these temperatures, the two grain boundaries again account for the majority of resistance at low temperatures up to $\sim 600^\circ\text{C}$. At 300°C the main grain boundary observed at low frequency, gb1, accounts for $\sim 70\%$ of the resistivity ($60000\ \Omega\text{cm}$) and the grain boundary occurring at high frequency, gb2, accounts for the $\sim 25\%$ of the resistivity ($20000\ \Omega\text{cm}$) (Table 4.17).

(Fig.4.62) shows the Arrhenius plot for the total conductivity and that of the main grain boundary. As well as having different activation energies on cooling, the sample also showed that the grain boundary resistances are ~ 10 times lower on cooling. This could either be due to the sintering of grain boundaries at 1000°C or a partial reduction of the sample, resulting in higher conductivity of the bulk and the grain boundary components.

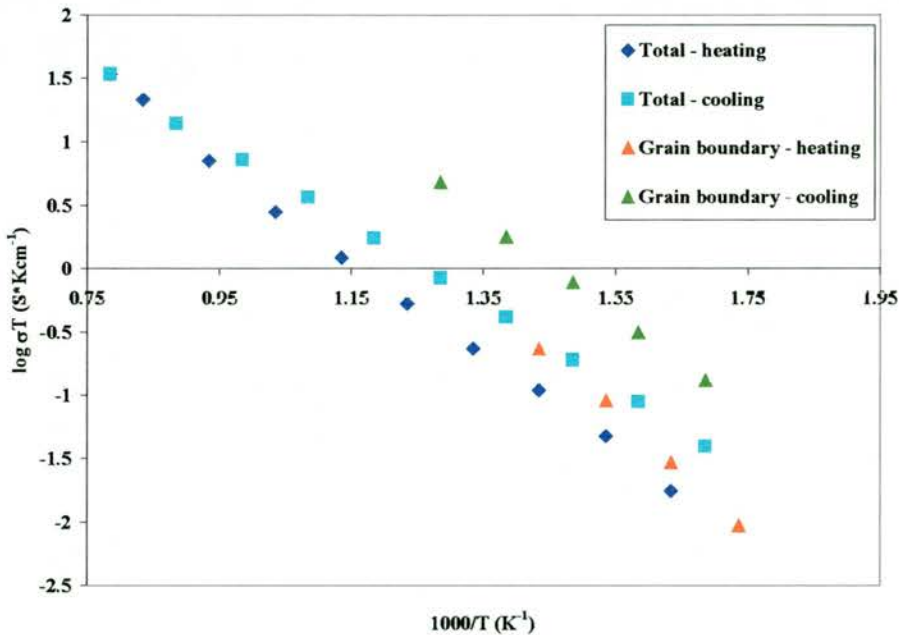
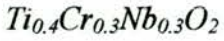


Fig.4.62 Arrhenius diagram for $\text{Ti}_{0.2}\text{Cr}_{0.4}\text{Nb}_{0.4}\text{O}_2$



In this sample there are also three visible components in the impedance plot, and as before, aside from the bulk, there are two grain boundaries. There is a greater degree of overlap between the two grain boundaries. When looking at the Bode plot of $Ti_{0.2}Cr_{0.4}Nb_{0.4}O_2$ and $Ti_{0.4}Cr_{0.3}Nb_{0.3}O_2$ (Fig.4.63) at 303°C it can be seen that the second, higher frequency grain boundary is not as easily distinguishable in the $Ti_{0.4}Cr_{0.3}Nb_{0.3}O_2$ and the bulk is now much more resistive, which can also be seen from the impedance plot (Fig.4.64).

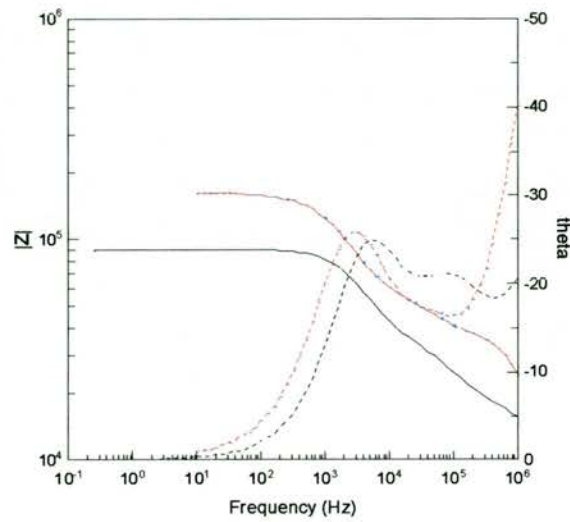


Fig.4.63 Geometry and density corrected bode plot for $Ti_{0.2}Cr_{0.4}Nb_{0.4}O_2$ (black) and $Ti_{0.4}Cr_{0.3}Nb_{0.3}O_2$ (red) at 303°C

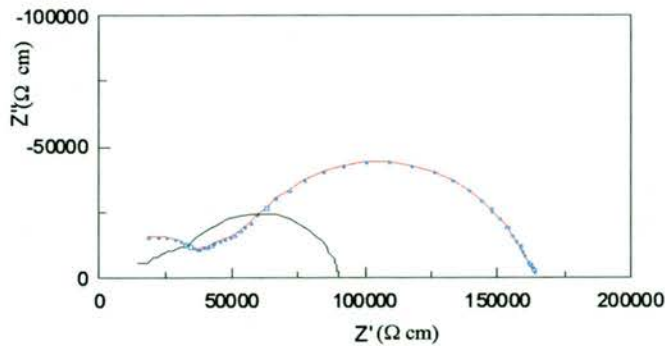
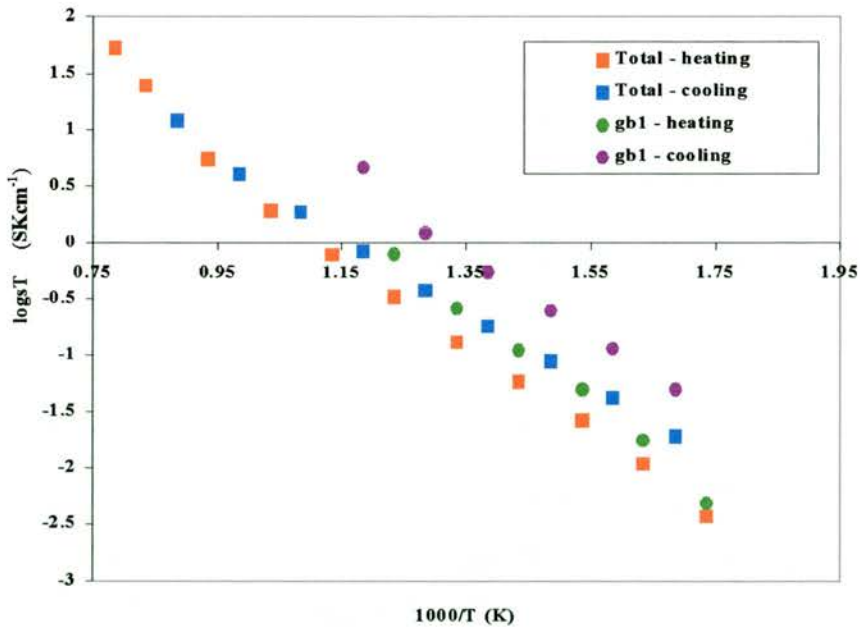


Fig.4.64 Geometry and density corrected Nyquist Impedance plot for $Ti_{0.4}Cr_{0.3}Nb_{0.3}O_2$ (red) and $Ti_{0.2}Cr_{0.4}Nb_{0.4}O_2$ (black) at 303°C

Table 4.18 Impedance data for Ti_{0.4}Cr_{0.3}Nb_{0.3}O₂

Temperature	303°C
Ea total (eV) Heating:	0.73±0.01 (300-700°C) 1.30±0.01 (700-1000°C)
Cooling:	1.30±0.01 (700-1000°C) 0.66±0.01 (300-700°C)
R bulk (kΩcm)	41.5
Ea bulk (eV)	1.30±0.01
C bulk (Fcm ⁻¹)	4±1x10 ⁻¹²
R gb1(kΩcm)	115
Ea gb1 (eV)	0.84±0.01 heating 0.75±0.02 cooling
Cgb1 (Fcm ⁻¹)	9.0±0.5x10 ⁻¹⁰

The resistivity of the bulk at 300°C was 41.5 kΩcm, ~25% of the total resistance, and the two grain boundaries account for the rest of the resistance with the low frequency gb1 having the resistivity of 115 kΩcm, accounting for ~70% of the total resistance (Table 4.18), and gb2 accounts for 5% of the total resistance.

Fig.4.65 Arrhenius plot for Ti_{0.4}Cr_{0.3}Nb_{0.3}O₂

The Arrhenius plot shows the activation energy for the total conduction and gb1. From 700° to 1000°C the activation energy is very high at 1.30±0.01 eV, and can be considered to be an activation energy of the bulk response only, as the grain boundary contribution to the resistance disappears by 600°C. The total E_a on the cooling cycle is lower than on the heating cycle at 0.66±0.01 eV (700°-300°C). This may in part be due to the lower grain boundary resistivity (Fig.4.65), which at 300°C on cooling is 12kΩcm i.e. 10 times lower than on heating. The E_a of gb1 on cooling is lower than for heating at 0.75±0.01 eV (700°-300°C).

The bulk response at these temperatures is impossible to separate and data at lower temperatures is required to study the electrochemistry of these materials in more detail.



As x is decreasing to 0.2 the bulk resistance is seen to play a major role in the resistance of the material at lower temperature. As before, at least three components are visible; the bulk and the two grain boundaries. Only one grain boundary is visible, however, up to 700°C as there is a very large overlap between the low frequency and the much smaller, high frequency grain boundary

Again there is a change in the material with thermal cycling. The grain boundary is not only visible with initial heating, but plays a major role in the resistance of the material accounting for almost 50% of the resistance up to ~700°C. On cooling the grain boundary is very small and accounts for <5% of the total resistance (Fig.4.66). This shows a change in the grain boundary with thermal cycling. The possibility of cation migration or the effect of accumulation of impurities in the grain boundaries could cause the observed decrease.

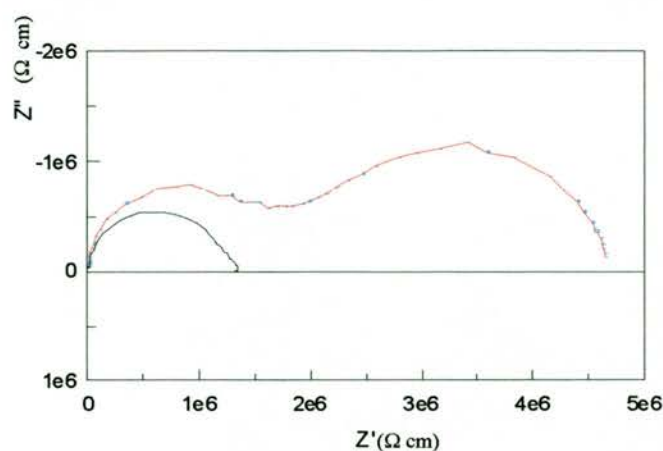


Fig.4.66 Geometry and density corrected Nyquist Impedance plot for $Ti_{0.6}Cr_{0.2}Nb_{0.2}O_2$ at 303°C on heating (red) and 320°C on cooling(black)

Table 5.19 Impedance data for $Ti_{0.6}Cr_{0.2}Nb_{0.2}O_2$

Temperature	174°C
Ea total (eV) Heating:	1.55±0.01 (>600°C) 0.77±0.01 (600°-200°C)
Cooling:	1.37±0.01 (>600°C) 0.71±0.01 (600°-200°C)
Ea bulk (eV) Heating:	0.69±0.01
Cooling	0.71±0.01
C bulk (Fcm ⁻¹)	5.0±0.5x10 ⁻¹²
R gb1(kΩcm)	120
Ea gb1 (eV)	0.83±0.01
Cgb1 (Fcm ⁻¹)	4.0±0.5x10 ⁻¹⁰

The total, the bulk and the grain boundary conductivities are plotted in the Arrhenius plot (Fig.4.67). With heating, the bulk accounts for ~50% of the total resistance. On cooling, however, the bulk is seen to account for the majority of the total resistance and $E_a=0.71\pm0.01$ eV, is the same as that for the total. At temperatures above 600°C the grain boundary has no or insignificant contribution to the total resistance and the total resistance, can thus be considered to consist solely of the bulk resistance.

Although there are at least two grain boundaries, due to the large overlap between them and the bulk, and the small size of the high frequency grain boundary arc, only the low frequency grain boundary was analysed. Although on heating it accounts for ~50% of the total resistance, after it disappears at ~600°C, it is not visible on the cooling cycle. There is a small grain boundary on cooling, but it is not clear whether it is the low or the high frequency grain boundary due to a large overlap with the bulk.

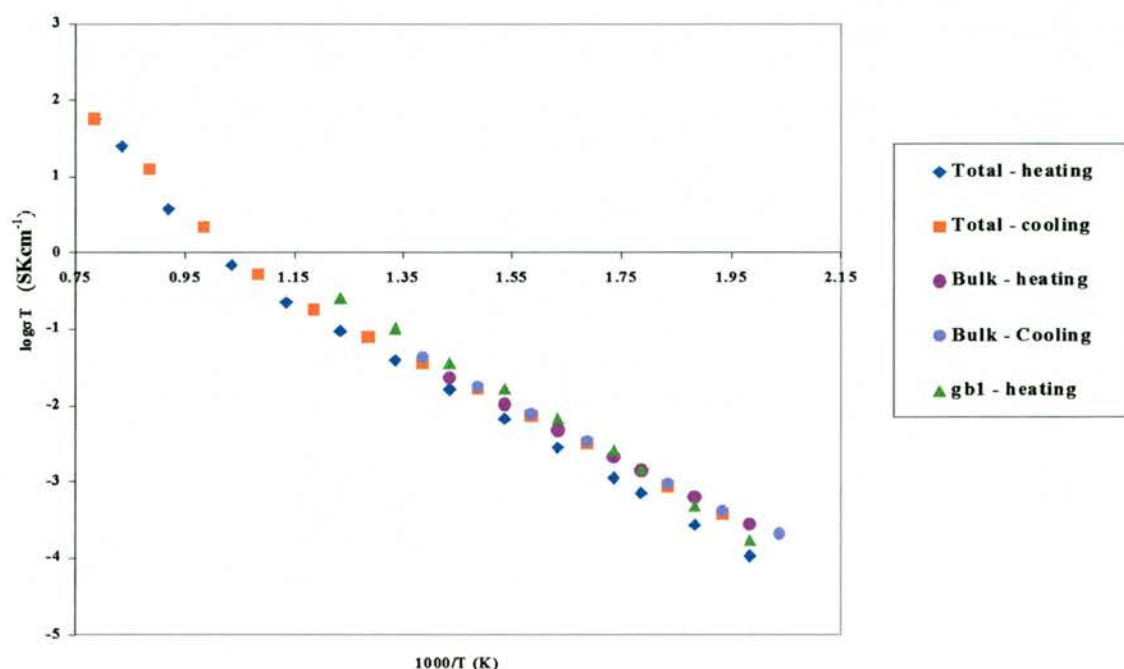


Fig.4.67 Arrhenius plot for $Ti_{0.6}Cr_{0.2}Nb_{0.2}O_2$



Due to the low density of this sample of ~68% of theoretical, the impedance data shows two large, overlapping grain boundaries. Although it is clear that they are accounting for the vast majority of the resistance up to ~700°C it is not possible to separate the bulk at temperatures >200°C. Hence only the total resistance was calculated which gives a straight line across the temperatures in the Arrhenius plot (Fig.4.68), with $E_a=1.07\pm 0.01$ eV on heating and $E_a=1.15\pm 0.01$ eV on cooling.

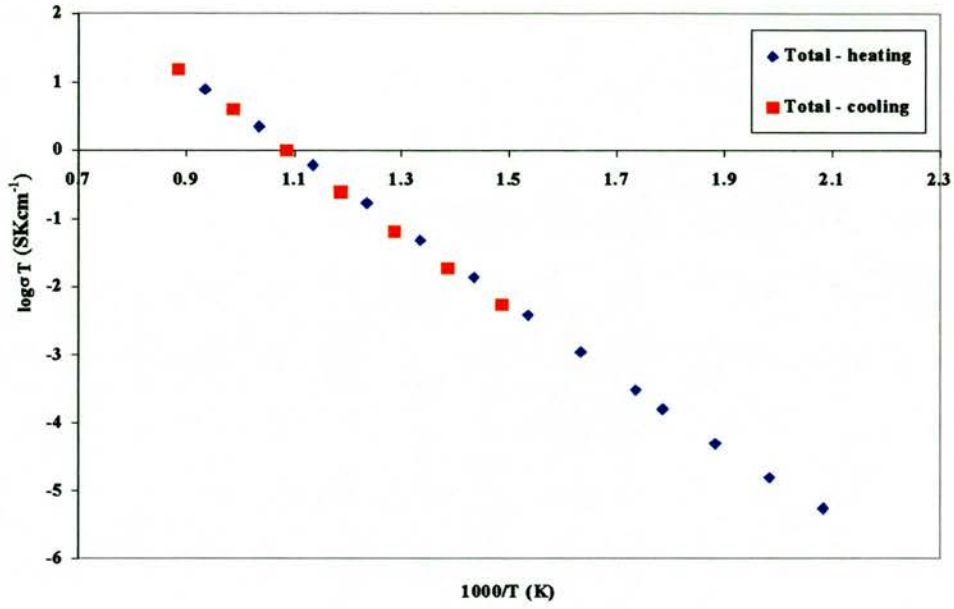


Fig.4.68 Arrhenius plot for $Ti_{0.8}Cr_{0.1}Nb_{0.1}O_2$

4.7 Conclusion

It was originally thought that due to their high conductivity in their reduced form, niobium titanates exhibit a real promise as a replacement for Ni-current collectors in SOFC. Nb₂TiO₇ is reduced to Nb_{1.33}Ti_{0.67}O₄ which has a rutile type structure, and complete reduction is achieved in 72 hours. Both phases display n-type conductivity, and under hydrogen at 900°C, conductivities of up to 200-300 Scm⁻¹ are observed. Single cell tests on the sample showed a better stability at high temperature and reducing atmosphere than a dip of pure nickel slurry. Nb_{1.33}Ti_{0.67}O₄ achieved power outputs of >0.4Wcm⁻² and the power output was seen to increase with time.

In the study of these materials a number of problems associated with this material were found:

- In its oxidised form Nb₂TiO₇ has a very low thermal expansion coefficient of 2.59x10⁻⁶ K⁻¹ (300°C-900°C), and in its reduced, rutile form its thermal expansion is 3.21x10⁻⁶ K⁻¹ (300°C-900°C). The change in the thermal expansion upon reduction is ~25%, which in an operating fuel cell may in itself cause cracking.
- Reducing Nb₂TiO₇ increases the theoretical density of 4.55 gcm⁻³ to 5.38 gcm⁻³ for Nb_{1.33}Ti_{0.67}O₄. Very slow heating rates were required when reducing the sample under flowing 5%H₂/Ar, to prevent the cracking of pellets.
- Nb₂TiO₇ when studied as a composite with Ce_{0.8}Gd_{0.2}O_{1.9}, niobium reacted with ceria at temperatures above 900°-950°C to form CeNbO₄. Niobium was also seen to react with ceria when ceria was used as a dopant. Thus Nb_{1.33}Ti_{0.67}O₄ may never be used in the CGO anode.

Doping with Zr was successful, but only when substituting for Ti. This is probably due to similar sizes of Nb, Ti and Zr, leading to increase in the unit cell in both the oxidised and the reduced samples. In the oxidised form, Nb₂TiO₇ does not accept oxygen vacancies, thus when substituting Zr for Nb, TiO₂ rutile phase is observed. Upon reduction, however, TiO₂ phase was no longer present, and the unit cell was the same as that of Nb_{0.67}Ti_{0.33}O₂, indicating that Zr may go on to the now larger Nb/Ti site, however more detailed x-ray analysis is required to determine if that is the case.

Doping with ZrO₂ and Fe₂O₃ increased the thermal expansion of the reduced sample to $6.28 \pm 0.05 \times 10^{-6} \text{ K}^{-1}$ for 2.5% Fe and $6.09 \pm 0.05 \times 10^{-6} \text{ K}^{-1}$ for 15% Zr. The mismatch in the thermal expansion between the reduced and the oxidised sample is still very high, with a three-fold increase in the thermal expansion coefficient upon reduction. This makes these materials unsuitable for use in the anode of the fuel cell.

A range of samples were made in the range Nb₂Ti_{1-x}Zr_xO₇ where $0 \leq x \leq 1$. Above ~20% dopant level, ZrO₂ impurity was observed indicating that the solubility level has been reached.

The Ti_{1-2x}Cr_xNb_xO₂ solid solution series was investigated because they crystallise in a rutile structure, which may facilitate the reduction of niobium and show high conductivity. With low Cr content $x=0.1-0.3$, the samples showed good conductivities of $\sim 20 \text{ Scm}^{-1}$ in reducing conditions. The samples, however, did not seem to reach the maximum conductivity after 48 hours of reduction, thus their conductivity may be significantly higher than the values reported in this thesis. Large hysteresis and very slow re-oxidation kinetic were observed in the conductivity as a function of $p(\text{O}_2)$ data. Again, equilibrium in these samples may not have been achieved. The thermal expansion of these samples was high with $8.57 \times 10^{-6} \text{ K}^{-1}$ for the $x=0.1$, dropping to $6.04 \times 10^{-6} \text{ K}^{-1}$ for the $x=0.5$. There was little change in the thermal expansion on reduction, which is important for fuel cell application.

Due to their high conductivities and thermal expansion, these materials show good promise for use as a current collector. Further work, however is required to increase the conductivity of these materials to above 100 Scm^{-1} before they can be considered for that purpose. Impedance studies showed changes in the grain boundary and bulk properties with thermal cycling. $p(\text{O}_2)$ data showed that stability to different oxygen partial pressures may not be good due to the large difference between the initial conductivity at atmospheric $p(\text{O}_2)$ value and the final, post reduction conductivity at atmospheric $p(\text{O}_2)$. Hence long term ageing studies at different temperatures and atmospheres are required in order to examine this phenomenon more closely.

TEM studies of Ti_{1-2x}Cr_xNb_xO_{2-x} showed that reduction of Ti_{1-2x}Cr_xNb_xO₂ produces crystallographic shear defects, which remove oxygen vacancies. This may be responsible for a change in the conductivities of the bulk and the grain boundary from heating to cooling, which was seen in the AC impedance data.

4.8 References:

- 1 N.F.Fedorov, O.V.Mel'nikova, V.A.Saltykova, A.P.Pivovarova, M.Dib, V.I.Strakhov, *Russ.J.Inorg.Chem.(Engl.Transl.)*, (1989), **34 (5)**, 741
- 2 E.A.Durbin, C.G.Harman, *BMI-791* (1952) 1/12, 5, 7, N.S.A. 7, (1953) 1109
- 3 Wong-Ng, W., McMurdie, H., Paretzkin, B., Hubbard, C., Dragoo, A., *Powder Diffraction*, (1989), **4**, 54
- 4 M.Gasperin. *J. Solid State Chem.*, (1984), **53**, 144
- 5 C.Keller, *Zeitschrift fuer Anorganische und Allgemeine Chemie*, (1962), **318**, 89
- 6 A.Petersen, H.K.Mueller-Buschbaum, *Zeitschrift fuer Anorganische und Allgemeine Chemie*, (1992), **609**, 51
- 7 A.D.Wadsley, *Acta Cryst.*, (1961), **14**, 660
- 8 C.M.Reich, A.Kaiser and J.T.S.Irvine, *Fuel Cells-From Fundamentals to Systems*, (2001), **1**, 249
- 9 J.Sfeir, "Alternative anode materials for methane oxidation in solid oxide fuel cells", Thesis (N^o. 2446) (2001), Ecole Polytechnique Federale de Lausanne
- 10 In *Gmelin Handbuch der Anorganischen Chemie*, 49, TB3
- 11 N.A.Godina, T.I.Panova and E.K.Keler, *Izvestiya Akademii Nauk SSSR, Neorganicheskie Materialy*, (1971), **7**, 1205
- 12 G.G.Kasimov, N.D.Samsonova, M.F.Sorokina and L.D.Finkel'shtein, *Izvestiya Akademii Nauk SSSR, Neorganicheskie Materialy*, (1978), **14**, 301
- 13 M.A.Tena, P.Escribano, G.Monros, J.Carda, J.Alarcon, *Mat. Res. Bull.*, (1992), **27**, 1301
- 14 N.N.Greenwood and A.Earnshaw, "Chemistry of the Elements", 2nd ed., (1997), Butterworth-Heinemann, Oxford, 1005
- 15 P.Kofstad, *J.Less-Common Metals*, (1967), **13**, 635

Chapter 5. Strontium Niobates

5.1 INTRODUCTION.....	169
5.1.1 <i>Strontium Niobates: General outlook.....</i>	169
5.1.2 <i>Experimental</i>	171
5.2 Sr₄Nb₂O₉ AND Sr₄Nb₂O_{9.8}.....	172
5.2.1 <i>Structure.....</i>	172
(1) STRUCTURAL CHANGES ON REDUCTION.....	173
(2) PRELIMINARY TEM STUDIES OF Sr ₄ Nb ₂ O ₉ REDUCED AT 1000°C.....	175
5.2.2 <i>Dilatometry</i>	178
5.2.3 <i>Thermogravimetric analysis (TGA).....</i>	179
5.2.4 <i>AC Impedance studies.....</i>	180
5.2.5 <i>DC Conductivity studies</i>	185
5.3 Sr₂Nb₂O₇, Sr₂Nb₂O_{7.8}, AND Sr₅Nb₅O₁₇.....	187
5.3.1 <i>Structure.....</i>	187
5.3.2 <i>Dilatometry</i>	189
5.3.3 <i>Thermogravimetric analysis (TGA).....</i>	192
5.3.4 <i>DC Conductivity studies</i>	193
5.3.5 <i>Conductivity as a function of p(O₂).....</i>	196
5.3.6 <i>AC Impedance</i>	197

5.4 SrNb₂O₆, SrNb₂O_{5.98} AND SrNb₂O_{5.76}.....	198
5.4.1 Structure.....	198
5.4.2 TGA.....	200
5.4.3 Dilatometry	200
5.4.4 DC Conductivity studies	204
5.4.5 Conductivity as a function of p(O ₂).....	206
5.4.6 AC Conductivity Studies	208
5.5 Sr_{0.6}NbO₃.....	210
5.5.1 Structure.....	210
5.5.2 Conductivity Studies	211
5.5.3 Experimental	211
6.5.4 X-ray powder diffraction	212
5.6 CONCLUSIONS.....	214
5.7 REFERENCES	215

5.1 Introduction

5.1.1 Strontium Niobates: General outlook

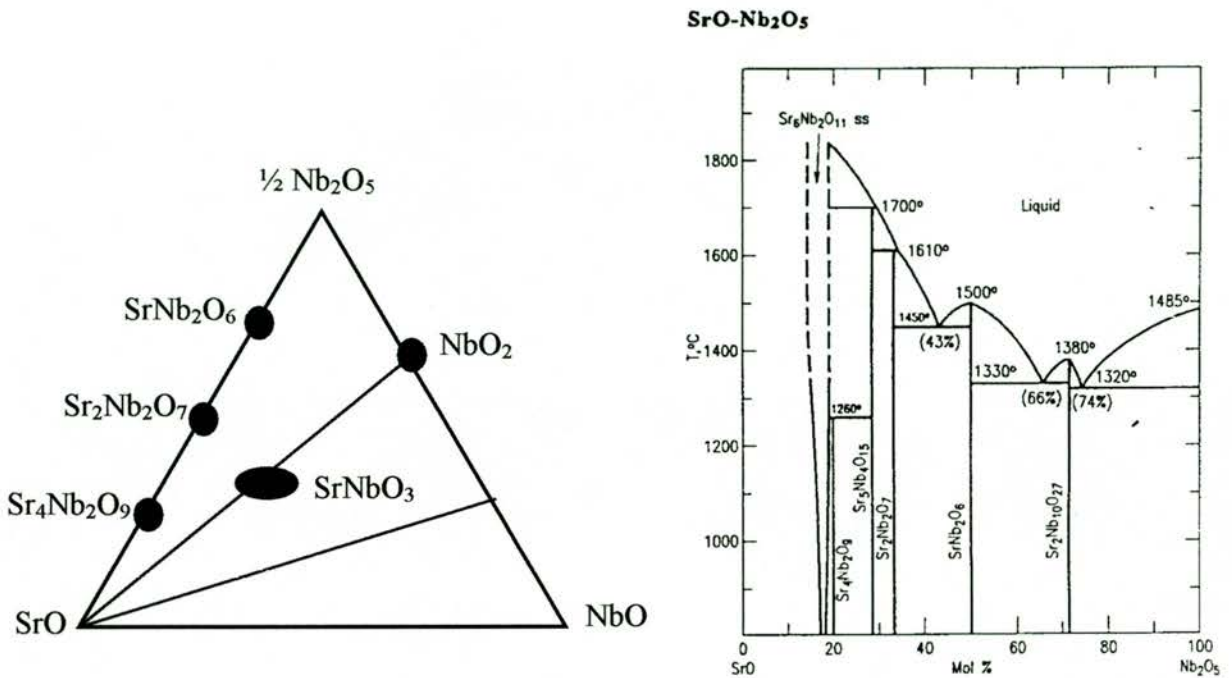


Fig.5.1 Phase diagram of the system SrO-Nb₂O₅ [1]

As can be seen from the phase diagrams in (Fig.5.1) there are many known Strontium Niobates whose structures and properties have been investigated. When looking for electronically conducting oxides, niobates are strong candidates due to their high electronic conductivity upon reduction. As will be discussed later, there have been a number of studies into the electronic conductivity of strontium niobate phases, but mostly these were performed below 300K.

The aim of this study was to examine the conductivity of these materials in air and under reducing conditions, at temperatures up to 900°C. Relating the conductivity to the structure of the materials may aid in making other niobium based materials with high electronic conductivity.

A number of perovskite related phases were synthesised in which the Sr to Nb ratio was gradually reduced. By increasing the Nb content it is possible to increase the electronic conductivity. The range of compounds with the general formula of $\text{Sr}_x\text{Nb}_y\text{O}_{x+2.5y}$, moving towards a higher Nb content, were looked at. These phases were studied:

- $\text{Sr}_4\text{Nb}_2\text{O}_9$
- $\text{Sr}_2\text{Nb}_2\text{O}_7$
- SrNb_2O_6
- $\text{Sr}_{1-x}\text{NbO}_3$

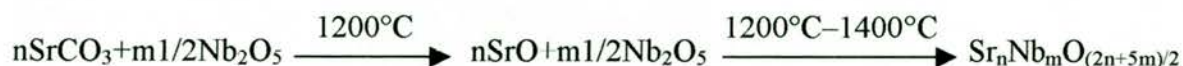
$\text{Sr}_{1-x}\text{NbO}_3$ has a normal perovskite structure. The rest of the strontium phases above are a deviation from this normal perovskite structure, collectively known as the layered perovskite phases, similar to Ruddlesden-Popper phases. Going along the Nb_2O_5 -SrO line on the phase diagram (Fig.5.1), SrNb_2O_6 has the first recognisable perovskite type region, which is linked to other perovskite regions by edge-shared octahedra. This is different from the layered perovskite phases, the first of which is $\text{Sr}_2\text{Nb}_2\text{O}_7$, also known a member of the title series $\text{Sr}_n\text{Nb}_n\text{O}_{3n+2}$, where $n=4$, i.e. $\text{Sr}_4\text{Nb}_4\text{O}_{14}$. This phase consists of perovskite-like slabs cut along the (110), and stacked to accommodate the extra SrO between the layers(Fig.5.16)[2]. The normal perovskite structure is achieved in Sr_xNbO_3 where, $0.6 < x < 1$, found just off the midpoint in the Nb_2O_5 -SrO line on the phase diagram (Fig.5.1). The only other perovskite related phase on the Nb_2O_5 -SrO line is $\text{Sr}_4\text{Nb}_2\text{O}_9$, with the highest possible Sr/Nb ratio, and it has a disordered cubic perovskite structure.

As can be seen from the formula unit for the studied phases, the Sr content is being systematically halved, whilst keeping Nb content the same. Although many strontium niobates have been studied previously, due to superconducting properties of NbO and hence the interest in Nb containing materials, few studies have looked at the high temperature properties of these materials, especially under reducing conditions.

$\text{Sr}_{1-x}\text{NbO}_3$ perovskite phases were also looked at, which are known to have very high electronic conductivity at low temperatures of up to 300K, and superconductivity at temperatures of 2-9K, but have not been studied at higher temperatures. Thus their stability in reducing conditions at high temperature were investigated.

5.1.2 Experimental

$Sr_xNb_2O_{5+x}$ materials were synthesised by mixing stoichiometric ratios of pre-dried powders of $SrCO_3$ and Nb_2O_5 . The powders were calcined at $1200^\circ C$ for 24 hours, then fired at $1200-1400^\circ C$ (taken from the phase diagram for the appropriate material) for 72 hours, with intermediate regrinding:



The reduction was done in 5% H_2 /Ar at $1000^\circ C$, $1200^\circ C$ and $1350^\circ C$ for 40 hours.

$Sr_{1-x}NbO_3$ is a difficult series of materials to synthesise phase pure and fully reduced, as they require extremely reducing conditions and repetitive refiring. So a number of different methods were used to try and make these phases:

1. High temperature solid state reaction, at $1200^\circ-1400^\circ C$ in flowing Ar or 5% H_2 /Ar gas conditions, of mixed stoichiometric amounts of $Sr_4Nb_2O_9$, Nb_2O_5 and Nb metal powders. This method produced $Sr_{1-x}NbO_3$ but only if 5% H_2 /Ar was used rather than pure Ar.
2. Synthesising oxidised sample of Sr_xNbO_3 (i.e. $Sr_{2-x}Nb_2O_{5+x}$ where $x=0.4-0.8$), by firing stoichiometric amounts of $SrCO_3$ and Nb_2O_5 in air at $1200-1300^\circ C$, then reducing at $1400^\circ C$. This approach did not produce single phase Sr_xNbO_3 .

5.2 Sr₄Nb₂O₉ and Sr₄Nb₂O_{9-δ}

Sr₄Nb₂O₉ has the largest possible ratio x/y in Sr_xNb_yO_{x+2.5y} found in strontium niobates to date. Weiden et al's attempts to prepare compounds with a ratio x/y>2 failed [3], and thus they concluded that the only compounds in the system Sr-Nb-O with x/y>1 are Sr₄Nb₂O₉ and Sr₅Nb₄O₁₅. However, that is inaccurate as amongst some of the x/y>1 strontium niobates synthesised are Sr₇Nb₆O₂₁ [4] and Sr₆Nb₂O₁₁.

5.2.1 Structure

Previous work on Sr₄Nb₂O₉ reported the structure to be triclinic with a=5.820Å, b=14.392Å, c=5.819, α=119.734, β=89.827, γ=90.221, space group P-1(2) [3]. Sr₄Nb₂O₉ is a member of the alkali earth niobates with the general formula A'₃(A''_{1+x}B_{2-x})O_{9-3x/2} (A'=Sr,Ba; A''=Ca, Sr; B=Nb, Ta). Thus the more exact way of representing the structure is as Sr₃(SrNb₂)O₉, and it can be described as the perovskite related structure in which A'' and B (i.e. SrNb₂) occupy the octahedral sites and A' (i.e.Sr₃) occupies the 12 co-ordinated site (Fig.5.2). Thus there is a sequence of two Sr+Nb and one Nb-only layers, giving a 2:1 order. Increasing the Sr content will increase the Sr:Nb ratio on the B-site, hence decreasing the average charge on the B-site. This introduces oxygen vacancies for charge compensation, more on which will be said in a later section. The much larger size of Sr²⁺ than Nb⁵⁺ means that the structure is pseudo-cubic (not triclinic as was reported by M.Weiden [3]), and the lattice parameter *a* increases with increasing Sr content [5, 8].

The results are consistent with J.Lecomte et al[5] and R.Glockner[8] et al, showing that the unit cell of Sr₄Nb₂O₉ is pseudo-cubic (P) with *a*=8.2792(8) and V=567.50(9), when made in air at 1300°-1400°C. The difference with the unit cell parameter reported by M.Weiden is due to the different synthesis procedures. M.Weiden et al reported the synthesis of Sr₄Nb₂O₉ under flowing Ar atmosphere at 1200°C, whereas the samples in this study were prepared at 1300°C in air. The mildly reducing conditions distort the structure, as will be discussed later regarding the samples reduced at 1000°C in 5%H₂/Ar.

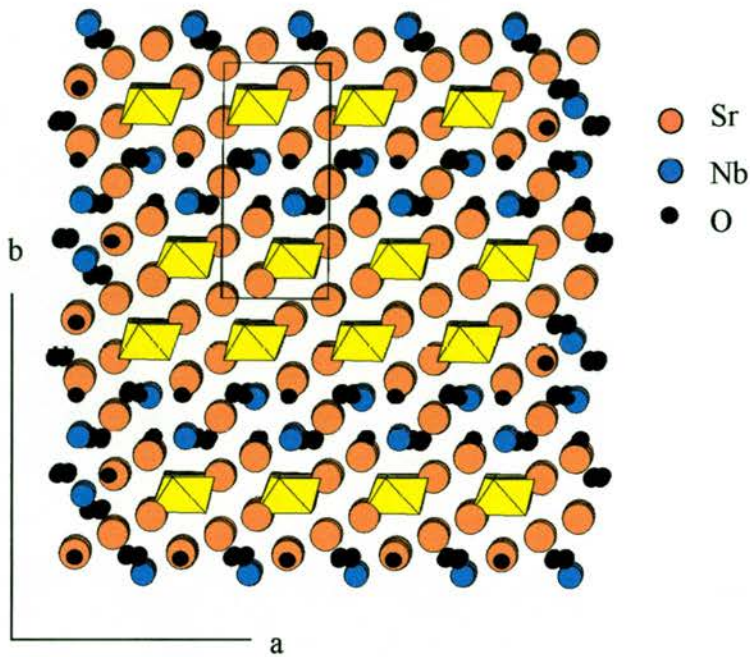


Fig.5.2 The crystal structure of $\text{Sr}_4\text{Nb}_2\text{O}_9$

(1) Structural Changes on reduction

From the x-ray diffraction pattern in (Fig.5.3), a very small change in the unit cell can be seen upon reduction at 1000°C and 1350°C , also shown in Table 5.1. In reducing conditions at 1000°C $\text{Sr}_4\text{Nb}_2\text{O}_9$, however, shows splitting of the major peaks at high angles, and additional low intensity peaks throughout the pattern. Further increase in temperature, under the same reducing conditions, produces an ordered structure with a similar, though smaller unit cell, with no visible low intensity peaks.

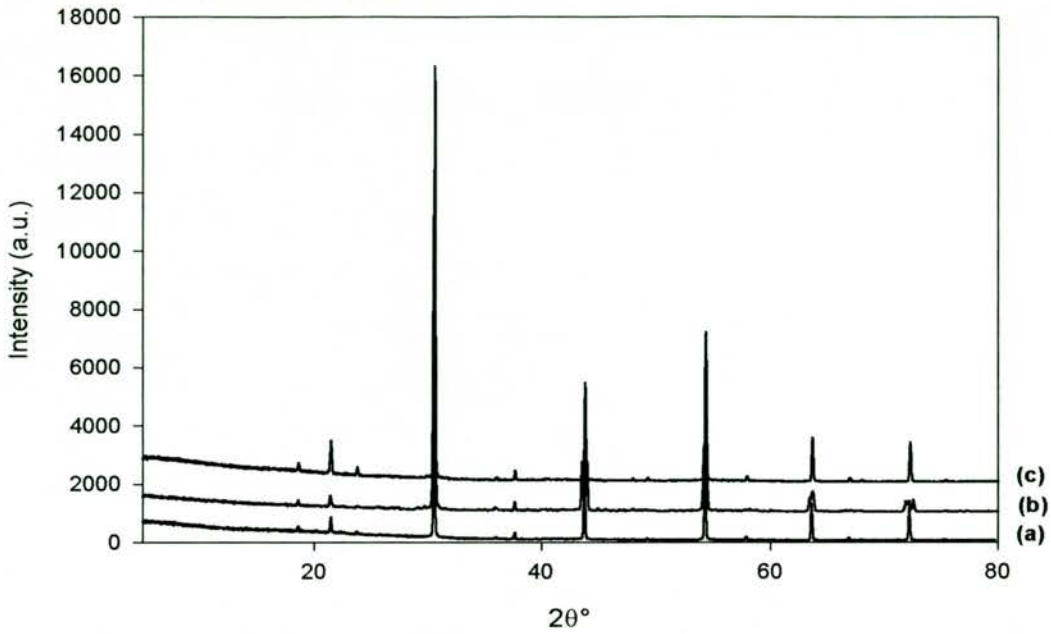


Fig. 5.3 XRD pattern of (a) $\text{Sr}_4\text{Nb}_2\text{O}_9$ as made in air, (b) $\text{Sr}_4\text{Nb}_2\text{O}_9$ reduced in flowing 5% H_2/Ar at 1000°C and (c) $\text{Sr}_4\text{Nb}_2\text{O}_9$ reduced at 1350°C in flowing 5% H_2/Ar

Table 5.1 Showing the refined unit cell parameters of $\text{Sr}_4\text{Nb}_2\text{O}_9$

Phase	Reduction T (°C)	Symmetry	a(Å)	Cell Volume(Å ³)
$\text{Sr}_4\text{Nb}_2\text{O}_9$	N/A	Cubic P	8.2792(8)	567.50(9)
$\text{Sr}_4\text{Nb}_2\text{O}_{9-\delta}$	1000	Complex microdomains, with some pseudo-cubic regions		
$\text{Sr}_4\text{Nb}_2\text{O}_{9-\delta}$	1350	Cubic P	8.2704(10)	565.69(11)

(2) Preliminary TEM studies of Sr₄Nb₂O₉ reduced at 1000°C

To understand the change in structure on reduction, TEM was performed on the sample reduced at 1000°C, as that showed additional peaks. Preliminary TEM studies were performed on a Jeol JEM 2011 microscope operating at 200 kv and equipped with a double tilt ($\pm 20^\circ$) sample holder, and the EDS analysis performed in a number of particles confirmed that the expected stoichiometry was achieved.

The structure of Sr₄Nb₂O₉ when reduced at 1000°C in flowing 5%H₂/Ar, is far more complex than the double cubic unit cell ($a=8.3\text{\AA}$) first suggested by XRD. Although in some domains such a description may be valid (Fig.5.4), a displacement to a different region in the same crystal reveals the presence of superstructure fringes; i.e. there is a long range ordering that breaks the cubic symmetry (Fig.5.5). This indicates that there is a microdomain structure, with oxygen rich and reduced domains intergrowing in the same crystals. The corresponding SAED patterns strongly support this hypothesis. The inset of (Fig.5.4) does not show any evidence of superstructure whereas the inset of (Fig.5.5) reveals the presence of superstructure reflections at $1/12 [122]_c$ (c =cubic).

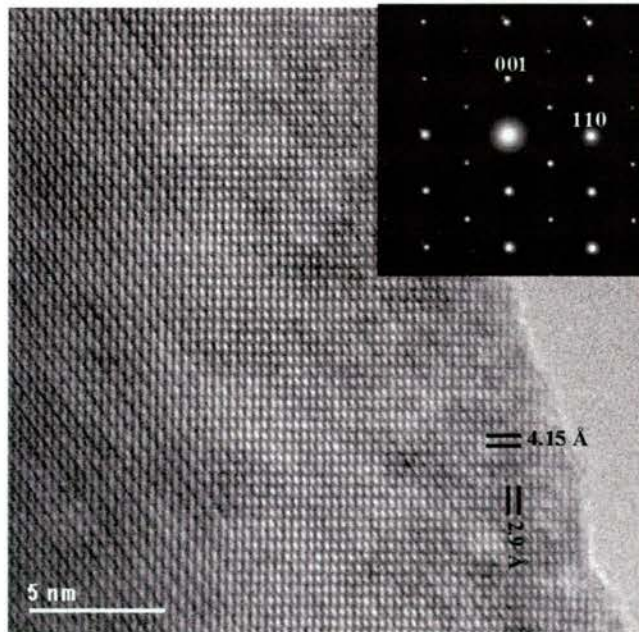


Fig.5.4 HRTEM image of a cubic domain of Sr₄Nb₂O₉ reduced at 1000°C, showing a view down the $[1-10]_c$ projection and its corresponding SAED pattern (inset)

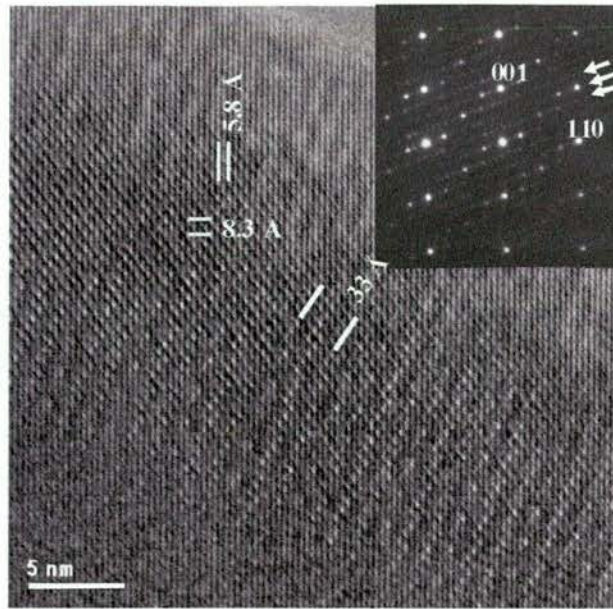


Fig.5.5 HRTEM image of a non-cubic domain recorded on a different area of the same crystal of fig.5.4. It shows a view down the $[1-10]_c$ projection and the corresponding SAED pattern (inset). Small white arrows indicate the superstructure reflections along the $[122]_c$

The structure of $\text{Sr}(\text{Sr}_{1/3}\text{Nb}_{2/3})\text{O}_3$ sintered in air was the subject of investigation by I. Levin et al [6] using a combination of HRTEM and neutron diffraction. They concluded that there were two polymorphs: a high temperature one with a pseudo-cubic symmetry, $a=8.27\text{\AA}$ (space group $Fm-3m$) and one at low temperature with a rather complex and slightly monoclinic unit cell, $a\sim 6a_c\sqrt{3}$, $b\sim 2a_c\sqrt{2}$, $c\sim a_c\sqrt{6}$. Furthermore in the low temperature polymorph, they found that there is a rather complex microdomain microstructure, derived from different phases which are stoichiometrically very close to each other. Although there are certain similarities between the low temperature polymorph and the non-cubic domains, the nature of the superstructure observed is somehow different, because the superstructure reflections observed along the $[122]$ were always commensurate and the (pseudo) cubic domains were quite frequent.

In his paper, Levin describes four types of domains in his low temperature polymorph: incommensurate (dominant), commensurate (minor), monoclinic (minor) and pseudo-cubic (very minor, with a slight Sr deficiency). In the sample studied here, only the commensurate and the pseudo-cubic structures are apparent. All of these structures are a result of a combination of factors, such as B cation ordering (1:2, 1:3 and occasionally 1:4), the tilting of the octahedra and the presence of oxygen vacancies.

The structure of the domains showing commensurate superstructure reflections is rather complex and does not involve only the $[122]_c$ as pointed out by Levin. The inset of (Fig.5.6) reveals that there are also commensurate reflections at $1/10 [123]_c$. The corresponding HRTEM image shows the presence of a large number of very small regions with a darker contrast, which could be related to the superstructure observed in the SAED patterns because they may represent some ordering.

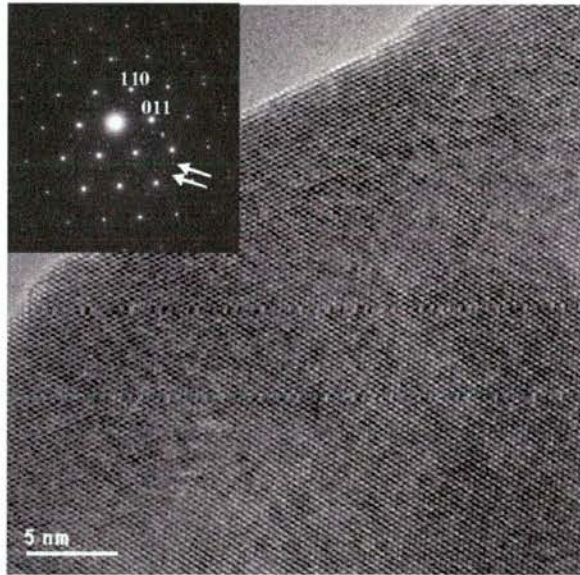


Fig.5.6 HRTEM image corresponding to the $[111]_c$ zone axis of $Sr_4Nb_2O_9$ reduced at 1000°C . A large number of darker contrast areas appear, which would be responsible for the superstructure reflection observed in the corresponding SAED pattern (inset) along the $[123]_c$.

5.2.2 Dilatometry

As can be seen from (Fig.5.7), there is very little difference observed in the thermal expansion coefficient upon reduction. When looking at a physical α curve (Fig.5.8), i.e. the change in thermal expansion coefficient with temperature, the materials seem to behave differently. The thermal expansion coefficient at $T=900^{\circ}\text{C}$ varies upon reduction. At first it is seen to drop when reduced at 1000°C to $14.8 \times 10^{-6} \text{K}^{-1}$ from $15.3 \times 10^{-6} \text{K}^{-1}$, then it rises to $18.3 \times 10^{-6} \text{K}^{-1}$ for the sample reduced at 1350°C .

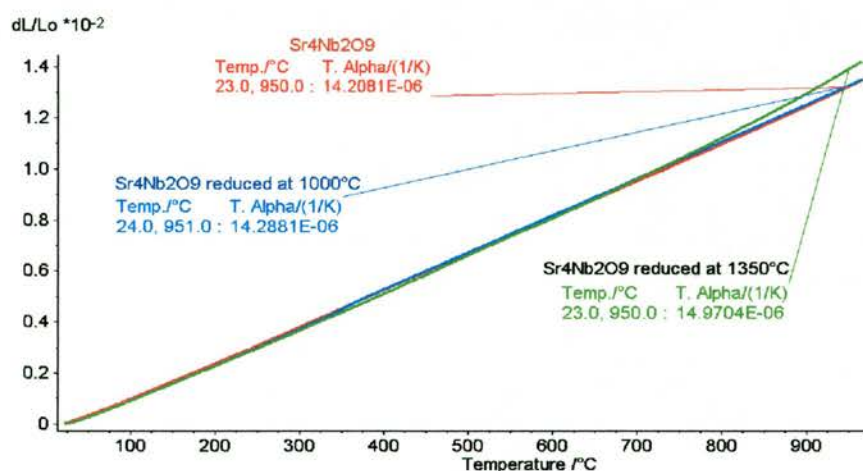


Fig.5.7 Thermal expansion data of $\text{Sr}_4\text{Nb}_2\text{O}_9$ in oxidised and reduced forms

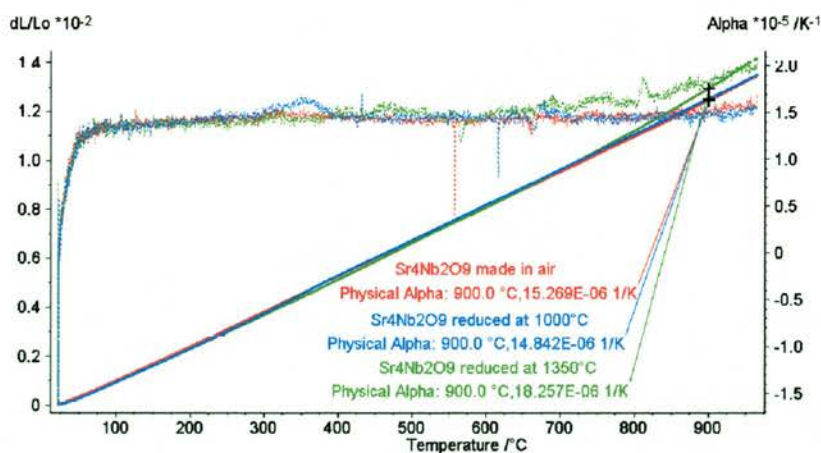


Fig.5.8 Physical α curve for $\text{Sr}_4\text{Nb}_2\text{O}_9$ as made in air and when reduced at 1000°C or 1350°C

As was seen from the crystal structure in (Fig.5.2), there is a large distance between Nb metal atoms, (~10Å). This may be stabilising the unit cell to reduction and any major structural changes in reducing conditions. This may also ultimately play a part in the low electronic conductivity of this material.

5.2.3 Thermogravimetric analysis (TGA)

The oxidation state of Nb is important when considering unit cell size and electronic conductivity of Nb based materials. The ionic radius of Nb(IV) is 0.69Å, compared to 0.64Å of Nb(V). Although a small change, it does decrease the distance between Nb atom in the structure, making the electronic transition from one d orbital to another easier. The degree of reduction, looking at the unit cell change and thermal expansion coefficient is clearly small in which $\delta < 0.01$ in the $\text{Sr}_4\text{Nb}_2\text{O}_{9-\delta}$. This is further confirmed with TGA oxidation runs on the reduced samples (Fig.5.9).

Repeated TGA runs on different analysis machines showed no perceptible weight change in the sample, and the only fluctuation in the line is due to “drift”. This confirms that $\text{Sr}_4\text{Nb}_2\text{O}_9$ is structurally stable to very reducing conditions, and niobium oxidation state is not less than 4.99, i.e. $5.00-\delta$. The slight possible weight change at 300°-500°C (Fig.5.9) may be showing water loss. It was found that alkali earth niobates and tantalates of the general formula $A'_3(A''_{1+x}B_{2-x})O_{9-3x/2}$ where (A' =Sr,Ba; A'' =Ca, Sr; B=Nb, Ta) [7], uptake water, and as a result display protonic conduction. Similarly, $\text{Sr}_4\text{Nb}_2\text{O}_9$ can be expressed as $\text{Sr}_3(\text{SrNb}_2)\text{O}_9$, and was also demonstrated to uptake water with a resultant ionic conduction, which will be discussed later.

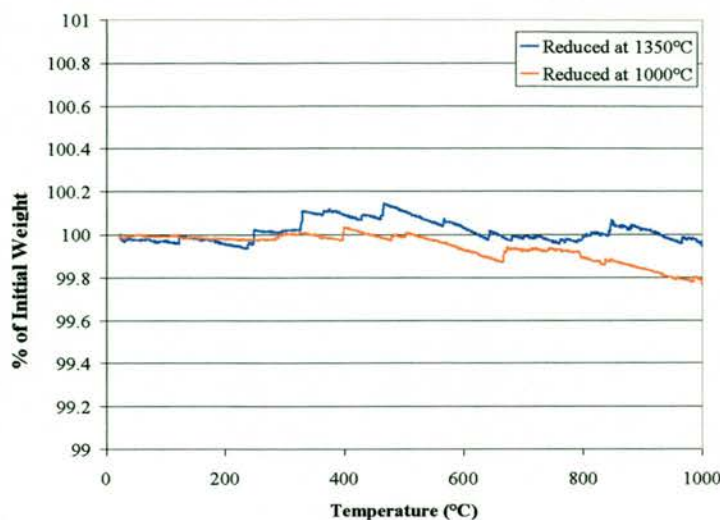


Fig.5.9 TGA oxidation runs in flowing air for the reduced $Sr_4Nb_2O_9$ samples.

5.2.4 AC Impedance studies

As can be seen in (Fig.5.10) the bulk, with a capacitance of $4.5 \pm 0.5 \times 10^{-12} \text{ Fcm}^{-1}$, accounts for the majority of the resistance. The conductivity at 900°C is $5.2 \times 10^{-5} \text{ Scm}^{-1}$.

The Nyquist plot of the reduced sample (Fig.5.11), shows the conduction at 580°C and 549°C to be mainly electronic and the resistance of the bulk is significantly lower than for the oxidised sample. The grain boundary is now an insignificant contributor to the conductivity and can not be clearly seen. The conductivity at 900°C is $2.5\text{-}2.8 \times 10^{-3} \text{ Scm}^{-1}$.

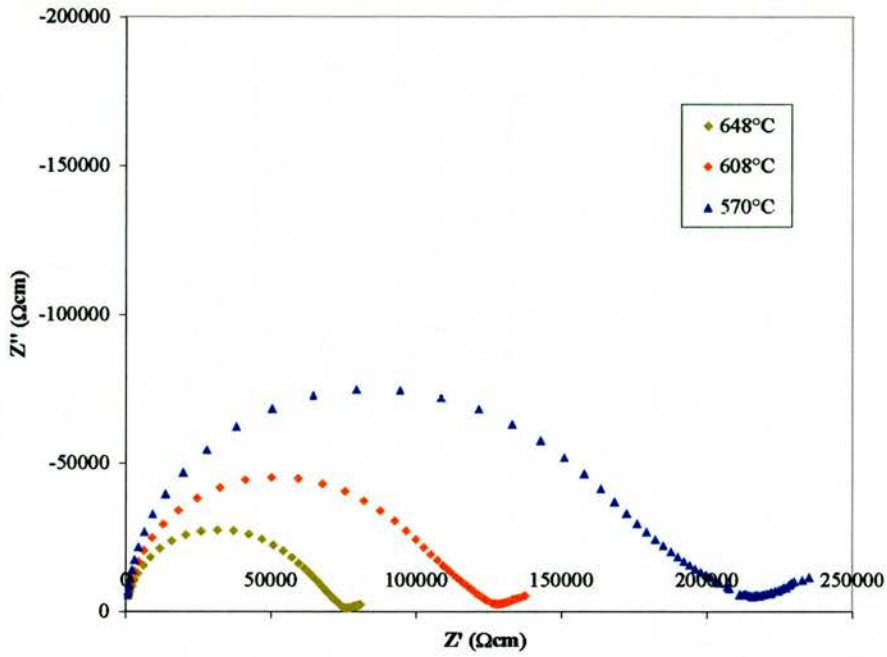


Fig.5.10 Geometry corrected nyquist Impedance plot for $Sr_4Nb_2O_9$ at various temperatures and in air

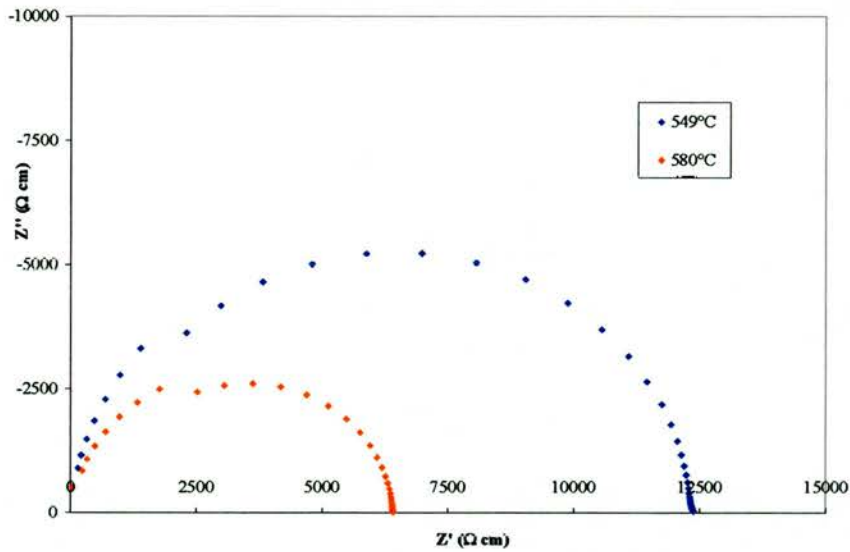


Fig.5.11 Geometry corrected impedance plots for $Sr_4Nb_2O_{9-\delta}$ reduced at 1000°C in 5% H_2/Ar

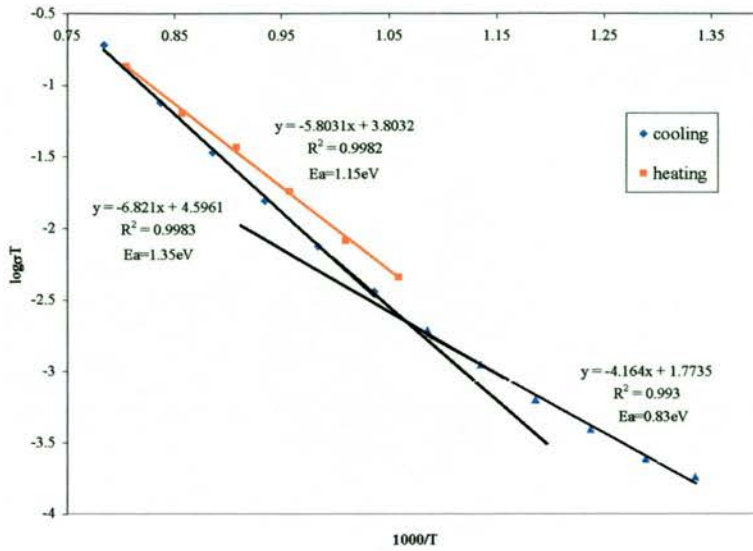


Fig.5.12 Arrhenius diagram for $\text{Sr}_4\text{Nb}_2\text{O}_9$ oxidised sample from ac impedance data

The activation energy for the total resistance was found to be $0.83 \pm 0.01\text{eV}$ for the temperature range $470^\circ\text{-}650^\circ\text{C}$ and $1.35 \pm 0.01\text{eV}$ for the temperature ranges $650^\circ\text{-}1000^\circ\text{C}$ (Fig.5.12). Once the high temperature was reached and the sample allowed to equilibrate, the cooling run showed a decrease in the activation energy, being $1.15 \pm 0.01\text{eV}$ down to 670°C . This is probably due to a slight reduction of Nb at 1000°C .

$\text{Sr}_4\text{Nb}_2\text{O}_9$ reduced at 1000°C for 48 hours showed a higher activation energy of $1.41 \pm 0.01\text{eV}$ ($600^\circ\text{-}1000^\circ\text{C}$) and $1.02 \pm 0.01\text{eV}$ ($350^\circ\text{-}600^\circ\text{C}$) than the oxidised sample, even though the conductivity of the reduced sample is lower (Fig.5.13).

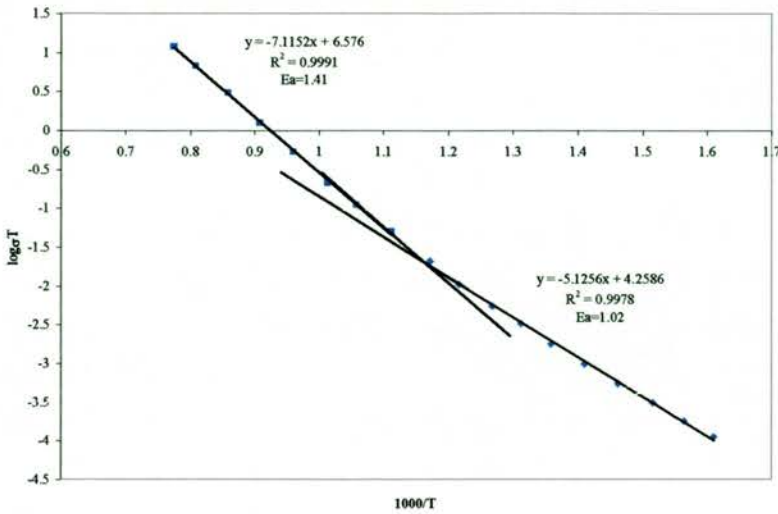
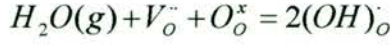


Fig.5.13 Arrhenius diagram for $Sr_4Nb_2O_{9-\delta}$ sample reduced at 1000°C from ac impedance data

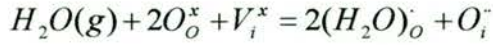
A small tail at low frequency seen in the Nyquist plot (Fig.5.10) may indicate some ionic conduction if the sample is not stoichiometric. Although the stoichiometric $Sr_4Nb_2O_9$ studied is an insulator with no ionic conductivity, exact stoichiometry cannot be guaranteed due to: (i) error in weighing starting powders and (ii) possible volatility of strontium at synthesis temperatures of 1300°-1400°C. This is consistent with the R.Glückner et al [8].

R.Glückner et al. [8] studied the conductivity of $Sr_2(SrNb_2)O_9$ as a function of temperature, pO_2 and pH_2O , and found oxygen ion conduction at high temperatures and hydrogen ion conduction at lower temperatures.. J.Lacomte et al discussed the dissolution of excess SrO in $Sr_4Nb_2O_9$ leading to the formation of $Sr_{Nb}^{''}$ and $V_O^{''}$ [5]: $Sr_3(Sr_{1+x}Nb_{2-x})O_{9-3x/2}$ where $0 \leq x \leq 1/2$. When $x=1/2$ the stoichiometry is $Sr_4(Sr_2Nb_2)O_{11}$, which has 8.33% (1/12) of the oxygen sites structurally empty [9], i.e. $Sr_4(Sr_2Nb_2)O_{11}V_i$. Thus the dissolution of Nb_2O_5 as $Nb_{Sr}^{''}$ defects fills the structural oxygen vacancies with oxygen ions: $Sr_4(Sr_{2-2y}Nb_{2+2y})O_{11+3y}V_{i1-3y}$ where $0 \leq y \leq 1/3$. When $y=1/3$ the stoichiometry

is $\text{Sr}_2(\text{SrNb}_2)\text{O}_9$ and all oxygen sites are occupied. Thus in the presence of water, defect structure is dominated by the electroneutrality condition: $3[\text{Sr}_{\text{Nb}}^{\text{m}}] = 2[V_{\text{O}}^-] + [(OH)_{\text{O}}]$ and $3[\text{Nb}_{\text{Sr}}^{\text{r}}] + [(OH)_{\text{O}}] = 2[\text{O}_i^{\text{r}}]$ [8]. From this the reaction between the disordered oxygen vacancies and water is:



and the reaction between the structural (i.e. ordered) oxygen vacancies and the dissolution of water is:



From the equations and from the study carried out by R.Glöckner et al.[8], when the concentration of H^+ is low, in dry atmosphere and at high temperature, the structural vacancies are proportional to $(p_{\text{H}_2\text{O}})^{1/2}$. In an intermediate $p_{\text{H}_2\text{O}}$ range structural vacancies give a $[(OH)_{\text{O}}] = 2[\text{O}_i^{\text{r}}] \propto (p_{\text{H}_2\text{O}})^{1/3}$ dependency [10]. Thus at low temperatures the $\text{Sr}_{\text{Nb}}^{\text{m}}$ acceptor defects are charge balanced by protons $((OH)_{\text{O}})$ and at higher temperatures they are balanced by oxygen vacancies (V_{O}^-). Hence at low temperatures ($<550^\circ\text{C}$) H^+ conduction is dominant and at high temperatures O^{2-} conduction dominates [8].

From the finding by R.Glöckner et al.[8] that increasing the Sr/Nb ratio, or $(V_{\text{O}}^-)_0$ increases the ionic conductivity, they concluded that the oxygen ion transport takes place via oxygen vacancies.

5.2.5 DC Conductivity studies

DC conductivity was performed on oxidised samples in air and the pre-reduced samples in flowing 5% H_2 /Ar. The ramp rate was 2°C/min on the cooling and heating cycle. The conductivity of the fully oxidised sample is very low, as expected, at $5 \times 10^{-5} \text{ Scm}^{-1}$ at 900°C. The activation energy of the reduced sample changes with temperature, giving a curve in the Arrhenius plot (Fig.5.14) which at higher temperatures becomes closer to a straight line.

The electronic conductivity goes up 2 orders of magnitude upon, what has been seen to be a very small amount of reduction. For the 1000°C reduced sample it is $1.5\text{--}2.0 \times 10^{-3} \text{ Scm}^{-1}$ at 900°C, with high activation energies of $1.36 \pm 0.01 \text{ eV}$ on cooling from 900°C to 470°C, and $1.42 \pm 0.01 \text{ eV}$ for heating curve 470°-900°C (Fig.5.14).

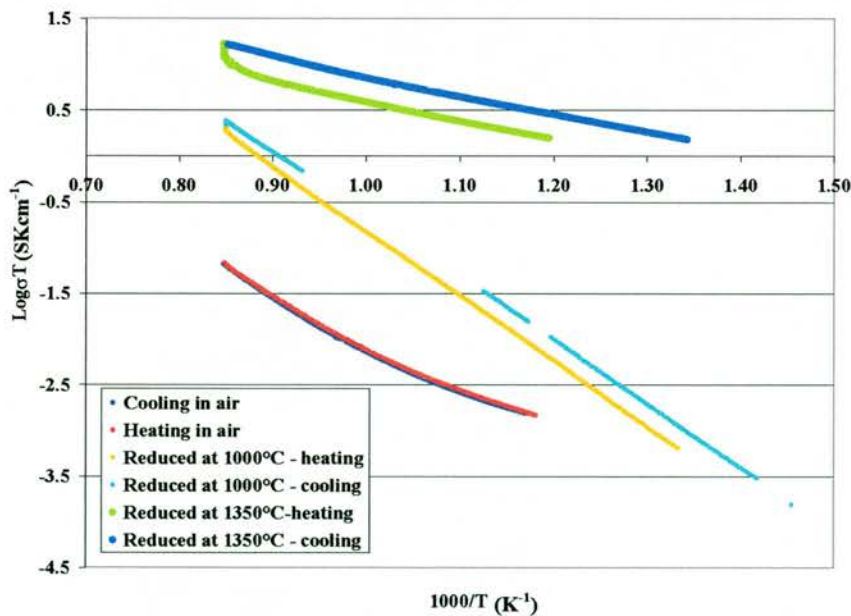


Fig.5.14 Arrhenius plot of DC conductivity with temperature of $Sr_4Nb_2O_9$ made in air and $Sr_4Nb_2O_9$ reduced at 1000°C and at 1350°C

Table 5.2 Conductivity and activation energies for Sr₄Nb₂O₉ and its reduced analogues

Sample	Conductivity at 900°C (Scm ⁻¹)	Heating Ea (eV)	Cooling Ea (eV)
Sr ₄ Nb ₂ O ₉	5.0±0.5 x10 ⁻⁵	Changes with temperature	
Sr ₄ Nb ₂ O ₉ reduced at 1000°C	2.8±0.5 x10 ⁻³	1.42±0.01	1.36±0.01
Sr ₄ Nb ₂ O ₉ reduced at 1350°C	1.4±0.5 x10 ⁻²	0.42±0.01	0.42±0.01

Further reduction at 1350°C does not increase the conductivity significantly, reaching a maximum of $\sim 1.4 \times 10^{-2} \text{ Scm}^{-1}$ at 900°C. As might be expected the activation energy decreases on reduction to $0.42 \pm 0.01 \text{ eV}$ (Table 5.2).

5.3 $\text{Sr}_2\text{Nb}_2\text{O}_7$, $\text{Sr}_2\text{Nb}_2\text{O}_{7-\delta}$, and $\text{Sr}_5\text{Nb}_5\text{O}_{17}$

5.3.1 Structure

$\text{Sr}_2\text{Nb}_2\text{O}_7$ is the $n=4$ member of the homologous series of layered perovskite phases $A_nB_nO_{3n+2}$. These materials are structurally similar to Ruddlesden-Popper phases $A_{m+1}B_mO_{3m+1}$, first established by S.Ruddlesden and P.Popper [11, 12] for the Sr-Ti-O system. The Ruddlesden-Popper phases, however, are known for many B cations, whereas the perovskite phases $A_nB_nO_{3n+2}$ exist only for $B=\text{Ti}$, Nb or Ta [13]. When $n=m=\infty$ then the ideal three dimensional perovskite structure is achieved: ABO_3 . The homologous series $A_nB_nO_{3n+2}$ consists of perovskite layers, n octahedra thick (Fig.5.15).

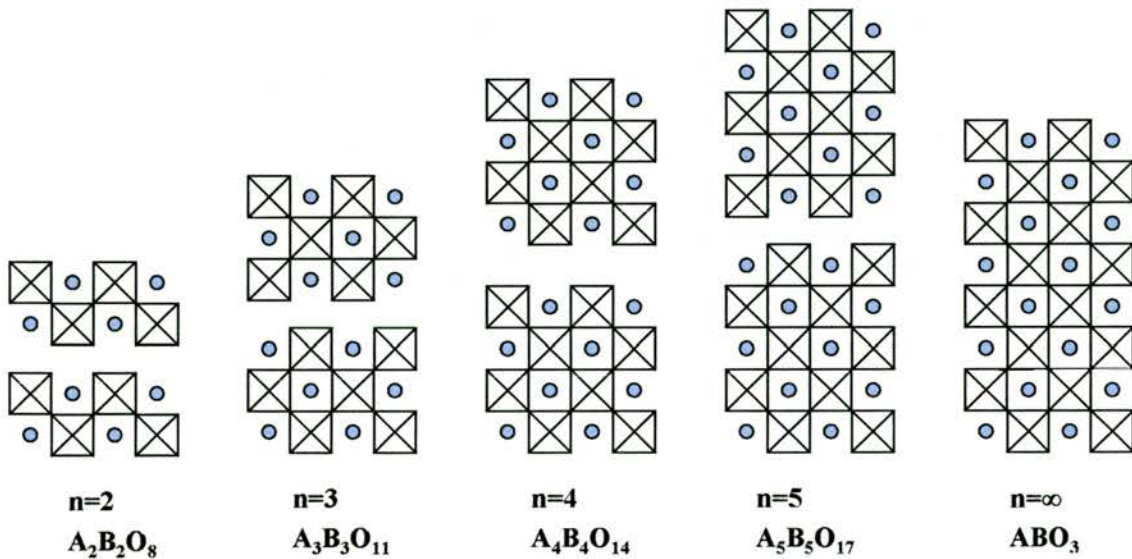


Fig.5.15 $A_nB_nO_{3n+2}$ crystal structures of the $n=2,3,4,5$ and ∞ members showing BO_6 octahedra as squares and A as blue circles in between the octahedra

Thus for the $\text{Sr}_2\text{Nb}_2\text{O}_7$ member it can be seen that the perovskite slabs are four octahedra thick, hence the more accurate designation is $\text{Sr}_4\text{Nb}_4\text{O}_{14}$ (Fig. 5.16).

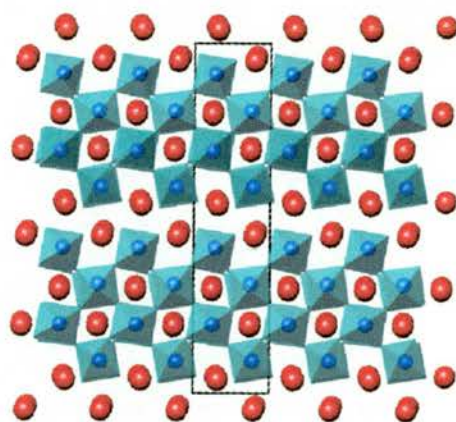
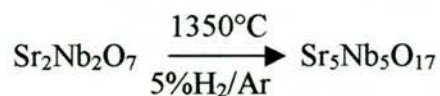


Fig.5.16 $Sr_2Nb_2O_7$ from the atomic co-ordinates provided by N.Ishizawa [2]

Under 5% H_2 /Ar at 1350°C for 20-40 hours, $Sr_2Nb_2O_7$ undergoes a phase change to the $n=5$ member of this series, $Sr_5Nb_5O_{17}$, with Nb in oxidation state of 4.8.



This is due to the removal of 1/35 oxygens from the NbO_6 octahedra, producing additional layer of corner sharing octahedra. Thus the layers in the $n=5$ series are 5 octahedra thick (Fig.5.15).

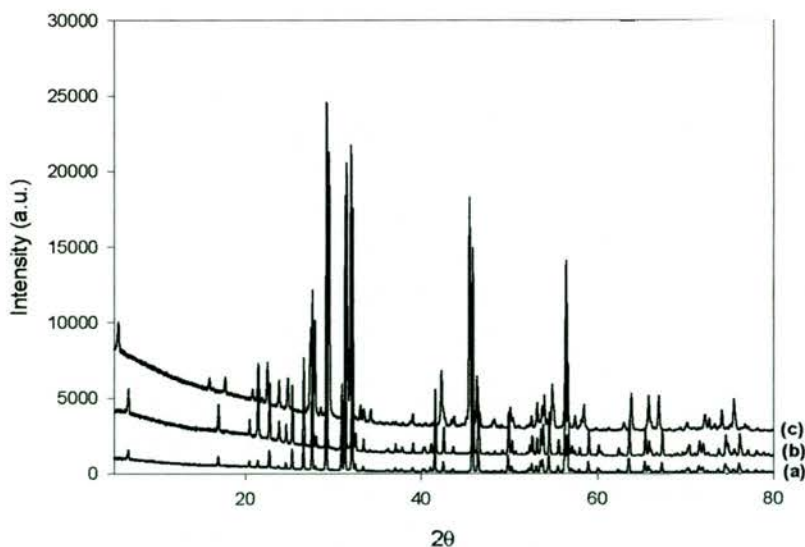


Fig.5.17 STOE X-ray pattern for (a) $Sr_2Nb_2O_7$ made in air (b) $Sr_2Nb_2O_7$ reduced at 1000°C in 5% H_2 /Ar (c) $Sr_2Nb_2O_7$ reduced at 1350°C in 5% H_2 /Ar.

Whereas reduction at 1350°C produces the $n=5$ phase, $\text{Sr}_5\text{Nb}_5\text{O}_{17}$, reduction at 1000°C shows little change in the pattern and the unit cell (Fig.5.17). Refinement of the X-ray data for the sample reduced at 1000°C showed the unit cell to be orthorhombic(C), and almost identical, although smaller, to the unit cell of $\text{Sr}_2\text{Nb}_2\text{O}_7$. The unit cell of $\text{Sr}_5\text{Nb}_5\text{O}_{17}$ is orthorhombic(P) (Table 5.3), and the unit cell parameters are consistent with those reported by H.W.Schmalle et al [14].

Table 5.3 Refined unit cell parameters for $\text{Sr}_2\text{Nb}_2\text{O}_7$ when oxidised and reduced at 1000°C or 1350°C

Phase	Reduction T (°C)	Symmetry	a(Å)	b(Å)	c(Å)	Cell Volume(Å ³)
$\text{Sr}_2\text{Nb}_2\text{O}_7$	N/A	Orthorhombic(C)	3.9622(2)	26.8188(16)	5.7116(3)	606.92(8)
$\text{Sr}_2\text{Nb}_2\text{O}_{7-8}$	1000	Orthorhombic(C)	3.95796(22)	26.7958(17)	5.7061(3)	605.17(8)
$\text{Sr}_5\text{Nb}_5\text{O}_{17}$ ($\text{Sr}_2\text{Nb}_2\text{O}_{6.83}$)	1350	Orthorhombic(P)	32.4851(16)	5.6799(3)	3.9898(2)	736.17(8)

The oxygen content determination is discussed in sec.5.3.3.

5.3.2 Dilatometry

There is a clear shrinkage in the unit cell upon reduction, which is also reflected in the small decrease in the average thermal expansion coefficient between room temperature and 900°C (Fig.5.18), i.e. technical alpha, $\alpha_t(300^\circ\text{-}900^\circ\text{C})$. $\text{Sr}_2\text{Nb}_2\text{O}_7$ has the largest thermal expansion at $10.89 \pm 0.05 \times 10^{-6} \text{K}^{-1}$ between 28°C and 900°C. The thermal expansion of the reduced samples is similar with $10.36 \pm 0.05 \times 10^{-6} \text{K}^{-1}$ for $\text{Sr}_2\text{Nb}_2\text{O}_7$ reduced at 1000°C, and $10.38 \pm 0.05 \times 10^{-6} \text{K}^{-1}$ for $\text{Sr}_2\text{Nb}_2\text{O}_7$ reduced at 1350°C, i.e. $\text{Sr}_5\text{Nb}_5\text{O}_{17}$.

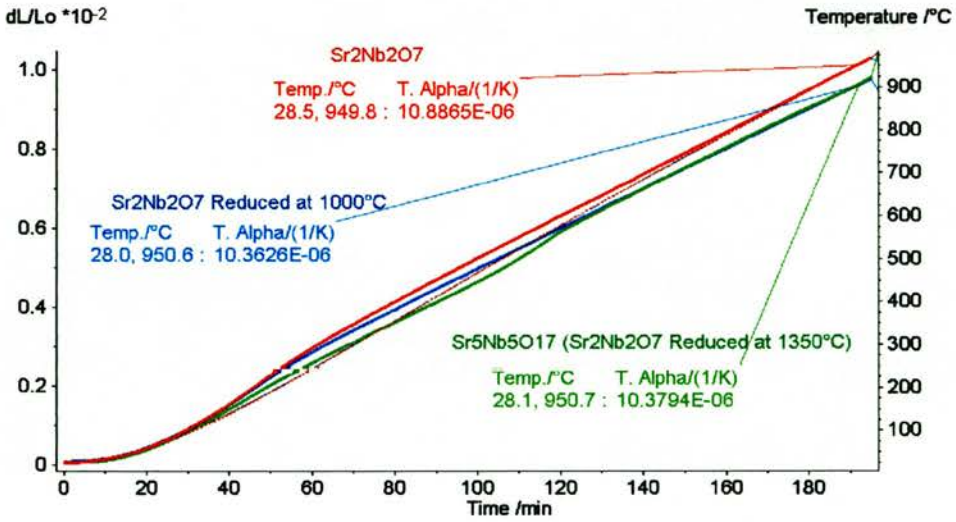


Fig.5.18 Thermal expansion data of $Sr_2Nb_2O_7$ in oxidised and reduced forms

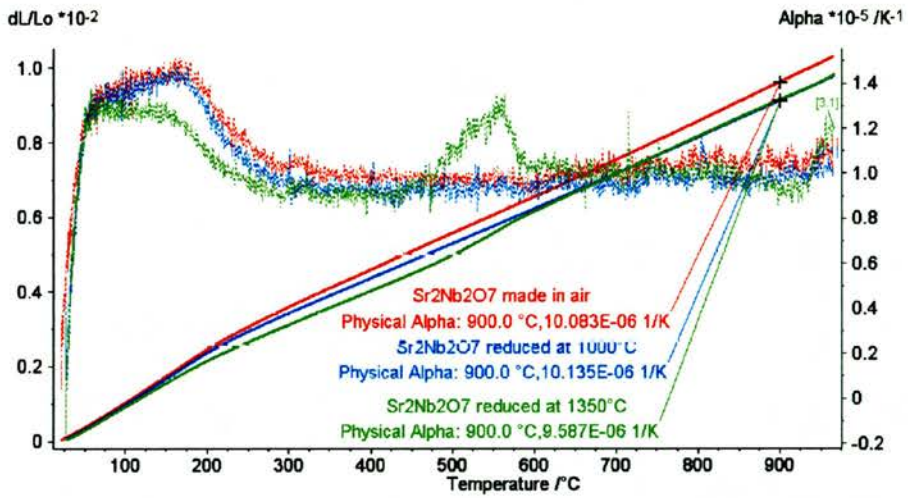


Fig.5.19 Physical α curve for $Sr_2Nb_2O_7$ as made in air and when reduced at 1000°C or 1350°C

When looking at a physical α curve, $\alpha_p(T)$ (Fig.5.19), i.e. the change in thermal expansion coefficient with temperature, the materials seem to behave differently. The thermal expansion coefficient varies upon reduction. The average thermal expansion coefficient of the sample reduced at 1000°C, $\alpha_p(900^\circ\text{C})=10.14\pm 0.05\times 10^{-6}\text{K}^{-1}$, is the same as the thermal expansion of the oxidised sample, $\text{Sr}_2\text{Nb}_2\text{O}_7$, $\alpha_p(900^\circ\text{C})=10.08\pm 0.05\times 10^{-6}\text{K}^{-1}$. In contrast, the $\alpha_p(900^\circ\text{C})$ of $\text{Sr}_5\text{Nb}_5\text{O}_{17}$ is significantly lower at $9.59\pm 0.05\times 10^{-6}\text{K}^{-1}$ compared to its $\alpha_t(300^\circ\text{-}900^\circ\text{C})=10.38\pm 0.05\times 10^{-6}\text{K}^{-1}$.

The physical alpha curve of the samples in (Fig.5.19) follows a similar, though unusual trend. The thermal expansion of $\text{Sr}_2\text{Nb}_2\text{O}_7$ and its reduced phases is quite high at low temperatures up to about 200°C. After 200°C the thermal expansion decreases and is then mostly constant up to 950°C. $\text{Sr}_5\text{Nb}_5\text{O}_{17}$, however, shows a spike at 500°-600°C, in which the thermal expansion increases to $12.5\text{-}13 \times 10^{-6}\text{K}^{-1}$ and then drops again to $\sim 9\text{-}10\times 10^{-6}\text{K}^{-1}$. There is no simple explanation for this behaviour, and could be due to structural rearrangement or loss of water. At 400°-600°C, $\text{Sr}_5\text{Nb}_5\text{O}_{17}$ undergoes a metal-insulator transition (discussed in a later section), this is the same range that the thermal expansion spike occurs in (Fig.5.19).

5.3.3 Thermogravimetric analysis (TGA)

As for $\text{Sr}_4\text{Nb}_2\text{O}_9$, the TGA has shown no noticeable change in weight when $\text{Sr}_2\text{Nb}_2\text{O}_7$ is reduced at 1000°C . There is, however, a weight change of 0.5% in the sample reduced at 1350°C (Fig.5.20), corresponding to Nb oxidation state of 4.80 ± 0.02 , which is equivalent to the stoichiometry $\text{Sr}_5\text{Nb}_5\text{O}_{17}$ indicated by the x-ray pattern.

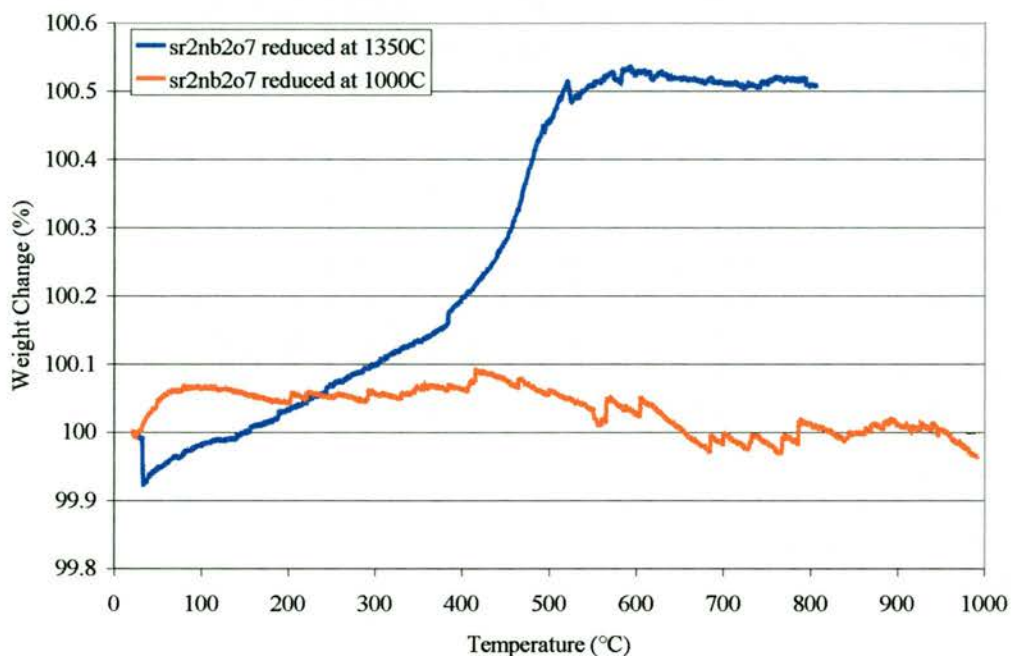


Fig.5.20 TGA oxidation runs in flowing air for the reduced $\text{Sr}_2\text{Nb}_2\text{O}_7$ samples.

$\text{Sr}_2\text{Nb}_2\text{O}_7$ is structurally stable to relatively mild reducing conditions, and niobium oxidation state is not less than 4.99, i.e. $5.00 - \delta = \text{Sr}_2\text{Nb}_2\text{O}_{7-\delta}$. The stability can be related back to the layered perovskite structure. In order to reduce niobium sufficiently the structure has to rearrange in order to accommodate oxygen vacancies. In the case of reduction to $\text{Nb}^{4.8+}$ the structure has to change to a higher, n^{th} member of the layered perovskite in the series $\text{Sr}_n\text{Nb}_n\text{O}_{3n+2}$; i.e. $\text{Sr}_5\text{Nb}_5\text{O}_{17}$, the $n=5$ member. If you reduce $\text{Sr}_2\text{Nb}_2\text{O}_7$ further it will be approaching the $n=\infty$ member of the series, i.e. SrNbO_3 with an ideal perovskite structure and niobium oxidation $4+$, with no layers in between Nb octahedra.

5.3.4 DC Conductivity studies

Four terminal DC measurement showed the conductivity of $\text{Sr}_2\text{Nb}_2\text{O}_7$ to be $2 \times 10^{-5} \text{ Scm}^{-1}$, half that of $\text{Sr}_4\text{Nb}_2\text{O}_9$. Two regions with different slope can be seen in the Arrhenius plot of $\text{Sr}_2\text{Nb}_2\text{O}_7$ (Fig.5.21). At lower temperatures of $400^\circ\text{-}700^\circ\text{C}$ the activation energy for the conduction pathway is low at $0.76 \pm 0.03 \text{ eV}$. Above 700°C , however, the activation energy increases to $1.41 \pm 0.02 \text{ eV}$. There is no significant hysteresis between cooling and heating cycles.

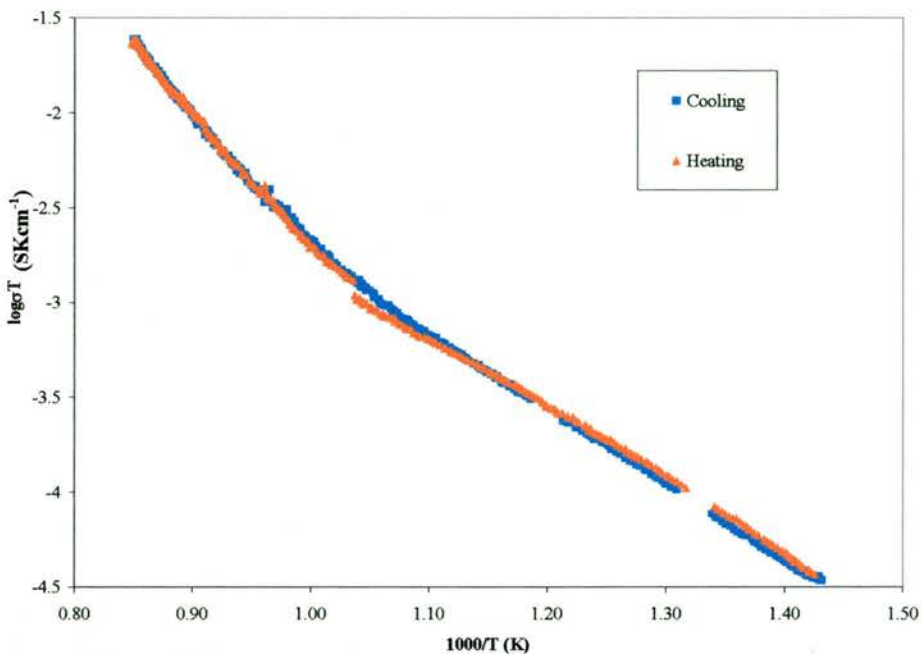


Fig.5.21 Arrhenius plot of $\text{Sr}_2\text{Nb}_2\text{O}_7$ for conductivity in air

Reducing $\text{Sr}_2\text{Nb}_2\text{O}_7$ at 1000°C increases its conductivity to $0.15\text{-}0.17 \text{ Scm}^{-1}$, which is 100 times higher than that for $\text{Sr}_4\text{Nb}_2\text{O}_{9.8}$ when reduced at 1000°C . This is expected from materials with higher Nb content. The Arrhenius plot in (Fig.5.22) shows a change in the activation energy with temperature. The change, however, is very small and the overall activation energy can be approximated to $0.15 \pm 0.03 \text{ eV}$.

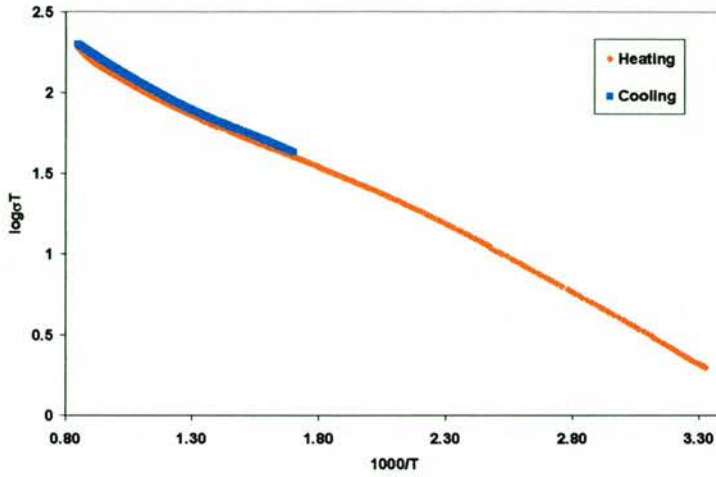


Fig.5.22 Arrhenius plot of $Sr_2Nb_2O_{7-\delta}$ in 5% H_2/Ar

The reduction of this material at 1000°C was too small to be observable with TGA, where $\delta < 0.01$ in $Sr_2Nb_2O_{7-\delta}$.

Table 5.4 Summary of conductivity and activation energies of $Sr_2Nb_2O_7$

Phase	Nb Oxidation state	Scm^{-1} (900°C)	E_a (eV) from 4 terminal DC
$Sr_2Nb_2O_7$	5.00	$\sim 2 \times 10^{-5}$	1.41±0.02(900°C-700°C)
			0.76±0.03 (700°-400°C)
$Sr_2Nb_2O_{7-\delta}$	5.00- δ	0.15-0.17	0.15±0.03 (100°-900°C)
$Sr_5Nb_5O_{17}$	4.8	0.3-0.5	

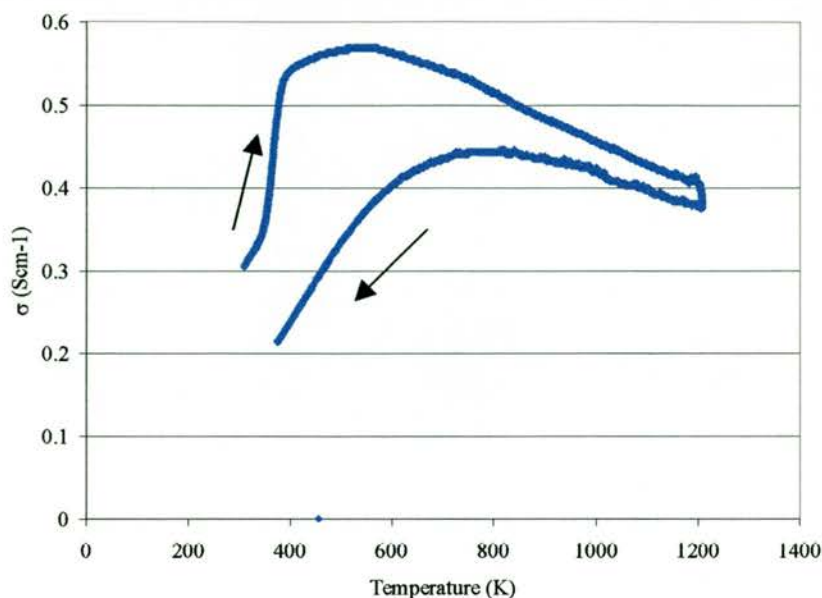


Fig.5.23 Conductivity as a function of temperature of $Sr_5Nb_5O_{17}$

A low temperature study (>0K-300K) of the conductivity behaviour of $Sr_5Nb_5O_{17}$, by F.Lichtenberg et al [13], found a complex electronic behaviour in which $Sr_5Nb_5O_{17}$ undergoes a metal-semiconductor transition at ~ 50 K along the a and b axis. Between 50K and 120K there is another metal-insulator transition along the a and b axis, and the material seems to show semiconducting behaviour up to room temperature. The conductivity along the c axis was reported as being semiconducting <300K.

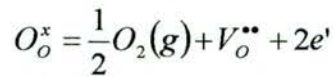
In this study 4-Terminal DC conductivity of $Sr_5Nb_5O_{17}$ shows behaviour similar to a metal-semiconductor transition at higher temperatures. On heating the transition occurs at 400-500°C, which may be too low for the oxidation of the sample to occur. On cooling, the transition occurs at 600°-800°C (Fig.5.23), but the sample has poor stability under the less reducing conditions of 900°C in 5% H_2 /Ar than those under which it was synthesised, i.e. 1350°C. Thus there is a decrease in conductivity during the 12-hour isotherm at 900°C, and ultimately lower conductivity on the cooling cycle as is shown in the figure above.

5.3.5 Conductivity as a function of $p(\text{O}_2)$

Although no information can be gathered from the reduction curve due to the uncontrolled and rather rapid rate of reduction, the much slower oxidation run shows a slope of -0.18 ± 0.01 up to 10^{-11} atm (Fig.5.24). At higher oxygen partial pressures of 10^{-10} - 10^{-4} atm the rate of oxidation is too fast for the sample to reach equilibrium, providing unreliable data. The extrapolation from fully oxidised at $p(\text{O}_2)=10^{-1}$ atm to fully reduced at $p(\text{O}_2)=10^{-20}$ atm indicates simple defect relationship over the entire $p(\text{O}_2)$ range. The concentration of electrons can be considered to be twice that of the oxygen vacancies:



$$[\text{Nb}'_{\text{Nb}}] \sim [p(\text{O}_2)]^{-1/6}$$



$$[e'] = 2[\text{V}_\text{o}^{\bullet\bullet}]$$

thus the equation for the law of mass action is:

$$[e'] = (2K_1)^{1/3} p_{\text{O}_2}^{-1/6}$$

$$\sigma_e \propto p_{\text{O}_2}^{-1/6}$$

When the majority of vacancies are formed as a result of oxygen loss the conductivity has a $p(\text{O}_2)$ dependence of $-1/6$.

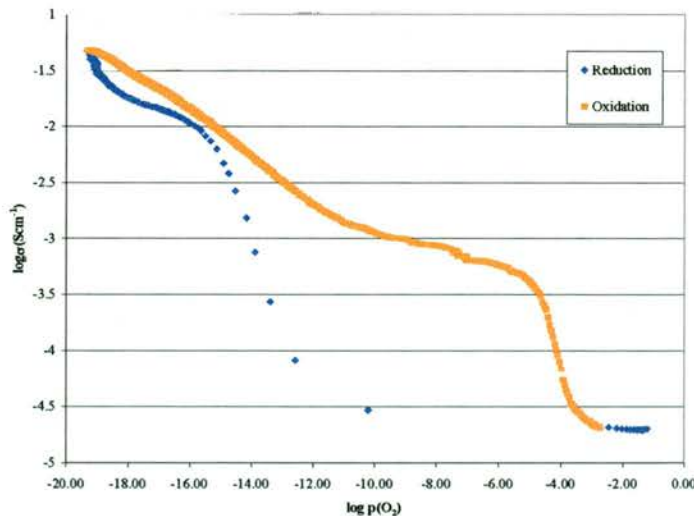


Fig.5.24 Conductivity as a function of $p(\text{O}_2)$ of $\text{Sr}_2\text{Nb}_2\text{O}_7$ at 900°C

5.3.6 AC Impedance

Although no hysteresis was observed in the Arrhenius plot from the 4-terminal DC measurement, AC impedance shows higher activation energy on cooling of $1.65 \pm 0.02 \text{ eV}$, compared to $1.40 \pm 0.02 \text{ eV}$ on heating (Fig.5.25). The difference between the DC and AC measurements is due to the length of time the sample was allowed to spend at anyone temperature. In the DC measurement, the measurement technique involved a constant and steady temperature change of $3^\circ\text{C}/\text{min}$, and thus the technique is transient and equilibrium is not certainly attained. In the AC measurements, by contrast, the sample was allowed to equilibrate at any one temperature for 30-60 minutes. Holding the sample at high temperature, however, for any extended period of time may change the composition of the sample, resulting in the observed change in the activation energy going from heating to cooling in (Fig5.25).

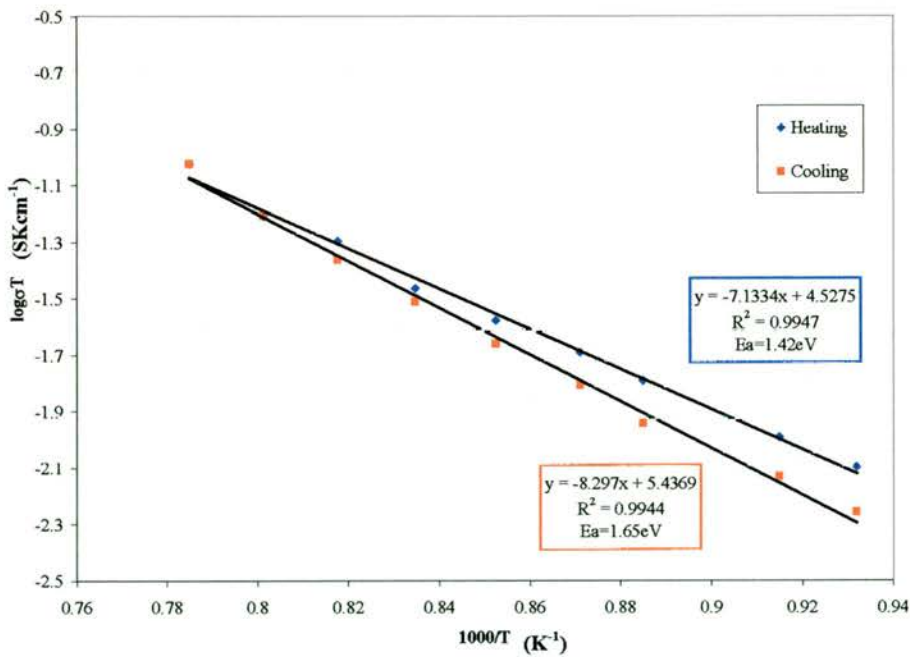


Fig.5.25 Arrhenius plot from AC impedance for $\text{Sr}_2\text{Nb}_2\text{O}_7$

5.4 SrNb_2O_6 , $\text{SrNb}_2\text{O}_{5.98}$ and $\text{SrNb}_2\text{O}_{5.76}$

5.4.1 Structure

SrNb_2O_6 adopts a framework structure similar to CaTa_2O_6 which is built from edge- and corner-sharing octahedra along the c-axis, and corner-sharing along the b-axis (Fig.5.26). Again this structure is perovskite related. In this structure NbO_6 octahedra are joined at the corners in the same layer and at the edge with the NbO_6 octahedra in the next layer, thus the pairs of edge-sharing octahedra share corners to form a perovskite-like structure (Fig.5.27). Whereas in the normal perovskite structure the ratio of A/B sites is 1:1, in this structure only half of the perovskite A sites exist.

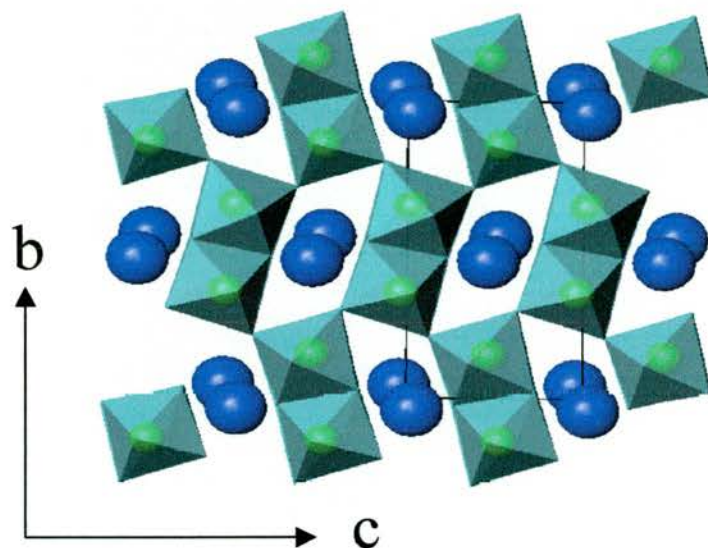


Fig.5.26 Edge-sharing and corner sharing NbO_6 octahedra(green) with Sr in between (blue)

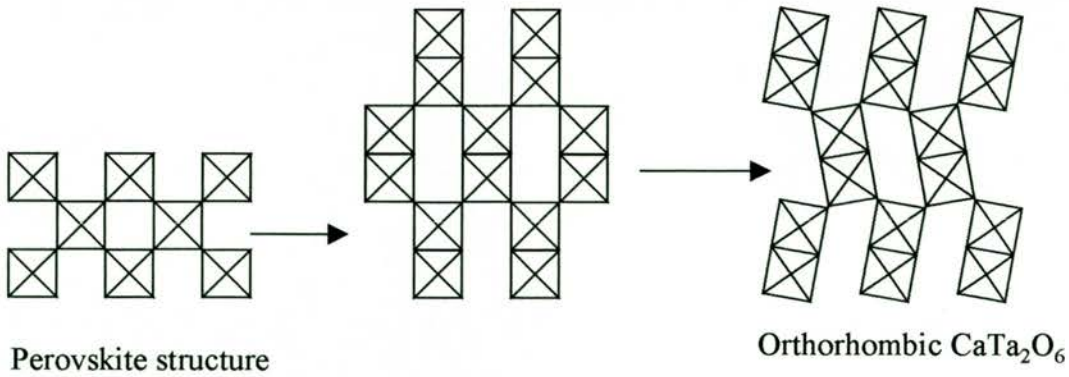


Fig.5.27 Layers of octahedra in the perovskite and perovskite type CaTa_2O_6 structure

Hence from (Fig.5.26) and (Fig.5.27) it can be seen that the structure of SrNb_2O_6 can be viewed as a sheared perovskite. In this structure there are the same number of A -sites as A atoms, thus all of the sites are occupied.

The unit cell parameters of SrNb_2O_6 were originally refined by H.G.Hess and H.J.Trumpor [15] as orthorhombic CaNb_2O_6 type structure with $a=11.02\text{\AA}$, $b=7.33\text{\AA}$ and $c=5.60\text{\AA}$. Later study by B.O.Marinder et al. [16] found the distortion of the β angle hence the monoclinic unit cell.

Table 5.5 Refined unit cell parameters of SrNb_2O_6 and reduced phases

Reduction T (°C)	Unit cell symmetry	a(Å)	b(Å)	c (Å)	β (°)	V (Å ³)	TEC(10 ⁻⁶ K ⁻¹) (300-900°C)
SrNb_2O_6	Monoclinic P	7.7325(6)	5.6023(4)	10.9976(8)	90.372 (4)	476.40(9)	5.90
$\text{SrNb}_2\text{O}_{5.98}$	Monoclinic P	7.7353(6)	5.6029(4)	11.0003(8)	90.362(4)	476.74(8)	5.45
$\text{SrNb}_2\text{O}_{5.76-5.77}$	Tetragonal P	12.3854(8)	12.3854(8)	7.8101(7)	90	1198.04(20)	11.18

Reduction of SrNb_2O_6 at 1000°C shows no obvious change in the unit cell parameters (Table 5.5), and is marked only by the slight increase in the unit cell size. Niobium is reduced to an average oxidation state of 4.98. Reduction at 1200°C, however, produces a tetragonal tungsten bronze structure of the stoichiometry $\text{SrNb}_2\text{O}_{5.76}$, and in this structure niobium is in the oxidation state 4.76-4.77.

5.4.2 TGA

TGA was run on the pre-reduced sample in flowing air, and at 900°C the sample was allowed to oxidise for 3 hours. Oxidation was fully complete within that time.

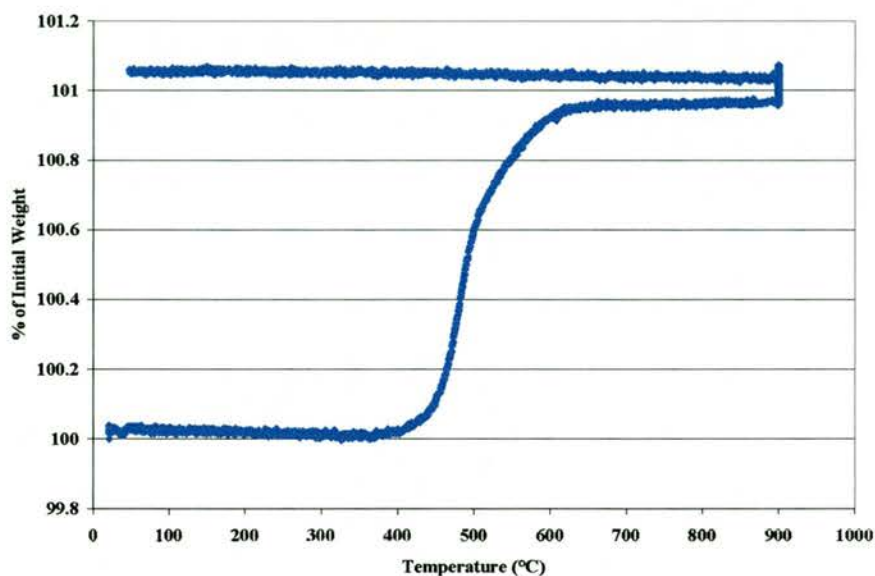


Fig.5.28 TGA oxidation run for SrNb₂O_{5.76}

The sample underwent a rapid re-oxidation between 450°-600°C (Fig.5.28) indicating slower kinetics of the reduction process, which may in part be due to structural changes in this material. It is common for niobium based materials, especially in niobium rich materials, that the oxidation kinetics are much faster than the reduction.

5.4.3 Dilatometry

Thermal expansion studies of SrNb₂O₆ and its reduced phases showed quite different thermal expansion behaviour. All phases showed an initial drop in thermal expansion coefficient with increasing temperature until 400°C (Fig.5.29), after which it slowly rises with temperature to reach a maximum of $\alpha_{(900^{\circ}\text{C})}=7.49\pm 0.05\times 10^{-6}\text{K}^{-1}$ for SrNb₂O₆ and $\alpha_{(900^{\circ}\text{C})}=9.55\pm 0.05\times 10^{-6}\text{K}^{-1}$ for SrNb₂O_{5.98} (SrNb₂O₆ reduced at 1000°C). Although the overall thermal expansion of SrNb₂O₆ at $\alpha_{(300-900^{\circ}\text{C})}=5.90\pm 0.05\times 10^{-6}\text{K}^{-1}$ is higher than that

of $\text{SrNb}_2\text{O}_{5.98}$, with $\alpha_{(300-900^\circ\text{C})}=5.45\pm 0.05\times 10^{-6}\text{K}^{-1}$, the reduced sample has a significantly higher thermal expansion at 900°C (Fig.5.29).

$\text{SrNb}_2\text{O}_{5.76}$ shows unusual thermal expansion behaviour. During a heating cycle, the thermal expansion at 900°C is $9.4\times 10^{-6}\text{K}^{-1}$ (Fig.5.29), which is similar to that of $\text{SrNb}_2\text{O}_{5.98}$ and is markedly higher than that of the oxidised sample. However, the cooling curve indicated the thermal expansion to be $11.9\times 10^{-6}\text{K}^{-1}$ (Fig.5.31).

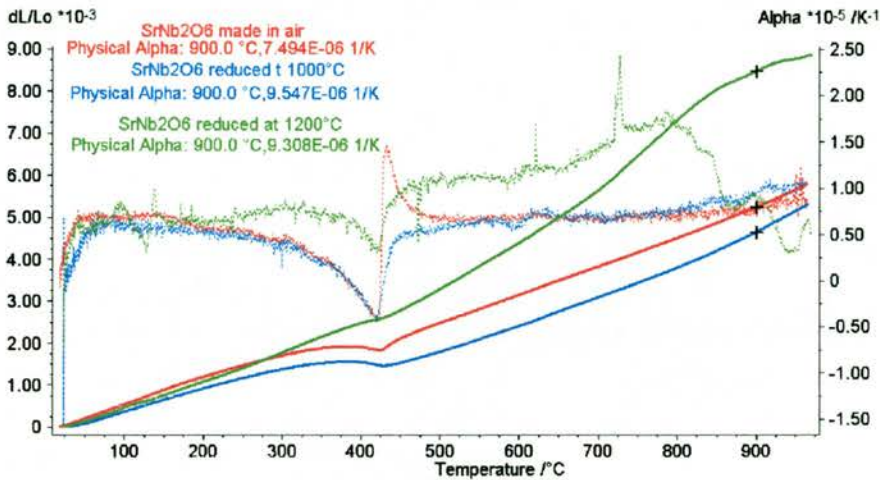


Fig.5.29 Physical α heating curve for SrNb_2O_6 as made in air and when reduced at 1000°C or 1200°C

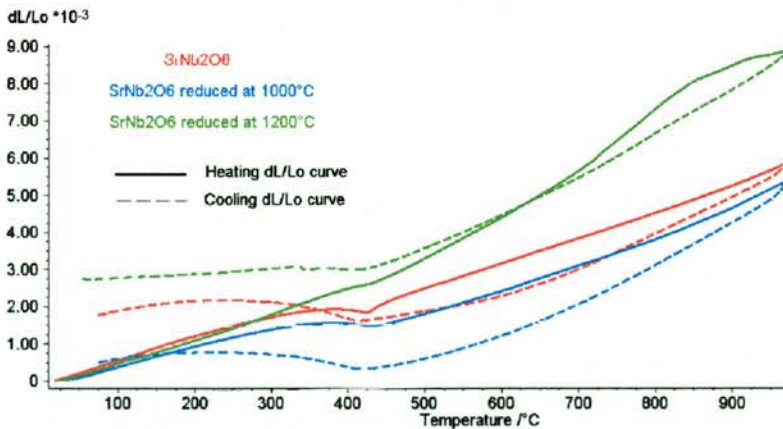


Fig.5.30 Technical alpha curve on heating and cooling for SrNb_2O_6 and its reduced analogues

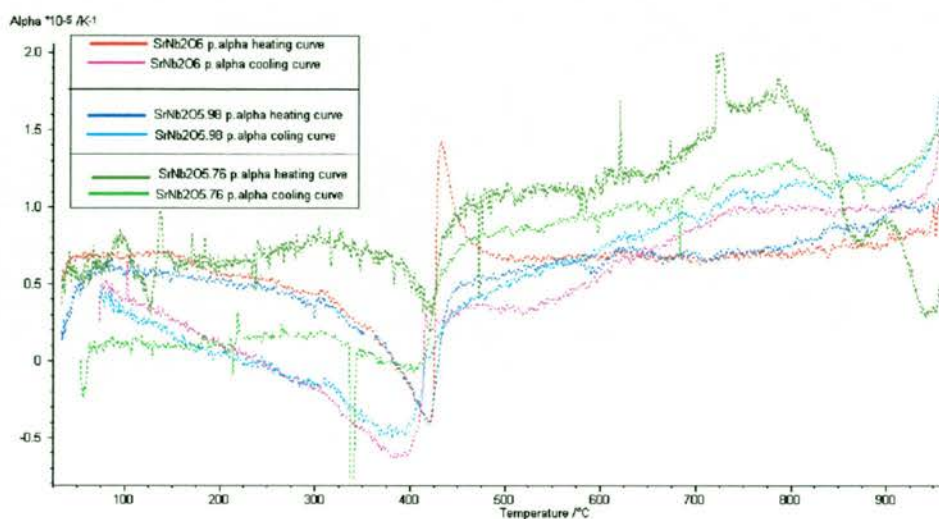


Fig.5.31 Physical α heating and cooling curves for SrNb_2O_6 as made in air and when reduced at 1000°C or 1200°C

Physical alpha curves for these samples show unusual expansion behaviour (Fig.5.31). SrNb_2O_6 , for example, has a constant thermal expansion between room temperature and 180°C - 200°C , with $\alpha_{tech} \sim 6.6\text{--}6.7 \times 10^{-6} \text{K}^{-1}$. With further increase in temperature the thermal expansion decreases, until $\sim 380^\circ\text{C}$ when the negative thermal expansion is observed, with $\alpha_{(383^\circ\text{--}423^\circ\text{C})} \sim -2.1 \times 10^{-6} \text{K}^{-1}$. At $\sim 430^\circ\text{C}$ there is a rapid rise in the thermal expansion coefficient to $\sim \alpha_{tech} \sim 6 \times 10^{-6} \text{K}^{-1}$. In the heating curve (Fig.5.31) there is a large overshoot immediately after the negative thermal expansion curve, which is not observed in the cooling curve; this is an artefact of the measurement technique, which may produce spikes, due to the sensitivity of the instrument, upon sudden change in the thermal expansion of the material. Similarly, the cooling curve for the same sample shows a gradual decrease in the thermal expansion with temperature, and until $\sim 415^\circ\text{C}$ - 245°C the sample has a negative thermal expansion, with $\alpha_{(415^\circ\text{--}245^\circ\text{C})} \sim -3.3 \times 10^{-6} \text{K}^{-1}$.

Similar behaviour is also observed for the sample reduced at 1000°C which also displayed a negative thermal expansion between 380°-430°C, $\alpha_{(383^{\circ}\text{-}423^{\circ}\text{C})}\sim -2.0\times 10^{-6}\text{K}^{-1}$, on heating, and $\alpha_{(415^{\circ}\text{-}245^{\circ}\text{C})}\sim -2.5\times 10^{-6}\text{K}^{-1}$ between 420°-245°C on cooling. The overall pattern for the thermal expansion curve of the oxidised and 1000°C reduced sample is very similar, with only a significant difference in the thermal expansion coefficient at 900°C.

Although $\text{SrNb}_2\text{O}_{5.76}$ shows a similar overall trend to the SrNb_2O_6 and $\text{SrNb}_2\text{O}_{5.98}$ samples, with a drop in the thermal expansion coefficient up to $\sim 400^{\circ}\text{C}$, the thermal expansion is not negative at any point on the heating cycle, though it does drop from $6\text{-}7\times 10^{-6}\text{K}^{-1}$ at $\sim 200^{\circ}\text{-}350^{\circ}\text{C}$ to $\sim 2.8\times 10^{-6}\text{K}^{-1}$ at 400°C , then rises again to a maximum of $16.8\times 10^{-6}\text{K}^{-1}$ at 800°C . After 800°C there is another drop in the thermal expansion coefficient to $9.4\times 10^{-6}\text{K}^{-1}$ at 900°C and by 950°C the thermal expansion is $3.8\times 10^{-6}\text{K}^{-1}$. On cooling the behaviour of the material is slightly different; the thermal expansion at 950°C is $14.5\times 10^{-6}\text{K}^{-1}$ and at 900°C it is $11.9\times 10^{-6}\text{K}^{-1}$, indicating some change in the structure of this material or possible oxidation at higher temperatures. Further cooling sees a gradual drop in the thermal expansion coefficient, and at $415^{\circ}\text{-}380^{\circ}\text{C}$ the thermal expansion is negative, with $\alpha_{(415^{\circ}\text{-}380^{\circ}\text{C})}\sim -0.35\times 10^{-6}\text{K}^{-1}$.

When looking to explain such unusual thermal expansion behaviour, it is necessary to look at other properties of the material, such as conductivity and structure, and see how these change with temperature.

5.4.4 DC Conductivity studies

4 terminal DC measurements of SrNb_2O_6 showed a conductivity of $5\text{-}7 \times 10^{-5} \text{ Scm}^{-1}$ at 900°C in air, with $E_a=1.48 \pm 0.02\text{eV}$ on heating and a lower $E_a=1.34 \pm 0.02\text{eV}$ on cooling (Fig.5.32). The resistance of the sample did not allow measurement to temperatures below $650^\circ\text{-}700^\circ\text{C}$.

Table 5.6 Electronic conductivity and activation energies for SrNb_2O_6 and its reduced analogues

Phase	x in Nb^x	$\text{Scm}^{-1}(900^\circ\text{C})$	$E_a(\text{eV})$ Heating	$E_a(\text{eV})$ Cooling
SrNb_2O_6	5.00	$5.6\text{-}6.8 \times 10^{-5}$	1.48 ± 0.01	1.34 ± 0.01
$\text{SrNb}_2\text{O}_{5.98}$	4.98	$7\text{-}8 \times 10^{-2}$	0.96 ± 0.02 (250-450) 0.76 ± 0.02 (450-720) 1.33 ± 0.02 (720-900)	1.00 ± 0.02 (250-450) 0.81 ± 0.02 (450-720) 1.10 ± 0.02 (720-900)
$\text{SrNb}_2\text{O}_{5.76}$	4.76	40	_____	_____

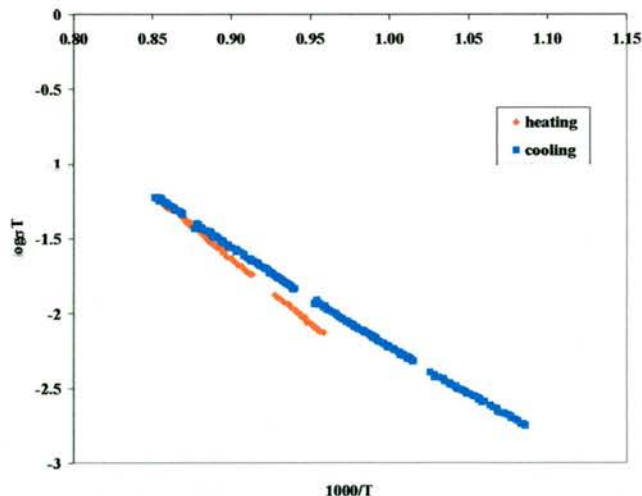


Fig.5.32 Arrhenius plot for the conductivity in air of SrNb_2O_6

Reduction at 900°C in 5%H₂/Ar, however, increased the conductivity to $7-8 \times 10^{-2} \text{ Scm}^{-1}$, and was shown by TGA to have a stoichiometry of SrNb₂O_{5.98}, i.e. Nb^{+4.98}. The Arrhenius plot (Fig.5.33) shows a change in the activation energy. At low temperatures, 250°-450°C the $E_a=0.98 \pm 0.02 \text{ eV}$, which then drops to $E_a=0.78 \pm 0.03 \text{ eV}$ for the intermediate temperature range of 450°-720°C. At high temperatures of 720°-900°C the $E_a=1.33 \pm 0.02 \text{ eV}$ on heating, and $E_a=1.10 \pm 0.02 \text{ eV}$ on cooling.

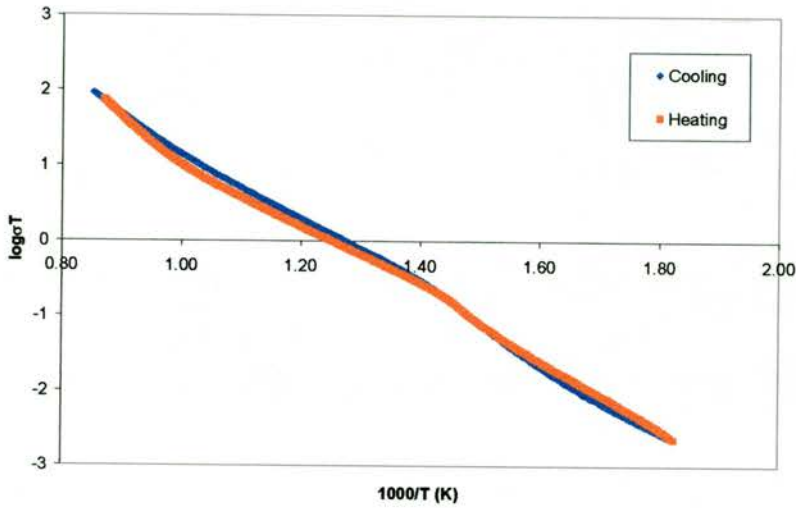


Fig.5.33 Arrhenius plot for the conductivity in 5%H₂/Ar of SrNb₂O_{5.98}

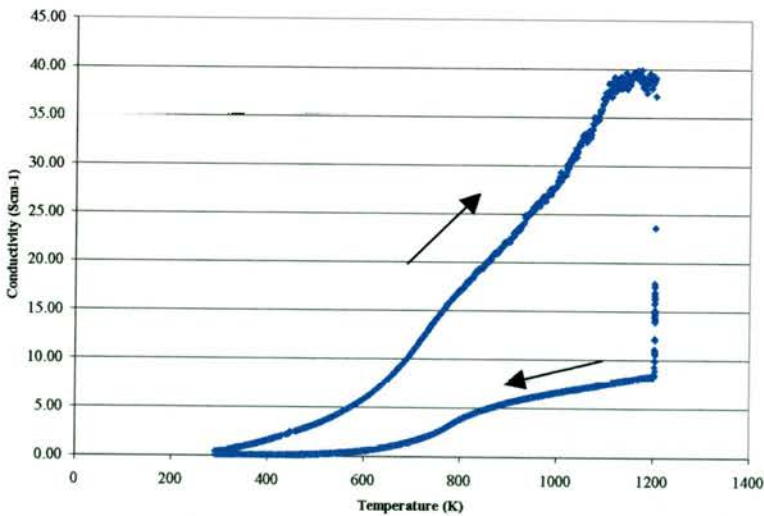


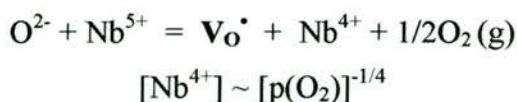
Fig.5.34 Conductivity as a function of temperature in 5%H₂/Ar for SrNb₂O_{5.76}

Further reduction at 1200°C in 5% H_2 /Ar of $SrNb_2O_6$ gives $SrNb_2O_{5.76}$, with high electronic conductivity of 40-50 Scm^{-1} at 900°C. In flowing 5% H_2 /Ar at 900°C this structure is not stable and a rapid drop in conductivity is observed in these conditions.

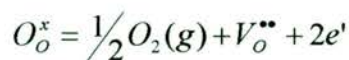
5.4.5 Conductivity as a function of $p(O_2)$

$SrNb_2O_6$ is seen to have good reduction and oxidation kinetics (Fig.5.35). A small hysteresis is observed for the reduction and oxidation and is mainly due to the temperature difference of the two runs, as the oxidation run was performed at a temperature 20°C lower than the reduction run. Both the reduction and the oxidation show very similar slopes of 0.22 ± 0.02 , for the $p(O_2)$ range 10^{-17} - 10^{-12} atm, that is $\sigma \propto p(O_2)^{-1/4.5}$. The curve observed at lower partial pressures to 10^{-19} atm is not likely to be real. Due to the transient nature of this technique, where the rate of change of $p(O_2)$ is not controlled and the sample is not allowed to reach an equilibrium at any partial pressure, only the initial and final points are certain. Hence a -1/4.5 slope is observed across the partial pressure range down to 10^{-5} atm. The oxidation is mostly complete by 10^{-5} atm, with no slope observed at higher oxygen partial pressures. The region between 10^{-12} and 10^{-5} atm is traversed too fast for any information to be gathered from it, hence the last points at 10^{-12} atm and the first at 10^{-5} atm are used as indicators of the slope across that region. This would be consistent with no phase transitions or structural reorganisation.

The reduction of Nb to give an oxygen vacancy liberating an electron. Thus for one electron coupled to an oxygen vacancy:



Thus for an n -type electronic conductor the defect equation describing the incorporation of oxygen into the lattice at low $p(O_2)$ is:



and the mass action relation for this equation is given by:

$$K_1 = p_{O_2}^{1/2} [V_O^{\bullet\bullet}] [e]^2$$

If $2[V_O^{\bullet\bullet}] = [e]$ the equation reduces to:

$$[e] \propto p_{O_2}^{-1/4}$$

Hence the conductivity of the electrons, σ_e , is proportional to the inverse fourth root of $p(O_2)$:

$$\sigma_e \propto p_{O_2}^{-1/4}$$

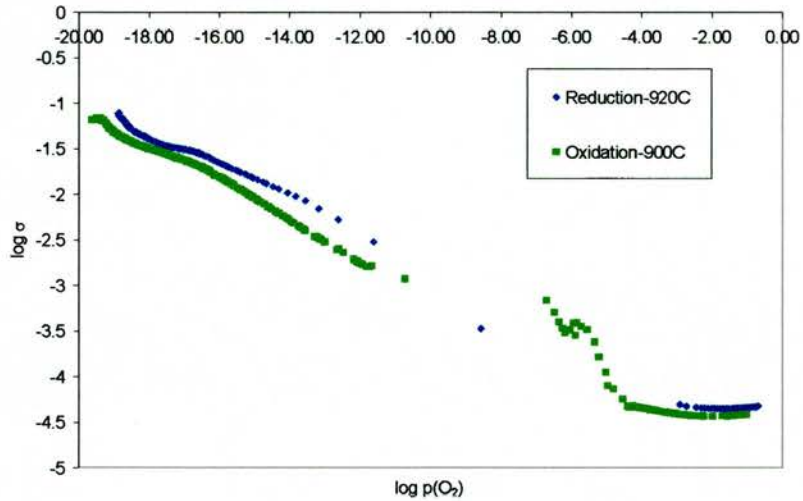


Fig.5.35 conductivity as a function of $p(O_2)$ for $SrNb_2O_6$

There is a degree of uncertainty, however, as to whether the slope is $-1/4$ or $-1/5$.

5.4.6 AC Conductivity Studies

From the impedance response at 800°C and 820°C (Fig.5.36) it can be seen that the bulk accounts for the majority of the resistance, with a well defined grain boundary accounting for a small percentage of the total resistance. The density of the pellet was 90%. At 800°C the bulk resistivity was estimated to be 50kΩcm and its capacitance in the 7×10^{-12} Fcm⁻¹ range. This resistance accounts for 82% of the total, with the grain boundary resistivity being 11kΩcm, with an estimated capacitance in the range of 9×10^{-8} Fcm⁻¹.

At 820°C the bulk resistance drops to 41kΩcm and the bulk resistivity is estimated to be 8.8kΩcm, with the bulk still accounting for the 82% of the total resistance. By 875°C the bulk accounts for 81% of the total resistivity with 20.6kΩcm, compared to 4.9kΩcm for the grain boundary. At 900°C the bulk resistivity is 15kΩcm and the grain boundary resistance is 3.4kΩcm; the bulk still accounting for 81% of the total resistance (Fig.5.36).

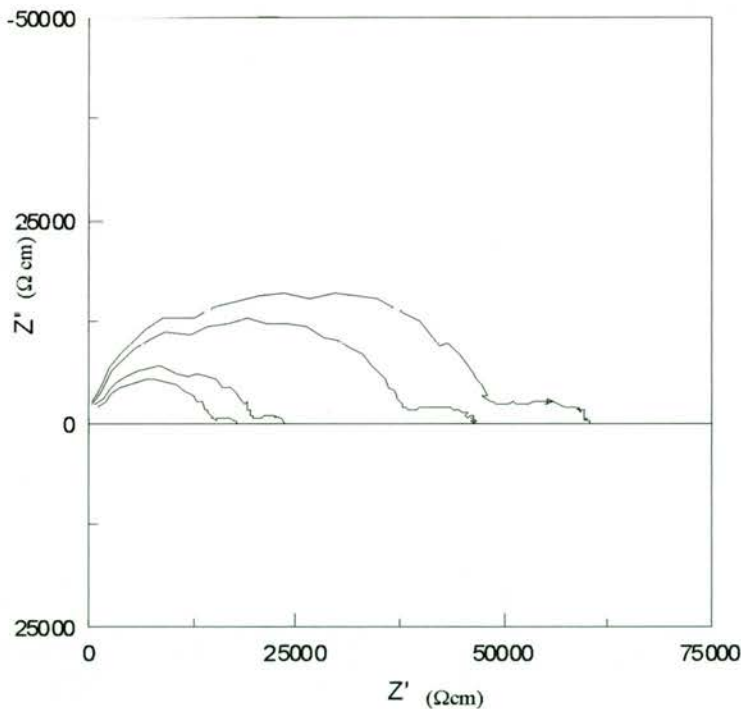


Fig.5.36 Geometry corrected impedance plots of SrNb₂O₆ at 800°C, 820°C, 875°C and 900°C

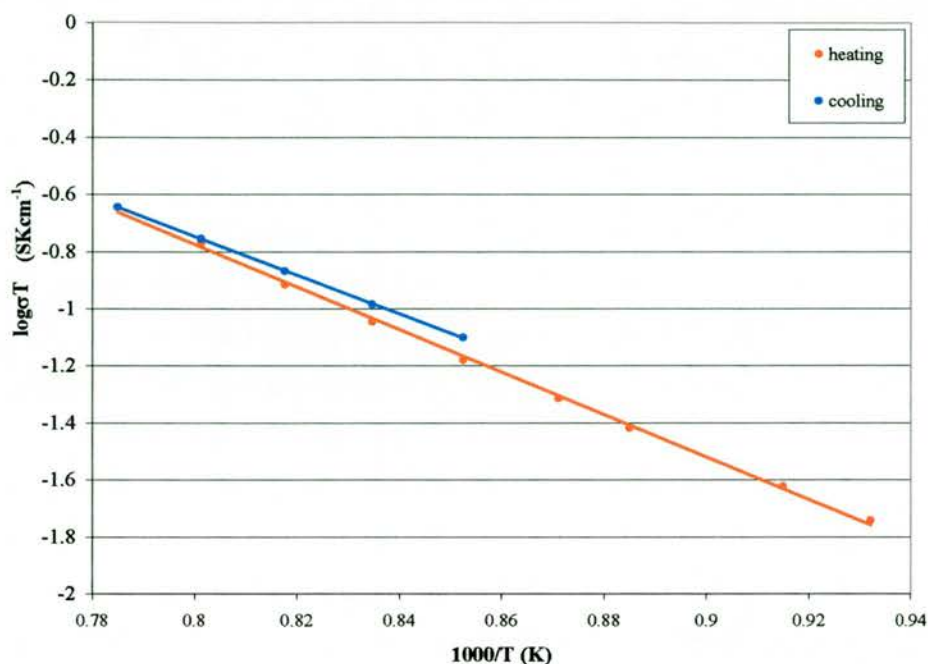


Fig.5.37 Arrhenius diagram for SrNb₂O₆ as made in air

The Arrhenius diagram (Fig.5.37) shows high activation energy of 1.48 ± 0.01 eV for the heating cycle and 1.34 ± 0.01 eV for the cooling cycle. The sample was measured only down to 800°C due to the high resistance of the sample and the difficulty in getting good impedance data due to the inductive effects of the furnace at high temperatures, which is only apparent if the sample has a high resistance of $\sim 10^5 \Omega$ at 900°C , giving a large “scatter” of data points.

5.5 Sr_{0.6}NbO₃

5.5.1 Structure

Sr_xNbO₃ (0.70 ≤ x ≤ 0.97) phases have been investigated by several researchers after D.Ridgeley and R.Ward (1955) [17] conducted the first investigation into their synthesis and structure. The main interest in these materials has been driven by the search for new superconductors.

For 0.70 ≤ x ≤ 0.95 the structure of the perovskite is usually described as cubic, with $a \approx 4 \text{ \AA}$ and containing an array of NbO₆ octahedra, [18],[19]. In this structure the Sr atoms, located at the A site, are randomly absent. This feature is also seen in other tungsten bronzes and ReO₃. None of the authors have claimed to have synthesised Sr_xNbO₃ where x=1. Istomin *et.al.* [20], for example, have reported the structure of the material, Sr_{0.99(5)}NbO₃, with possibly the highest Sr content reported to date, with a tetragonal unit cell in which $a=4.0242(1) \text{ \AA}$ and $c=4.0320(1) \text{ \AA}$.

N.Peng [21], for example reported the structure of Sr_xNbO₃ with x=0.97, as simple cubic perovskite structure with $a_p=4.023(1) \text{ \AA}$. Neutron studies, however, revealed a non-cubic distortion and enlargement of the pseudo-cubic cell, due to the presence of extra peaks not observed with powder X-ray diffraction or electron diffraction studies. He found that the real unit cell is actually at least four times the distorted cubic cell reported by other authors, and the distorted orthorhombic unit cell was refined with $a=5.688 \text{ \AA}$ $b=5.682 \text{ \AA}$ $c=8.057 \text{ \AA}$ (sgt=P 21 21 2 (18)) [21], and $\sqrt{2}a_p \times \sqrt{2}a_p \times 2a_p$. The structure was found to be built up from two types of NbO₆ octahedra, one elongated and the other compressed along the *c* axis. The lattice distortion from cubic symmetry originates from the tilting of the NbO₆ octahedra, and the $\sqrt{2}a_p \times \sqrt{2}a_p \times 2a_p$ superstructure was found to arise from the ordering of alternate elongated and compressed octahedra.

5.5.2 Conductivity Studies

The search for new, non copper oxide based, superconductors has lead researchers to study d^1 oxides, such as $(3d)^1 V^{4+}$ and $(4d)^1 Nb^{4+}$ oxides. Isawa *et al* [19], for example looked at Sr_xNbO_3 with $0.70 \leq x \leq 0.90$ and measured electronic conductivity up to 300K. They found the electronic conductivity to be high, with $500-800 Scm^{-1}$ for $Sr_{0.90}NbO_3$ and $Sr_{0.80}NbO_3$ respectively. They also studied the temperature dependence of thermoelectric power, and found that to be negative for all the samples in the temperature range 10-300K. From that they deduced that the dominant charge carriers are electrons.

N.Peng found that $Sr_{0.97}NbO_3$ also has a very high metallic type conductivity of over $1000 Scm^{-1}$ [21] between 2.6K and 300K and was seen to be independent of temperature. Again this was verified by Istomin *et al* [20] who found metal like conductivity up to 300K.

5.5.3 Experimental

These materials have to be made under extremely reducing conditions, at $1300^{\circ}-1400^{\circ}C$ in flowing $5\%H_2/Ar$. Two samples were made under similar conditions, $Sr_{0.6}NbO_3$ and $Sr_{0.7}NbO_3$, both of which were found to be unstable in less reducing conditions.

6.5.4 X-ray powder diffraction

Rapid cooling of the samples to room temperature produced two types of unit cell (Table 5.7): tungsten bronze tetragonal and a cubic perovskite (Fig.5.38). The TGA data confirmed the average niobium oxidation state to be 4.8 for $\text{Sr}_{0.6}\text{NbO}_3$ and 4.6 for $\text{Sr}_{0.7}\text{NbO}_3$ (Fig.5.39).

Table 5.7 Unit cell parameters of $\text{Sr}_{0.6}\text{NbO}_3$ and $\text{Sr}_{0.7}\text{NbO}_3$

	Reduction T (°C)	Phases present	N in Nb ⁿ⁺	Structure of main phase	Unit cell	Perovskite unit cell
$\text{Sr}_{0.6}\text{NbO}_3$	1350	$\text{Sr}_{0.6}\text{NbO}_3$, $\text{Sr}_{0.6}\text{NbO}_3$	4.8	Tungsten bronze tetragonal	a=12.3795(6) b=3.9062(2) V=598.64(7)	a=3.9891(3) V=63.478(8)
$\text{Sr}_{0.6}\text{NbO}_3$	1000			Multiphase: $\text{Sr}_4\text{Nb}_2\text{O}_9$, $\text{Nb}_2\text{O}_{5-x}$ and $\text{Sr}_{1-x}\text{NbO}_3$		
$\text{Sr}_{0.7}\text{NbO}_3$	1350	$\text{Sr}_{0.7}\text{NbO}_3$, $\text{Sr}_{1-x}\text{NbO}_3$	4.6	Tungsten bronze tetragonal	a=12.3821(6) b=3.9065(2) V=598.94(6)	a=3.9895(3) V=63.498(8)
$\text{Sr}_{0.7}\text{NbO}_3$	1000			Multiphase: $\text{Sr}_4\text{Nb}_2\text{O}_9$, $\text{Nb}_2\text{O}_{5-x}$ and $\text{Sr}_{1-x}\text{NbO}_3$		

In order to check the stability of $\text{Sr}_{0.6}\text{NbO}_3$, the pre-made material was put into a tube furnace in flowing 5% H_2 /Ar at 900°C for 10 hours. Once the sample was cooled, x-ray showed a decomposition into starting materials, $\text{Sr}_4\text{Nb}_2\text{O}_9$, $\text{Nb}_2\text{O}_{5-x}$ and some $\text{Sr}_{1-x}\text{NbO}_3$ (Fig.5.38). The instability of these samples in 5% H_2 /Ar at 900°C means that these materials can not be used in the solid oxide fuel cell anode and no further work was carried out to investigate their properties.

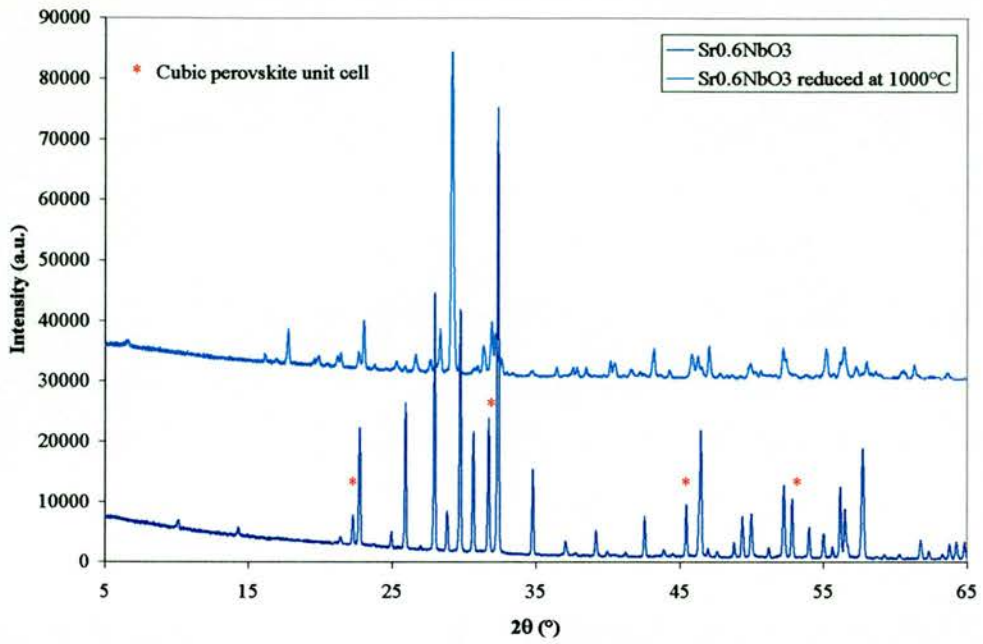


Fig.5.38 X-ray pattern of $Sr_{0.6}NbO_3$ and $Sr_{0.6}NbO_3$ after firing at 900°C in flowing 5% H_2 /Ar

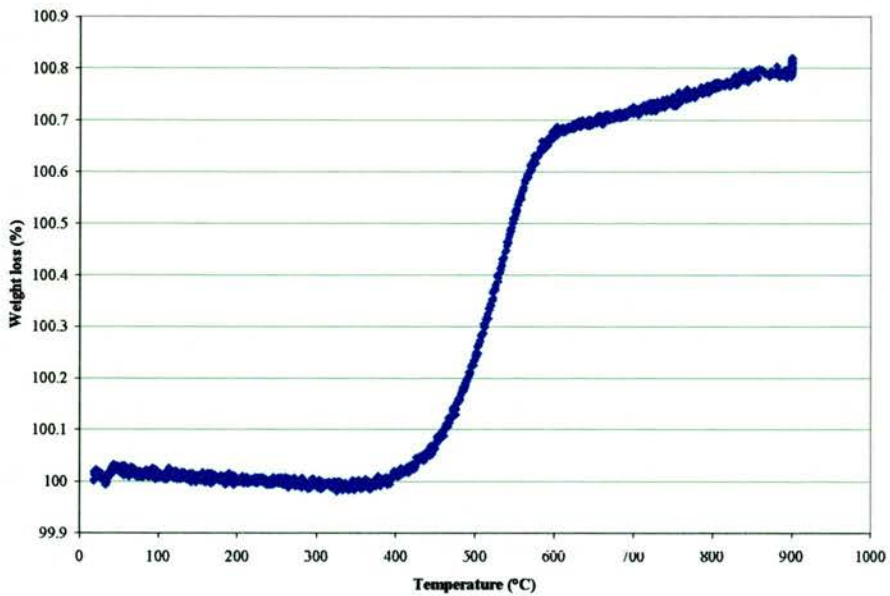


Fig.5.39 Weight change (%) under flowing air $Sr_{0.6}NbO_3$.

5.6 Conclusions

To summarise, the structure of $\text{Sr}_4\text{Nb}_2\text{O}_9$ sintered under reducing conditions is rather complex and shows a microdomain structure, which initially seems to be related to the degree of reduction in the different domains. "Oxidised" domains are apparently cubic ($a=8.27\text{\AA}$), whereas more reduced domains give rise to rather complex superstructures, which may be the result of ordering of oxygen vacancies. Further TEM work performed in specimens sintered in a range of atmospheric conditions is required to fully understand the nature of the structure of these domains. $\text{Sr}_4\text{Nb}_2\text{O}_7$ is an insulator, but on a slight oxidation shows a large increase in conductivity from $7\text{-}8\times 10^{-6}\text{ Scm}^{-1}$ to $1.3\text{-}1.6\times 10^{-3}\text{ Scm}^{-1}$ at 900°C .

$\text{Sr}_2\text{Nb}_2\text{O}_7$ is the $n=4$ member of the homologous series of layered perovskite phases $A_nB_nO_{3n+2}$. It has an electronic conductivity of $0.15\text{-}0.17\text{ Scm}^{-1}$ in $5\%\text{H}_2/\text{Ar}$ at 900°C . Further reduction in $5\%\text{H}_2/\text{Ar}$ at 1350°C reduces niobium from $5+$ to $4.8+$, corresponding to the $\text{Sr}_5\text{Nb}_5\text{O}_{17}$ phase. Electronic conductivity is increased to $0.3\text{-}0.5\text{ Scm}^{-1}$ and a metal insulator transition is observed at $\sim 600^\circ\text{C}$. The stability of the sample, however, is poor and in $5\%\text{H}_2/\text{Ar}$ at 900°C there is a decrease in conductivity during the 12-hour isotherm.

SrNb_2O_6 crystallises in a framework structure similar to CaTa_2O_6 . It is much more readily reduced than $\text{Sr}_4\text{Nb}_2\text{O}_9$ and $\text{Sr}_2\text{Nb}_2\text{O}_7$, thus reduction in $5\%\text{H}_2/\text{Ar}$ at 1000°C gives niobium in the oxidation state $4.98+$ with a conductivity of $\sim 8\times 10^{-2}\text{ Scm}^{-1}$ at 900°C and a $p(\text{O}_2)$ dependence of $-1/4.5$. Further reduction at 1200°C reduces niobium to $4.76+$, with a conductivity of 40Scm^{-1} at 900°C . As with $\text{Sr}_2\text{Nb}_2\text{O}_7$, this phase is not stable under $5\%\text{H}_2/\text{Ar}$ at 900°C resulting in a rapid drop in conductivity during a 10 hour isotherm.

$\text{Sr}_{0.6}\text{NbO}_3$ proved to be a very difficult material to synthesise phase pure and fully reduced, producing two phases, tetragonal tungsten bronze and a simple cubic perovskite. Heating the sample up to 900°C in $5\%\text{H}_2/\text{Ar}$ decomposed the material into the starting components, $\text{Sr}_4\text{Nb}_2\text{O}_9$, $\text{Nb}_2\text{O}_{5-x}$ and $\text{Sr}_{1-x}\text{NbO}_3$.

5.7 References

- 1 P.P.Leshchenko, A.V.Shevchenko, L.N.Lykova, L.M.Kovba and E.A.Ippolitova, *Izv.Akad.Nauk SSSR, Neorg.Mater.*, (1982), **18** (7), 1202; *Inorg.Mater.(Engl.Transl.)*, (1982), **18** (7), 1013
- 2 N.Ishizawa, F.Narumo, T.Kawamura and M.Kimura, *Acta Crystallogr., Sect.B:Struct.Crystallogr.Cryst.Chem.*, (1975), **B31**, 1912
- 3 M.Weiden, A.Grauel, J.Norwig, S.Horn and F.Steglich, *J.Alloys and Compounds*, (1995), **218**, 13
- 4 K.Schueckel and H.K. Müller-Buschbaum, *Zeitschrift für Anorganische und Allgemeine Chemie*, (1985), **523**, 69
- 5 J.Lecomte, J.P.Loup, M.Hervieu and B.Raveau, *Phys.Status Solidi(a)*, (1981), **65**, 743
- 6 I.Levin, J.Y.Chan, J.H.Scott, L.Farber, T.A.Vanderah and J.E.Maslar, *J.Solid State Chem.*, (2002), **166**, 24
- 7 Y.Du and A.S.Nowick, *Mater.Res.Symp.Proc.*, (1995), **369**, 289
- 8 R.Glückner, A.Neiman, Y.Larring and T.Norby, *Solis State Ionics*, (1999), **125**, 369
- 9 A.Ya.Neiman, A.L.Podkorytov and V.M.Zhukovskii, *Phys.Status Solidi(a)*, (1987), **101**, 371
- 10 T.Norby, *Adv.Ceram.*,(1987), **23**, 107
- 11 S.N.Ruddlesden and P.Popper, *Act.Cryst.*,(1957), **10**, 538
- 12 S.N.Ruddlesden and P.Popper, *Act.Cryst.*,(1958), **11**, 54
- 13 F.Lichtenberg, A.Herrnberger, K.Wiedenmann and J.Mannhart, *Progr.Solid State Chem.*,(2001), **29**, 1

- 14 H.W.Schmalle, T.Williams, A.Reller, F.Lichtenberg, D.Widmer and J.G.Bednorz, *Acta Cryst.C.*, (1995), **51**, 1243
- 15 H.G.Hess and H.J.Trumpor, *Am.Min.*,(1959), **1**, 44
- 16 B.O.Marinder, P-L.Wang and P.E.Werner, *Acta Chem.Scand. Series A*, (1986) **40**, 467
- 17 D.Ridgley and R.Ward, *J.Am.Chem.Soc.*,(1955), **77**, 6132
- 18 B.Hessen, S.A.Sunshine, T.Siegrist and R.Jimenez, *Mater.Res.Bull.*, (1991), **26**, 85
- 19 K.Isawa, J.Sugiyama, K.Matsuura, A.Nozaki and H.Yamauchi, *Phys.Rev.B*, (1993), **47**, 2849
- 20 S.Ya.Istomin, G.Svensson, O.G.D'yachenko, W.Holm and E.V.Antipov, *J.Solid State Chem.*, (1998), **141**, 514
- 21 N.Peng, J.T.S.Irvine and A.G.Fitzgerald, *J.Mater.Chem.*, (1998), **8**(4), 1033

Chapter 6. MNb₂O₆ (M=Ba,Ca)

6.1 BaNb₂O₆.....	218
6.1.1 <i>Introduction</i>	218
6.1.2 <i>Structure</i>	218
6.1.3 <i>Structural changes on reduction</i>	220
6.1.4 <i>Thermal expansion coefficient</i>	221
6.1.5 <i>Electronic conductivity</i>	223
6.2 CaNb₂O₆	228
6.2.1 <i>Introduction</i>	228
6.2.2 <i>Structure</i>	228
6.2.3 <i>Structural change on reduction</i>	230
6.2.4 <i>Electronic conductivity</i>	231
6.2.5 <i>Thermal expansion coefficient</i>	236
6.3 CONCLUSION	237
6.4 REFERENCES.....	239

6.1 BaNb₂O₆

6.1.1 Introduction

In Chapter 5 SrNb₂O₆ was found to have the highest conductivity upon reduction out of the Sr_xNb_yO_{x+2.5y} series, hence it was interesting to have a look at barium and calcium analogues of this material to see how the properties changed with the *A* site cation substitution. Barium is the next element after strontium in the alkaline earth series, in the oxidation state (II) and octahedral oxygen co-ordination it has a larger ionic radius of 1.36Å, compared to strontium's ionic radius under the same conditions of 1.16Å. As such, there will be significant differences in analogous structures, which will affect their properties.

6.1.2 Structure

The structure of BaNb₂O₆ is orthorhombic with a relatively large unit cell of 7.87Åx12.22Åx10.29Å (Table 6.1) with a space group C2221[4]. The structure itself is similar to that of SrNb₂O₆ discussed in the previous chapter, but neither BaNb₂O₆ nor SrNb₂O₆ adopt the tetragonal tungsten bronze structure. Solid solutions, however, of the compositions Ba_{1-x}Sr_xNb₂O₆, were studied extensively by many researchers [1, 2, 5], due to the excellent electro-optic, pyro- and piezoelectric properties of this material, making it suitable for a number of applications in optoelectronic devices.

Between the two phases in which $x=0$ or 1, Ba_{1-x}Sr_xNb₂O₆ crystallise with the tungsten bronze structure. This is because the tetragonal tungsten bronze structure contains four big voids with co-ordination number (CN)15, two voids with CN12, and four small voids with CN9. The strontium barium niobates of the above composition are partially filled tetragonal tungsten bronzes, in which only five of the six CN15 and CN12 sites are occupied with Sr and Ba atoms. The two sizes of cation facilitate the formation of the partially filled tetragonal tungsten bronze structure, in which the rest of the voids are empty.

The structure of BaNb₂O₆ (Fig.6.1) consists of a zig-zag pattern of pairs of edge-sharing NbO₆ octahedra, which are joined at corners at ~60° and 120° angles [3] to produce a ring of 6 octahedra. Barium ions occupy the interstices in this network of Nb₂O₁₀ octahedra.

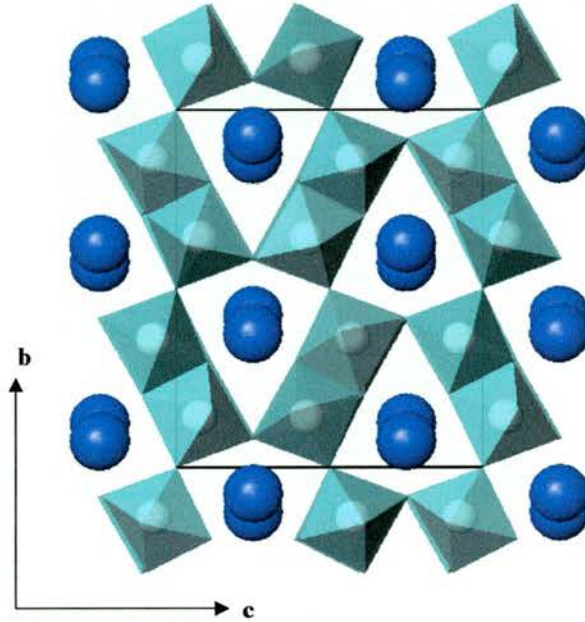


Fig.6.1 Edge-sharing and corner sharing NbO₆ octahedra with Ba in between (blue)[4]

Table 6.1 Unit cell parameters and thermal expansion coefficient (300°-900°C) for BaNb₂O₆ made in air and reduced at 1000°C or 1200°C

	Reduction T (°C)	Unit cell symmetry	a(Å)	b(Å)	c (Å)	V (Å ³)	TEC (10 ⁻⁶ K ⁻¹)
BaNb ₂ O ₆	N/A	Orthorhombic C	7.8678(3)	12.2127(5)	10.2868(4)	988.43(10)	11.9(±0.5)
BaNb ₂ O _{6-δ}	1000	Orthorhombic C	7.8702(4)	12.2143(5)	10.2886(4)	989.03(10)	12.4(±0.5)
BaNb ₂ O _{6-δ}	1200	Orthorhombic C	7.8714(3)	12.2202(5)	10.2933(5)	990.11(10)	11.9(±0.5)

The difference in the SrNb₂O₆ and BaNb₂O₆ structures lies in the arrangement of the edge-sharing Nb₂O₁₀ octahedra (Fig.6.2). In the SrNb₂O₆ structure the Sr is 12-fold co-ordinate to surrounding oxygens, eight of which are near co-ordinate and 4 oxygens are further away, and the Nb₂O₁₀ groups tilt in phase in each row.

The Ba atoms, being of a much larger size are 16-fold co-ordinate to the surrounding oxygens. Six oxygens are in closest packing with Ba, 8 oxygens are slightly more distant and two others form a 16-fold co-ordination for the Ba atoms.

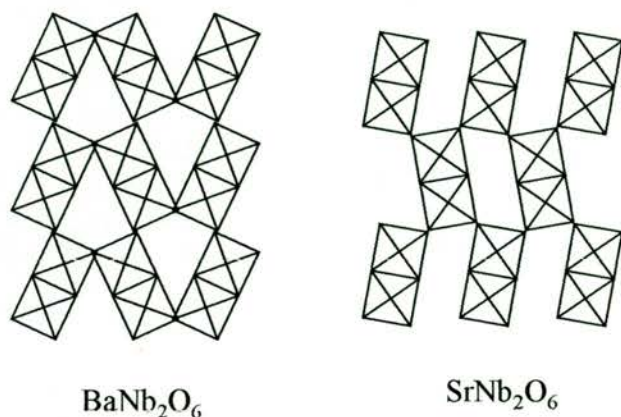


Fig.6.2 Layers of octahedra in the perovskite type BaNb₂O₆ and SrNb₂O₆ structures

The difference in the arrangement of Nb₂O₁₀ groups in these structures allows the incorporation of a much larger *A* cation between Nb₂O₁₀ octahedra. The differences in the reduction behaviour, conductivity and thermal expansion are discussed in the following sections.

6.1.3 Structural changes on reduction

As can be seen from (Table 6.1), BaNb₂O₆ is structurally very stable to reduction, even at 1200°C. No additional impurity peaks were seen in the X-ray pattern (Fig.6.3), and the only visible effect on the structure is a very slight increase in the unit cell size. All peaks were indexed, some of which are indexed in (Fig.6.3). In comparison, SrNb₂O₆ adopted a tetragonal tungsten bronze structure when reduced at 1200°C. This may be due to the high activation energy required to rearrange the niobium octahedra in order to incorporate the much larger Ba atoms.

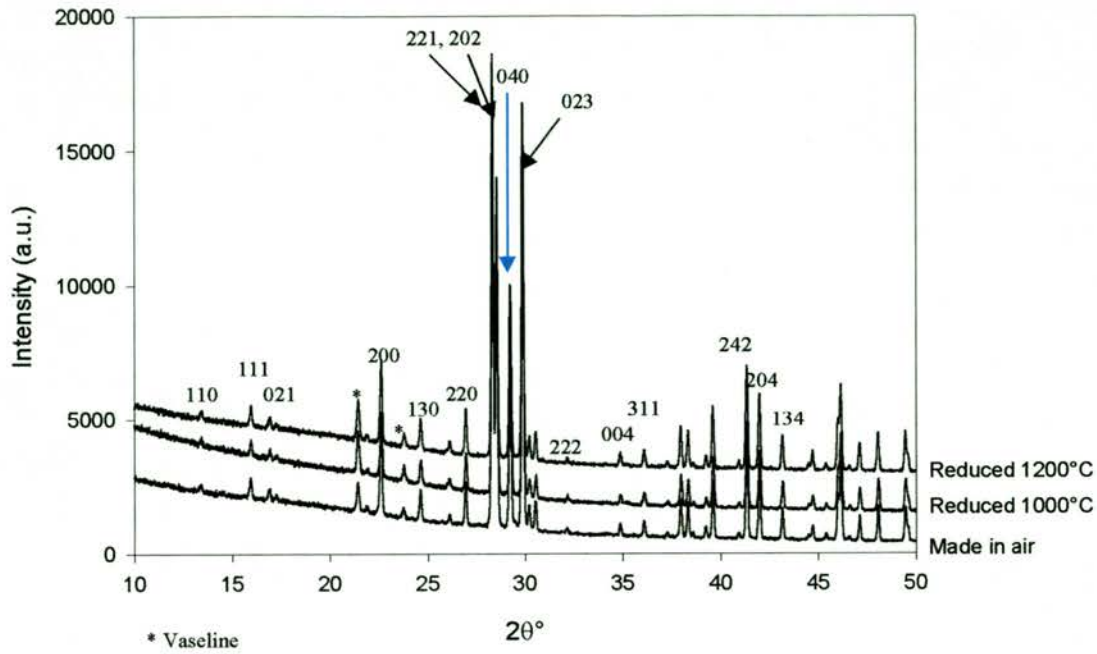


Fig.6.3 BaNb₂O₆ as made in air and reduced at 1000° and 1200°C.

Although it is clear that the sample undergoes reduction, in which the colour changes from white to pale blue, when reduced at 1000°C, to dark blue when reduced at 1200°C, the change is too small to be reliably measured by the TGA. Pre-reduced samples of 20-45mg were heated under flowing air, with a heating ramp rate of 20°-50°C/min up to 900°C. The sample was allowed to remain at 900°C for up to 3 hours, at the end of which white powder was obtained, indicating complete re-oxidation. The TGA data showed only a small reduction showing δ to be <0.02 in BaNb₂O_{6- δ} .

6.1.4 Thermal expansion coefficient

The resistance to reduction is further reflected in the thermal expansion coefficient of BaNb₂O₆ (Fig.6.4). Although initially the thermal expansion coefficient is seen to increase from $\alpha_{300^{\circ}\text{C}-900^{\circ}\text{C}}=11.9\pm 0.5\times 10^{-6}\text{K}^{-1}$ to $\alpha_{300^{\circ}\text{C}-900^{\circ}\text{C}}=12.4\pm 0.5\times 10^{-6}\text{K}^{-1}$, it decreases back to $\alpha_{300^{\circ}\text{C}-900^{\circ}\text{C}}=11.9\pm 0.5\times 10^{-6}\text{K}^{-1}$ (Table 6.2) for 1200°C reduced sample, the variation is within the experimental error of $0.5\times 10^{-6}\text{K}^{-1}$.

Table 6.2 Technical and physical alpha for BaNb₂O₆

	Reduction T (°C)	α_t 300°C-900°C (10 ⁻⁶ K ⁻¹)	α_p 900°C (10 ⁻⁶ K ⁻¹)
BaNb ₂ O ₆	N/A	11.9(±0.5)	12.8(±0.5)
BaNb ₂ O _{6-δ}	1000	12.4(±0.5)	13.1(±0.5)
BaNb ₂ O _{6-δ}	1200	11.9(±0.5)	12.1(±0.5)

The $\alpha_{900^\circ\text{C}}$ (Table 6.2) shows negligible difference in the thermal expansion coefficient of the reduced samples. The differences in values are within the error range, hence it can be concluded that reduction of BaNb₂O₆ has little effect on the structural properties of the material, such as the unit cell, oxygen stoichiometry and the thermal expansion coefficient.

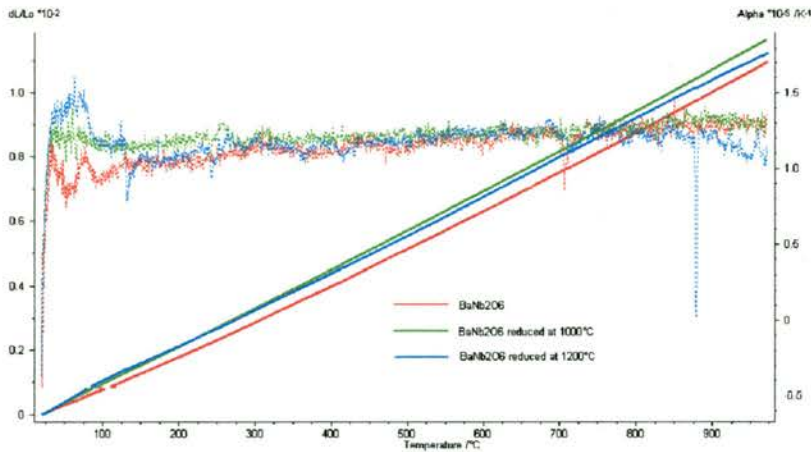


Fig.6.4 dL/L_0 as a function of temperature (straight line) and α_p curve as a function of temperature for BaNb₂O₆

It is of interest to note that the sample reduced at 1200°C shows a significant decrease in the thermal expansion coefficient above 900°C as can be seen from the physical alpha curve (Fig.6.4). As will be seen in the next section, BaNb₂O_{6-δ} reduced at 1200°C has poor stability in 5%H₂/Ar at 900°C, with a rapidly decreasing electronic conductivity due to re-oxidation in the milder conditions than those under which it was reduced. The fluctuation in the thermal expansion coefficient above 900°C may be a reflection of these changes in the sample.

6.1.5 Electronic conductivity

In the early work on MNb₂O₆ (M=Ba, Sr) L.Marta and M.Vancea [5] found the conductivity of BaNb₂O₆ to be $\sim 1.5\text{-}2.0 \times 10^{-5} \text{ Scm}^{-1}$ at 900°C and that of SrNb₂O₆ to be $3.0\text{-}3.5 \times 10^{-5} \text{ Scm}^{-1}$ at 900°C, however they did not look at the effects of reduction on these samples. The conductivity data here is in agreement with their results for the oxidised sample, displaying a conductivity of $\sim 2 \times 10^{-5} \text{ Scm}^{-1}$ at 900°C for BaNb₂O₆, and $6 \times 10^{-5} \text{ Scm}^{-1}$ at 900°C for SrNb₂O₆ in the previous Chapter.

The oxidised sample BaNb₂O₆, similar to SrNb₂O₆, is very resistive with a conductivity of $\sim 2 \times 10^{-5} \text{ Scm}^{-1}$. The activation energy for this material is quite high at $2.0 \pm 0.1 \text{ eV}$ on heating and $2.3 \pm 0.1 \text{ eV}$ on cooling (Fig.6.5).

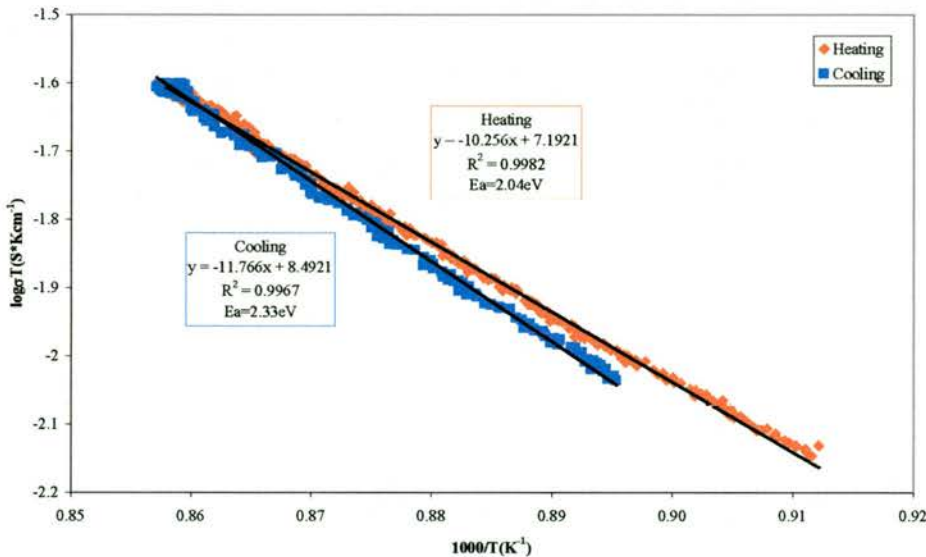


Fig.6.5 Arrhenius plot for BaNb₂O₆ from the 4-terminal DC measurement in air

On reduction, however, the conductivity increases by 5 orders of magnitude to $0.6 \pm 0.1 \text{ Scm}^{-1}$, with low activation energy of $0.48 \pm 0.01 \text{ eV}$ at low temperatures (50°-200°C). At higher temperatures, the activation energy varies with temperature, giving a curve in the Arrhenius plot (Fig.6.6). E_a decreases between 200°C and 350°C, is then constant until $\sim 600^\circ\text{C}$, and above this temperature E_a increases rapidly with increasing temperature.

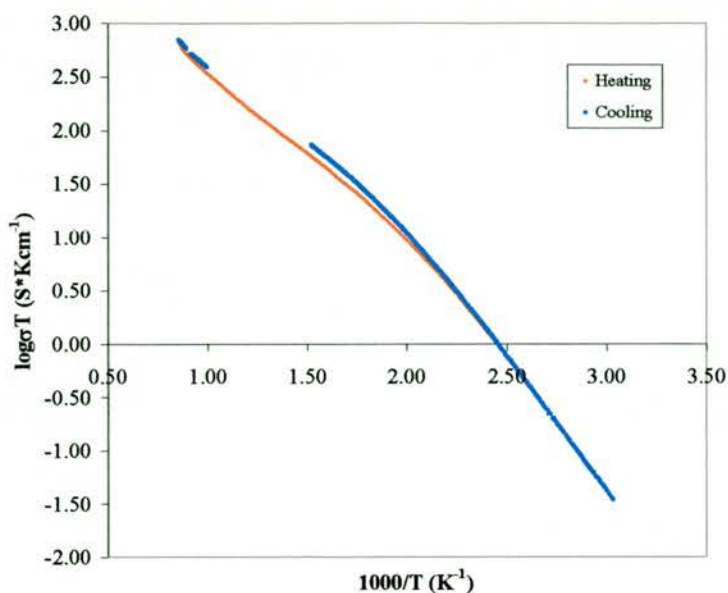


Fig.6.6 Arrhenius plot for BaNb₂O_{6-δ} reduced at 1000°C from the 4-terminal DC measurement

Further reduction at 1200°C increases the electronic conductivity of BaNb₂O₆ to 12 Scm⁻¹, at 900°C (Fig.6.7). This phase, however, is not stable in 5%/H₂/Ar, and repeated heating and cooling in flowing gas showed a gradual decrease in the electronic conductivity. The material seems to undergo a metal-semiconductor transition at ~500°-650°C, although this transition becomes less pronounced with additional cycles, as the material changes to niobium's more stable oxidation state at 900°C, which in this structure is 5 δ, where δ<0.02.

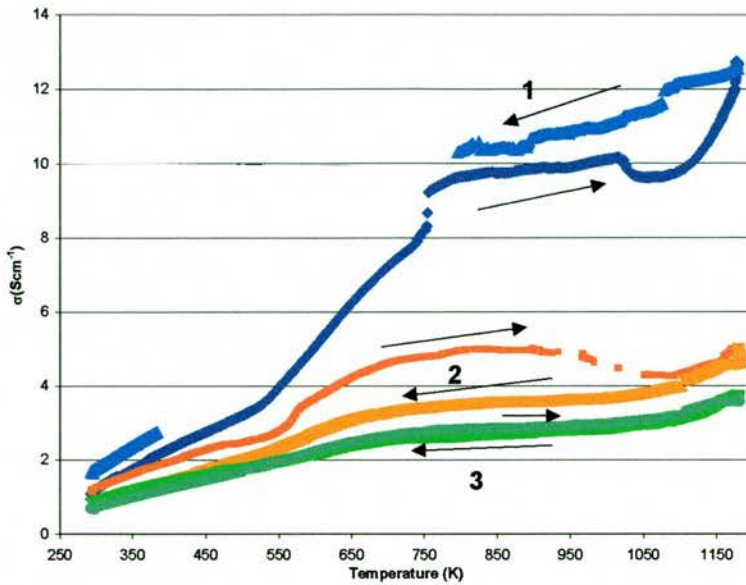


Fig.6.7 Plot of conductivity versus temperature of BaNb₂O_{5.x} in flowing 5%H₂/Ar for the three consecutive runs

Table 6.3 compares the conductivities and activation energies for BaNb₂O_{6-x}. As is typical of niobium based materials, and was also seen in the strontium niobates, the conductivity increases rapidly with a very small amount of reduction.

Table 6.3 Electronic conductivities and activation energies for BaNb₂O_{6-x}

MNb ₂ O ₆	Reduction T(°C)	Conductivity (Scm ⁻¹) at 900°C	Ea (eV) heating	Ea (eV) cooling
BaNb ₂ O ₆	N/A	2.2-2.6x10 ⁻⁵	2.04 (800°-900°C)	2.33 (800°-900°C)
BaNb ₂ O _{6.5}	1000	0.58-0.60	0.48 (50°-200°C) curve (200°-900°C)	0.49 (50°-200°C) curve (200°-900°C)
BaNb ₂ O _{6.3}	1200	12.7-3.7	_____	_____

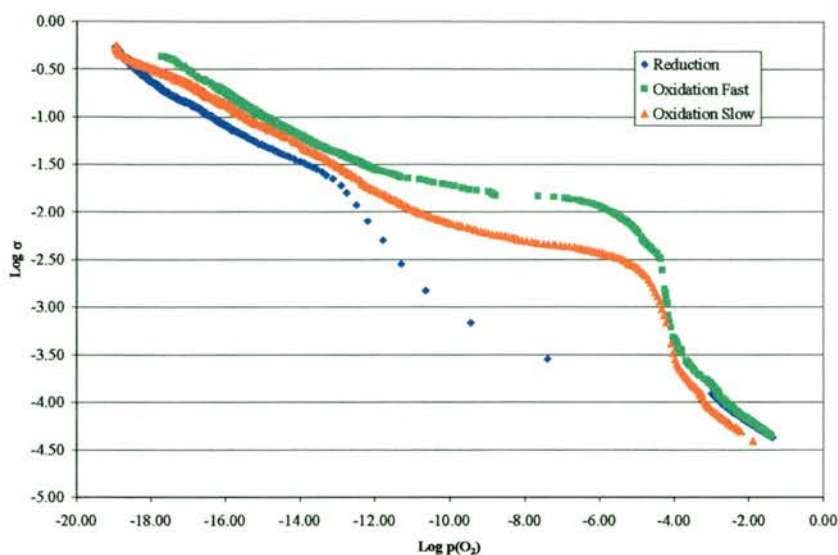


Fig.6.8 $p(\text{O}_2)$ measurement for BaNb_2O_6 , with oxidation runs performed at fast and slow rates

The $p(\text{O}_2)$ measurement shows the n -type conductivity with a slope of 0.20-0.22, i.e. $\sigma \propto p(\text{O}_2)^{-1/5}$ (Fig.6.8). The slow and fast runs were done to demonstrate how the rate of oxidation determines the equilibrium reached in the region of $\log p(\text{O}_2)$ from -12 to -5. In the fast oxidation run, green data, the oxidation in the range $p(\text{O}_2) = 10^{-12} - 10^{-5}$ atm took 20 minutes and in the slow oxidation, red data, the same region took 96 minutes to complete. In this region the equilibrium sought after to get accurate data cannot normally be attained.

The hysteresis seen between the oxidation and the reduction run may be either due to the diffusion length through the sample, and the three related factors which affect it are: the porosity of the sample, surface exchange kinetics of the sample and the diffusion coefficient; or the hysteresis may be caused by different rates of reduction and oxidation. In this transient technique the reduction rate cannot be controlled, and the only certainty is that the reduction up to 10^{-18} atm is much faster than the reverse oxidation. Between 10^{-18} and 10^{-20} atm there is a good match between the oxidation and the reduction paths, and the hysteresis is minimal.

It is thus difficult to say whether in this sample the rate of reduction/oxidation or the diffusion length through the sample is the cause of the hysteresis. In this sample the hysteresis seen (red and blue data) probably reflects the surface exchange kinetics. The sample has a density of 72%, porous enough to allow enough gas to permeate the sample, hence either the slow surface exchange kinetics or a low diffusion coefficient (or both) may be responsible for the hysteresis. Surface exchange kinetics are also affected by the particle size. Smaller particles, with larger surface area will reach equilibrium much faster with the same surface exchange kinetics and diffusion coefficient.

In the case of very dense pellets it is difficult to distinguish the effects of the density from the surface exchange kinetics. If the sample is very dense, the gas cannot quickly permeate into the centre of the pellet and that is then the limiting factor.

6.2 CaNb₂O₆

6.2.1 Introduction

Calcium is the element above strontium in the alkaline earth series, in the oxidation state (II) and octahedral oxygen co-ordination it has a smaller ionic radius of 1.00Å compared to strontium's ionic radius under the same conditions of 1.16Å and that of barium is 1.36Å. This alone should make a difference to the chemistry of calcium niobates compared to the barium and strontium analogues.

6.2.2 Structure

CaNb₂O₆ has a fersmite structure, which is very different from CaTa₂O₆, BaNb₂O₆ and SrNb₂O₆. It consists of the zig-zag edge-sharing niobium oxide octahedra along the *c*-axis. These edge-sharing layers are corner linked to an adjacent edge sharing layer along the the *b*-axis, and this forms a plane, with calcium between the layers going in the [100] direction (Fig.6.9(a) and (b)). In this structure the Ca²⁺ ions are six co-ordinate, compared to twelve co-ordinate strontium and sixteen co-ordinate barium.

The arrangement of octahedra are clearly influenced by the size of the *A* site cation, which must fit into the interstices in the network. The *A* site cation size alone, however, is insufficient to determine the structure, so for example, SrNb₂O₆ and SrTa₂O₆ form different structures, as do CaNb₂O₆ and CaTa₂O₆.

Although Nb and Ta are the same size, the metal-metal interaction is strong in Nb⁵⁺ and is much weaker in Ta⁵⁺. As such the strength of this interaction promotes shorter Nb⁵⁺-Nb⁵⁺ distances than Ta⁵⁺-Ta⁵⁺ distances. In the octahedral co-ordination by oxygen in the oxide structures closer metal-metal distances are possible with edge-sharing, rather than corner sharing.

G.Blasse [6] has thus predicted that there will be a stronger tendency to edge share in ANb_2O_6 structures than in ATa_2O_6 structures. Thus the tendency of the niobium oxide to share edges is balanced by the size of the cation in the structure. Where the cation is large, edge sharing is limited and may not be allowed, whereas in the case of a smaller cation, such as Ca^{2+} , edge-sharing may be extended along one axis. In the $CaTa_2O_6$ structure (Fig.6.9(c)), the edge sharing is limited, and the pairs of edge-sharing octahedra are joined in such a way so as to allow a higher co-ordination for Ca^{2+} ions. In $CaNb_2O_6$ there are chains of edge-sharing NbO_6 octahedra, allowing a small co-ordination of 6 for Ca^{2+} ions.

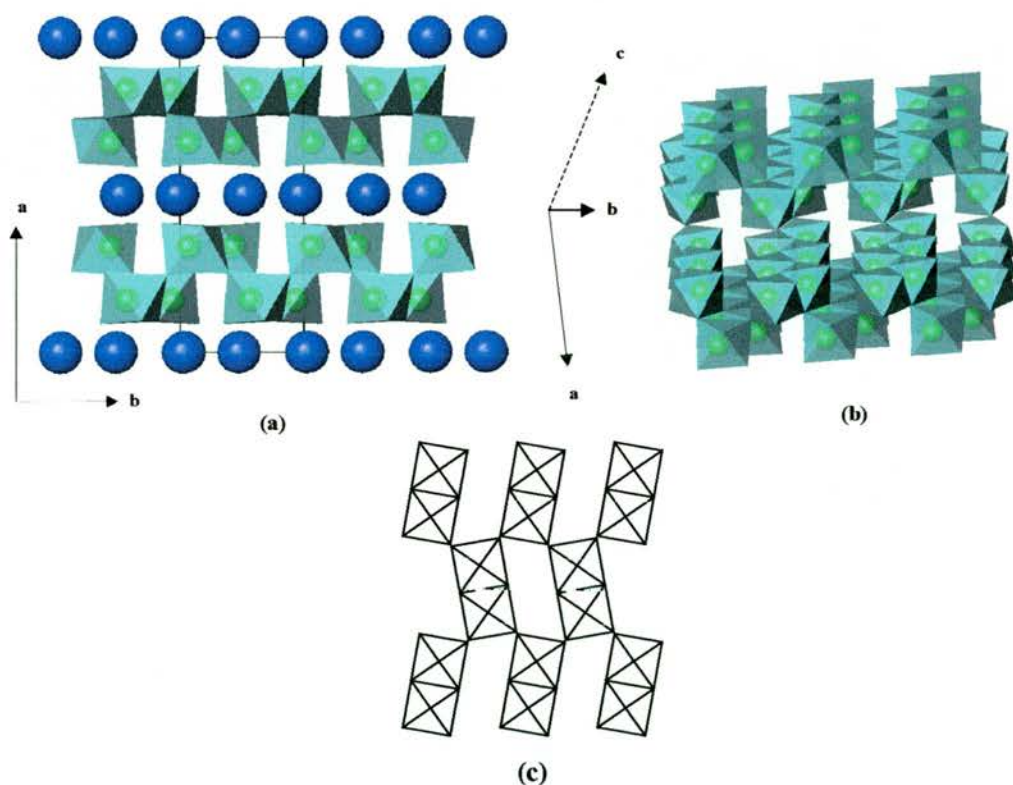


Fig.6.9 (a) Planes of edge and corner sharing niobium octahedra with calcium atoms between the planes (blue) in $CaNb_2O_6$ (b) Calcium atoms removed to see more clearly the edge sharing octahedra in the c-axis and corner linked to the next one in the b-axis (c) Orthorhombic $CaTa_2O_6$ structure

6.2.3 Structural change on reduction

The unit cell parameters shown in Table 6.4 of CaNb₂O₆ show the unit cell to be orthorhombic, with $a=14.997\text{\AA}$, $b=5.754\text{\AA}$ and $c=5.230\text{\AA}$, and a space group PBCN [7]. The a -axis, is extended to 14.99\AA due to the layers of Ca ions between the octahedra planes. The c -axis is smaller than the b -axis, probably due to the edge-sharing of the octahedra reducing the metal-metal distance in the structure as was discussed earlier.

Table 6.4 Unit cell parameters of CaNb₂O_{6-δ} and the thermal expansion coefficients between 300°C and 900°C

MNb ₂ O ₆	Reduction T (°C)	Unit cell symmetry	a(Å)	b(Å)	c(Å)	V (Å ³)	TEC (10 ⁻⁶ K ⁻¹)
CaNb ₂ O ₆	N/A	Orthorhombic P	14.9971(9)	5.7542(3)	5.2301(3)	451.33(6)	9.25±0.05
CaNb ₂ O _{6-δ}	1000	Orthorhombic P	14.9884(8)	5.7510(3)	5.2268(3)	450.53(6)	9.63±0.05
CaNb ₂ O _{6-δ}	1200	Orthorhombic P	14.9900(8)	5.7517(3)	5.2276(3)	450.72(6)	9.38±0.05

As before the reduction was carried out in flowing 5%H₂/Ar at 1000°C or 1200°C.

Although the unit cell does not change much on reduction it is seen to decrease slightly when reduced at 1000°C, but then increases again with further reduction at 1200°C. The c -axis undergoes a greater shrinkage due to the stronger Nb-Nb interaction as it reduces from oxidation state 5 to 5- δ .

Again, as for BaNb₂O₆, the degree of reduction could not be measured reliably with the TGA, indicating that δ in CaNb₂O_{6-δ} is <0.02. The colour of the reduced sample did indicate some reduction though, although it was not very apparent, changing from white to very white/pale blue, to a slightly darker shade of pale blue.

6.2.4 Electronic conductivity

Whereas the electronic conductivity of SrNb₂O₆ and BaNb₂O₆ were very similar $\sim 2\text{--}6 \times 10^{-5} \text{ Scm}^{-1}$ at 900°C in air, the electronic conductivity of CaNb₂O₆ is 10 times lower at $\sim 3 \times 10^{-6} \text{ Scm}^{-1}$ at 900°C in air. Although an almost linear relationship is seen in the Arrhenius plot (Fig.6.10) there is slight curvature, showing an increase in the activation energy as the sample approaches higher temperatures. The activation energy is $1.06 \pm 0.03 \text{ eV}$ on cooling and $1.01 \pm 0.03 \text{ eV}$ on heating.

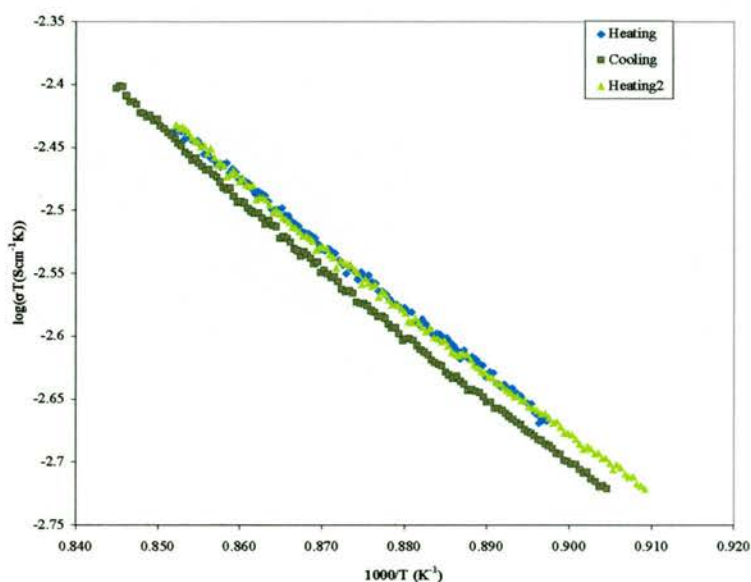


Fig.6.10 Arrhenius plot for CaNb₂O₆ from the 4-terminal DC measurement in air

Reducing CaNb₂O₆ at 1000°C increases the conductivity to $\sim 1.5 \times 10^{-3} \text{ Scm}^{-1}$ at 900°C. No hysteresis is seen in the cooling and heating curves, indicating faster kinetics in this sample than for the barium and strontium analogues. There is also curvature of the line in the Arrhenius plot (Fig.6.11), thus when plotting the apparent activation energy, as estimated from the gradient of the Arrhenius plot, against $1000/T$ (Fig.6.12), it can be seen that the activation energy increases with temperature, from $0.30 \pm 0.01 \text{ eV}$ at 400°C to $0.66 \pm 0.01 \text{ eV}$ at 900°C.

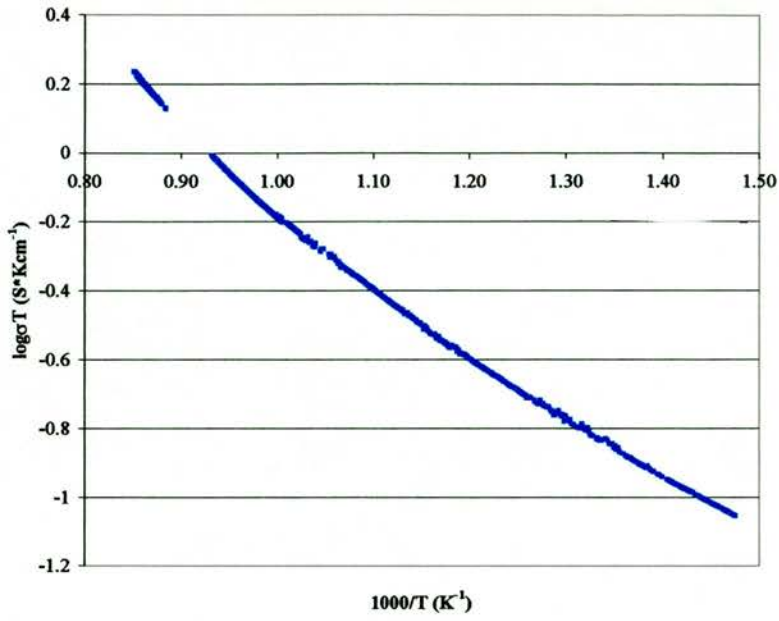


Fig.6.11 Arrhenius plot for CaNb₂O₆ reduced at 1000°C from the 4-terminal DC measurement

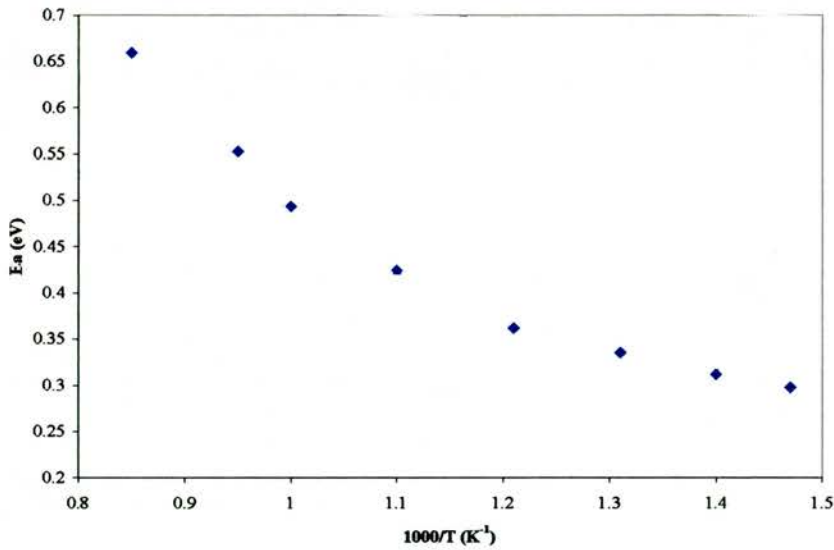


Fig.6.12 Apparent activation energy as a function of 1000/T for the 1000°C reduced CaNb₂O₆

Further reduction at 1200°C increases the conductivity only up to $1.0 \times 10^{-2} \text{ Scm}^{-1}$ at 900°C. The Arrhenius plot in (Fig.6.13) shows a hysteresis curve on cooling and heating, though it only occurs at lower temperatures, reflecting the difference in the rates of heating and cooling of the furnace below 200°C. At higher temperatures no hysteresis is observed.

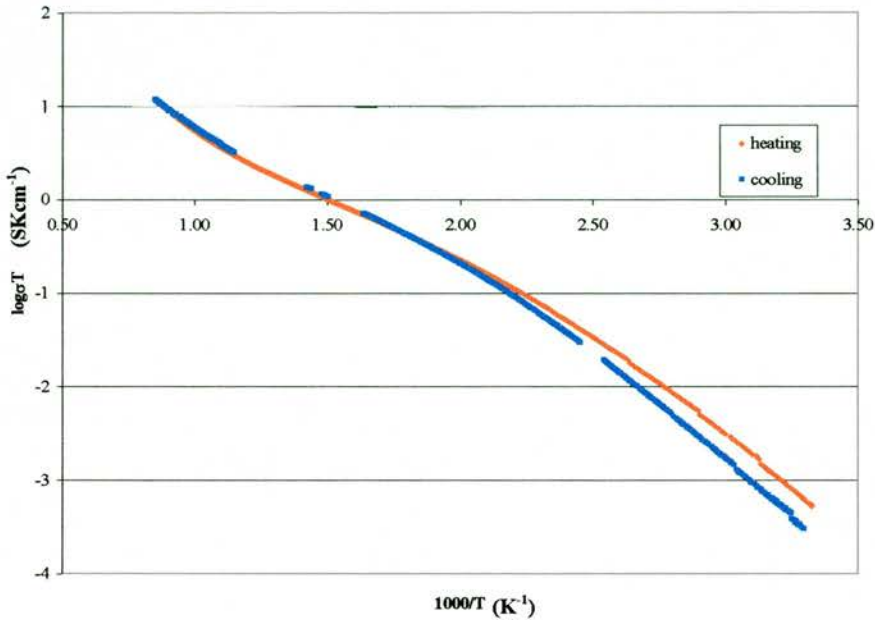


Fig.6.13 Arrhenius plot for CaNb₂O₆ pre-reduced at 1200°C from the 4-terminal DC measurement

Again the slope, and hence the activation energy, changes with temperature, but the pattern of change is similar to the BaNb₂O_{6-δ}, with initial decrease in the apparent activation energy, estimated from the slope to be from $0.32 \pm 0.01 \text{ eV}$ to $0.27 \pm 0.01 \text{ eV}$, with temperature between 200°C and 300°C respectively. There is then a period of constant activation energy up to 500°C of $0.25 \pm 0.01 \text{ eV}$, and this in turn is followed by a rapid increase in activation energy, which reaches $0.48 \pm 0.01 \text{ eV}$ at 900°C.

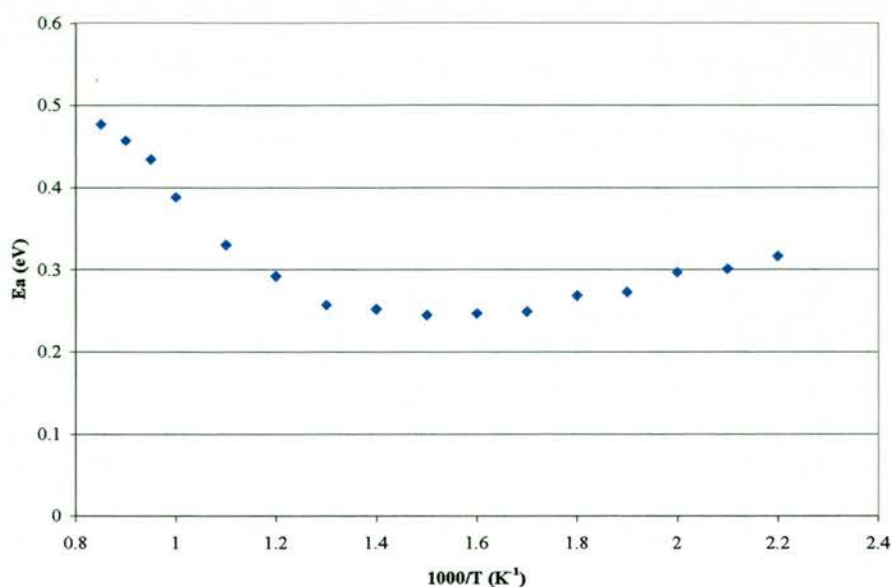


Fig.6.14 Apparent activation energy as a function of $1000/T$ for the 1200°C reduced CaNb_2O_6

Table 6.5 Conductivity data for CaNb_2O_6 and $\text{CaNb}_2\text{O}_{6-\delta}$

Reduction T(°C)	Conductivity (Scm^{-1}) at 900°C	Ea (eV) heating	Ea (eV) cooling	
CaNb_2O_6	N/A	3×10^{-6}	$1.00-1.02 \pm 0.03$ ($840^{\circ}-900^{\circ}\text{C}$)	1.06 ± 0.03 ($830^{\circ}-900^{\circ}\text{C}$)
$\text{CaNb}_2\text{O}_{6-\delta}$	1000	1.46×10^{-3}	0.66 ± 0.01 ($870^{\circ}-900^{\circ}\text{C}$)	0.61 ± 0.01 ($870^{\circ}-900^{\circ}\text{C}$)
$\text{CaNb}_2\text{O}_{6-\delta}$	1200	1.00×10^{-2}	curve < 870°C	curve < 870°C

Table 6.5 shows the conductivities and activation energies of CaNb_2O_6 . The TGA data showed no significant reduction of niobium, and a more sensitive technique is required to calculate the δ in $\text{CaNb}_2\text{O}_{6-\delta}$. As was clear with strontium niobates, a very small amount of reduction produces large increase in conductivities.

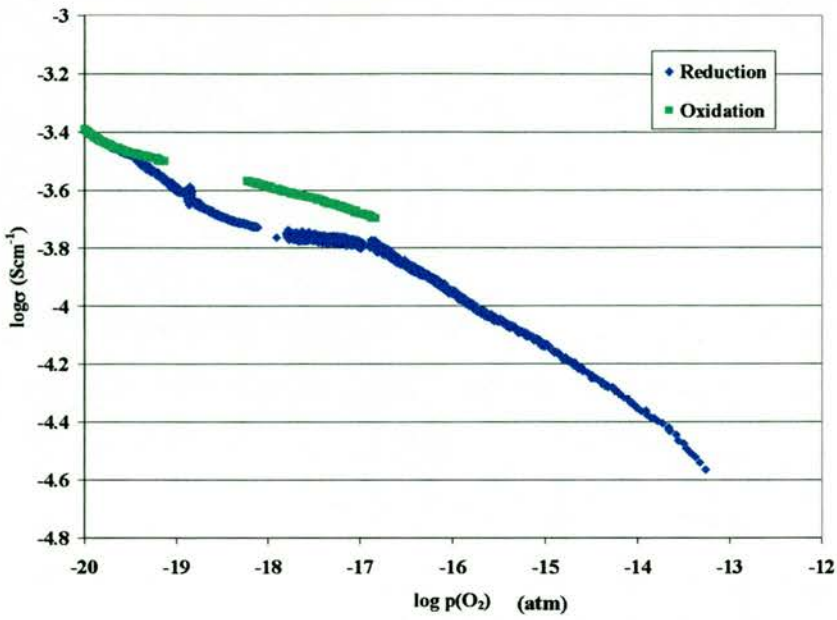


Fig. 6.15 Log conductivity as a function of $\log p(\text{O}_2)$

Conductivity as a function of partial pressure showed a $p(\text{O}_2)$ dependence of -0.19 , i.e. $-1/5$, from 10^{-13} to 10^{-17} atm. The slope then drops to -0.13 , i.e. $-1/8$, from 10^{-17} to 10^{-20} atm. The oxidation run showed a slope of 0.089 from 10^{-20} to 10^{-17} atm, i.e. $-1/11$, indicating that equilibrium on the oxidation reaction was not really achieved and the true slope is between the reduction and the oxidation hysteresis.

6.2.5 Thermal expansion coefficient

Like BaNb₂O₆, CaNb₂O₆ reflects stability to reduction through the thermal expansion coefficient. Table 6.4 shows the thermal expansion coefficient along with the unit cell size. As before there is no significant change in the thermal expansion with reduction, and any change observed is within the experimental error of $\pm 0.5 \times 10^{-6} \text{K}^{-1}$ (Fig.6.16). Physical alpha curve shows a very slight increase in the thermal expansion with temperature, hence the thermal expansion is higher at 900°C with $10.4 \pm 0.5 \times 10^{-6} \text{K}^{-1}$ than the average thermal expansion at 300°-900°C of $9.3 \pm 0.5 \times 10^{-6} \text{K}^{-1}$.

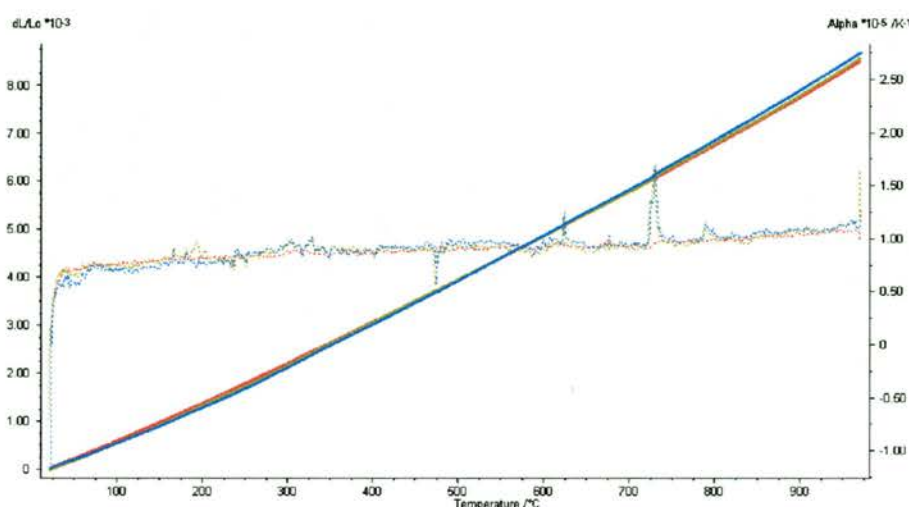


Fig.6.16 dL/L_0 (straight lines) and α_p curve for CaNb₂O₆

Table 6.6 Technical and physical alpha for CaNb₂O₆

	Reduction T(°C)	α_t 300°C-900°C (10^{-6}K^{-1})	α_p 900°C (10^{-6}K^{-1})
CaNb ₂ O ₆	N/A	9.3 ± 0.5	10.4 ± 0.5
CaNb ₂ O _{6-δ}	1000	9.6 ± 0.5	10.8 ± 0.5
CaNb ₂ O _{6-δ}	1200	9.4 ± 0.5	10.6 ± 0.5

6.3 Conclusion

Having looked at compositions MNb₂O₆ with M=Ca, Sr, Ba, it is clear that although these materials display interesting properties upon reduction, and variable stability to reduction, none show high enough electronic conductivity to make them of interest for further study in fuel cell development. Table 6.7 sums up their properties. The calcium compound is the worst performing in the conductivity studies, and is most stable to reduction.

BaNb₂O₆ has the largest thermal expansion of these structures with $11.9\text{-}12.3 \times 10^{-6} \text{K}^{-1}$. Its conductivity, however, upon reduction in 5%H₂/Ar at 900°C is 0.6 Scm^{-1} , with a conductivity dependence on $p(\text{O}_2)$ of $-1/5$ from 10^{-1} to 10^{-20} atm.

The study of these materials does, however, give an insight into niobium based materials and electronic conduction. Although a range of structures support niobium in the oxidation state +4, to allow the complete reduction of niobium from oxidation state +5 to oxidation state +4 there must be significant structural rearrangement to accommodate different bonding behaviour of Nb⁵⁺ and Nb⁴⁺. The materials which show structural stability to reduction, as in the case of MNb₂O₆ do not have a fully reduced Nb. Whereas in the case of Nb₂TiO₇ structural similarity between TiO₂ and NbO₂ allows the transition of this structure to rutile structure upon reduction and in 5%H₂/Ar niobium is in oxidation state 4+.

MNb ₂ O ₆	Reduction T (°C)	Unit cell symmetry	a(Å)	b(Å)	c(Å)	β (°)	V (Å ³)	TEC (10 ⁻⁶ K ⁻¹)	Conductivity (Scm ⁻¹) at 900°C	Ea (eV) heating	Ea (eV) cooling
CaNb ₂ O ₆	N/A	Orthorhombic P	14.9971(9)	5.7542(3)	5.2301(3)	90	451.33(6)	9.25	3x10 ⁻⁶	1.00-1.02 (840°- 900°C)	1.06 (830°-900°C)
CaNb ₂ O _{6-δ}	1000	Orthorhombic P	14.9884(8)	5.7510(3)	5.2268(3)	90	450.53(6)	9.63	1.46x10 ⁻³	curve	curve
CaNb ₂ O _{6-δ}	1200	Orthorhombic P	14.9900(8)	15.7517(3)	5.2276(3)	90	450.72(6)	9.38	1.00x10 ⁻²	curve	curve
SrNb ₂ O ₆	N/A	Monoclinic P	7.7325(6)	5.6023(4)	10.9976(8)	90.372 (4)	476.40(9)	5.90	5.6-6.8x10 ⁻⁵	1.48 ±0.01	1.34±0.01
SrNb ₂ O _{5.98}	1000	Monoclinic P	7.7353(6)	5.6029(4)	11.0003(8)	90.362(4)	476.74(8)	5.45	7-8x10 ⁻²	0.96±0.02 (250- 450)	1.00±0.02(250-450) 0.81±0.02(450-720)
										0.76±0.02(450-720)	1.10±0.02(720-900)
										1.33±0.02(720-900)	
SrNb ₂ O _{5.76-5.77}	1200	Tetragonal P	12.3854(8)	12.3854(8)	7.8101(7)	90	1198.04(20)	11.18	40	—	—
BaNb ₂ O ₆	N/A	Orthorhombic C	7.8678(3)	12.2127(5)	10.2868(4)	90	988.43(10)	11.93	2.2-2.6x10 ⁻³	2.04 (800°-900°C)	2.33 (800°-900°C)
BaNb ₂ O _{6-δ}	1000	Orthorhombic C	7.8702(4)	12.2143(5)	10.2886(4)	90	989.03(10)	12.37	0.58-0.60	0.48 (50°-200°C)	0.49 (50°-200°C)
										curve (200°-900°C)	curve (200°-900°C)
BaNb ₂ O _{6-δ}	1200	Orthorhombic C	7.8714(3)	12.2202(5)	10.2933(5)	90	990.11(10)	11.93	12.7-3.7	—	—

Table 6.7 Summary of unit cells, conductivity and thermal expansion of MNb₂O₆

6.4 References

- 1 M.H.Francombe, *Acta Cryst.*, (1960), **13**, 131
- 2 P.R.Slater and J.T.S.Irvine, *Solid state Ionics*, (1999), **120**, 125
- 3 F.Galasso, G.Layden and G.Ganung, *Mat.Res.Bull.*, (1968), **3**, 397
- 4 V.P.Sirotinkin, and S.P.Sirotinkin, *Zhurnal Neorganicheskoi Khimii*, (1990) **35**,
2189
- 5 L.Marta and M.Vancea, *Revista de Chimie*, (1982), **33** (6), 537
- 6 G.Blasse, *J.Inorg.Nucl.Chem.*(1964), **26**, 1191
- 7 J.P.Cummings and S.H.Simonsen, *American Mineralogist*, (1970) **55**, 90

Chapter 7. Discussion and further work

7.1 DISCUSSION	241
7.2 FURTHER WORK	243

7.1 Discussion

This work was carried out with a view of trying to find a suitable material for a partial or full replacement of Ni in the Ni/YSZ anode, i.e. to act as a current collector in the SOFC. Working on the premise that $\text{Nb}_{1.33}\text{Ti}_{0.67}\text{O}_4$, which is readily obtained by reducing Nb_2TiO_7 at 900°C in flowing $5\%\text{H}_2/\text{Ar}$, has a very high electronic conductivity of 300 Scm^{-1} but a low thermal expansion coefficient of $3\times 10^{-6}\text{K}^{-1}$, it was hoped that doping this material will increase the thermal expansion without too much effect on the electronic conductivity.

Doping with Zr did produce an increase in the thermal expansion coefficient up to $5.5\times 10^{-6}\text{K}^{-1}$ and $6.1\times 10^{-6}\text{K}^{-1}$ for 10% and 15% doped samples respectively, the resultant conductivities were significantly reduced to $\sim 150\text{Scm}^{-1}$. Doping with Fe was a little more successful with a maximum thermal expansion coefficient of $6.3\times 10^{-6}\text{K}^{-1}$ for $\text{Nb}_{1.347}\text{Ti}_{0.639}\text{Fe}_{0.014}\text{O}_4$ and a conductivity of $\sim 200\text{Scm}^{-1}$.

Niobium oxide reacts with Ce in the CGO composite at temperatures as low as 900°C to form additional phases, one of which is CeNbO_4 . It is therefore unsuitable for use in cerium based anodes/electrolytes.

Having looked at strontium niobates and CaNb_2O_6 and BaNb_2O_6 , and their low electronic conductivities, I decided to investigate other niobium based rutile structures, namely $\text{Ti}_{1-2x}\text{Cr}_x\text{Nb}_x\text{O}_2$ solid solution series. Although these materials show relatively low conductivities of $\sim 20\text{Scm}^{-1}$ at 900°C in flowing $5\%\text{H}_2/\text{Ar}$ I believe that they hold promise with further work, and my initial preliminary investigation into these materials found these to be relevant:

- The thermal expansion of these samples was high with $8.57\times 10^{-6}\text{K}^{-1}$ for the $x=0.1$, dropping to $6.04\times 10^{-6}\text{K}^{-1}$ for the $x=0.5$.
- There was little change in the thermal expansion with reduction, which is important for fuel cell application.
- These samples show much better sinterability compared to $\text{Nb}_{1.33}\text{Ti}_{0.67}\text{O}_4$, with densities of over 85% after regrinding and 2nd firing.

Strontium niobates were studied with a view to try to synthesise a highly conducting phase $\text{Sr}_{1-x}\text{NbO}_3$. This phase, however, was found to be very difficult to make requiring extremely reducing conditions and repeated firing. Once synthesised $\text{Sr}_{0.6}\text{NbO}_3$ was found to be very unstable under milder reducing conditions than those under which it was synthesized, hence at 900°C in $5\%\text{H}_2/\text{Ar}$ it decomposed into $\text{Sr}_4\text{Nb}_2\text{O}_9$ and $\text{Nb}_2\text{O}_{5-x}$.

When looking at $\text{Sr}_x\text{Nb}_y\text{O}_{x+2.5y}$, these phases were studied:

- $\text{Sr}_4\text{Nb}_2\text{O}_9$
- $\text{Sr}_2\text{Nb}_2\text{O}_7$
- SrNb_2O_6

Although decreasing the Sr:Nb ratio gradually facilitated the reduction and hence the conductivity of the material, the conductivities were too low, with a maximum conductivity of $\sim 0.1\text{-}0.2 \text{ Scm}^{-1}$ for $\text{Sr}_2\text{Nb}_2\text{O}_7$ at 900°C in $5\%\text{H}_2/\text{Ar}$. These materials are therefore unsuitable for application as a current collector in the SOFC anode.

In the systems studied, there are two types of conductivity that dominate:

- Linear dependence over the range as in BaNb_2O_6 or $\text{Sr}_2\text{Nb}_2\text{O}_7$ with simple defect equilibrium and fair kinetics
- Series of difficult transitions, kinetically limited as in the rutile $\text{Ti}_{1-2x}\text{Cr}_x\text{Nb}_x\text{O}_2$ series

7.2 Further work

Having looked at different niobium based materials, I have found that for high conduction in the niobium based materials it is important to have some edge-sharing octahedra through out the structure, and preferably chains of edge sharing octahedra as is found in the rutile niobium titanates.

Further work should be carried out into $\text{Nb}_x\text{M}_x^{\text{III}}\text{Ti}_{1-2x}\text{O}_2$ (M=Al, Cr or Fe) solid solution materials as this thesis just reports the preliminary studies into their properties. These materials show interesting electronic and structural properties, which have been only superficially investigated. Further impedance studies along with SEM could reveal more about grain boundaries and their contribution to electronic conductivity. Gradually substituting Cr by Fe may increase both the conductivity and the thermal expansion of these systems.

Having found that the best doped samples for their highest conductivity and thermal expansion are $\text{Nb}_{1.347}\text{Ti}_{0.639}\text{Fe}_{0.014}\text{O}_4$, $\text{Nb}_{1.33}\text{Ti}_{0.634}\text{Zr}_{0.033}\text{O}_4$ and $\text{Nb}_{1.33}\text{Ti}_{0.600}\text{Zr}_{0.067}\text{O}_4$, further study can be carried into solid solutions occurring between these phases.